The Fabrication of Integrated Strain Sensors for “Smart” Implants using a Direct Write Additive Manufacturing Approach

LI-JU WEI

Submitted in partial fulfilment of the requirements for the award of Doctor of Philosophy

Faculty of Technology
De Montfort University
Leicester UK

May 2014

Abstract

Over the 1980's, the introduction of Additive Manufacturing (AM) technologies has provided alternative methods for the fabrication of complex three-dimensional (3D) synthetic bone tissue implant scaffolds. However, implants are still unable to provide post surgery feedback. Implants often loosen due to mismatched mechanical properties of implant material and host bone. The aim of this PhD research is to fabricate an integrated strain gauge that is able to monitor implant strain for diagnosis of the bone healing process. The research work presents a method of fabricating electrical resistance strain gauge sensors using rapid and mask-less process by experimental development (design of experiment) using the nScrypt 3Dn-300 micro dispensing direct write (MDDW) system.

Silver and carbon electrical resistance strain gauges were fabricated and characterised. Carbon resistive strain gauges with gauge factor values greater than 16 were measured using a proven cantilever bending arrangement. This represented a seven to eight fold increase in sensitivity over commercial gauges that would be glued to the implant materials.

The strain sensor fabrication process was specifically developed for directly fabricating resistive strain sensor structures on synthetic bone implant surface (ceramic and titanium) without the use of glue and to provide feedback for medical diagnosis. The reported novel approach employed a biocompatible parylene C as a dielectric layer between the electric conductive titanium and the strain gauge. Work also showed that parylene C could be used as an encapsulation material over strain gauges fabricated on ceramic without modifying the performance of the strain gauge. It was found that the strain gauges fabricated on titanium had a gauge factor of 10.0±0.7 with a near linear response to a maximum of 200 micro strain applied. In addition, the encapsulated ceramic strain gauge produced a gauge factor of 9.8±0.6. Both reported strain gauges had a much greater sensitivity than that of standard commercially available resistive strain gauges.

Acknowledgement

I would like to acknowledge and express my deepest thanks to my supervisor Dr. Chris Oxley for his guidance and continuous encouragement over the course of my PhD.

I am also grateful to Professor David Wimpenny for his dedication to my academic development.

I would like to express my appreciation to all my colleagues in the Additive Manufacturing Technology Group at De Montfort University for their support.

I would like to extend my gratitude to Paul, Mark and Glen, in the engineering department for providing their mechanical knowledge and support.

A special thanks to Russell Thomas, ParaTech Coating UK LTD., for the technical support of parylene C coating.

I am eternally gratefully to my family, my parents, my wife and son. Thank you for your endless encouragement, support and unwavering belief in me.

Table of Content

Abbreviations and Definitions

AM	Additive Manufacturing
Aspect ratio	The ratio of longer side to its shorter side
Autogenous bone graft	Grafting bone taken from other parts of the patient's body
Backing material	Supporting substrate of strain gauge sensor, interchangeable with carrier material
Biocompatibility	The acceptance of the implant material by the surrounding tissues of the body
Carrier material	See backing material
CNC	Computer Numerically Controlled
Conformal printing	The ability to transfer and patterning materials on a curvature surface
CVD	Chemical vapour deposition
Distraction osteogenesis	A surgical tool that can be used to apply mechanical stress to promote bone-forming process and to activate the tissue growth and regeneration
DW	Direct Write
Free tissue transfer	A surgical technique where the damaged bone segments are removed and replaced by the bone graft taken from another part of the patient's body. Interchangeable with free flap.
Gauge factor	The sensitivity of the strain gauge
In vitro	When the process is taken outside a living organism
In vivo	When the process is taken in a living organism
MDDW	Micro Dispensing Direct Write
Osseointegration	Direct contact of bone tissues to an implant surface without forming fibrous membrane
Parylene	Poly-para-xylylenes
PDMS	Poly-dimethyl-siloxane
Strain gauge	A device that measures strain of a structure at the point of attachment. Interchangeable with sensor.
Stress shielding	The phenomenon causing bone resorbs when the replaced implant is stiffer than the surrounding host bone
Vascularisation	The development of blood vessel inside the implant scaffold

Table of figures

List of tables

Research output

Poster presentation, “Generation of “Smart” Implants using Direct Writing Additive Manufacturing Approach”, 8th Annual IeMRC Conference, 2013.

L. J. Wei and C. H. Oxley, “Carbon based resistive Strain Gauge Sensor fabricated on titanium using Micro-Dispensing Direct Write technology”, IET Healthcare Technology Letters [in review], 2015.

Chapter 1. Introduction

1.1 Background

Since the 1990's, Additive Manufacturing (AM) technologies have given manufacturing potential in various industrial sectors such as medical devices, aerospace, power generation, and automotive. Medical devices now account for the third largest sector in AM [1]. The techniques are primarily used in providing visual aid three-dimensional (3D) medical models for surgical planning, and direct customised scaffold implant fabrication for surgeries.

Conventionally, "free tissue transfer" is usually recommended to treat segmental bone defect, which is a surgical procedure that uses the patients' own bone graft, referred to as an autogenous bone graft, to replace the defective bone. However, it is a lengthy process as secondary surgery is required on the donor site to harvest bone graft. When considering donor site morbidity and limitation of autogenous bone graft, the synthetic bone grafts will be required [2].

Synthetic bone grafts are aimed to replace defective bone and ideally should be patient-specific that matches both mechanical properties and structure to the surrounding bone. Mismatched mechanical properties between synthetic bone implant and surrounding host bone may cause implant loosening or "stress-shielding" and eventually leading to implant failure. AM technologies opened a new method of medical bone scaffold fabrication. It enables fabrication of porous structure using biocompatible materials that can be custom-built using current medical imaging technology and implanted after fabrication. The mechanical properties often can be tailored by matching the porosity of the scaffold to the natural bone.

Although AM has provided promising results on customised implant fabrication. Most of the current implants are fabricated in a single material and provides no performance feedback once implanted. As bone loading environment and deformation can profoundly influence the bone ingrowth, remodelling and repair would be

advantageous to monitor bone loading. The most common sensor used in bone monitoring is the one that measures strain, as strain is the most critical and fundamental factor in bone remodelling, repair and regeneration [3]. *In vivo* bone strain measurements were carried out as early as 1975 by Lanyon et al [3]. To date, studies on human bone strain measurement have focused on long bones, for example, the tibial shaft, by bonding electrical resistance strain gauges directly to the bone. The positioning and attachment of the strain gauge requires highly invasive surgery procedures, therefore the use of strain sensors is limited to a number of superficial bones [4]. An alternative approach to monitoring bone healing is the use of strain gauges bonded on bone plates. Bone plates are used to immobilise bone fracture site to promote healing. During the bone healing process, fracture site will become stiffer. By measuring the strain distribution on bone plate an indication of the healing progress can be monitored [5].

Direct Writing technology, a branch of AM technology, is a new class of additive material processing. The Additive Manufacturing Technology Group (AMTG) at De Montfort University is equipped with the only biomedical Direct Write (DW) machine (nScrypt 3dn-300) in the UK. Recent work conducted at De Montfort University [6][7], combining Direct Writing and freeze casting has been used for the deposition of porcelain, alumina and hydroxyapatite for the fabrication of bone scaffolds. In addition to depositing monolithic homogenous material as 3D objects, the potential also exists to generate multi-material 3D objects. This will enable both mechanical and electrical functions to be realised giving the potential of integrating electrical sensors on the bone scaffold for monitoring implant performance. Using this approach it is possible to generate smart implants with embedded strain sensing capability.

This research explores novel methods of fabricating electrical resistance strain gauges using rapid, low-cost and mask-less additive direct-write technology directly to bone implant surfaces (i.e. ceramic, titanium) to provide feedback of the mechanical properties of the implant for medical diagnoses.

1.2 Aims and Objectives of the project

The overall aim of this study is to fabricate an integrated strain gauge sensor using Micro-Dispensing Direct Write (MDDW) technology from nScrypt, which can be used for real-time implant strain monitoring.

The objectives are:

1. Identify the MDDW processing parameters, dispensing quality control and curing conditions

2. The fabrication of resistive strain gauges on polymeric carriers and investigate gauge performance

3. Explore the feasibility of fabricating integrated resistive strain gauges on bioinert test-plates with deposited parylene C layer as the encapsulation and dielectric layer.

1.3 Novelty and Significance

The key areas of novelty of this PhD research include:

- The fabrication of highly sensitive (gauge factor >10) miniature strain gauge sensors using nScrypt 3Dn-300 Micro Dispensing Direct Write (MDDW) system
- Fabrication of MDDW carbon strain gauge sensor on ceramic test-plate and Parylene C coated titanium test-plate without polymeric backing or use of glue for medical implant application

1.4 Overview of the thesis

Chapter	Description
1- Introduction	This chapter described the research background, aim and objective, overview of the thesis
2- Bone tissue engineering	This chapter explores the mechanical properties of bone, bone healing progress, conventional bone reconstruction procedure and the need for synthetic bone scaffold.
3- Additive manufacturing technology	A brief introduction to the AM technologies used to produce bone scaffolds and possible biocompatible materials employed.
4- Bone strain measurement	This chapter describes the current use of strain gauge technology for bone surface strain measurement.
5- Direct Writing technology	This chapter introduces the direct writing technology and the strain gauge fabrication methods employing DW and non-DW fabrication technologies.
6- Research approach and equipment	This chapter covers the key findings from the literature review and presents the aim and objectives of the research. The significance of the work and the experimental approach will be covered.
7- Direct write silver resistive strain gauges	This chapter described the experimental work of resistive strain gauge fabrication employed MDDW nScrypt machine using commercial silver paste. The processing parameters and gauge performance will be discussed in this chapter.
8- Direct write carbon resistive strain gauges	This chapter describes the experimental work of resistive strain gauge fabrication employing MDDW nScrypt machine using commercial carbon paste. The processing parameters, gauge performance and fabrication using fine nozzle are discussed.
9- Direct write integrated carbon strain gauges	This chapter describes the experimental work on the fabrication of integrated strain gauge and the investigation of gauge performance.
10- Conclusion and further work	This chapter concludes overall research and suggestions for further work.

Chapter 2. Bone tissue engineering

2.1 Introduction

Conventionally, the diseased bone or damaged bone caused from a trauma is excised and replaced by autogenous bone graft, which is taken from other parts of the patient's body (donor site) along with its blood vessels [2]. The surgical term is often referred as "free flap" or "free tissue transfer". However, the use of autogenous bone graft involves harvesting bone and requires secondary surgery from the donor site. When autogenous bone graft is limited or the donor site is diseased, synthetic bone graft materials are often needed.

Bone tissue engineering is based on the understanding of bone structure, bone mechanics and tissue generation to recreate substitute scaffold structure. Tissue engineering was defined by R. Langer and C. Vacanti "as seeding cells and generation of biologic scaffolds in which the principles of engineering and the life sciences are applied for the purpose of restoration, creation or preservation of lost function and provide alternatives for autologous grafting and organ replacement" [8][9].

The synthetic scaffolds aim to mimic the function of the natural bone being able to be substituted temporally or permanently while providing a structural support for new bone tissue ingrowth [10]. The aim of this chapter is to understand the composite and mechanical properties of the bone and to investigate biocompatible materials. Furthermore, to define possible synthetic materials that are suitable for sensor integration.

2.2 Bone structure and mechanical properties

Bone is a complex material that is comprised of an inorganic component of hydroxyapatite and organic matrix of collagen. It is the hard connective tissue that gives support to the body structure and provides a framework for skeletal motion [11]. On the macro-scale, bone structure can be classified into cancellous (trabecular or spongy) bone and cortical (compact) bone. The physical properties are shown in Table 2.1, trabecular bone and cortical bone have different porosities range from 0.2 to 0.3 g/cm^3 and from 1.64 to 1.85 g/cm^3 respectively that result in different mechanical properties [12].

Table 2.1 Physical Properties and Biomechanical Properties of Human Bone [12]

Physical Properties	*Cancellous Bone (Trabecular Bone)*	*Compact Bone (Cortical Bone)*
Density (g/cm^3)	0.2-0.3	1.64-1.85
Biomechanical Properties	Trabecular Bone	Cortical Bone
Young's Modulus (GPa)	0.4	17.7 (Longitudinal) /12.8 (Transverse)
Tensile Strength (MPa)	7.4	133 (Longitudinal) /52 (Transverse)

Cancellous bone has a higher surface area and is highly vascularise, while cortical bone's main function is to support the body and protect organs. There are defined porosity differences between the trabecular and cortical bone that can be seen in the following cross-sectional scan electron microscope (SEM) micrographs shown in Figure 2.1, which explain their difference in mechanical properties [13].

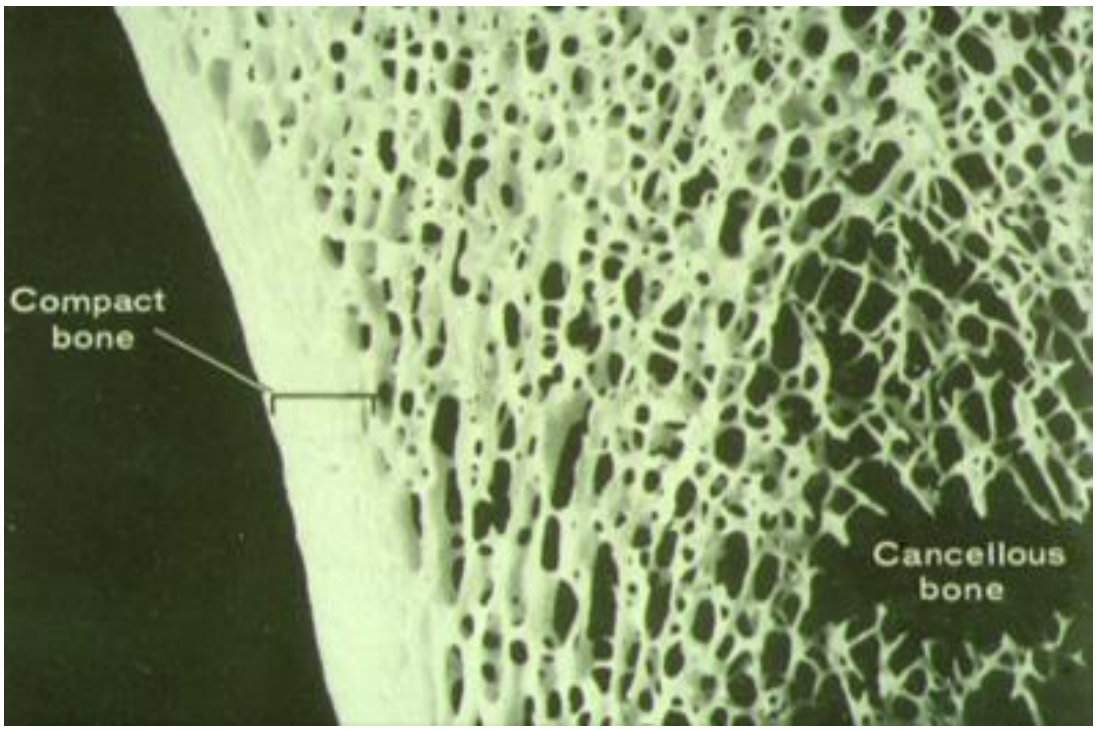

Figure 2.1 SEM micrograph of femur bone [13]

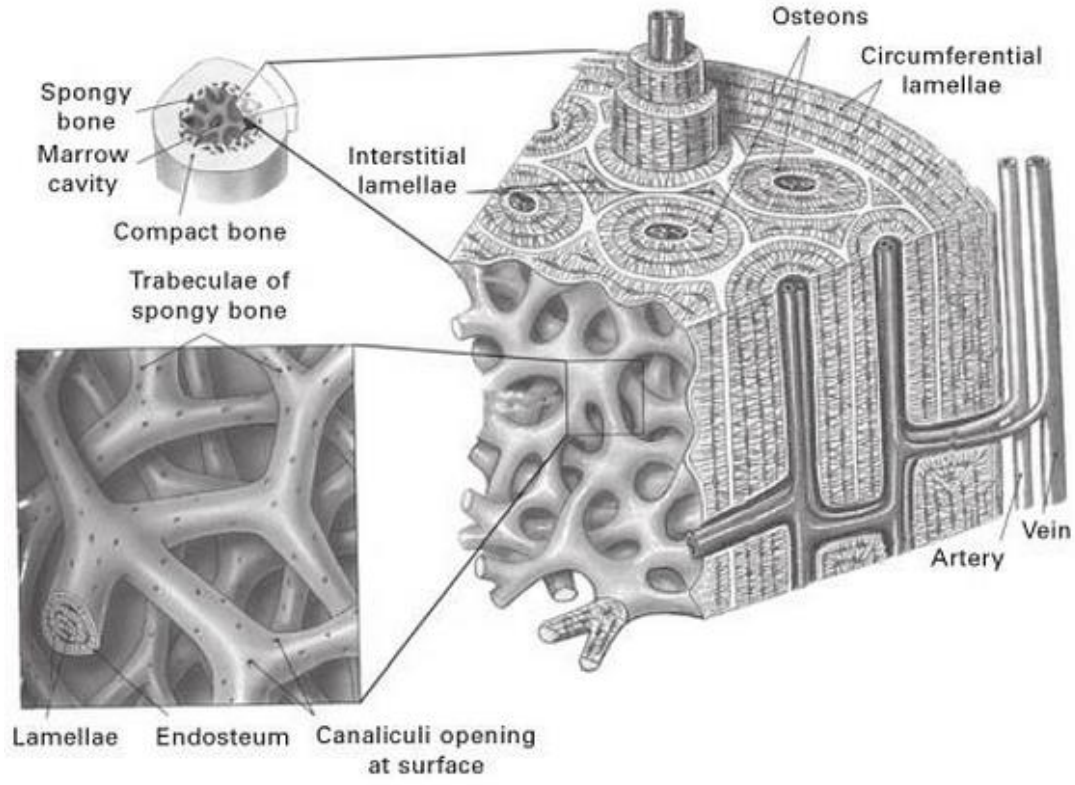

Figure 2.2 Structure of bone tissue [14]

Imaging bone on the micro scale level it can be seen to consist of a number of irregular cylindrical units, namely osteons. A central canal is surrounded by concentric lamellae of bony tissue as shown in Figure 2.2 [14]. The anisotropic biomechanical property of the bone is due to the oriented structure of the osteons [15]. Therefore, cortical bone is stiffer and stronger when load is applied in the longitudinal direction rather than in transverse direction.

2.3 Bone Fracture and Healing Process

Following a fracture of the bone there are different types of mechanisms the body uses to repair the bone, these include 'micromotion' and 'macromotion'. The micromotion allows fracture fragments to heal with a small amount of fracture-line callus, which is known as primary healing. The macromotion occurs when a complete fracture occurs, and is known as the secondary healing.

New bone is formed and approach each other [16]. The callus is the new-formed hard substance surrounding the bone fracture during healing as shown in Figure 2.3 (A) and is usually replaced with compact bone shown in Figure 2.3 (B).

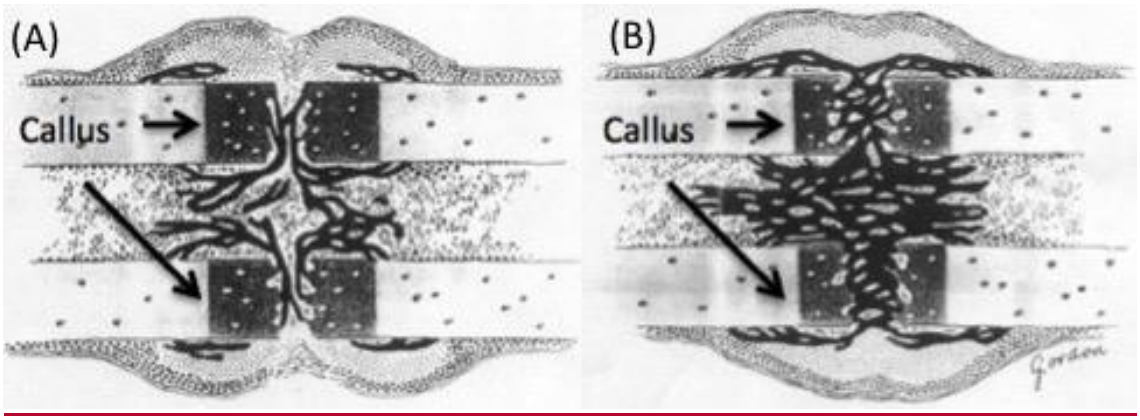

Figure 2.3 Bone repair under macromotion surround with complete fracture [16]

In order to promote cell in-growth in the bone during bone repair/healing, internal fixation plates, wires or screws are often used to stabilise the bone. Various types of bone fractures and prostheses used for bone fixations are shown in Figure 2.4 [17]. The most commonly used biomaterials for internal fixtures are as shown in Table 2.2 [16].

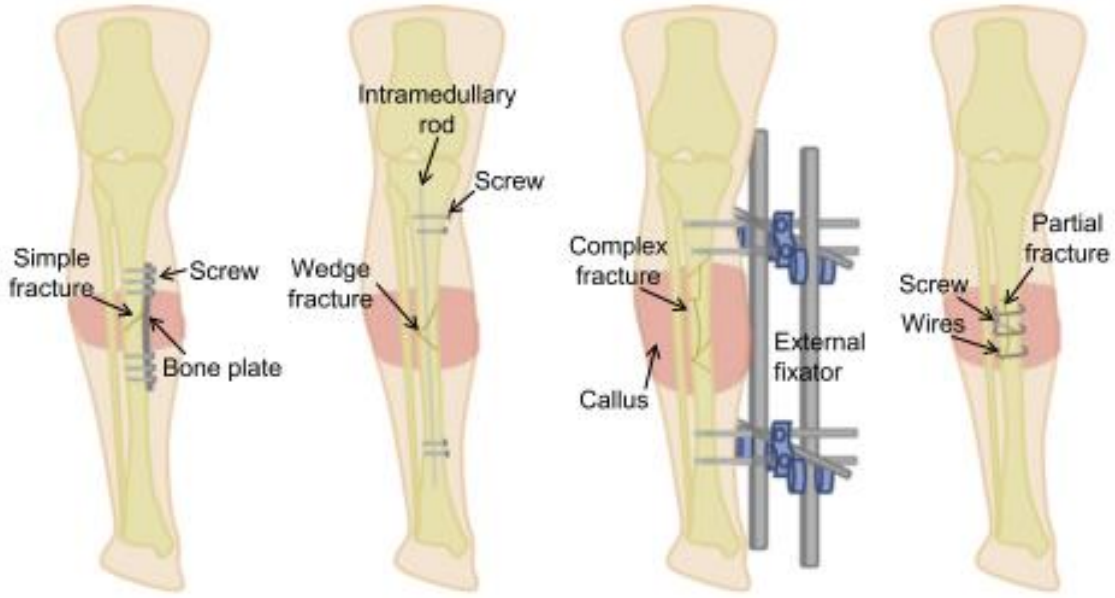

Figure 2.4 Types of bone factures and prostheses used for bone fixation [17]

Table 2.2 Biomaterials applications in internal fixation [16]

Materials	Properties	Application
Stainless steel	Low cost	Surgical wire; pin, plate, screws, IM nail
Ti alloy	High cost, low density and Young's modulus; excellent osteointegration	Surgical wire; pin, plate, screws, IM nail
Co-Cr alloys	High cost; high density and Young's modulus; difficult to fabricate	Surgical wire, IM nail

2.4 Bone Healing

Bone constantly undergoes self-regeneration and remodelling that involves bone-forming (osteogenic) and bone-removing (osteoclastic) processes. According to Wolff's Law [16] of bone remodelling, changing the mechanical environment will break the equilibrium between the two processes. If a stress greater than normal physiological level is applied, the equilibrium will favour the bone-forming process and vice versa. In order to promote bone-forming process on bone healing site, distraction osteogenesis, is a commonly used surgical tool to apply mechanical stress and stimulate the tissue growth and regeneration.

An animal study was carried out to show that new bone growth resulted from distraction osteogenesis as shown in Figure 2.5 [9]. The translucency area can be seen in the fracture site after osteotomy (shown by arrow in Figure 2.5a), and after 12 weeks period (shown between two arrows in Figure 2.5b) the opaque area of the distraction site increased indicating cortical bone of the same density as the base segment [9]. As the distraction device is in direct contact with the bone, a strain sensor can be embedded to provide strain feedback for monitoring healing. The detail will be cover later in section 4.4.

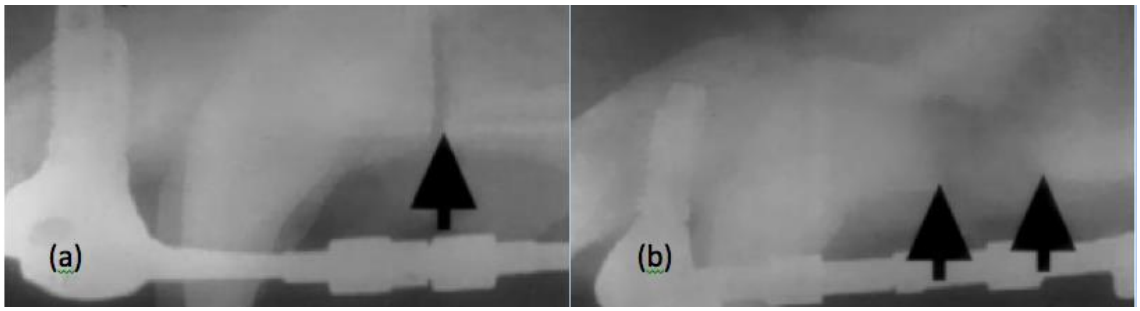

Figure 2.5 Radiograph of maxillofacial distraction (a) after osteotomy (b) after distraction [9]

If the bone suffers a severe defect as a result of cancer or an accident, a bone graft will be needed to replace the missing bone. One approach is to use a process known as 'free tissue flap'.

2.5 Free-Tissue Flap

Conventionally, the diseased bone or damaged bone is removed and replaced by bone graft substitute. If the bone graft is taken from another part of the patient's body, the bone substitutes are called autogenous bone graft. The area where the bone is taken from is known as the donor site. The three main donor sites used in mandibular reconstruction for free-tissue flap are fibula, iliac crest and scapula. Other autogenous grafts options includes rib and tibia [18]. The surgery technique is called 'free-tissue flap' or 'free-tissue transfer'. This technique is often recommended as the autogenous bone grafts have greatest potential to promote direct structural and functional connection between the implant and living host bone [2]. An example of autogenous bone graft is to replace a defective segmental mandibular with an iliac crest (a margin of the greater pelvis) free-tissue transfer as shown in Figure 2.6.

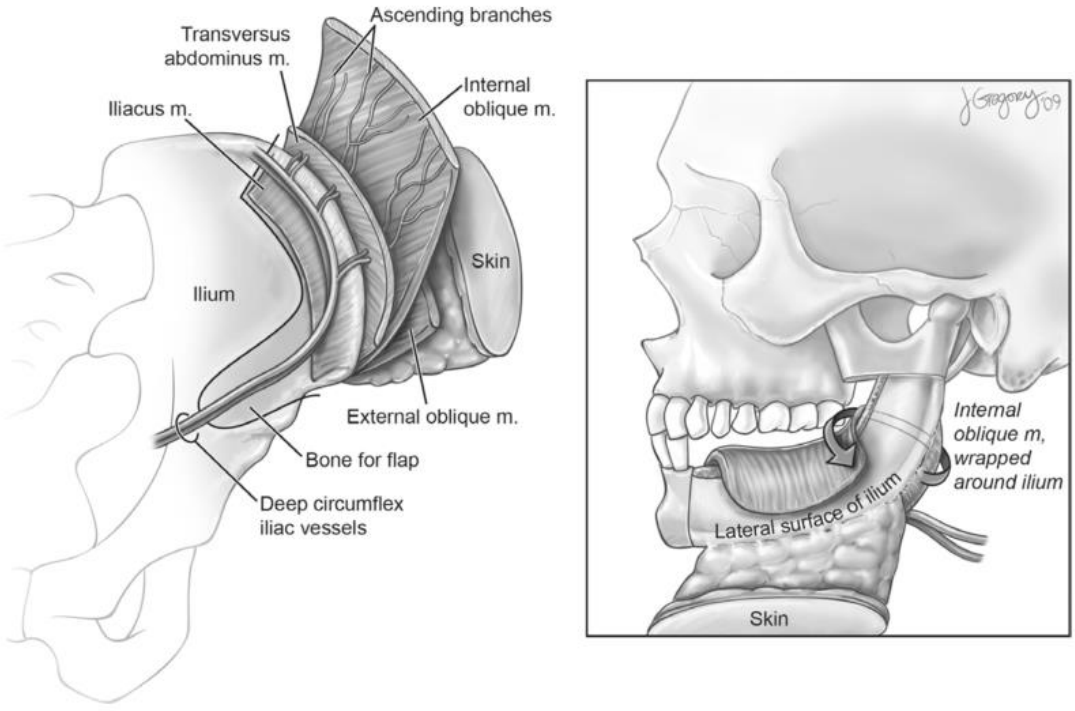

Figure 2.6 Schematic diagram of iliac crest free-tissue flap example [2]

However, there are several scenarios that the free flap surgery may not apply:

(a) If the bone defect is too large and the amount of autogenous bone graft may not be sufficient from the donor site
(b) It may require a very lengthy surgical procedure as secondary surgery is required to harvest bone graft from the donor site
(c) If the donor site is diseased or considering the donor site morbidity due to secondary surgery

Therefore an alternative to bone substitute may be considered. The alternatives to autogenous bone graft for substitute includes allogenic (human-driven), xenogenic (animal-driven), or synthetic bone graft materials [19]. Synthetic bone graft materials are often the preferred choice over allogenic and xenogenic bone graft materials as these may result in problems of immune rejection and disease transfer [20]. There are many synthetic materials available that can be implanted and are dependent to the biological response of the material to the surrounding tissue. This is known as biocompatibility of the material.

2.6 Biocompatibility of synthetic materials

Biocompatibility is a general term that addresses the acceptance of the implant material by the surrounding tissues of the body. The implant material should be compatible with the tissues in terms of mechanical, chemical, surface and pharmacological properties [12]. Due to the various biological responses to the biocompatible materials, the biocompatibility of material can be split into three classes: bioinert, bioactive and bioresorbable.

Bioinert materials generally exhibit good chemical stability and consolidate into the bone tissue with the pattern of contact osteogenesis. Bioinert materials generally have greater mechanical strength than bioactive and bioresorbable materials. When bioinert tissue is implanted, a fibrous tissue will encapsulate the implant. Bioactive materials

have the ability to chemically bond with adjacent bone tissue known as bonding osteogenesis. Bioresorbable materials are used as temporary support *in vivo* load as they will be gradually degraded in biological environment, producing biocompatible degradation byproducts and promote new formed bone tissue in-growth [21]. The dissolution products of the scaffold should be metabolised by the body. Polymers and hydrogels are most commonly used as bioresorbable scaffolds. A list of the biocompatible classes including examples of the material and biological response are shown in Table 2.3 [22].

Table 2.3 List of biocompatible classes with their example and biological response [22]

Class	*Example*	*Biological response*
Bioinert	Medical grade alumina Zirconia Pure titanium[23] Parylene C [24]	Encapsulation of the implant by fibrous tissue
Bioactive	***Osteoconductive***	
	Hydroxyapatite (HA) Tri-calcium phosphate	Bond to hard tissue and stimulate bone growth along the surface of the bioactive material
	Osteoproductive	
	Bioactive glasses	Stimulate the growth of new bone on the material away from bone/implant interface
Bioresorbable	Polyglycolic acids (PGA) Polylactic acids (PLLA) Polycaprolactone (PCL) Calcium phosphates	Dissolve in contact with body fluids and dissolution products are secreted via kidney

2.7 Synthetic scaffold material

Synthetic bone grafts using tissue engineering is aimed at overcoming the limitation of autogenous bone grafts. The synthetic bone grafts are produced in the form of scaffolds with a similar structure and geometry to the defective bone, to assist in cell regeneration and restore aesthetical functions.

The synthetic scaffold structure needs to fulfil the requirements including pore size, porosity, interconnectivity, surface topology and surface area to volume ratio. The pore size and porosity are the primary factors for cell-ingrowth and vascularisation. The pore size must have diameters of at least 100µm with interconnected micro-pores of minimum diameters of 10-12µm in order to promote host bone tissue in-growth. A high level of porosity increases internal surface area, and high internal surface area to volume ratio is necessary as it is beneficial to cell adhesion, migration and vascularisation. The rough surface texture of the synthetic bone scaffold that consists of nanometre sized pores can also promote cell activity [22].

Common scaffold materials can be categorised into three categories: polymer, metal and ceramics. The choice of substitute scaffold materials requires the mechanical properties to be comparable with the biologic materials, for example the stiffness (Young's modulus). Mano et al [25] has indicated, "The development of synthetic materials for bone replacement should be based ideally on a complete understanding of the bone structure to be substituted." The relationship of the mechanical properties between biologic and synthetic materials are shown in Figure 2.7 [25]. It can be seen that commonly synthetic materials, for example ceramics and metals, are stiffer and exhibit higher mechanical strength than the biologic hard tissues, which they are replacing.

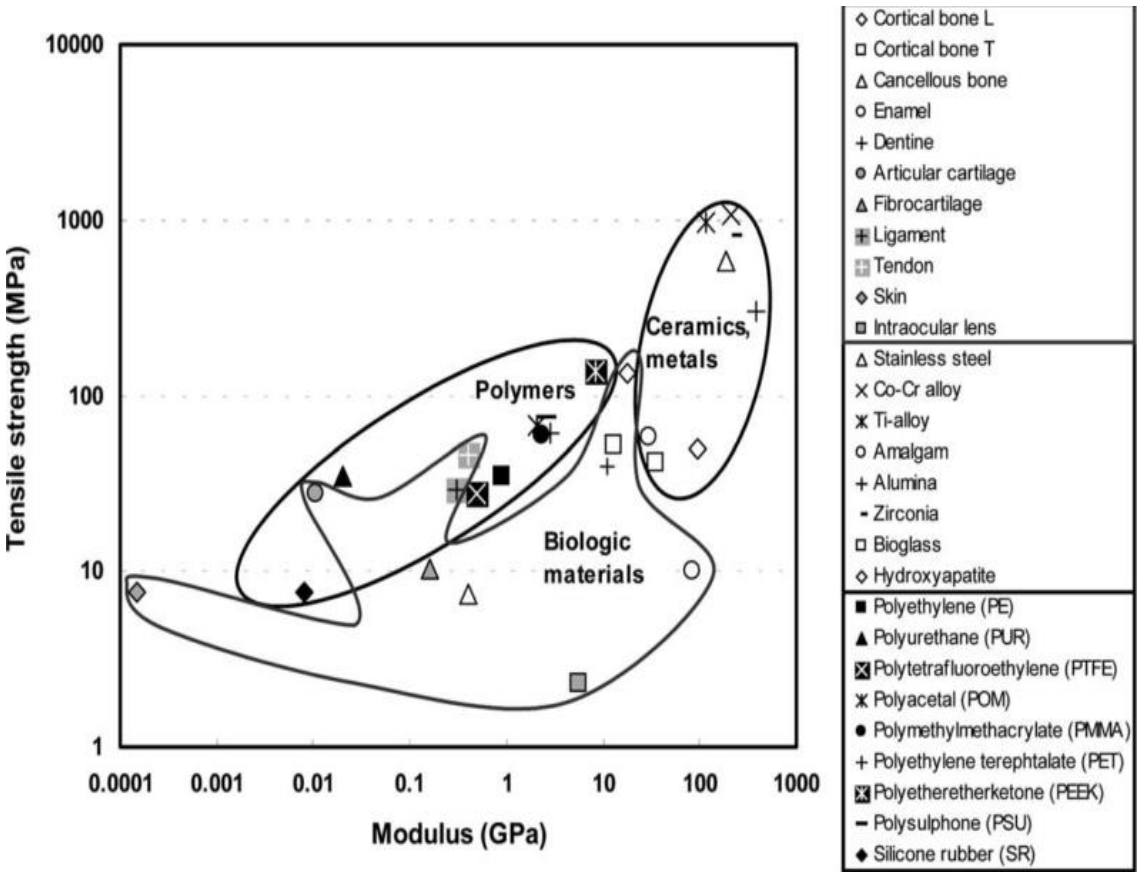

Figure 2.7 Tensile strength and modulus of biologic and synthetic materials [25]

The mismatch between the mechanical strength of the engineered scaffold and the host tissue can lead to an effect called the stress shielding. It was found in the early days of total hip replacement, all the load was transferred through the metal causing the body to resorb the bone [22], leading to early failure of the hip replacement. Therefore, the mechanical properties of final scaffold construction are critical to longevity of the synthetic implant.

2.7.1 Polymer

Polymeric scaffolds [26]–[28] have been widely investigated and often used as a temporary support matrix for tissue repair and regeneration. Polymeric biomaterials can be natural or synthetic. Polymers are long chain molecules that are formed by linking repetitive monomer units. Natural polymers contain bio-functional molecules,

which can aid in tissue attachment, and proliferation of cells. However, if it is a degradable biomaterial, its degradation rate inhibits cell function.

The degradation rate of natural polymers is hard to control and they are complex, thus hard to characterise [29]. Therefore, synthetic polymers are the area of interest. The mechanical properties of synthetic polymers can be controlled by molecular weight of the polymer. Bioresorbable synthetic polymers have been used for decades as dissolving surgical stitches used to hold tissue together; therefore, polymers such as polylactic acid and polyglicolic acids have passed the United States Food and Drug Administration (FDA) regulations. Commonly used polymeric scaffold materials are shown in Figure 2.8.

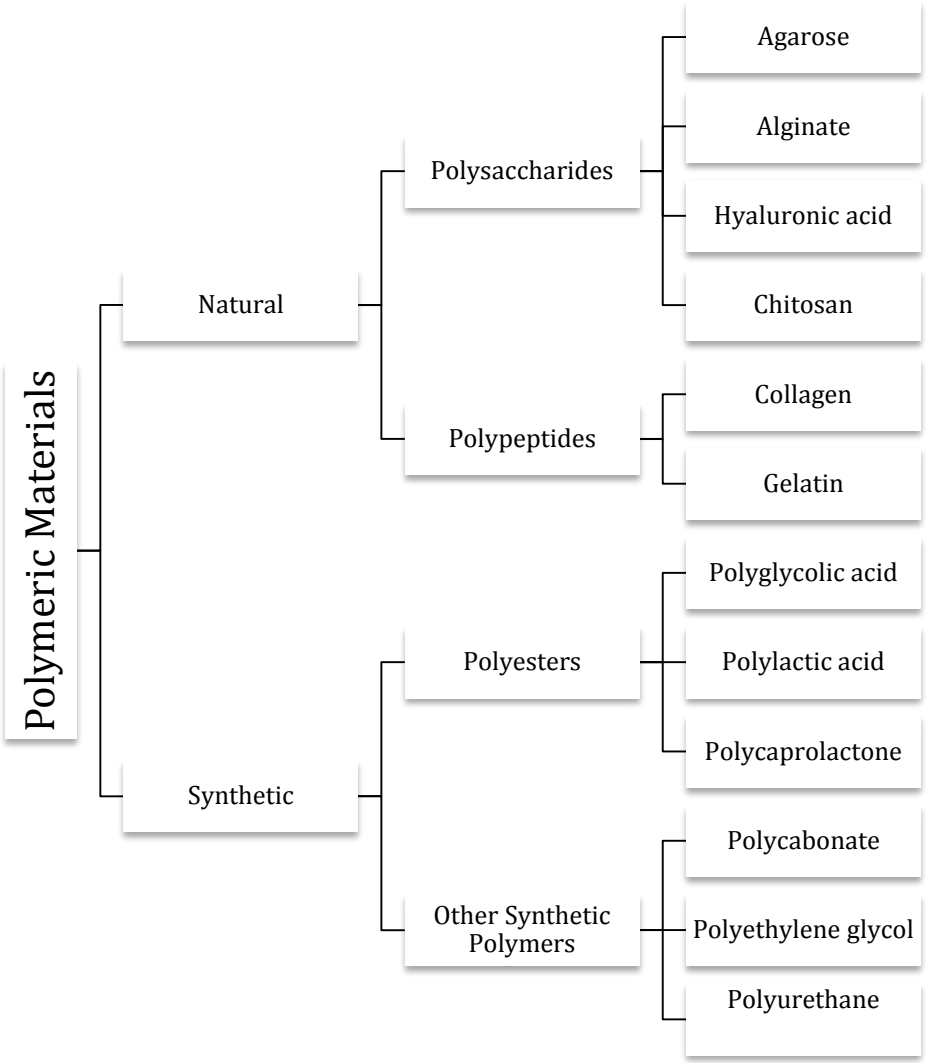

Figure 2.8 Polymeric scaffold materials [29]

Conventionally, polymeric materials can be fabricated into porous structures using techniques such as salt leaching, gas forming, solvent casting, freeze-drying and extrusion for bone tissue engineering [27], [28], [30]. However, the problem of using polymers for load bearing applications is that the mechanical strength of the polymer decreases and there is also degradation of the polymer, both are time dependent. The degradation of the polymer will lead to generation of acidic by-products, which can lead to inflammatory response from the tissues [20].

2.7.2 Metallic

Titanium and its alloys are often the choice of the fabrication of biomedical scaffolds for load bearing applications due to its mechanical strength, biocompatibility and chemical stability [31]–[33]. The permanent metallic bone scaffolds rely on osseointegration where the implant surface can withstand the load for long-term period of time [34]. The osseointegration was defined as "direct contact of bone tissues to an implant surface without forming fibrous membrane" [35]. The mechanical properties of commonly used metallic biomaterials are shown in Table 2.4. The current approach for fabricating porous metallic scaffolds includes Additive Manufacturing (AM); freeze casting, space holder and sponge replication. Typical AM processes are Selective Laser Melting (SLM) and Electron Beam Melting (EBM) providing great potential for fabrication of metallic three-dimensional porous scaffold structures [32].

Table 2.4 Mechanical properties of typical metallic biomaterials [12]

Material (metal alloys)	*Modulus (GPa)*	*Tensile Strength (MPa)*
Stainless Steel	190	586
Co-Cr alloy	210	1085
Ti-alloy	116	965

2.7.3 Ceramics

Ceramic materials have excellent properties in wear resistance, high compressive strength, and are capable of supporting high load applications for example in 3D scaffolds. Alumina porous scaffold provides good mechanical strength and Jun et al [36] have demonstrated the fabrication of alumina reinforced calcium phosphate porous implants, which exhibited biocompatibility and osteoconduction properties. Zirconia is another commonly studied ceramic materials with proven biocompatibility. Moreover the use of alumina ceramic scaffolds have gained a lot of interest for a range of medical applications including augmentation and implantation, such as hip joint replacement components [12]. While hydroxyapatite/glass ceramics are used as coatings on prosthetic stems and calcium phosphate based ceramics are used as porous scaffolds, spinal implants and bone grafts [14].

Table 2.5 Mechanical properties of typical ceramic biomaterials [12]

Ceramic Material	*Young's Modulus (GPa)*	*Tensile Strength (MPa)*
Alumina	380	300
Zirconia	220	820
Bioglass	35	42
Hydroxyapatite	95	50

Vascularisation, the development of blood vessels, is an important requirement for implanted scaffold in bone scaffold reconstruction. To understand the vascularisation requirement, Kokemueller et al [37] conducted experimental research of mandibular reconstruction on humans with predrilled cylindrical ceramic artificial bone grafts to promote vascularisation process as shown in Figure 2.9E.

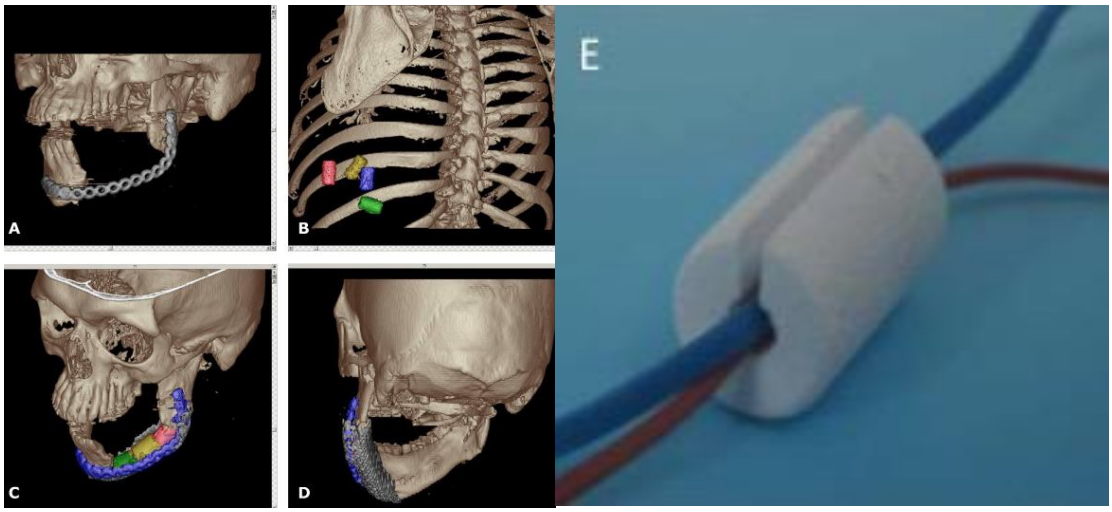

Figure 2.9 (A) CT scan image before mandible reconstruction (B) prefabrication of artificial bone graft for 6 months (C)(D) after mandible reconstruction (E) *predrilled cylindrical ceramic artificial bone graft* [37]

2.8 Summary

Bone healing is a complex process and can undergo self-healing. In other cases, bone graft materials may be required if the site cannot be healed using natural processes. The surgical technique of free-tissue flap, which use autogenous bone graft for bone reconstruction provides the advantages of vascularisation and elimination of the possibility of immune rejection. When autogenous bone graft is limited, or considering the donor site infection due to secondary surgery required for harvesting autogenous bone graft, then synthetic bone graft materials may be required to provide temporary or permanent load bearing as the site heals.

Bone graft materials are usually constructed in scaffold form to promote cell in-growth. The permanent synthetic bone scaffolds rely on osseointegration where the implant surface can withstand the load for long-term period of time [34]. With new bone in-growth, the scaffold becomes more rigid. By monitoring the stiffness of the bone implant, it is possible to monitor the bone healing progress and degree of osseointegration.

Polymeric, metallic and ceramic biomaterials have been widely used for bone scaffold fabrication. Due to their good mechanical properties, ceramic and metallic scaffolds are most suitable for substitution of biological hard tissue when compared with polymers. Typically, the implants are fabricated from the latter materials by methods such as casting; gas foaming, freeze-drying, injection moulding and computer numerically controlled (CNC) machining. Using the above conventional fabrication technologies there are limitations to control scaffold's pore size, pore geometry, interconnectivity, and spatial distribution.

More recent, manufacturing technologies such as Additive Manufacturing (AM), offer real advantages over the more conventional technologies. In chapter 3, the use of AM technologies for medical applications and bone scaffold fabrication is discussed.

Chapter 3. Additive manufacturing technology

3.1 Introduction

Additive Manufacturing (AM) or Additive Layered Manufacturing (ALM) technologies were first introduced in the late 1980's [38]. A wide range of materials can be used in AM technologies for example polymers, ceramics, metals and composites. The early applications using AM fabrication included the manufacture of prototypes thus also named Rapid Prototyping (RP). The technology is widely used in the production of complex parts for aerospace, automobile, consumer and medical applications.

The prototyping aspect of the fabrication process is ideal for medical applications where specialised "one off parts" are required, for example patient implants and anatomical patient modelling for surgical planning. It was in 2012 that AM started to be used for the direct production of implants or scaffolds, meeting the mechanical and biocompatible properties for tissue engineering [38].

Tissue engineering is an interdisciplinary field which employs the principles of engineering and life science to develop biological substitutes to restore, maintain and improve lost tissue function [39]. As already discussed, medical parts often need to be custom-made to the patient's individual requirement. For this reason, AM in medical production applications have gained great interest.

There are several AM techniques that are compatible with biocompatible materials required for the fabrication of implantable synthetic bone scaffolds. The common AM processes used in medical application include Stereolithography Apparatus (SLA), Fused Deposition Modelling (FDM), Selective Laser Sintering (SLS), Selective Laser Melting (SLM) and Electron Beam Melting (EBM), and these will be briefly discussed. The different AM processes and the year they started are summarised in Table 3.1 [40].

Table 3.1 AM processes, acronym and year started [40]

Name	*Acronym*	*Year commercialised*
Stereolithography	SLA	1988
Fused Deposition Modelling	FDM	1991
Selective Laser Sintering	SLS	1987
Selective Laser Melting	SLM	1995
Electron Beam Melting	EBM	2002

3.2 Stereolithography Apparatus (SLA)

Stereolithography Apparatus (SLA) was the first developed AM method and was commercialised by 3D System Inc. (South Carolina, USA) in 1988 [41]. The SLA process is based on a build platform of perforated steel plate, and a container holding photosensitive resin that can be deposited in layers. An ultraviolet (UV) laser will selectively cure a layer of the liquid photosensitive resin forming the cross-section and leaving the remaining areas in liquid form. After a cross section is processed, the build platform is lowered according to layer thickness of the process, a wiper blade passes over to ensure even coverage of resin for the next layer to be processed [42].

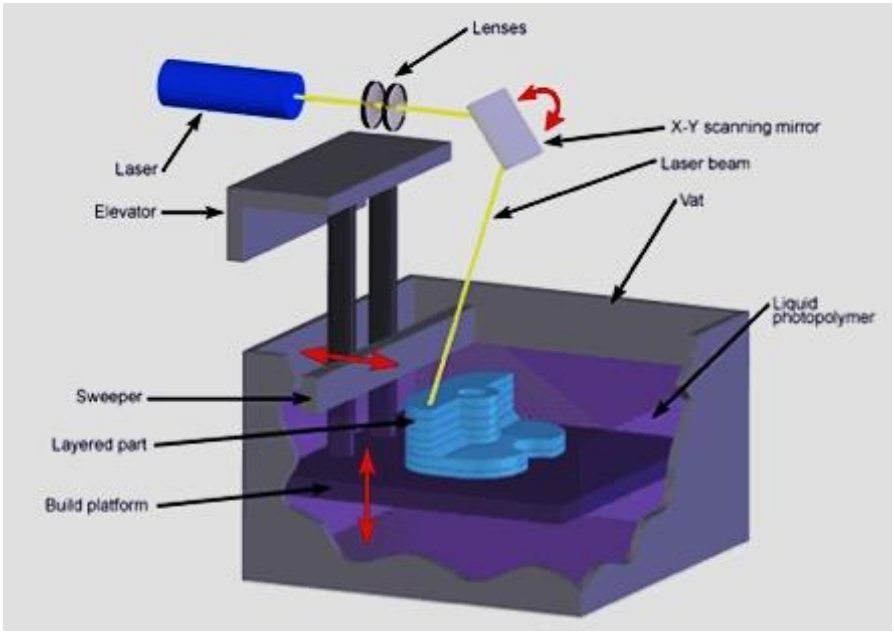

Figure 3.1 Schematic diagram of Stereolithography Apparatus [42]

SLA parts are limited by materials, which are biocompatible for scaffold fabrication; this is due to the materials having to be ultra-violet (UV) curable liquid resins. For this reason the process involves material particles in dilute or suspension form. Scalera et al [43] demonstrated the feasibility of developing UV curable epoxy in a ceramic hydroxyapatite (HA) suspension that can be used for bone tissue engineering using SLA fabrication process. Green ceramic parts were built using SLA from material suspension containing HA 60% by weight and later sintered at a maximum temperature of 1300˚C. A shrinkage rate of 19% is accounted for. The built parts have given measured mechanical strengths of 22±1MPa. The presented work by Scalera et al has not yet gone through biocompatibility test, but the work has shown the feasibility of fabrication of ceramic parts for bone tissue engineering using the SLA process.

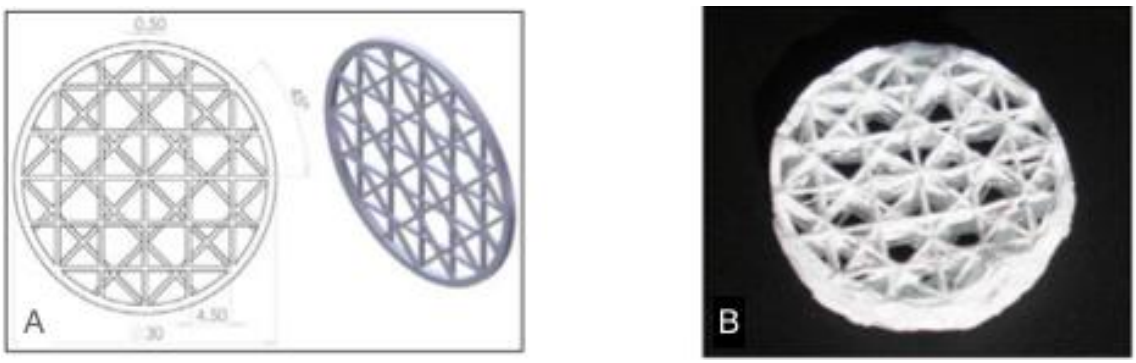

Figure 3.2 SLA built ceramic prototype for bone tissue engineering (A) CAD model (B) Sintered prototype

Alternatively SLA process is a useful tool for building anatomical three-dimensional (3D) models for surgical planning [12]. In recent years 3D medical models are commonly built using patients' CT scan data for surgical planning for tumour ablation, reconstruction, and jaw deformities. A typical mandibular reconstruction is a lengthy procedure that can take up to 15 hours [44]. It has been shown by Yamada et al [45] if the surgeon use a 3D model to pre-contour mandibular plate, the operation time can be shortened and therefore the patient's volume of blood loss is reduced during the surgery. Figure 3.3 shows the pre-bending mandibular plate fitting check using 3D SLA model and the radiograph after it was implanted.

Figure 3.3 Pre-contoured mandibular plate with 3D model [45]

3.3 Fused Deposition Modelling (FDM)

Fused deposition modelling (FDM) was first introduced and commercialised in 1991 by Stratasys Inc. Filaments of thermoplastic material are fused slightly above its melting temperature and extruded through a nozzle to form the cross-sectional profiles of the desired part on to a foam-built platform. The filaments can be used for both build and support material, and are formed by feeding the material through fine nozzles. The extruded material filaments solidify after it has been deposited due to the drop in temperature. After the part has been fabricated, the supporting foam base can be broken down by hand or washed away if a water-soluble material is used. A schematic diagram of Fused Deposition system is shown in Figure 3.4.

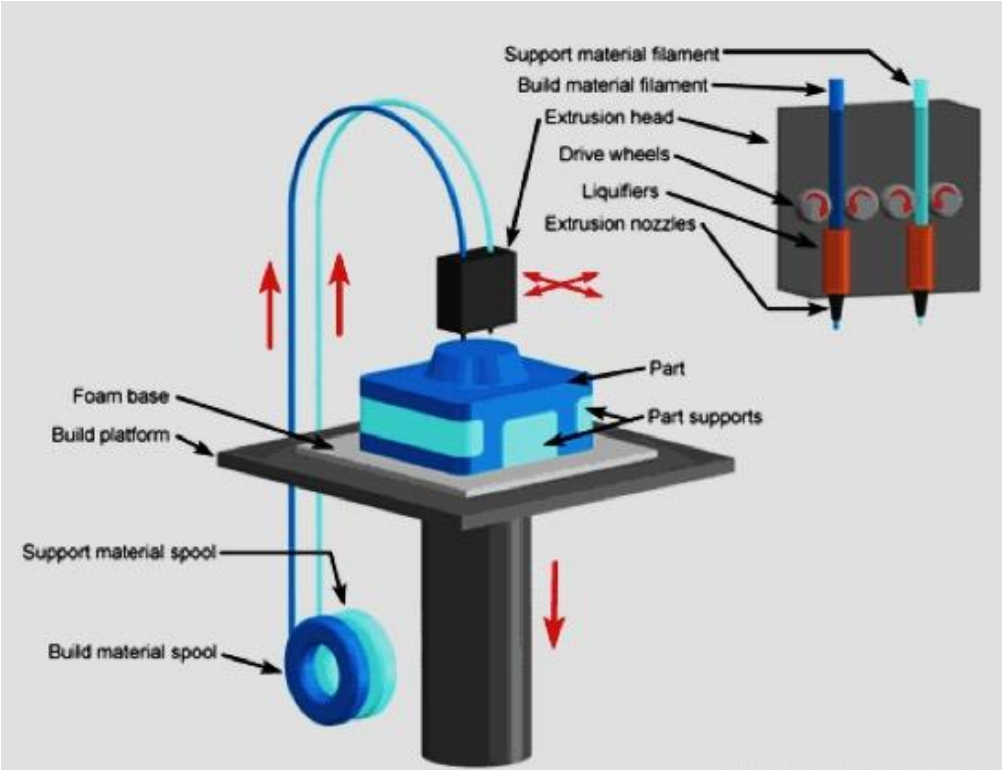

Figure 3.4 Schematic diagram of fused deposition modelling [46]

Scaffold fabrication is not feasible using commercially available FDM systems due to the thermoplastics having low melting point and low melt viscosity. Thus, current FDM systems have been modified by researchers to extrude materials with more suitable physical properties for fabrication of 3D scaffolds [47]. To fabricate FDM scaffolds, biodegradable materials for example polycaprolactone (PCL) and hydroxyapatite (HA) /PCL mixture have been prepared as filaments and fed into the heated nozzle to form the scaffold. Such PCL FDM scaffolds are designed to retain their mechanical properties for 5-6 months and normally will degrade over a couple of years depending on the scaffold size. The highest compressive strength of the interconnected porous scaffold was measured to be at 10.44±2.09MPa. The mechanical testing results suggest feasibility of FDM produced PCL bio-scaffold fabricated for load-bearing applications [48].

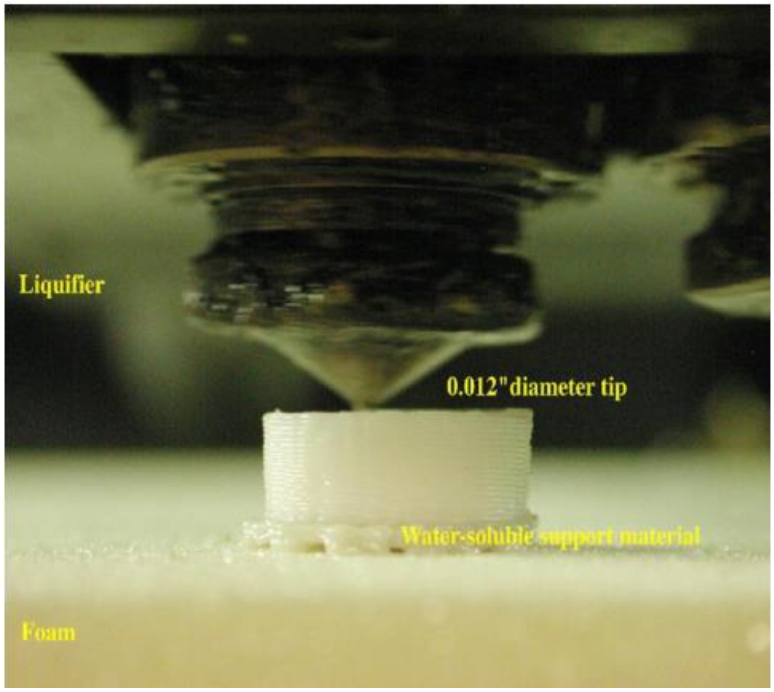

Figure 3.5 Bone scaffold fabrication using FDM [48]

3.4 Selective Laser Sintering (SLS)

Selective laser sintering (SLS) was developed and patented by the University of Texas, Austin, USA in the mid 1980's [49]. The build materials are in a powder form sitting in a heated build chamber to minimise the required laser energy to sinter the material. An inert nitrogen gas is used to fill the heated build chamber to prevent oxidation during the sintering process. The laser used in SLS is normally CO_2, however recently, Nd:YAG lasers have shown a degree of success in the SLS process [38]. The part is generated by sequentially sintering cross-sectional layer formed by selectively sintering the powder. The formed layer sits on a piston, which is dropped down a thickness of one layer (typically less than 150µm) and then a roller applies a new layer of pre-heated powder for the next layer to be formed by laser sintering [49].

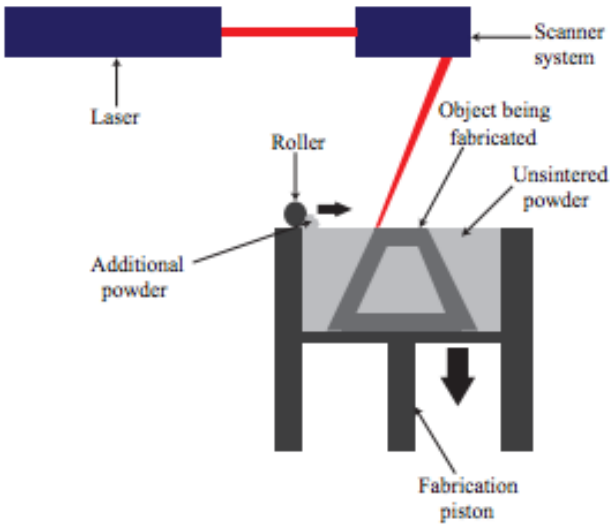

Figure 3.6 Schematic drawing of selective laser sintering process [49]

Williams et al [26] have employed the SLS process to fabricate polymeric bioresorbable polycaprolactone (PCL) for tissue engineering scaffolds. The mechanical properties of the PCL scaffold fit the lower range of the natural trabecular bones, which range from 52 to 67MPa compressive modulus. The in vivo results also showed promotion of cell in-growth within the scaffold. The mechanical properties can be computationally analysed. The computational modulus values compared with experimental values were giving a correlation coefficient R^2= 0.564.

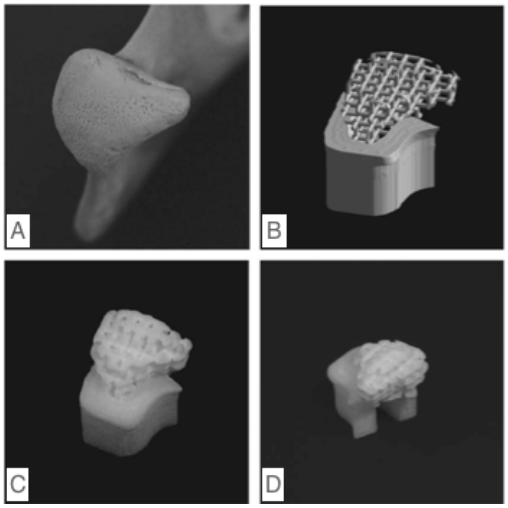

Figure 3.7 (A) Pig mandibular condyle (B) CAD rendered design file (C)(D) PCL scaffold using SLS process [26]

The minimum feature size of the SLS process is limited to around 400µm due to the laser spot size diameter of about 400 to 500µm [50]. To compensate for the laser spot diameter when scanning, the laser is usually offset from the edges of the cross-section. A parameter scan is often performed after the fill scans to improve the surface quality. Lohfeld et al [50] has proposed a method using overlap laser scanning without offset to reduce strut thickness (See Figure 3.8) to push the limit of constructing minimal feature size to that less than the laser spot diameter.

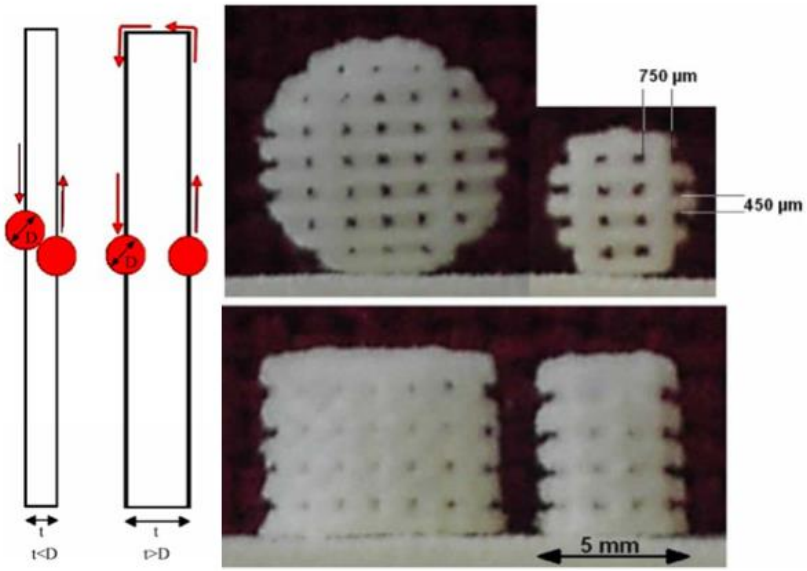

Figure 3.8 Left: Laser spot (D) overlapping to reduce strut thickness (t) Right: PCL porous scaffold with thin struts by overlapping laser spot [50]

3.5 Selective Laser Melting (SLM)

The process was developed at the Fraunhofer Institute (Aachen, Germany). Selective laser melting is very similar to selective laser sintering; the parts are produced in a powder bed with laser-induced consolidation process. The major difference is that the SLM process requires a high-power laser beam to fully melt and fuse the metallic powder as shown in Figure 3.10. Various metallic powders such as stainless steel, titanium, gold, nickel alloys and cobalt-chromium alloys can be used in the SLM fabrication process [51].

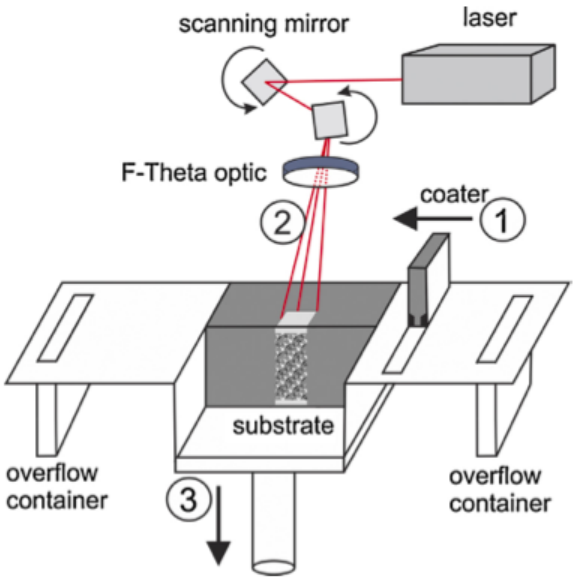

Figure 3.9 Schematic diagram of SLM process [52]

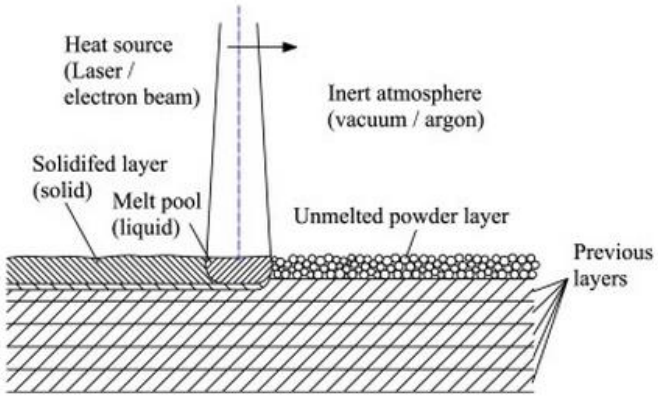

Figure 3.10 Schematic diagram of SLM powder bed in process [53]

The SLM fabrication of porous structure has application in medical implant, aerospace and other lightweight manufacturing applications. Critical factors for fabrication of porous structures include inclined angle, powder adhesion and the size of the porous structure may be limited to fit the SLM process. Figure 3.11 shows an example of a porous scaffold structure fabricated using SLM [51]. Mullen et al [54] have reported SLM to produce titanium porous structures, which can have a wide range of mechanical properties. The mechanical properties of SLM produced titanium structures can be tailored comparable to those of human bone using various structural

designs. It was found by increasing the porosity from 10% to 95%, the compression strength of the titanium structure reduced from 350Mpa to 0.5Mpa, which fits into the range of human bone.

In addition, Kawase et al [55] recently reported biocompatibility of SLM fabricated Ti-6Al-4V alloy films. These experiments were carried out on mouse fibroblast-like and osteoblast-like cells, which underwent cell proliferation on the Ti-6Al-4V alloy film surface during the culture period. The results further confirmed the cell-compatibility of SLM produced titanium alloy parts.

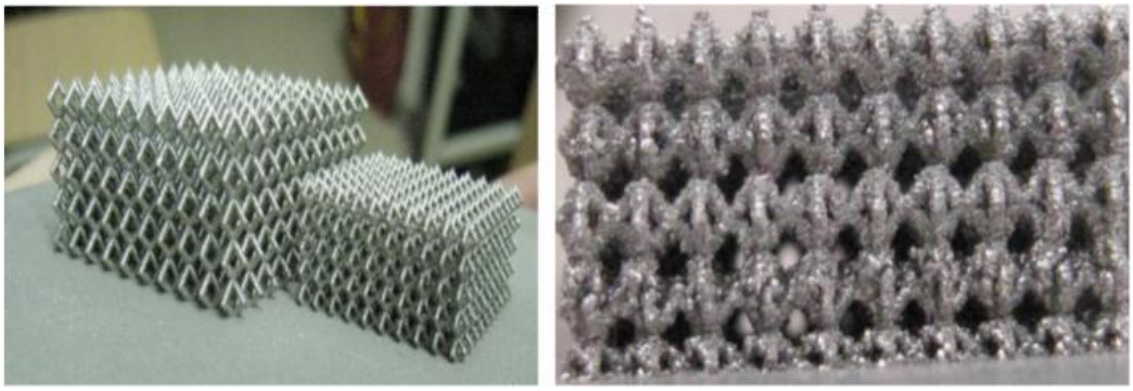

Figure 3.11 Porous scaffold structure fabricated by SLM [51]

3.6 Electron Beam Melting (EBM)

Electron beam melting (EBM) process was developed by Arcam AB in Sweden in 2002. The process uses focused electron beam scans over a cross-section, which melts the metal powder in a preheated powder bed under high vacuum. Like SLM, EBM parts are highly dense and exhibit very good mechanical properties. Electron beam melting technology has been used to manufacture titanium acetabular cup implants, which has received FDA clearance and has been in production since 2007.

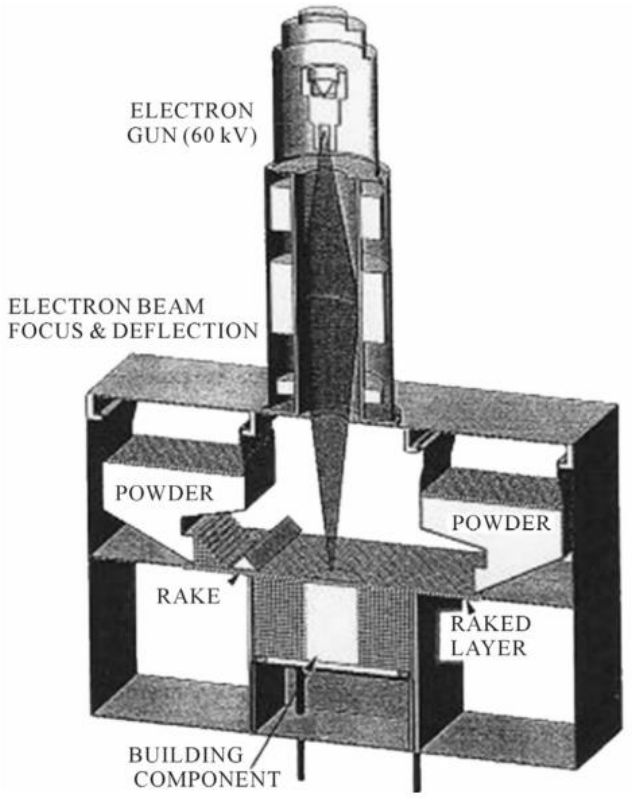

Figure 3.12 Schematic diagram of EBM process [56]

A schematic diagram of the EBM process is shown in Figure 3.12. Poukens et al [57] performed customised implants using EBM to reconstruct large human skull defect. The 3D design of the implant was created using Mimics® (Materialise's Interactive Medical Image Control System) software from CT scan data. The EBM implant was produced from medical grade V titanium alloy. An AM produced medical model was used as a validation tool to check the fit of the EMB titanium implant, shown in Figure 3.13.

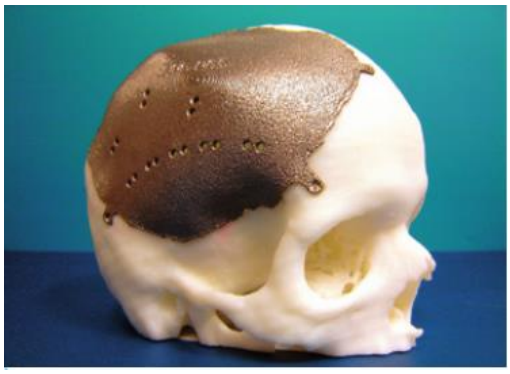

Figure 3.13 Titanium skull implant using EBM [57]

The mechanical properties, compressive stiffness and ultimate compressive strength, of a titanium scaffold structure can be altered and tailored with its build porosity, the examples shown in Table 3.2 [58].

Table 3.2 Porosity vs. compressive strength of porous Ti structure [58]

Porosity	Compressive stiffness (GPa)	Ultimate compressive strength (MPa)
50.75±0.69	2.92±0.17	163.02±11.98
60.41±0.81	2.68±0.12	117.05±5.54
70.32±0.63	2.13±0.21	83.13±10.25
49.75±1.00	0.57±0.05	7.28±0.93

3.7 Customised Implant

A customised scaffold should be produced for the specific defect site in a patient. Good quality patient medical data is needed for AM fabrication to produce exact parts required to aid tissue regeneration. Three of the most commonly used bone imaging techniques are three-dimensional computed tomography (CT), cone-beam computed tomography (CBCT) and magnetic resonance imaging (MRI) [1]. Computer tomography scan results provide the best resolution of bone images; whereas for soft tissues, magnetic resonance imaging scans provide the best resolution. Computer tomography scan uses Hounsfield unit, which varies depending on the density of material being scanned. An example of basic materials and the corresponding Hounsfield units are given in Table 3.3 [59].

Table 3.3 Hounsfield units [59]

Material	*Hounsfield units*
Air	-1024
Water	0
Bone	+3072

In recent years, customised implants have been fabricated by integrating computer imaging with selected AM technologies. Surgeons often use medical image data to replicate bone structures. Merging AM technologies with current imaging technology, enables pre-fabrication of a patient specific scaffold that match the contour of surrounding bone [60]. The method is shown in Figure 3.14 [1].

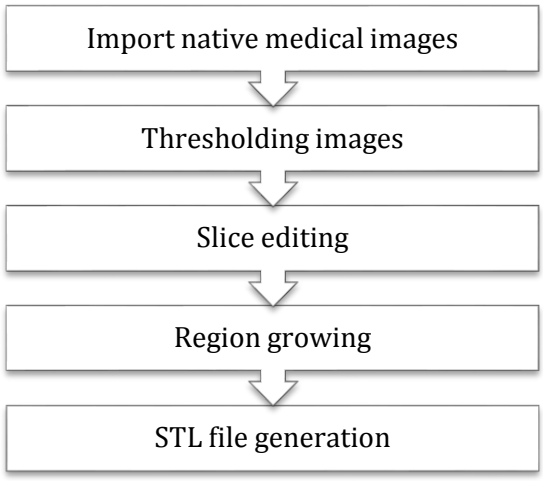

Figure 3.14 AM customised image generation flow

Imaging data collected can be transferred and manipulated through software such as Mimics™ to create tissue segment profiles. Naing et al [61] proposed to build a parametric library system for improving scaffold structure fabrication using an in-house algorithm. As the desired pore size, surface area and strut length of the scaffold can be created through a designer's toolbox. The prototype system is called computer-aided system for tissue scaffold (CASTS). The process flow diagram is shown in Figure 3.15 [61].

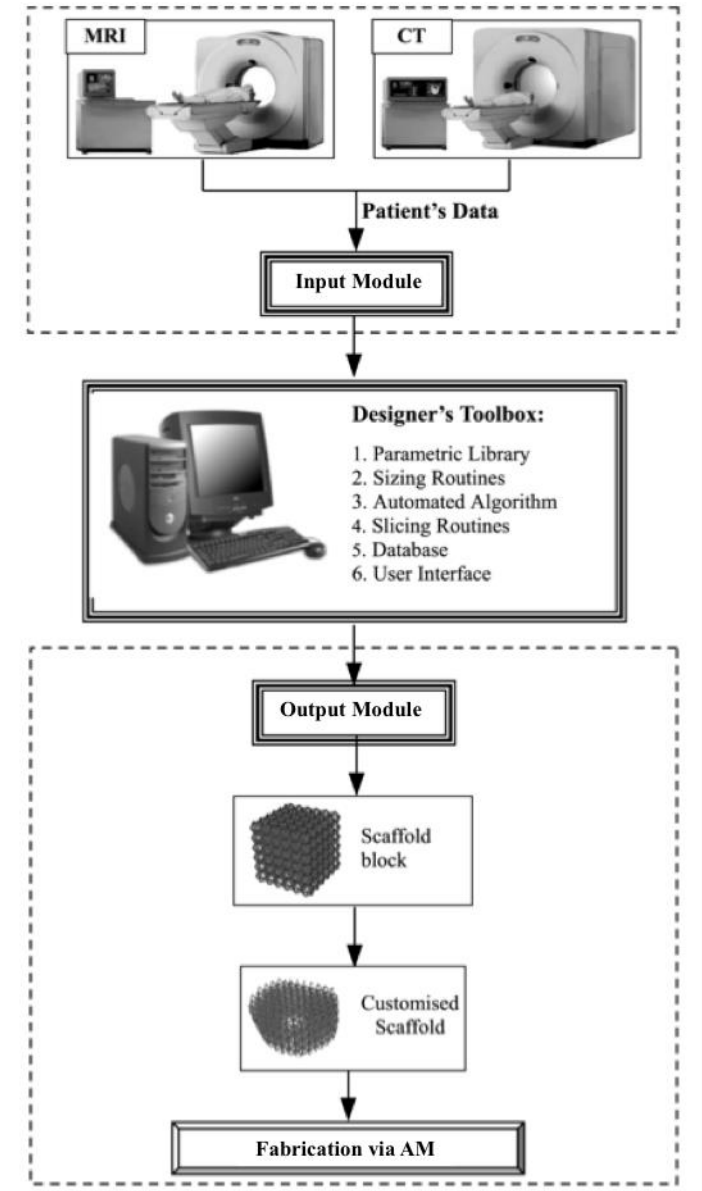

Figure 3.15 Computer aided system for Tissue Scaffolds (Adapted from [61]*)*

3.8 Summary

Additive Manufacturing for bone tissue scaffolds/fixation plates fabrication has the potential to produce customised bone tissue substitutes as an alternative to autogenous bone graft retrieved from the patient's donor site. The main benefits of using AM fabricated tissue scaffold and fixation plates are:

- Shortened surgical procedure reducing the need of repeat surgery due to advanced surgical planning with 3D medical model
- A bespoke implant fabricated using the patient's own scan data results in a better fit and is less time consuming.
- The AM implants are cost effective compared to other conventional techniques.

AM process	Material	Application	Ultimate compressive strength
SLA	Polymeric photo sensitive resin Ceramic (Hydroxyl apatite)	3D anatomical modelling Bone scaffold	22+-1MPa
FDM	Polymeric (PCL, HA/PCL composite)	Bioresorbable bone scaffold fabrication	10.44±2.09MPa
SLS	Polymeric (PCL)	Bioresorbable bone scaffold	52 to 67MPa
SLM	Titanium	Porous scaffold	0.5 to 350MPa
EBM	Titanium	Porous scaffold	7.28 to 163.02MPa

However, AM produces scaffolds in a single material, which do not give the opportunity of using materials to construct sensors to give feedback on the performance once implanted. As mechanical strain is one of the main factors for bone in-growth, monitoring strain directly on an implant will be valuable to determine the bone-implant attachment and is an early indication of any problems. The current strain measurement technique in human is discussed in chapter 4.

Chapter 4. Bone strain measurement

4.1 Introduction

Strain gauges are widely used for measuring surface deformation in a material. In medical applications, metal foil strain gauges have been used for real-time bone strain measurement. This chapter describes the principle of strain gauges and their use for medical applications. Further, several bone healing monitoring techniques are summarised later in the chapter.

4.2 Strain Gauge

The basic principle of the strain gauge was reported in 1856 by Lord Kelvin [62] who found that certain electrical conductors exhibit a resistance change with change in mechanical strain. As shown in Figure 4.1, when a conductor is extended in the axial direction, its length will change as well as its cross-sectional area according to the Poisson effect. When the length of the conductor is increased, the cross-sectional area decreases and vice versa, resulting in a change to its electrical resistivity (ρ). The electrical resistivity $\rho\,(\Omega\cdot\mathrm{cm})$ of a conductor can be expressed as following:

$$\rho = R\frac{A}{L} \tag{1}$$

Where $R(\Omega)$ is the electrical resistance, $A(\mathrm{m}^2)$ is the cross-sectional area of the conductor and L(m) is the length of the conductor.

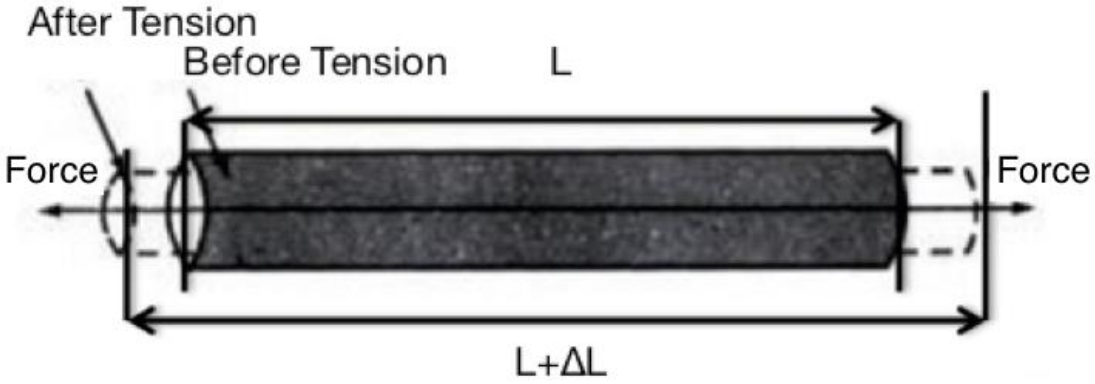

Figure 4.1 Schematic diagram of strained conductor (adapted from [62]*)*

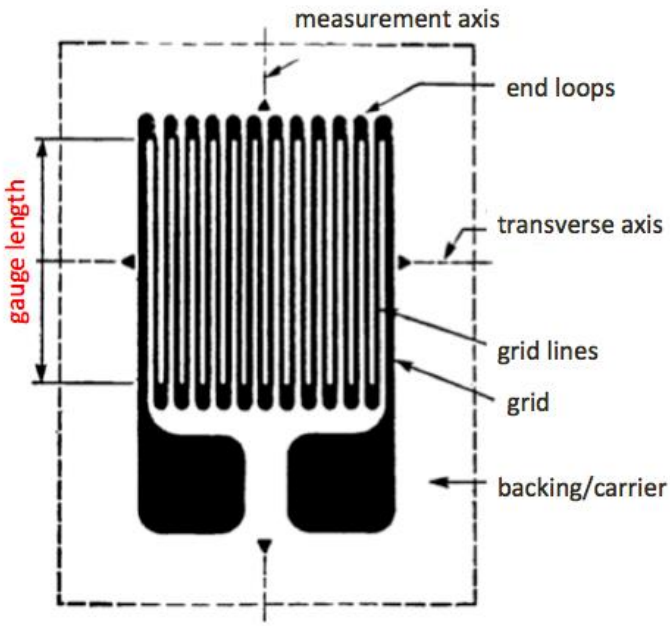

Figure 4.2 Typical foil strain gauge structure (adapted from [63]*)*

Figure 4.2 shows a typical commercial foil strain gauge structure using serpentine grid lines, which covers the area of the material to be monitored for strain. The sensing (monitoring) direction is parallel to the grid lines. The strain gauge tends to average the strain covered by the grid lines; therefore, the strain gauge footprint size is critical when measuring strain over a small surface area. When the sensing area is larger than maximum strain area, the measured strain magnitude is lower than the actual strain [64], therefore small area strain gauges are required to obtain accurate strain measurement of point surface areas. The strain gauge physical size is often described by gauge length.

The foil strain gauge made with foil and cemented to a lacquer sheet was first introduced in 1952 in UK. The conventional fabrication of metal foil strain gauge employs both photolithographic and photo-etching techniques to realise the strain sensor geometry [65]. Typical strain gauge materials used in commercial strain gauges and their gauge factors (defined in section 4.2.1) are summarised in Table 4.1.

Table 4.1 Typical Metal Strain Gauge Factor [65]

Material	*Strain Gauge Factor*
Copper	2.6
Nichrome	2.1
Silver	2.9
Iron	3.9
Ferry (60/40 Cu-Ni)	2.6
Platinum	6.1

More recently, various strain gauge fabrication methods have been explored such as ink-jet, aerosol jet printing, ion implantation, carbon nanotube, micro dispensing and MicroPen writing. The processes and corresponding gauge factor performance is discussed in chapter 5.

4.2.1 Strain gauge sensitivity

The principle of the strain gauge is based on the electrical resistance change with strain applied. Strain (ε) is expressed as the ratio of total deformation to initial dimension of the body (ΔL/L), where ΔL (m) is the change in length and L the initial length (m). Thus, strain is a dimensionless parameter and can be expressed as a percentage strain (ex. 0.01 strain equals 1% strain) or microstrain. When a strain gauge is firmly attached (glued) on to a material to be tested, the assumption is made that the glue material has the same deformation as the material. The sensitivity of the gauge, gauge factor (GF), can be expressed as the amount of the resistance change in relation to the change in strain. For conductors with uniform cross section the equation can be expressed as follows [62]:

$$GF = \frac{unit\ change\ in\ resistance}{unit\ change\ in\ length}$$
$$= \frac{unit\ change\ in\ resistance}{\varepsilon}$$

In symbols,

$$GF = \frac{\frac{R - Ro}{Ro}}{\frac{L - Lo}{Lo}} = \frac{\Delta R/Ro}{\Delta L/Lo} = \frac{\Delta R/Ro}{\varepsilon} \quad (2)$$

Where:

GF (no unit) = the gauge factor

R (Ω) = the strain gauge resistance at test strain

Ro (Ω) = the strain gauge resistance at zero strain

L (m) = the test structure length under the strain gauge at test strain

Lo (m) = the test structure length under the strain gauge at zero strain

ΔR (Ω) = the change in strain gauge resistance when strain is changed from zero

ε (no unit) = the mechanical strain

4.3 Strain Gauge for Bone Strain Measurement

In medical applications, strain gauges have been applied in vitro to assess vertical misfit of implant framework manufactured in different material, e.g. titanium and zirconia [66]. The feedback of measuring the bone strain *in vivo* is valuable to understand the structural effects in responding to osteoporosis, tumour in bone and prosthetic implants [67]. To date, most in vivo bone strain measurements focus on the long bone shafts, for example the human tibia due to its large bone surface area. The sensor utilised is the resistive strain gauge glued to the bone surface and is referred to as the gold standard for bone strain measurement [4][68].

4.3.1 Types of bone deformation

As described, strain is the deformation of the material when a force is applied and can be expressed as the ratio of the change in length (L-L_0) referenced to the original length (L_0). Depending on the direction of the force being applied, axial strain can be compressive (negative value) or tensile (positive value) strain and is described by the equations below [68]:

$$\varepsilon_{\text{compressive}} = \frac{L-Lo}{Lo} = \frac{-|\Delta L|}{Lo} \tag{3}$$

$$\varepsilon_{\text{tensile}} = \frac{L-Lo}{Lo} = \frac{|\Delta L|}{Lo} \tag{4}$$

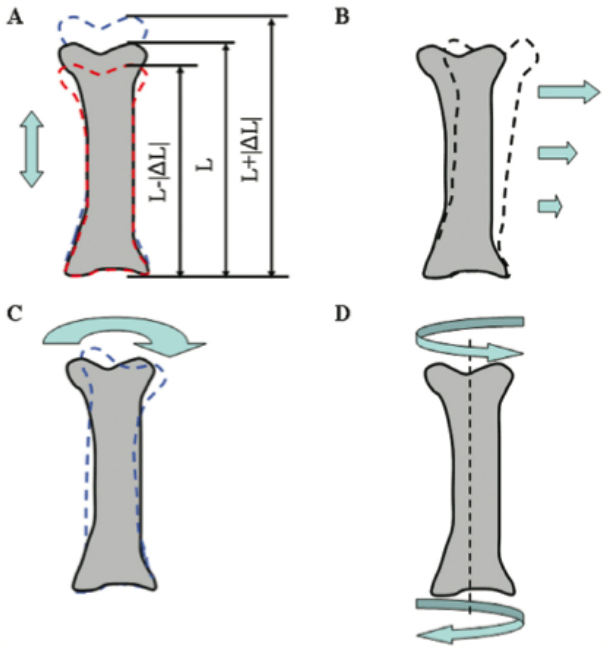

Figure 4.3 Types of bone strain (A) Axial (B) Shear (C) Bending (D) Torsion strain [68]

In most cases, bone strain direction is difficult to predict, as different types of bone strain may apply as shown in Figure 4.3. With unknown strain direction, rosette strain gauges are required to be used. There are three classifications of rosette strain gauges:

X rosette (see Figure 4.4 A), right-angled rosette (Figure 4.4 B) and delta rosette (Figure 4.4 C). The X rosette can be applied to biaxial strain conditions with known principal directions. Right-angled rosettes are placed with axes crossed at 0˚/45˚/90˚. Delta rosettes are placed with axes crossed 0˚/60˚/120˚. Both right-angled and delta rosettes are applied to biaxial stress conditions with unknown principal directions [69].

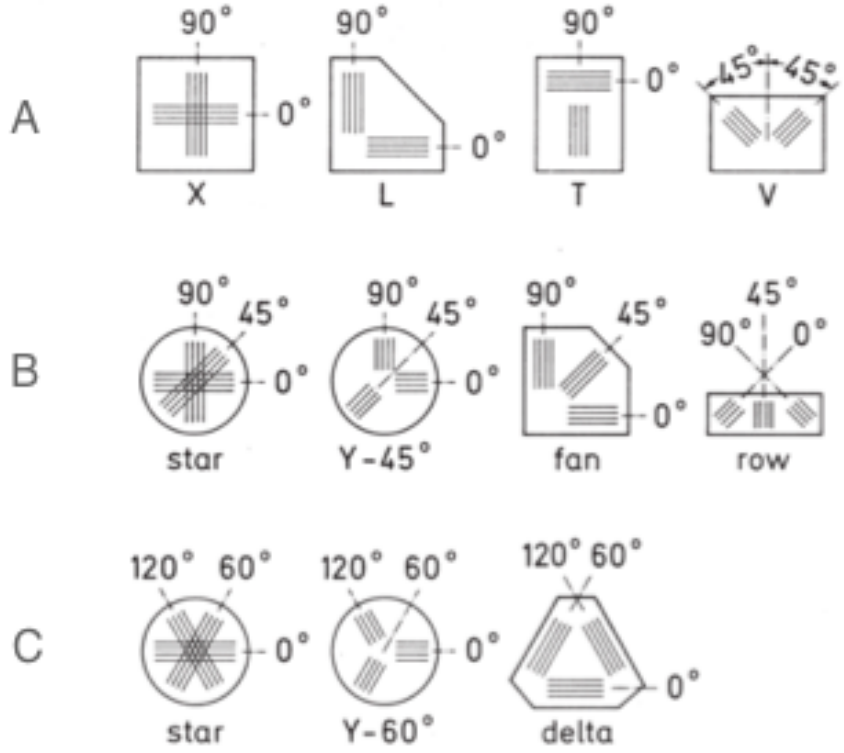

Figure 4.4 Strain gauge rosettes (A) X rosettes (B) right-angled rosettes (C) delta rosettes [69]

The main steps for applying a strain gauge to a bone shaft will involve a complex surgical procedure as follows:

1. Anaesthetised the tissue overlying the proposed gauge site
2. Incision of a 5-10cm length down to the periosteum of the bone
3. Remove part of periosteum and clean the bone surface
4. Apply strain gauges on the bone surface with adhesive such as isobutyl 2-cyanoacrylate monomer or polymethyl methacrylate.

4.4 Bone healing monitoring

Bone plates have been used for many years for bone repair allowing fracture healing. Since the bone plates are attached directly to bone portion, they are good media to monitor bone strain distribution and therefore bone healing process. Morgan et al [70] has patented orthopaedic implants in 2011 with plurality of strain sensors mounted on the implant body (e.g. bone plate, maxillofacial distractor) as shown in Figure 4.5. The patent claims indicate that by monitoring the contribution of load sharing of the bone plate enables the clinicians or medical staff to diagnose the life of the implant. More commonly, x-rays are used to examine the facture healing process, as the process is not invasive. However, the information was found to be inadequate for accurate prediction of the life of the implant.

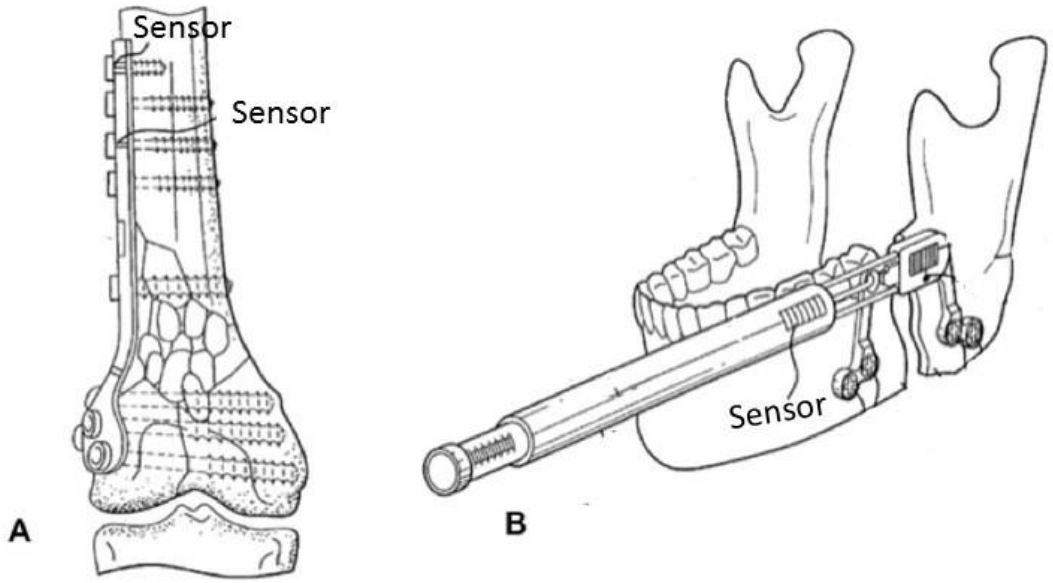

Figure 4.5 Strain sensor on (A) bone plate (B) maxillofacial distractor [70]

4.5 Telemetry system for bone strain measurement

Jong et al [72] demonstrated in vivo wireless recording of habitual mandibular bone strain in rabbits. Strain gauge rosettes were used to measure bone-surface deformation of the rabbit mandibular corpus. The telemetry system weighs approximately 100g, therefore, the measurement is suitable only for medium-sized and larger animals. The system using radio transmission enables recordings of habitual bone strain in freely moving rabbits and readings to be taken over 33 hours continuously. However, there were some failures through disconnected wires or short-circuiting of strain gauges due to moisture. Moreover, the battery depletion would constrain the recording time.

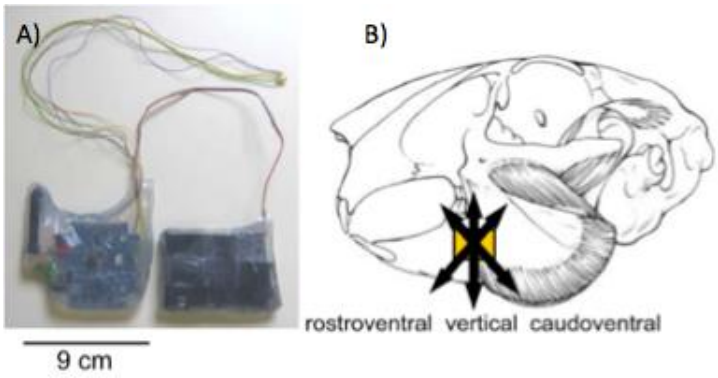

Figure 4.6 (A) Telemetry system for mandibular surface strain measurement (B) Strain gauge rosette location on mandibular surface in rabbit [72]

4.6 Summary

Monitoring strain on the bone surface in real time allows better understanding of the biomechanical behaviour of the musculoskeletal system. Strain monitoring via bone plate provides advances on musculoskeletal diagnosis, rehabilitation monitoring and feedback on bone healing progress. Although commercially available metal foil strain gauges have been widely used as strain sensor for real time bone strain measurement, these gauges are difficult to mount on bones due to their irregular surface topology.

Other problems such as the delamination of the strain gauges from the surface has often occurred during long term monitoring, as well as the breakage of the connecting wire has also made the in vivo measurement difficult. Moreover, the commercial gauges are too large to provide suitable resolution of strain measurement [73].

Researchers have explored alternative approaches for strain gauge fabrication, such as screen-printing, thermal spray and means of direct-writing fabrication technologies. Among these approaches, high sensitivity strain gauge can be manufactured using various sensing material that provide potential of fabricating integrated strain gauges directly on bone plates or bone substitute materials to overcome the limitation of the use of metal foil commercial strain gauge. Furthermore, combining strain gauge with a wireless telemetry circuit has been shown to be feasible to monitor bone strain in real time.

Chapter 5. Direct Write Technology

5.1 Introduction

The term Direct Write (DW) or Direct Printing (DP), is also a branch of AM technology, enabling the fabrication of two-dimensional pattern transfer and three-dimensional structures. In medical applications, DW offers bespoke parts, material flexibility and three-dimensional scaffold structures, all of which are necessary for scaffold fabrication. The DW method has been successfully used for scaffolds in tissue engineering using bio-scaffold material such as hydrogel [27], ceramic [74] and polymeric inks [75]. Using Direct Write technology and the micro extrusion of fine ceramic filaments, the porosity of the ceramic scaffold can be controlled; while for the more traditional foaming or particle leaching method, the porosity can only be defined over a narrow range and distribution [76].

Direct Write technology also offers the potential of fabrication of a wide range of electronic components such as thin film resistors [77], solar cells [78], RFIDs, antenna [79][80], sensor [81], displays etc. Traditional photolithography techniques are often used in electronic device/circuit for creating conductive tracks; however, it is a lengthy process involving conductive material deposition, mask and etch processing. For small bath production the use of expensive masks to realise complex conductive patterns on a substrate, results in increased production cost. Viable alternatives to photolithography for example screen printing [82] and DW technologies have been explored.

Direct Write technologies are environmentally friendly when compared to traditional photolithography fabrication methods as they require simply track or component printing and post thermal curing [83]. Although the conventional photolithography has its benefit of speed for mass production, DW methods provides the benefit of manufacturing flexibility, rapid design turnaround, conformal patterning, three-dimensional, bespoke/prototyping and multi-material capability [84][85].

This chapter reviews the state-of-the-art DW technologies that allow patterning of conductive tracks to form electrical resistive strain gauges in micron scale, and can be directly deposited onto an implant surface. Based on manufacturing processes, direct write technologies can be classified into four categories: droplet, energy beam, flow and tip based (Figure 5.1) [85].

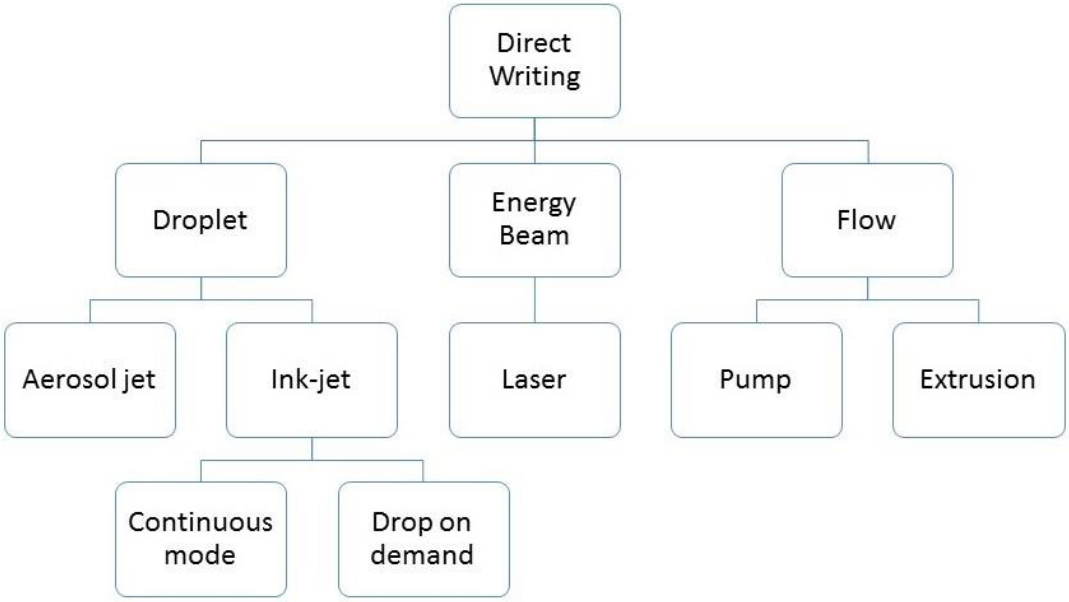

Figure 5.1 Classification of direct writing method [85]

Flow, droplet and tip based DW techniques are liquid based and depend on deposition of colloidal, nanoparticle, or organic based inks. The minimal printed feature size varies between the methods. Laser based DW techniques allow patterning through laser ablation to remove a desired pattern or to induce material transfer through reactive chemical reaction, thus enabling the fabrication of embedded structures in one process [86].

5.2 Laser-based Direct Writing

Laser-based DW techniques have various names: LIFT (Laser Induced Forward Transfer), MAPLE-DW (Matrix Assisted Pulsed Laser Evaporation-Direct Write), and MELD (Micro-structuring by Explosive Laser Deposition). Pique et al [85] first demonstrated the method in 1999. The mechanism uses the neodymium (Nd) laser to release material from the ribbon and transfer of the material to the substrate. Transferred materials can be screen-printable silver paste or polymers that are coated on one side of a ribbon by coating methods such as wire-coater and spray coating. A schematic diagram of MAPLE DW is shown in Figure 5.2. The main benefit of applying MAPLE DW to produce embedded electronic components is its ability to remove and add materials enabling interconnect circuitry to be realised in electronic circuits [87].

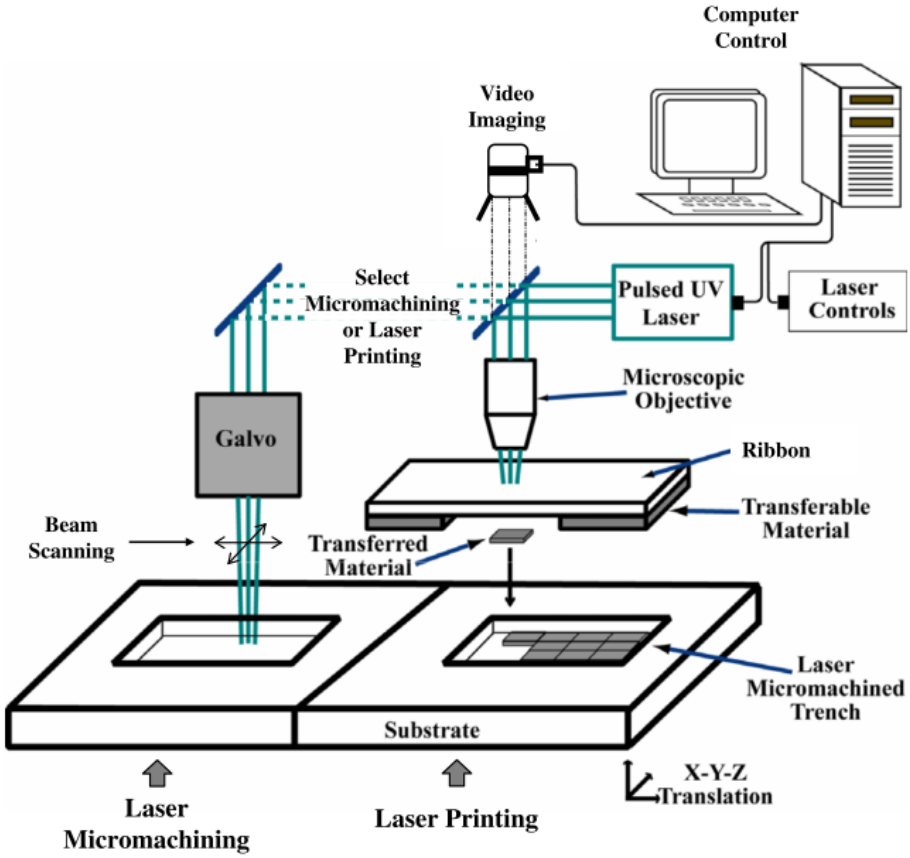

Figure 5.2 A schematic diagram of MAPLE DW process [85]

Pique et al [81] have demonstrated the fabrication of a temperature resistive sensor using MAPLE DW. A silver serpent-type pattern with resistance of about 100Ω was deposited on a polyimide substrate covering 5mm x 5mm area. The silver track was 10µm thickness and 100µm width and was modified using computer control. Post heat treatment involved drying the silver solvent at 100˚C on a hot plate and curing at 280˚C in an oven to decompose the organic silver precursors. Photograph of the sensor is shown in Figure 5.3.

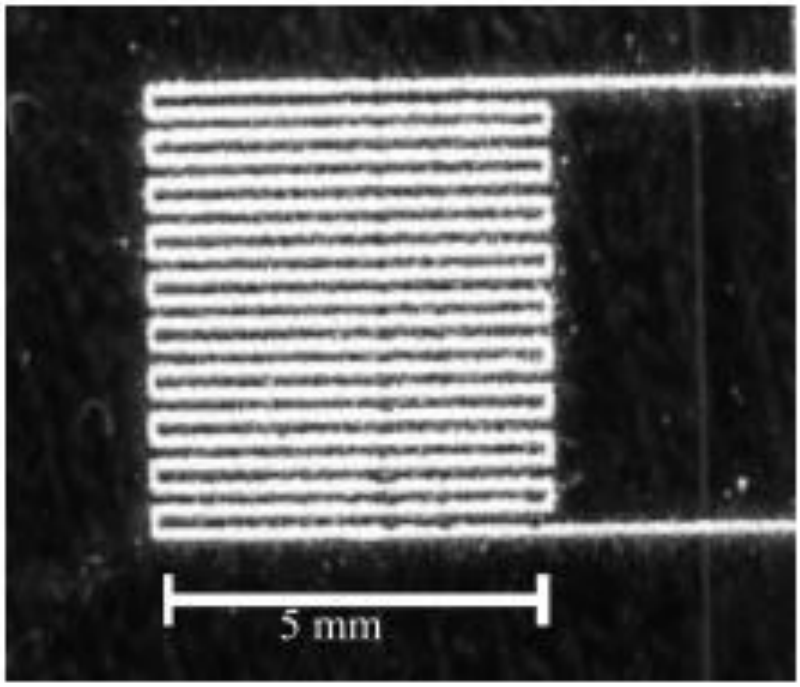

Figure 5.3 Silver serpentine line on a polyimide substrate fabricated by MAPLE DW [81]

5.3 Liquid-Based Direct Writing Processes

Liquid-based DW or “direct ink writing” can be divided into filamentary and droplet-based. Filamentary-based method such as MicroPen is based on extrusion of a liquid through a fine nozzle. Droplet-based methods such as ink-jet printing and aerosol jet deposit fluid drops are shown in Figure 5.4 [88].

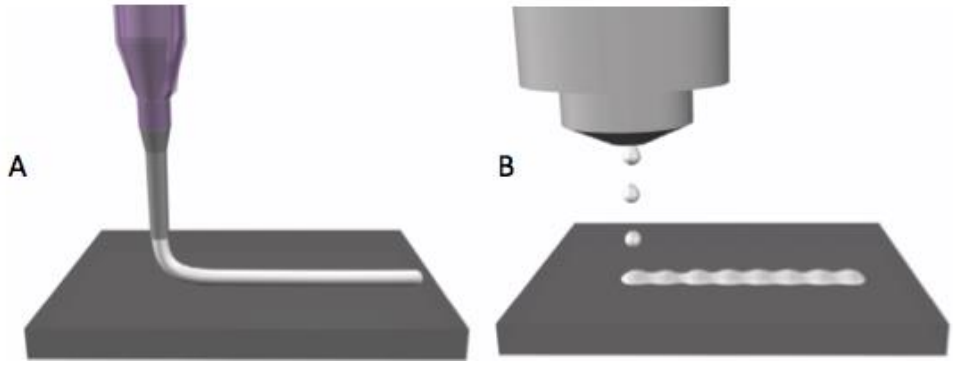

Figure 5.4 Liquid based Direct Write (A) filamentary-based (B) droplet-based [88]

5.3.1 Inkjet printing

Inkjet-based direct writing involves the formation and deposition of a sequence of droplets of liquid material, often called an ink or fluid. After deposition, the liquid material solidifies by evaporating the solvent, chemical reaction (cross-linking of a polymer) or through cooling (crystallisation or vitrification).

There are two common types of ink-jet technology defined by different actuators: continuous ink-jet printing (CIJ) and drop-on-demand (DOD). Continuous ink-jet printing is based on the fluid released from an orifice with size typically 50-80 μm in diameter, which breaks into uniform droplets in the presence of an electrostatic field. The drops are continuously produced and are directed by an applied electric field. [89]. A schematic diagram of continuous ink-jet printing is shown in Figure 5.5 [85].

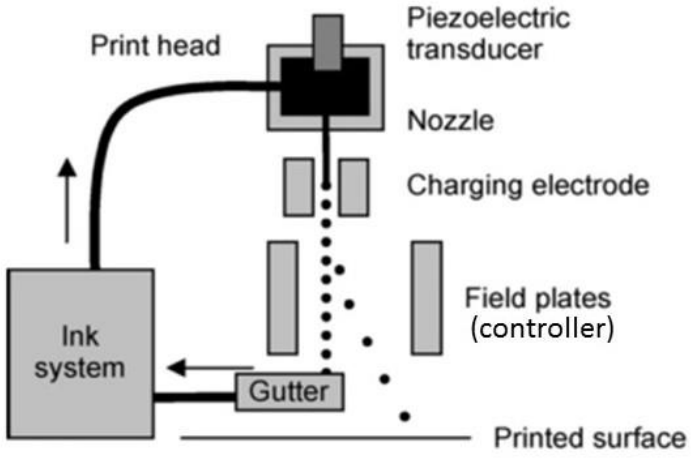

Figure 5.5 Schematic of continuous ink-jet printing system [85]

The drop-on-demand (DOD) method is based on a volumetric change in the fluid induced by a voltage pulse to a piezoelectric material (actuator) enabling the volume of fluid to be controlled. The volumetric change produces a pressure forcing the drop of fluid from the orifice. Drops occur when a voltage is applied, thus the process is referred to as drop-on-demand system. Drop-on-demand method is primarily used in home and small-office printers [89].

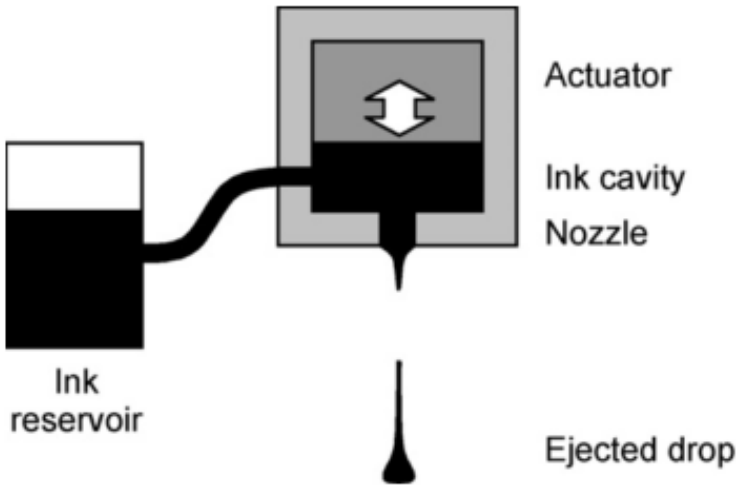

Figure 5.6 Schematic of drop-on-demand ink-jet system [85]

Typical dimensions of ink-jet printed features depend on the nozzle diameter, which are usually greater than 100µm. The ink-jet materials have Newtonian fluid behaviour,

viscosity of less than 40mPa.s and the particle suspensions are acceptable only with particle sizes less than 5% of the diameter of nozzle orifice. Researches in ink-jet printing have reported the fabrication of passive electrical components such as resistor, capacitors and inductors [89].

5.3.2 Aerosol Jet System

Aerosol Jet system was developed by Optomec Inc. (Albuquerque, New Mexico). Aerosol Jet is a printable electronics technology that allows the deposition of functional inks with a viscosity range from 0.7 to 2500mPa.s. The mechanism uses an atomizer to create dense aerosol of micro-droplets of 1-5µm diameters. The droplets are transferred by carrier gas, normally nitrogen, to the print head. A sheath of nitrogen gas inside the print head is used to focus the aerosol beam and prevent clogging of the nozzle. Inks with low viscosity and containing particles less than 50nm diameter are atomised with ultrasonic atomiser. Otherwise, a pneumatic atomizer is required with high viscosity ink in viscosity range from 1mPas to 2500mPa.s [85].

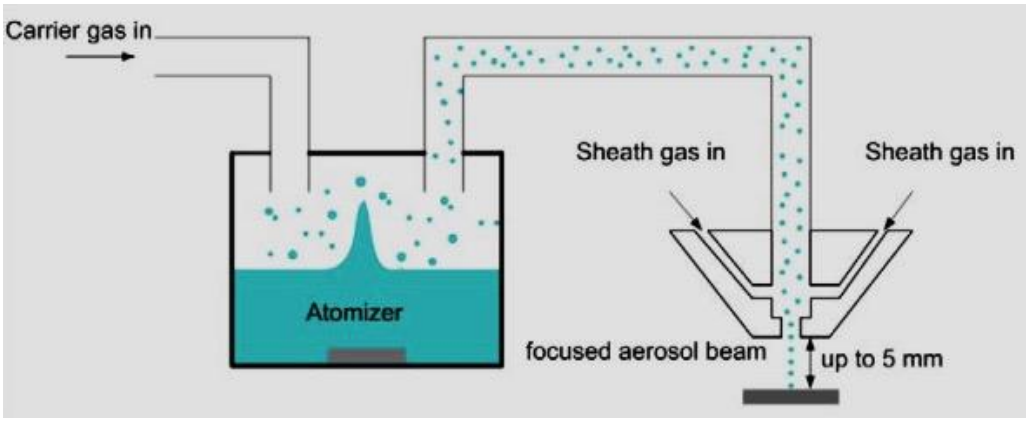

Figure 5.7 A schematic diagram of Aerosol Jet printing process by Optomec Inc. [1]

The increasing demand for Aerosol jet printing comes from the solar industry as it is used to produce cost effective high efficiency solar cells. The deposition process enables printing of narrow lines of less than 40µm in width [1].

5.3.3 MicroPen

The MicroPen system (OhmCraft, Inc., Honeyoye Halls, NY) is a computer-controlled device for the precision printing of liquid or particle suspensions. MicroPen tips are placed at a 15˚ angle, so that particles undergo continuous compression, as well as increasing acceleration of the flow.

The system uses a feedback control to maintain a constant force on the pen tip during deposition. Experimental studies to minimise clogging of the MicroPen tips requires the printing tip to be approximately two orders of diameter greater than the particle diameter. For example, particles can be approximately 1/100th the diameter of the inner diameter of the tip for a stable flow to be obtained. Tips of 25.4µm diameter have been successfully used for printing a paste of silver or gold particles of average diameters of 100nm [90]. The paste viscosity ranges from 100 to 700mPa.s can be dispensed. Materials with a lower viscosity tend to leak out and higher viscosity materials will require additional pressure, potentially damaging the tip [85].

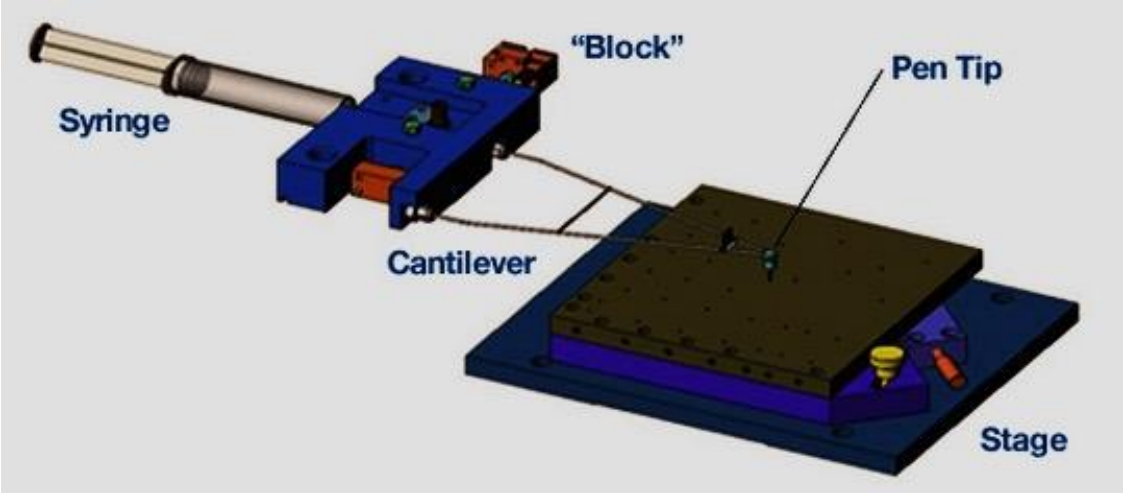

Figure 5.8 Schematic drawing of Micropen technology [91]

5.3.4 nScrypt

The nScrypt is an extrusion-based machine, which was developed through the US Defence Advanced Research Project Agency (DARPA) on project Mesoscopic Integrated Conformal Electronics (MICE) in 2002. The process is based on Sciperio's Micro Dispensing Direct Write (MDDW) technology [85]. Direct write through micro dispensing provides both precision and flexibility as dispensing methods are able to reproduce tracks on a micrometre scale using materials with high viscosity, thus allows dispensing of the ink with a high volume of solid content. The nScrypt machine allows dispensing of material with viscosity ranges from 1 to 1,000,000mPa.s. Micro dispensing direct writing material typically relies on a positive pressure to push the material through a fine nozzle. The nScrypt machine is equipped with a patented SmartPump (Figure 5.9) technology that uses a valve near the dispensing tip to control the start and stop of the material. This feature is unique to the nScrypt DW machine.

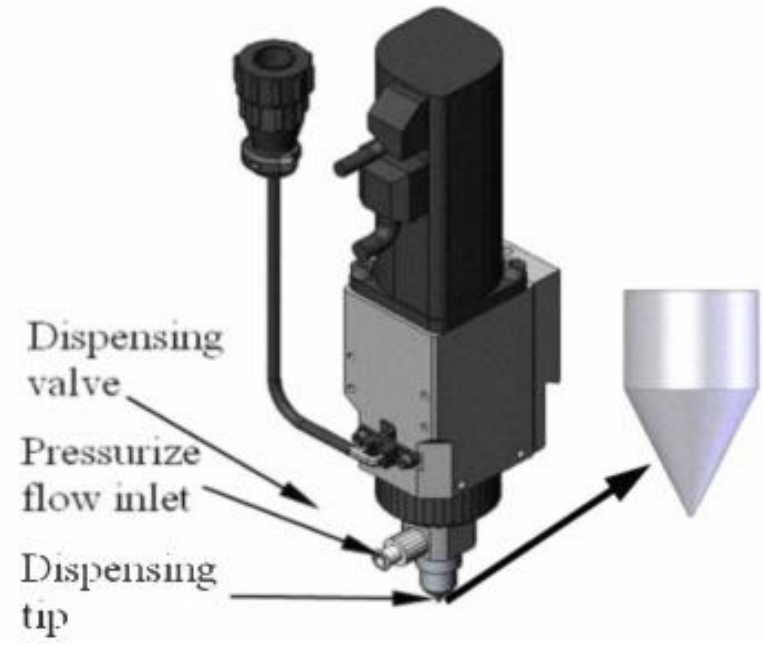

Figure 5.9 Schematic view of the nScrypt SmartPump [78]

To enable conformal dispensing of the nScrypt system, a laser displacement scanning system can be added. The operation of the laser displacement scanning system is shown in Figure 5.10 where the print height is adjusted by the scanning results.

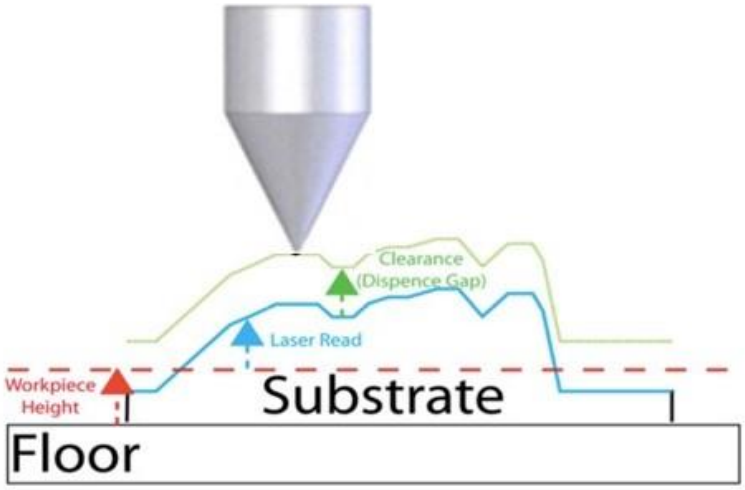

Figure 5.10 Laser displacement scanning for conformal deposition [92]

5.4 Strain Gauge Fabrication Using Direct Write Technology

5.4.1 Ink-jet printing

Ando et al [93] reported the fabrication of silver strain gauge sensors on polyethylene terephthalate (PET) substrate of thickness 100µm using a low cost ink-jet printer (See Figure 5.11). The ink used was commercially available silver nanoparticle solution Metalon® JS-B15P from Novacentrix. Resistive silver gauges were printed with track width of 200µm, track spacing of 200µm and a gauge length of 20mm. The measured gauge factors were between 2.7 to 3.0, which are similar in magnitude to a standard commercial resistive strain gauge.

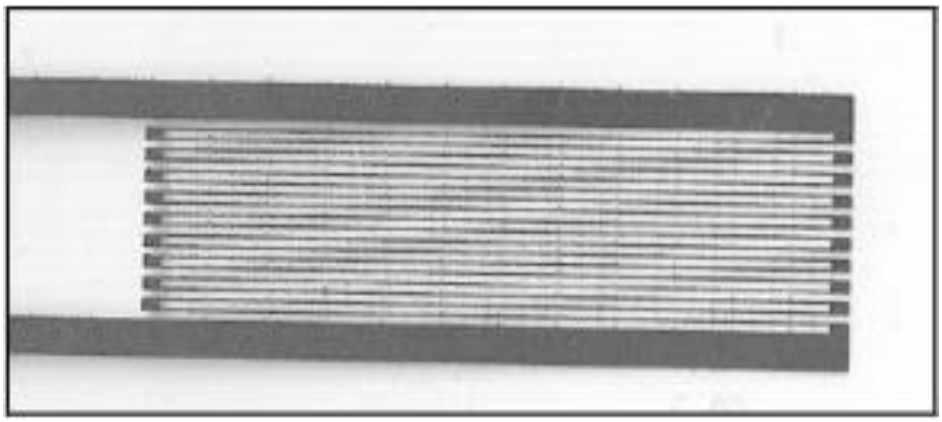

Figure 5.11 Silver strain gauge fabricated with EPSON ink-jet printer [93]

Silva et al [94] reported the fabrication of resistive strain gauges on polyimide film using Dimatix DOD ink-jet printing system. The tracks were deposited using conductive ink composed of silver nanoparticle (50%) in a polar solvent. A picture of the printed strain gauge is shown in Figure 5.12. The research was focused on finite element analysis of the stress-strain behaviour of printed strain gauge on a polyimide substrate. There was no published result regarding the measured gauge factor of the ink-jet printed silver strain gauge on a polyimide substrate.

Figure 5.12 Silver strain gauge fabricated with DOD ink-jet printing on polyimide film [94]

5.4.2 Aerosol Jet

Maiwald et al [95] reported the fabrication of silver-based resistive strain gauges directly on aluminium substrates using Aerosol Jet® technology. Initially a layer of dielectric polymer of 2µm thickness was deposited on to the aluminium surface to isolate the resistive strain sensor from the metal surface. The silver tracks sensing layer were then deposited with a layer thickness of 1-3µm. Post sintering at 350˚C for one hour was carried out to ensure homogeneity of the surface of the silver tracks. Finally, the sensor was encapsulated with a polymer layer. Using SEM small defective porous microstructures were found in the sintered silver track shown in Figure 5.13. The printed silver strain gauge had a measured gauge factor of 3.35±0.13 [95] [96], which was slightly higher than a standard commercial sensor.

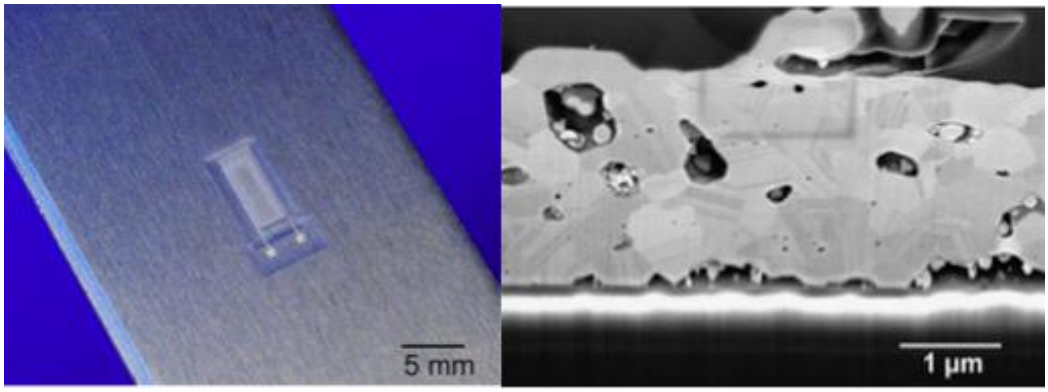

Figure 5.13 Left: Silver strain gauge fabricated by Aerosol Jet technology Right: SEM micrograph of porous structure after sintering[95]

5.5 Non-Direct Write Strain Gauge Fabrication

5.5.1 Screen Printing

Carbon-based

Gutierrez et al [97][98] demonstrated the fabrication of a strain gauge sensor for strain measurement of the urinary bladder. The fabrication process utilised with screen-printing commercially available carbon paste as shown in Figure 5.14. Medical grade silicone rubber (MDX-4) was used to encapsulate carbon conductive material.

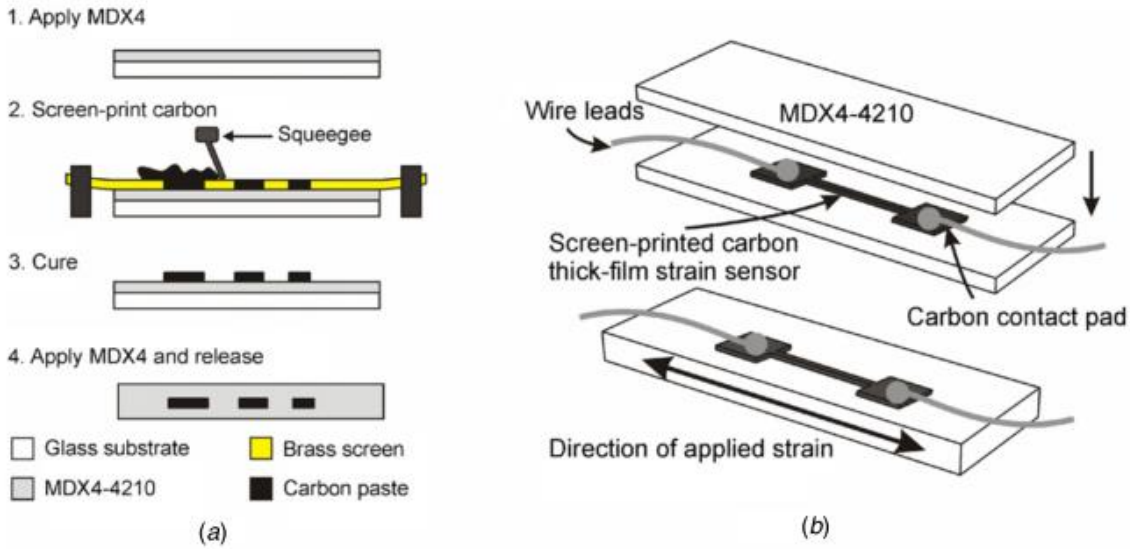

Figure 5.14 Schematic diagram of screen-printed carbon strain gauge sensor fabrication methods [98]

A photograph of the sample is shown in Figure 5.15. To measure the gauge factor, a dynamic mechanical testing machine was used to apply strain and the resistance was monitored simultaneously using a multimeter. Two single-track strain gauge designs with different gauge dimensions were reported. The sensor dimensions were length of 1mm and 500µm width a nominal resistance of 5kΩ and a length of 5.5mm and 75µm width a nominal resistance of 48kΩ, respectively. The gauge factor values measured were 0.85 and 2.48 respectively. Since the *in vivo* environment was considered to be highly temperature stable, the gauge sensitivity measurement was taken to near average body temperature of 37˚C and minimum error within 0.1% was observed. Therefore, Gutierrez et al have stated that the temperature compensation circuitry was not needed for sensor implementation [97].

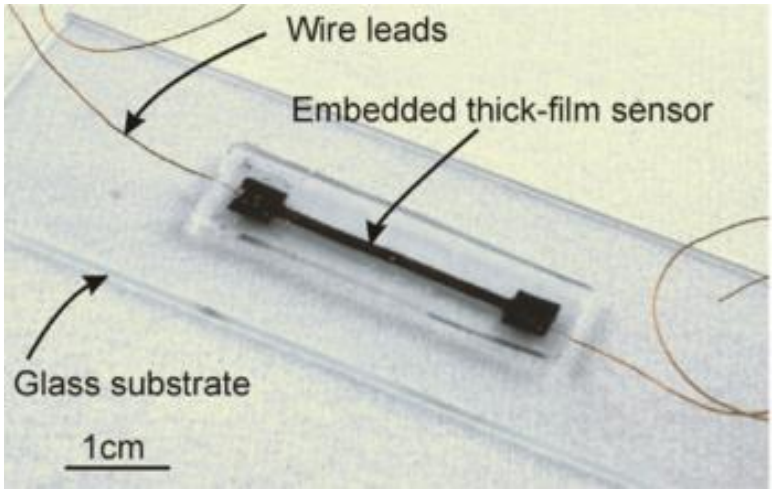

Figure 5.15 Photograph of the carbon strain gauge sample [97]

Graphite-Based

Recently Bessonov et al [99] reported the fabrication of a graphite-based strain gauge on flexible 125µm thickness poly(ethylene) naphthalate (PEN) substrate using screen-printing. For mass production, a photonic (xenon) flash was used for fast (approx. 10secs) curing of the graphite-based paste as opposed to conventional curing, which on average requires 30 minutes at 120˚C (Figure 5.16). The xenon flash enables selective curing as the graphite material strongly absorbs light with a wavelength range from 200 to 900nm. The curing process involves cross-linking of polymeric matrix and rapid evaporation of the solvent.

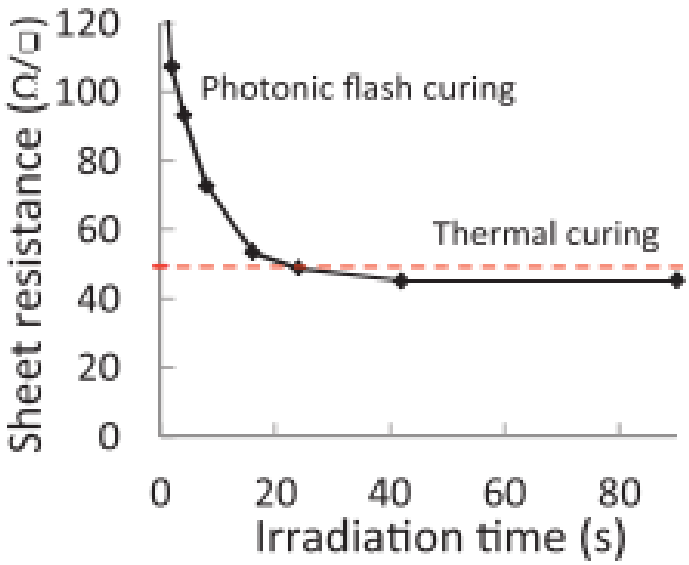

Figure 5.16 Sheet resistance vs irradiation time under photonic flash curing [99]

The dimensions of a linear geometry graphite based strain sensor were as follows, a single track width of 0.5-1.5mm, a track length of 20-30mm and average track thickness of 6.6±0.4µm. The measured gauge factor of the graphite-based strain gauge was approximately 19.3 ± 1.4. The gauge factor is greater than a standard commercial strain gauge, by approximately a factor of 10. The author states that graphite strain gauges can be used without significant temperature correction over temperature range from 20˚C to 50˚C.

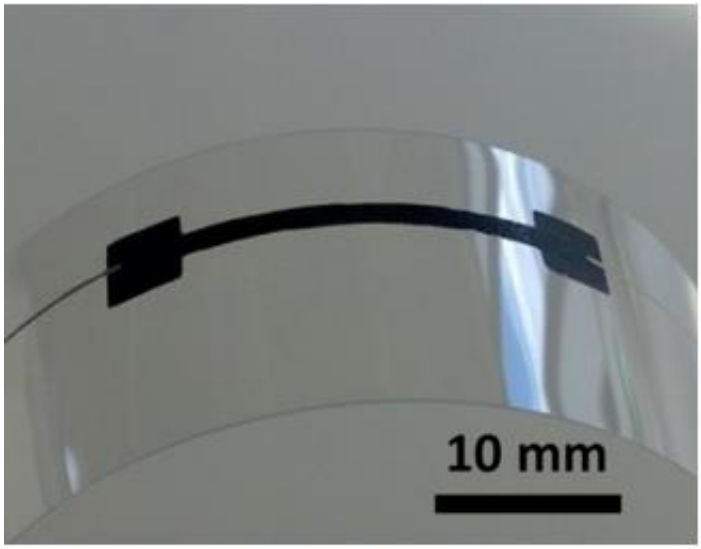

Figure 5.17 Graphite-based strain gauge fabricated by screen printing [99]

5.5.2 Ion Implantation

Ion implantation has also been used to produce thin conductive films by implanting the conductive carbon particles into an epoxy bulk substrate with a thickness of 3mm. The insulating epoxy substrate was irradiated at room temperature with a C^+ ions beam of energy 50-100KeV. The fabricated strain gauges were found to be more stable, exhibiting resistance to both abrasion and erosion when compared to conventional metal foil strain gauges deposited on a polymer substrate. This method of fabrication can be used to manufacture strain gauges to be used in hostile environments and has the benefit for measuring large strains (Figure 5.18) [100]. Therefore, the fabrication

method will not be useful for the manufacture of strain gauges for medical applications on implants.

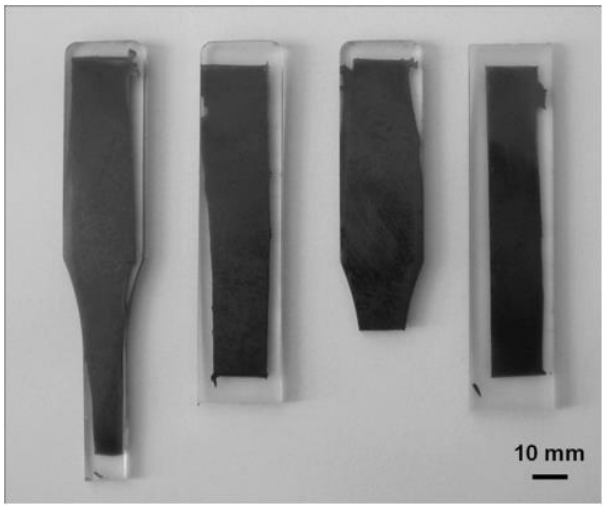

Figure 5.18 C^+ Ion implantation strain gauge [100]

Figure 5.19 shows the change in resistance as a function of applied load for the ion implantation strain gauge. When a load is applied, distortion occurs on the top-surface of the gauge, the conductive C^+ layer remain unstrained. The change in resistance starts only after a 300N load has been applied. No gauge factor measurement was reported in the literature on ion implantation strain gauges.

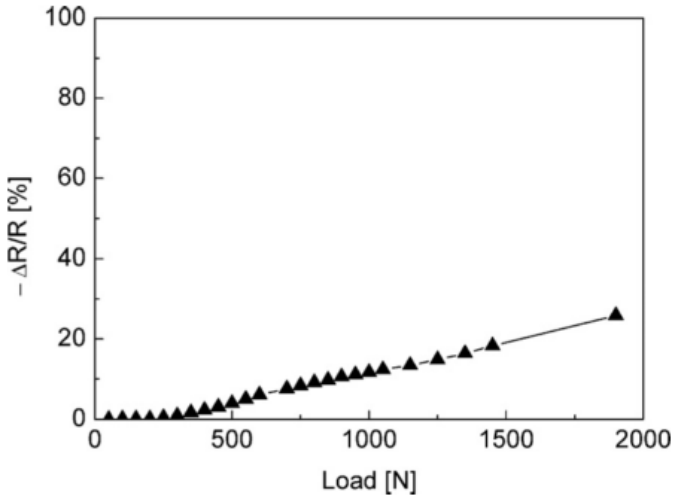

Figure 5.19 Resistance change vs. load of C^+ ion implantation strain gauge [100]

5.5.3 Thermal Spray

Thermal spray is a well-established process for the DW deposition of coatings, and it is commonly used to produce engineering components for use in harsh environments. Jon et al [101] reported the fabrication of silver and nickel chromium (NiCr) resistive strain gauge sensors. The fabrication of NiCr strain gauges using thermal spray is straightforward. The NiCr is used for both the strain sensor and the lead wires, provided the width and thickness of the lead wire are made thick and wide. Thus the effective resistance of the lead wire is negligible compared to the strain gauge element. The problem remains to fabricate highly dense lines for significant changes in resistance requires very fine line widths. Therefore, there was no gauge factor measurement reported on resistive strain gauges fabricated using thermal spray. Li et al [102] have demonstrated the fabrication of interdigital capacitive strain gauges using computer controlled thermal spray and ultrafast laser machining. The silver conductive material is sprayed directly on to various substrates (EEA, Polyethylene, Graphite composite) and no adhesive or mechanical bonding was required. Currently, thermal spray allows for deposition of minimum line width up to 200µm.

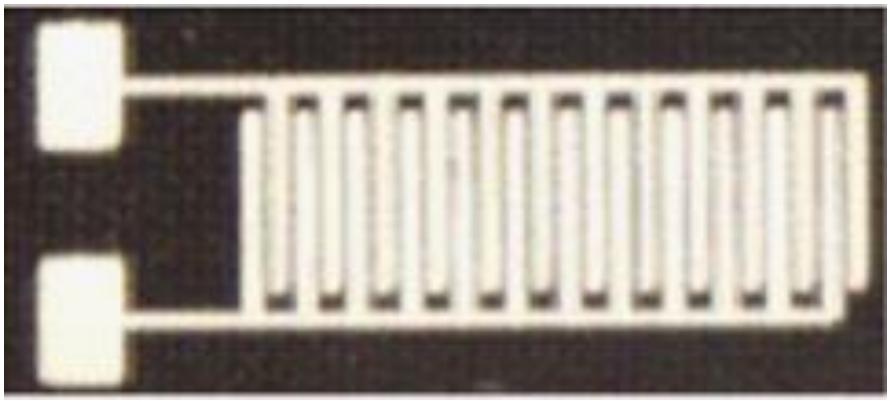

Figure 5.20 Silver interdigital capacitive strain gauges fabricated by thermal spray [102]

To overcome problems of realising narrow lines using thermal sprays interdigital capacitive strain gauges can be considered. They usually have higher gauge factors than resistive strain gauges, and are suitable for high temperature operation. The gauge factor of interdigital capacitive strain gauge is measured using the following equation:

$$GF = \frac{\Delta C/Co}{\Delta l/l} = \frac{\Delta C/Co}{\varepsilon} \tag{5}$$

Where C_0 is the initial capacitance and and l_0 is the gauge length, ΔC is the change in capacitance, and ε is the strain applied. A cantilever beam rig was used to apply mechanical strain (ε). Since the strain is linearly related to the deflection of the cantilever tip; the applied strain can be calculated using the following equation[102]:

$$\varepsilon(x) = \frac{3hy}{2L^3}x \tag{6}$$

Where L (cm) is the length of the substrate, h (cm) is the thickness of the substrate, x (cm) is the distance from centre of the gauge to where the load is applied, y (cm) is the deflection of the substrate applied by the micrometre. The schematic diagram of the cantilever arrangement is shown in Figure 5.21.

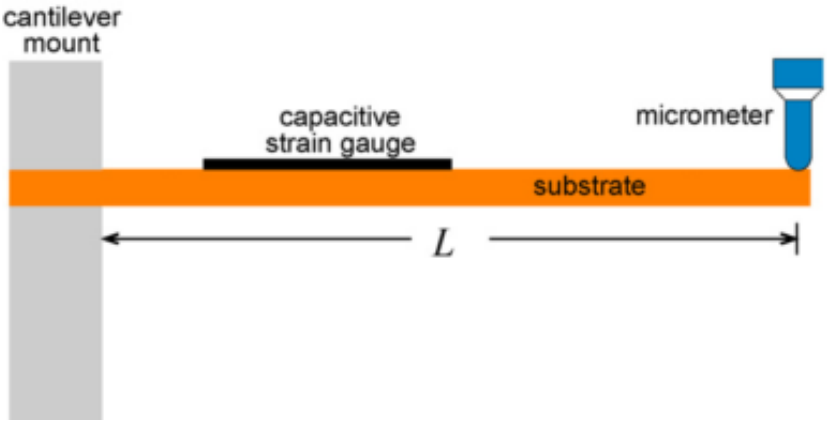

Figure 5.21 Illustration of cantilever beam measurement for mechanical test of strain gauges

The highest interdigital capacitive gauge factor measured is reported to be as high as 21.1. There is large variation in gauge factors from the same production batch where the gauge factor of some samples can be as low as 10, this variation is shown in Figure 5.7. The variation was found to be caused by non-uniform finger widths due to the poor width control when using the spray deposition system [102]. The fabrication of the capacitive strain gauge was not perused since additional polymeric passivation layer will be required to ensure the biocompatibility of the sensor component, and therefore the change in capacitance cannot be obtained due to the polymeric barrier between the sensing fingers.

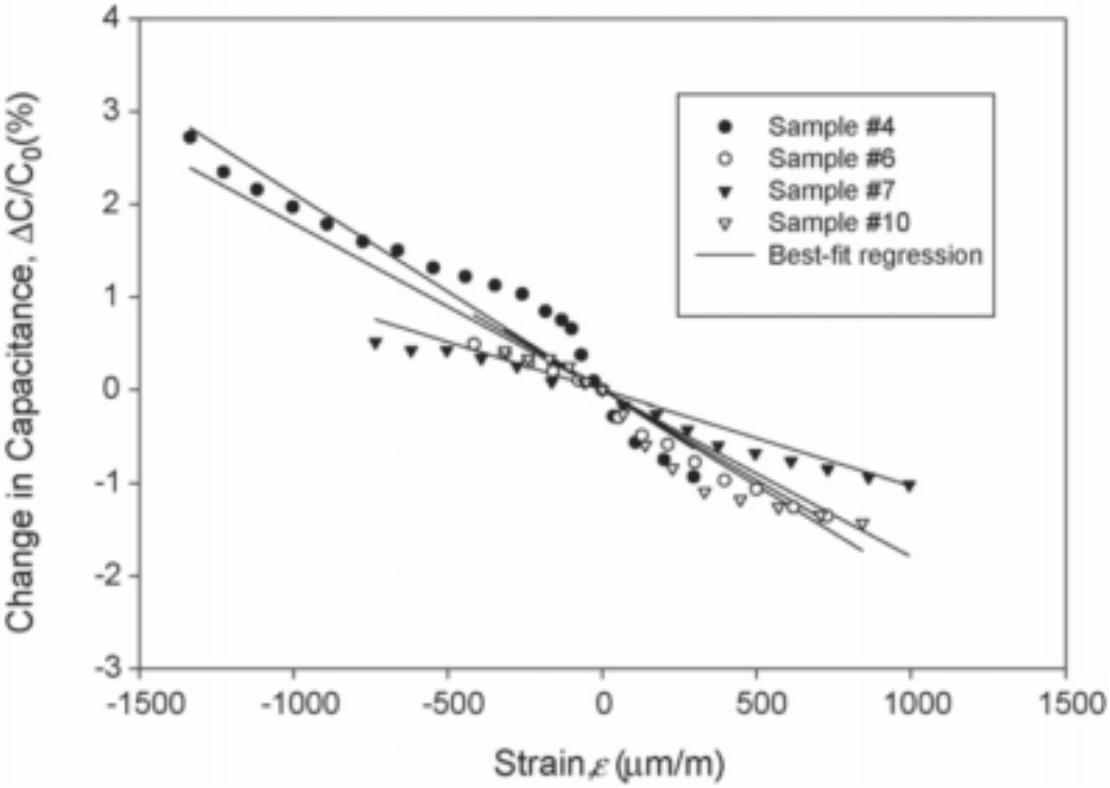

Figure 5.22 Linearity of thermal spray silver inter-digital capacitive strain gauge [102]

5.5.4 Carbon nanotube and carbon nanonet

Lee et al [64] have reported the fabrication of strain gauge using single walled carbon nanotubes. The carbon-based strain gauges have a high resistance compared to strain gauges fabricated using other conductive pastes for example silver, and advantages using carbon are listed below:

- Increase power signal without increasing power dissipation by increasing excitation voltage
- Reduce heat generation (V^2/R) by applied voltage (V), as resistance of the strain gauge is higher.
- Decrease lead wire effect as resistance of strain gauge is higher

The fabrication process of carbon nanotube strain gauges is shown in Figure 5.23. The main steps are[64]:

(a) Spin coat polyimide film on glass substrate. Curing for 1 hour at 350˚C.

(b) Evaporate Cr film on polyimide substrate. Photolithography was used for patterning the Cr electrode and wet-etching process applied using Cr7 etchant.

(c) Spray coated carbon nanotube suspension. RF oxygen plasma treated for enhance interaction between carbon nanotube and polyimide. Carbon nanotube etching was performed to form strain-sensitive lines using O_2 plasma equipment.

(d) Release film strain gauge from glass substrate.

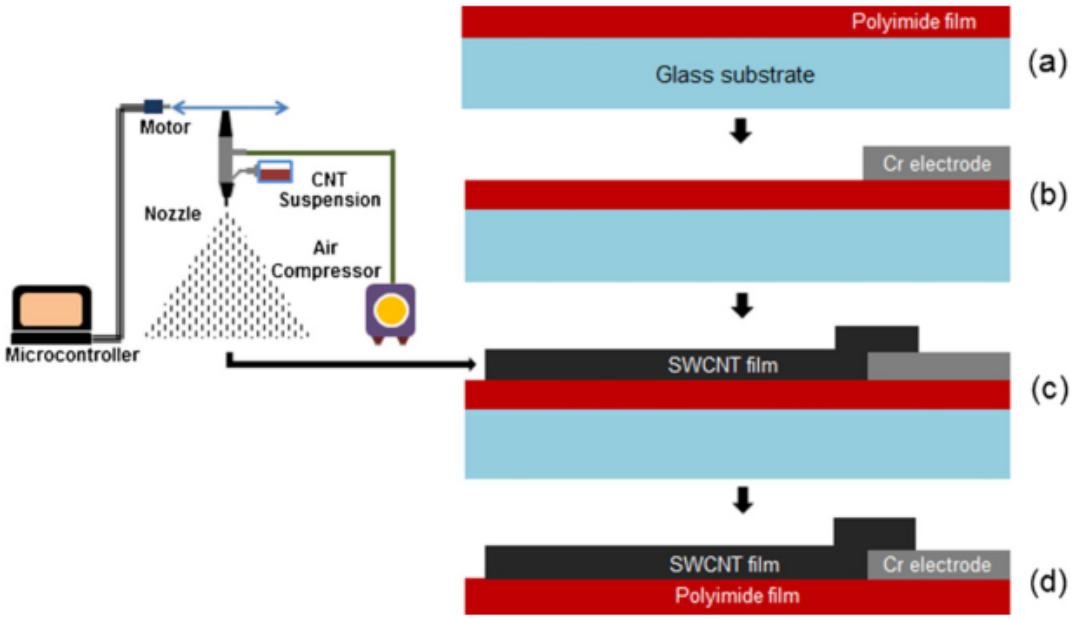

Figure 5.23 Carbon nanotube film strain gauge fabrication process

As can be seen from the steps above the process is very complicated when compared to strain gauges fabricated using the DW process. The carbon nanotube strain gauge dimensions are shown in Figure 5.24 where the track width was 200µm and gauge length was 3mm.

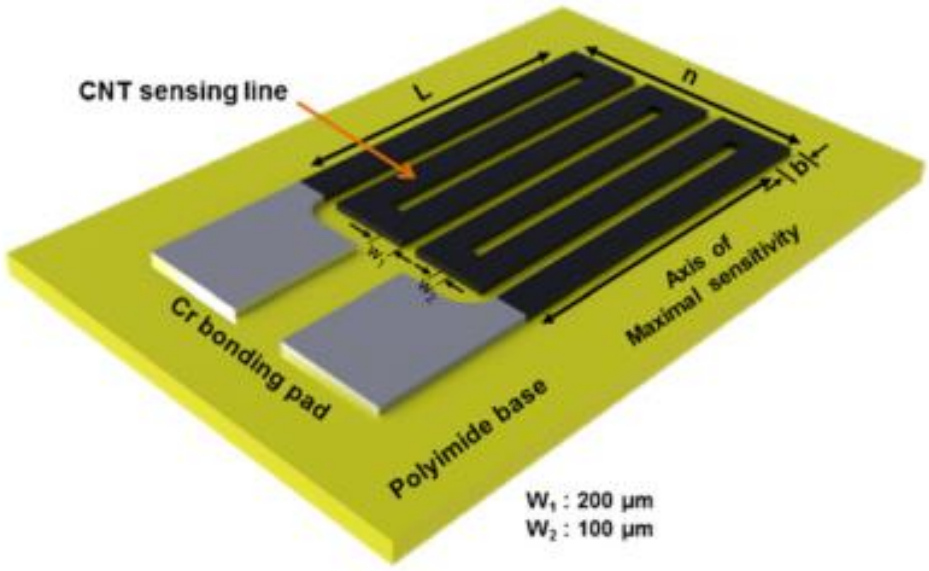

Figure 5.24 Carbon nanotube strain gauge design

The gauge factor values of the carbon nanotube strain gauges were measured using binocular spring element as shown in Figure 5.25. The measured gauge factor values under tensile and compressive strain were 59.2 and 62.1 respectively.

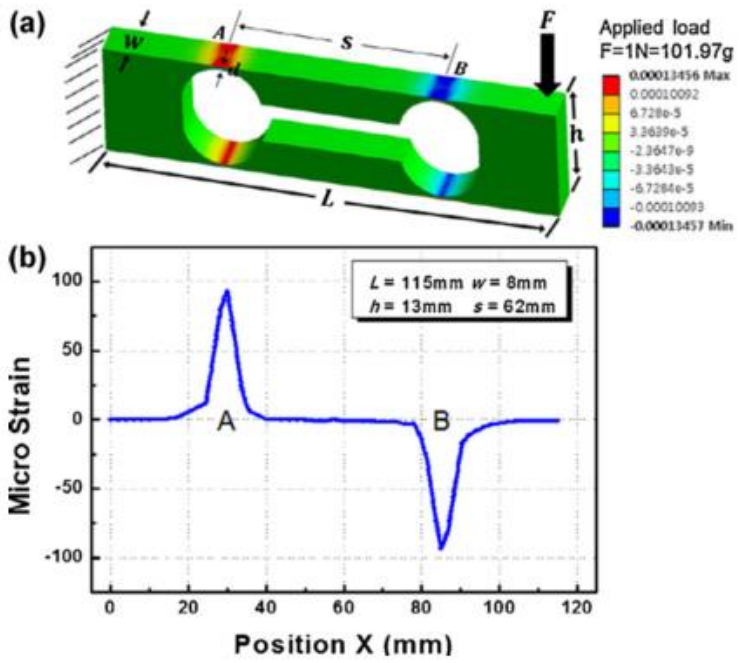

Figure 5.25 Binocular spring element for gauge factor measurement

5.5.5 Carbon nanonet

Carbon nanotubes are fabricated using laser ablation, arc-discharge and catalytic chemical vapour deposition (CCVD). Carbon nanotubes becomes carbon nanonet with certain thickness using CCVD fabrication method. Huang et al [103] has demonstrated the strain gauge fabrication using carbon nanonet for bone strain measurement. Parylene C was used to ensure the biocompatibility of the gauge. Moreover, the Young's modulus of parylene C is lower than those of human cortical bone and trabecular bone. Therefore, the mechanical properties of parylene C are suitable as a backing material and can be fully attached to bone surface. The fabrication process is shown in Figure 5.26 and described as follows:

a) To grow a 500nm silicon dioxide layer on a silicon wafer. Apply cleaning solution on the silicon dioxide surface and dipped in a catalyst Co/Mo solution to make surface hydrophilic.
b) Deposit carbon nanonet layer using alcohol catalytic chemical vapour deposition (CVD). The carbon nanonet grows at 750˚C.
c) Use reactive ion etching to form a serpentine carbon nanonet conductive layer
d) Deposit a 6µm layer parylene C on the track
e) Place a thermal release tape to bond the parylene C layer with carbon nanonet layer
f) Transfer the carbon nanonet layer and parylene C layer off the silicon wafer
g) A gold layer act as electrode using lift-off process
h) Encapsulation parylene C layer is formed using CVD
i) Heat release the strain gauge at 120˚C for 1 minute on a hot plate

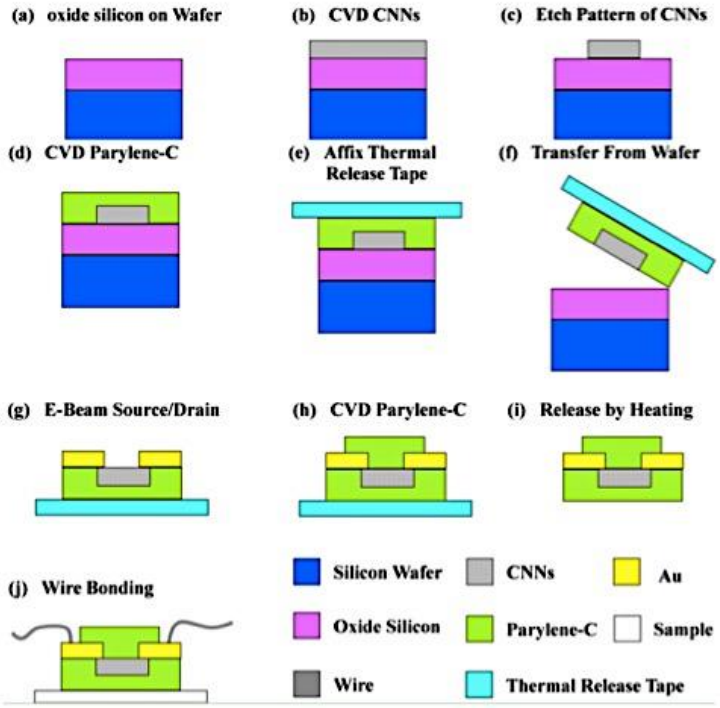

Figure 5.26 Fabrication process of carbon nanonet strain gauge [103]

A sample of carbon nanonet strain gauge sample is shown in Figure 5.27. The thickness of the carbon nanonet tracks was proportional to its growth time. With a constant

growth time, it was found that the gauge factor was higher with a narrower track width under the same number of turns. The authors stated that the higher the thickness of the carbon nanonet, the smaller effect was found on the gauge factor. The measured gauge factor of carbon nanonet strain gauge ranged from 4.64 to 5.56 with an average of 5.05.

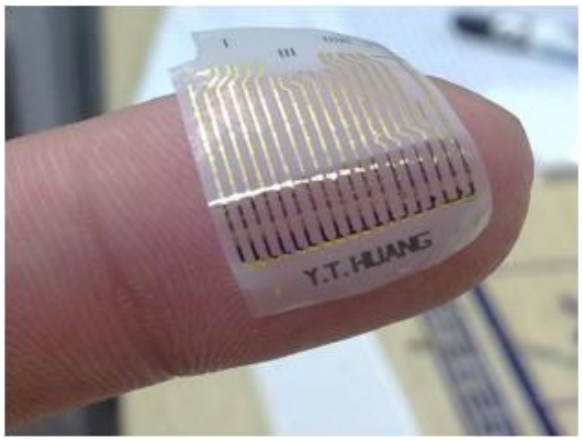

Figure 5.27 Photograph of carbon nanonet strain gauge sample [103]

5.6 Summary

This chapter has summarised the research into strain gauge fabrication from the literature. The work has indicated that most researchers use the gauge factor as the parameter to compare performance between strain gauges. Moreover, some of the fabrication processes are extremely complicated to realise strain gauges (for example the carbon nanotube) although with improved gauge factors. The latter fabrication complications may preclude the use of the process in volume production. Table 5.1 summarises each of fabrication methods and notes the sensitivity (gauge factor) of the strain gauge produced.

Table 5.1 Strain gauge fabrication methods summary

Researchers	*Type*	*Material*	*Method*	*Gauge factor*
Ando et al	Resistive	Silver	Inkjet printing (DW)	2.7 - 3.0
Maiwald et al	Resistive	Silver	Aerosol Jet (DW)	3.35±0.13
Gutierrez et al	Resistive	Carbon	Screen Printing	2.48
Bessonov et al	Resistive	Carbon	Screen Printing	19.3±1.4
G. Girolamo	Resistive	Carbon	Ion Implantation	n/a
Li et al	Capacitive	Silver	Thermal Spray	10 - 21
Lee et al	Resistive	Carbon	Carbon Nanotube	59.2
Huang et al	Resistive	Carbon	Carbon Nanonet	5.05

Photolithography and chemical etching were not included as the process is more expensive as it does not enable bespoke fabrication as required for medical applications. However, to ensure the biocompatibility of the sensor, Gutierrez et al used medical grade silicon rubber as biocompatible backing and encapsulation layer; Huang et al and Yang et al used parylene C. The work did show that the CVD process for depositing parylene C could be controlled to uniform micron layer thickness.

The findings from the literature have led to the proposed aim of manufacturing an integrated strain sensor directly on to implant for strain monitoring. As medical implants, for example bone scaffold or orthopaedic bone plates, are contoured to match the surrounding bone surface, DW technology such as Aerosol Jet, MicroPen and nScrypt are most suitable in the respect due to their conformal deposition ability. These methods also have the advantage of being easily adapted for bespoke structures, which most medical implants will be.

In addition, the deposition fabrication processes are relatively simple that involving only printing and curing process which can be made to be environmentally friendly without chemical etching process. Moreover, the process does not require expensive additional tools such as masks.

Chapter 6. Research approach and equipment

6.1 Introduction

This chapter describes the methodology adopted for the experimental approach used in this research based on findings from the literature review. In this chapter the following sections are presented:

- Key findings from the literature review
- The significance of the research work
- The overall structure of the research carried out
- The measurement and characterisation technologies required

6.2 Key findings from the literature review

A thorough review of the literature was undertaken regarding to state-of-the-art bone scaffold fabrication methods utilising Additive Manufacturing (AM). The review indicated an increasing interest in adopting suitable biocompatible materials for AM bone scaffold fabrication. Bone tissue scaffold is an artificial three-dimensional structure providing temporary or permanent support for the tissue. The present medical imaging technologies, for example X-ray and CT scan, can be used for post-operative assessment of implant performance but provides insufficient continuous information.

It has been shown that the strain measurement between the implant and surrounding bone is a critical factor during the bone healing process [3]. This has provided an alternative method of assessment using strain gauges, which researchers in the field have utilised to provide real-time strain monitoring of the bone surface [104]. The research work has been carried out using commercial metal foil strain gauges glued to the surface of the bone and the surgical process of attaching and removing the strain gauge is rather complicated and invasive [68].

Similar strain gauge methods for real-time strain monitoring on bone fixation plates has also been carried out for predicting the bone healing process and implant performance [105]. It has been shown the process of gluing the strain gauge to the implant can lead to a number of problems, including:

- The reliability of the adhesive bond particularly for long period monitoring [72].
- The possibility of surface delamination upon stress at bone surface [100].
- The addition of an undefined layer (the adhesive layer between the bone surface and strain gauge) can influence the strain measurement, as the measurement result relies on the adhesive bonding [63].

Recent published research work has recorded the use of carbon and silver based strain gauges. The carbon based strain gauges were fabricated using carbon paste [97]–[99], carbon nanonets [103] and nanotubes [64]. The strain gauge fabrication technologies included screen-printing [93], [97], and Aerosol Jet [96]. From the literature review, silver based strain gauges have been reported with low gauge sensitivity (Gauge Factor ~2.7 to 3.3) compared to carbon-based strain gauges (Gauge Factor ~2.47 to 59.2).

The deposition of parylene C using chemical vapour deposition (CVD) process has been shown to give a uniform thickness in the order of a few microns over a surface area [103][73]. The difference in the gauge factor values was primarily due to the material used for the sensing layer. It was worth noting that among these new fabrication methods, only a few approaches [73], [97], [103] were suitable for medical applications. The issues encountered in the fabrication of these strain gauges for medical applications are summarised in Table 6.1.

Table 6.1 Issues of previous work related to strain gauge fabrication

Primary Researcher	Area of research	Issues Highlighted
M. Maiwald [96]	**Aerosol jet** polymeric isolation layer on metal substrate, then deposition of silver and covered with polymeric protective layer	• Possible process for integrated sensor fabrication • Low gauge factor ≈ 3.35
Dongil Lee [64]	**Carbon nanotube** suspension strain gauge fabricated on polyimide film (wet etching process involved)	• Long curing time (1hr at 350˚C) • Requires adhesive of sensor • No conformal printing ability • Excellent gauge factor ≈ 59.2
Ya-Ting Huang [103]	**Carbon Nanonet** fabrication of strain gauge film sandwiched with parylene C for medical application	• No conformal printing ability • Adhesive required between sensor and implant • Complicated fabrication process that requires etching • Low gauge factor ≈ 5.05
Alexander Bessonov [99]	**Screen printing** graphite strain gauge on flexible substrate	• Method not suitable for conformal fabrication • Good gauge factor ≈ 19.3 • Adhesive required between the sensor and implant.

As reviewed in Chapter 5, Direct Write (DW) technology provides the potential to fabricate an integrated strain sensor on an implant surface without the use of adhesives. There are a number of potential DW technologies that can realise conductive tracks using paste or ink materials. In terms of conformal printing ability, the micro-dispensing direct write (MDDW), is the preferred technique when comparing with laser induced transfer, ink jetting and conventional lithographic techniques [106]. The MDDW method has capacity of depositing conductive paste, to realise strain-gauge geometry on different implant materials, e.g. bone scaffold, metal fixation implants without the use of expensive masks or the need to glue the strain gauge to the

structure. Therefore, the MDDW technology offers the potential to fabricate integrated 'bespoke' strain gauges to the implant for real-time strain monitoring. The use of MDDW fabrication offers significant potential advantages, which are listed below:

- The process is cost effective as no mask is required.
- Low cost screen printable pastes can be used and only small quantities are required.
- A simple fabrication process involving only dispensing and curing
- The process is environmentally friendly as no wet etching is involved, and as no mask is required offers the potential of bespoke strain gauge fabrication at low cost
- The nScrypt micro-dispensing system offers the potential of conformal printing (additional z tracking equipment required) i.e. the ability for deposition on to curvature surfaces.

The technology also offers the possibility of electrical resistive strain gauges to be integrated directly onto bone scaffold material or bone plate for medical implant applications. Therefore, there is no adhesive or mechanical bonding required. Moreover, the gauge design and location can be customised according to the specific implant by simply changing the dispensing path during software programming. Since the bone plates and bone scaffold design often follow the contour to the adjacent bone geometry, the DW system should present conformal deposition ability.

Aim:

The overall aim of this study is to fabricate an integrated strain gauge sensor using Micro-Dispensing Direct Write (MDDW) technology from nScrypt, which can be used for real-time implant strain monitoring.

Objectives:

To achieve the aim, an investigation into the fabrication and performance of MDDW silver and carbon strain gauges using the nScrypt 3Dn-300 will be carried out. Low cost screen printable silver and carbon paste from DuPont will be used to produce the conductive sensing layer of the strain gauge. Methods of integrating the strain gauges employing biocompatible layers without adhesives will be explored as follows:

1. Identify the MDDW processing parameters, dispensing quality control and curing conditions

2. The fabrication of resistive strain gauges on polymeric carriers and investigate gauge performance with the use of glue

3. Explore the feasibility of fabricating integrated resistive strain gauges on bioinert test-plates with deposited parylene C layer as the encapsulation and dielectric layer (without glue)

6.3 Experimental Approach

The following methodology was used to investigate the feasibility of the fabrication of strain gauge using MDDW approach.

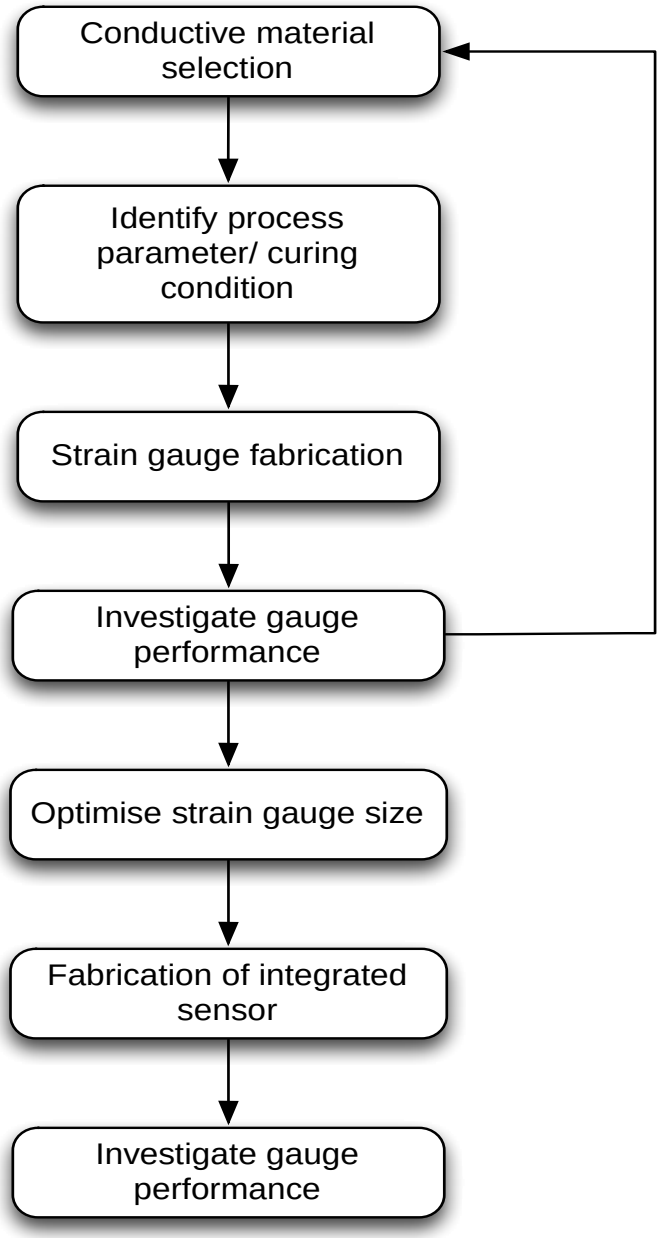

Figure 6.1 Method of experimental approach

6.3.1 Material

Conductive paste

The nScrypt machine allows dispensing of paste material with viscosities ranges from 1 to 1,000,000mPa.s [107]. Therefore, most screen printable pastes can be processed. The conductive pastes used in this experimental project were commercially available screen-printing silver 5025 and carbon 7082 paste (DuPont, Bristol, UK). The silver conductive paste consists of 68% - 72% of silver by weight with a viscosity range between 20 - 30Pa.s. The paste employs a carrier solvent (2-Methoxymethylethoxy) propanol and 2-(2-Ethoxyethoxy) ethyl acetate, as a dispersant. The carbon resistive paste had a viscosity range from 210 to 260 Pa.s. The carbon paste was selected due to its high resistivity and strain-response characteristics that allowed direct resistance measurement using a data logging multimeter without the need of Wheatstone bridge or amplification circuitry [97].

Carrier/backing material for strain gauge fabrication

A carrier (backing) material is needed to provide a mechanical support to the commercial metal resistive strain gauge, as the deposited metal and connecting wires are fragile. The backing material is usually made from a polymeric material that has sufficient dielectric properties to provide electrical insulation between the printed metal gauge and the test surface to which the strain gauge is attached.

Polyimide is the most widely used substrate material for this application and is normally the standard backing material for commercial metal resistive strain gauges suitable for use to temperatures approaching 230˚C [94] [104] [108]. The curing temperature for conductive pastes is limited by the maximum temperature that the substrate can be taken to, as higher temperature may cause damage or rupture of the substrate near the deposited pattern due to different expansion rates of the paste and substrate [109]. For the reasons given above, polyimide (Kapton® HN) was selected as the backing material to be used in this research. Moreover, the Kapton® film exhibits high surface energy when compared to other commercially available flexible substrates

(e.g. Teflon and polyarylate), which helps in producing straight and continuous tracks [110]. Poly-dimethyl-siloxane (PDMS) was an alternative biocompatible carrier material for strain gauge fabrication [73][99]. However, the PDMS carrier to form a strong adhesion require silicone based adhesives, which require a day to be fully cure at room temperature [111].

Adhesives used to glue strain gauges to samples

Conventionally, adhesives are required to attach the strain gauge (Kapton HN) on to the test surface. Typical adhesives used include, cyanoacrylate, two part epoxies and ceramic cement; however, they provide no biocompatibility. Biocompatible adhesives for example, Histoacryl are FDA approved typical skin adhesives for wound closure, and have been used in measuring bone strain gauge with implantable telemetry system [72]. The problem using Histoacryl is that the material only provides a limited bond time and debonding of the strain gauge from the bone surface can occur in longer periods of monitoring. An alternative biocompatible adhesive is a silicone-based adhesive, but these would require a day to be fully cured at room temperature [73].

6.3.2 Experimental Methods

Table 6.2 summarises the experimental methods and equipment used in each test trials.

Table 6.2 Experimental matrix of MDDW strain gauge fabrication

Experimental Matrix of MDDW Strain gauge			
Strain gauge fabrication, characterisation	Test Trials	Method	Equipment/Software
	Preliminary Printing Trial (125µm nozzle)	Micro-dispensing Direct Write	nScrypt 3Dn-300
	Extrusion Temperature	Real-time material temperature monitoring	Thermal Couple, TC-08 Data Logger
	Chamber Temperature	Infrared Thermal Camera	FLIR A40 IR Camera FLIR tool software
	Parameters Optimisation	Three factor three level Design of Experiment (DoE)	JMP statistical software
	Curing condition	Heat curing,	Box Oven, 25µm Probes,
	Silver elemental composition	Scanning Electron Microscope/ Energy Dispersive X-Ray Analysis	Carl Zeiss EVO HD 15/Oxford Instrument X-Max
	Resistance measurement	Four-point probe resistance measurement, Multimeter	Agilent Multimeter, TTI power supply, FLUKE 289 true-RMS Logging Multimeter
	Track Profile	3D microscope Surface Profilometer	Keyence vhx-600 Mitutoyo Surftest SJ-400
Gauge performance	In process wire bonding trial	Wire bonding strength test (WBST)	WBST tester Linwave Technology Ltd
	Resistance/Load tensile test trial	Tensile testing machine	SDL M250, 2.5kN load cell
	Gauge Factor measurement	3-point bending, cantilever bending	Agilent Multimeter, TTI power supply, FLUKE 289 True-RMS Logging Multimeter
	Parylene C Coating	Chemical Vapour Deposition	Para Tech Coating Ltd.
	Surface morphology	Atomic force microscope	Park XE 100 Atomic Force Microscope

6.3.3 Equipment

nScrypt 3Dn-300

The nScrypt model 3Dn-300 equipped with SmartPump (Figure 6.2) is an extrusion-based micro-dispensing direct write machine (MDDW), which relies on a positive pressure to extrude the paste through a fine nozzle. The SmartPump technology employs a valve near the dispensing tip to control the start and stop of the paste material. This feature is unique to the nScrypt machine. The SmartPump allows for the deposition of paste materials with a wide viscosity range (1 to 1,000,000mPa.s) [107], which enables patterning of the strain gauge using commercial available conductive pastes.

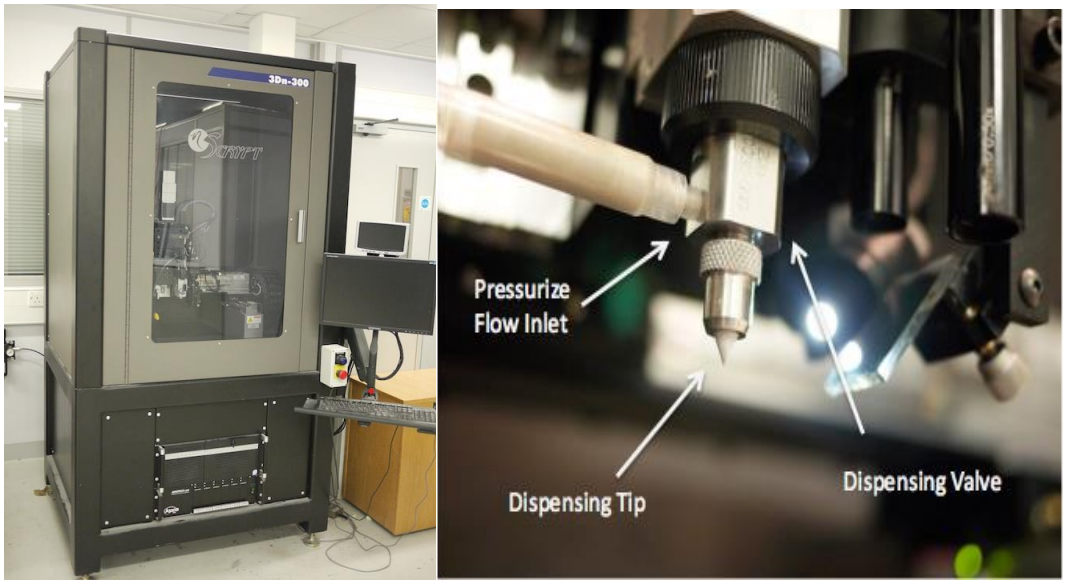

Figure 6.2 Right: the nScrypt 3Dn-300 Left: the SmartPump

The nScrypt process enables high speed, non-contact printing for patterning paste or ink material with tracks of high aspect ratio. The maximum linear printing speed along X and Y-axes can be as high as 500mm/sec. The X/Y axes dispensing accuracy is within 5µm. The machine provides maximum building volume of 300mm x 300mm x 100mm. The technical specification of the machine is shown in

Table 6.3 [78].

Table 6.3 Technical specification of nScrypt 3Dn-300 [78]

X/Y Stage Type	AGS1000
X/Y Travel	300mm x 300mm
X/Y Accuracy	±5µm
X/Y Repeatability	±2µm
X/Y Resolution	0.1µm
Z Stage Type	ATS115
Z Travel	100mm
Z Accuracy	±6µm
Z Repeatability	±1µm
Z Resolution	0.5µm
Max Z Travel Speed	200 mm/s

The nSoft Dispense Environment (nDE) software (see Figure 6.3) was used for controlling the dispensing SmartPump. The nDE software controls the following dispensing functions and parameters:

- Upload path script file created using PathCAD 2D
- Obtain SmartPump valve open and close position
- Material feed pressure

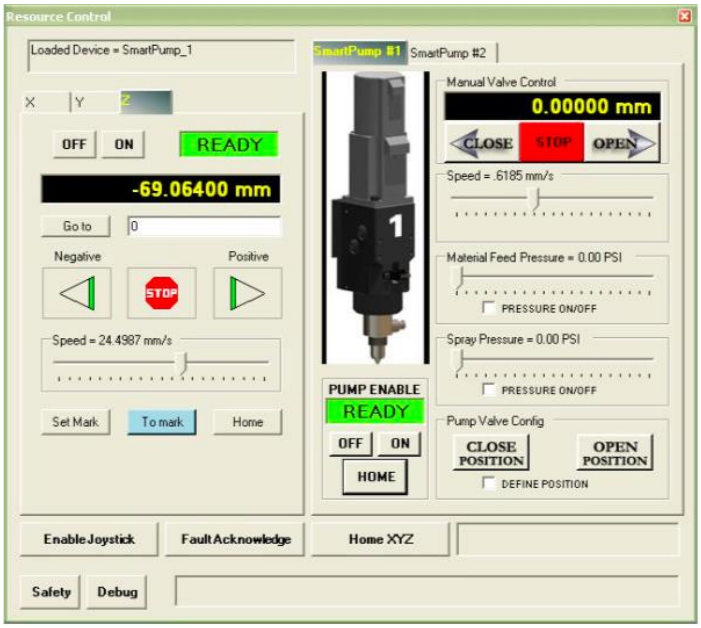

Figure 6.3 nDE Machine tool software process control panel [92]

To fabricate patterns using the nScrypt MDDW machine; the required two-dimensional pattern was first created using a polyline with PathCAD 2D software. PathCAD is a program, which allows inputting a script file to the nScrypt machine. The machine then transfers the script file to G-Code, which is a widely used numerically control programming language. An illustrative diagram of nScrypt file conversion workflow is shown in Figure 6.4.

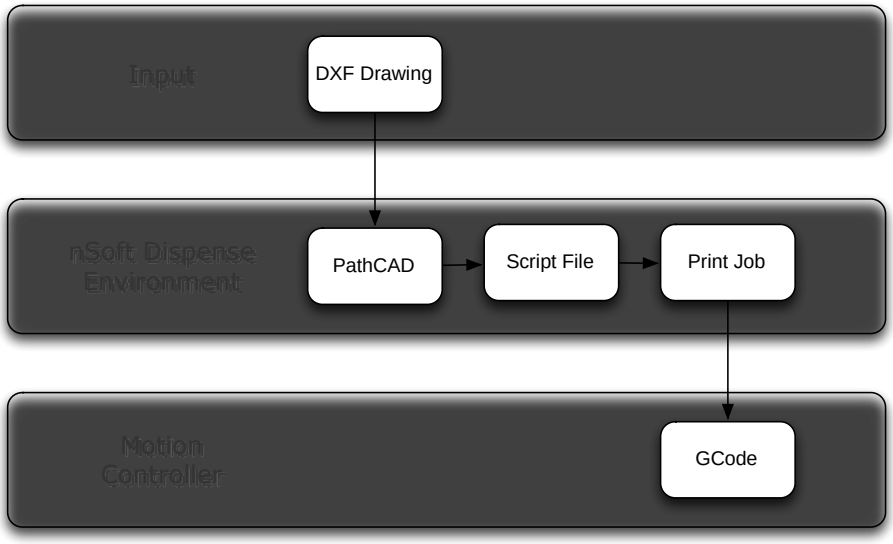

Figure 6.4 Illustrative diagram of nScrypt file conversion workflow

nScrypt process parameters

The process parameters for the nScrypt machine, which need to be inputted, include:

- Valve open/close position (process control panel)
- Dispensing height (process control panel)
- Dispensing speed (path script file)
- Material feed pressure (process control panel)
- Trigvalverel (path script file) - the distance in mm that valve opens (pushes down) and the speed in mm/sec that valve is pushed open
- Trigwait (path script file)- a specific wait time, a designated period of time in seconds, after trigvalverel command to wait for pen tip to fill up.

The nScrypt MDDW parameter settings utilising SmartPump™ technology requires optimisation for consistent ink printing since the parameters are specific to the chosen dispense paste. Prior to printing, it was required to determine the valve open and valve close positions. To obtain the open position, the valve rod was slowly positioned downwards, and as the dispense paste was pushed through the valve and out of the nozzle. At this point the valve rod position was set to the open position. To obtain the close position, the valve rod was slowly positioned upwards until the dispense material being extruded from the nozzle stopped and was “sucked back” into the nozzle. At this point the rod position was set at the closed position. The open and close positions determine the gap that allows the material to pass through the inside of the valve and secure the clean start with the “suck back” phenomenon actuated by the closed position. To achieve clean extrusion for each deposition, the determination of open and close valve positions was critical. An illustration of the valve movement and paste flow is shown in Figure 6.5.

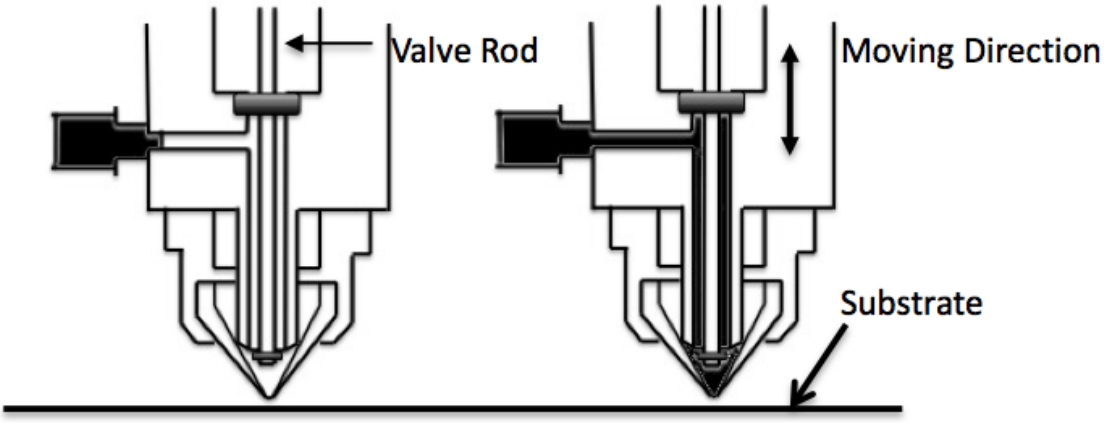

Figure 6.5 Paste flow inside of the dispensing valve

As the most influential process parameters to material flowrate and dispensing performance are dispensing height, dispensing speed and material feed pressure. These process parameters will have to be optimised for different paste materials and nTip nozzle sizes. The trigvalverel and trigwait can be used to further fine-tune the quality of the dispensed track at the start point.

Process parameters optimisation using the conductive tracks

The preliminary process parameter optimisation trials involved dispensing of the screen printable conductive paste using nScrypt SmartPump system using initially a 125µm inner diameter (ID) nTip nozzle. The overall experimental work comprised of the following steps:

1. Test extrusion performance using the nScrypt nTip nozzle. An empirical approach was used to find the range of levels (upper, medium and lower level) of the three main processing parameters: dispensing height, speed and material feed pressure (factors) to achieve a continuous and consistent dispensing.
2. Investigating the inter-relationship of each process parameters, which included dispensing height, dispensing speed, material feed pressure, trigwait, trigvalverel, valve open/close position, valve open speed.

3. Find the most critical parameters with their lower, medium and upper limits from steps 1 and 2. Optimisation of the processing parameters using a factorial design method for consistent track width deposition.

An experimental matrix was produced using three levels (upper, lower, medium level) on three dispensing parameters (factors) to optimise the processing parameters. A repetition of 5 separate runs was conducted and the results e.g. track width, resistance were analysed using the JMP statistical software. On each processed sample the track width was measured and the sets of process parameters, which produced the most consistent width with minimal breaks, necking or bulging was used to fabricate the strain gauges.

Curing trial

Both the selected conductive pastes had a low curing temperature of 120˚C, which is normally recommended for screen-printing on a flexible substrate to drive off the solvent and to ensure good electrical conduction through the deposited paste. The paste curing condition will vary depending on the chosen fabrication process. Trials were conducted to find the optimised curing condition for the MDDW processed tracks. To realise this condition a criteria from the literature was chosen as a guide: “When the deposited lines are cured sufficiently, there should be less than 10% change in resistivity” [112]. The strain gauge samples were cured using a general-purpose laboratory enclosed oven.

Resistance measurement

For silver tracks, a 4 DC probe system was used to make resistance measurements as it enabled a more accurate measurement of the low resistance conductive tracks than the standard two-probe method. In the four probe measurement system two of the probes were used to measure the voltage across the sample and therefore independent of the current. The other two probes were used to supply the current (TTI

PL303QMD-P) to the sample and may be subjected to self-heating (ohmic heating) at the probe tip changing the contact resistance. Figure 6.6 shows the 4 DC probe experimental set-up, the tungsten probe had tips with 25µm in diameter and the resistance was measured using an Agilent 34405A.

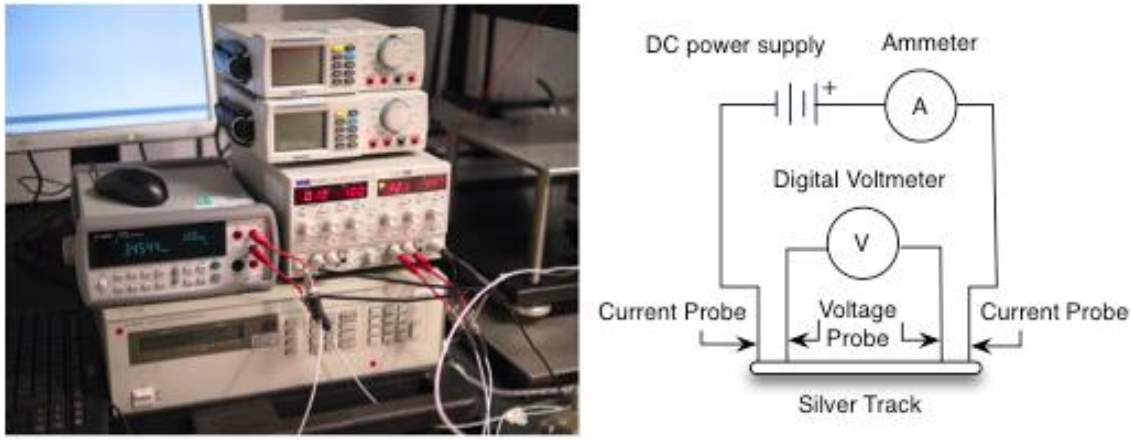

Figure 6.6 Four-point current-voltage characterization setup

As the carbon paste has a high resistivity when compared to the silver paste, the resistance of carbon conductive tracks were measured using a simple setup consisting of a digital Multimeter (FLUKE 289 True-RMS) in which the voltage and current were measured without the need of Wheatstone bridge or amplification circuitry.

Strain gauge sensitivity measurement

The sensitivity of a strain gauge can be express by its gauge factor, which is defined as the amount of the change in resistance in relation to the change in strain. Therefore, the gauge factor can be expressed by Equation (2), described in section 4.2.1.

$$GF = \frac{\Delta R/Ro}{\varepsilon} \qquad (2)$$

To measure the gauge factor, a known strain was applied to the strain gauge samples and corresponding change in resistance was measured. Two mechanical bending experimental setups were used: three point bending and cantilever beam bending.

A schematic diagram of three-point mechanical bending test is shown in Figure 6.7. Test strain gauge samples were attached to a centre of a steel test beam and strain applied by load weights to the centre of the test beam (Figure 6.7). The applied strain to the test strain gauge samples was measured using a calibrated commercial strain gauge. The change in resistance of the strain gauge was measured using either the 4-probe measurement method or the Fluke resistance meter with built in data logger.

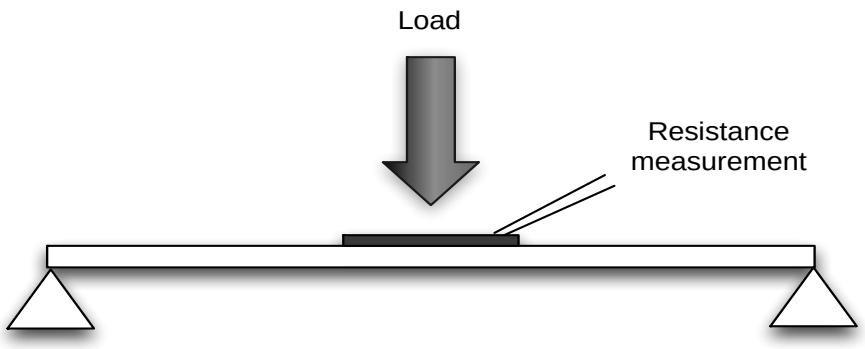

Figure 6.7 Schematic diagram of three-point bending mechanical test

The second method used a custom cantilever beam rig, which was designed and made by the engineering department at De Montfort University. A schematic diagram of the cantilever beam rig is shown in Figure 6.8. The method employs a micrometre (Moore & Wright, Sheffield, UK) to apply strain on a metal test-plate where a test strain gauge was attached. This eliminated the need to use commercial strain gauge after initial calibration to verify the applied strain on test sample gauges. Moreover, the resolution of deflection applied at the end of the metal test-plat by the micrometre was 0.01mm. The strain applied on the test strain gauge attached site can be calculated by following Equation (2) according to Arshak et al [113] and Li et al [102].

$$\varepsilon(x) = \frac{3hy}{2L^3}x \quad (6)$$

Where x(cm) the distance between the strain gauge sensor and the position where the bending force was applied; L(cm) the distance between the clamped end of the test-plate and the position where the bending force was applied; h(cm) the thickness of the test-plate, and y(cm) the deflection of the test-plate by the micrometre.

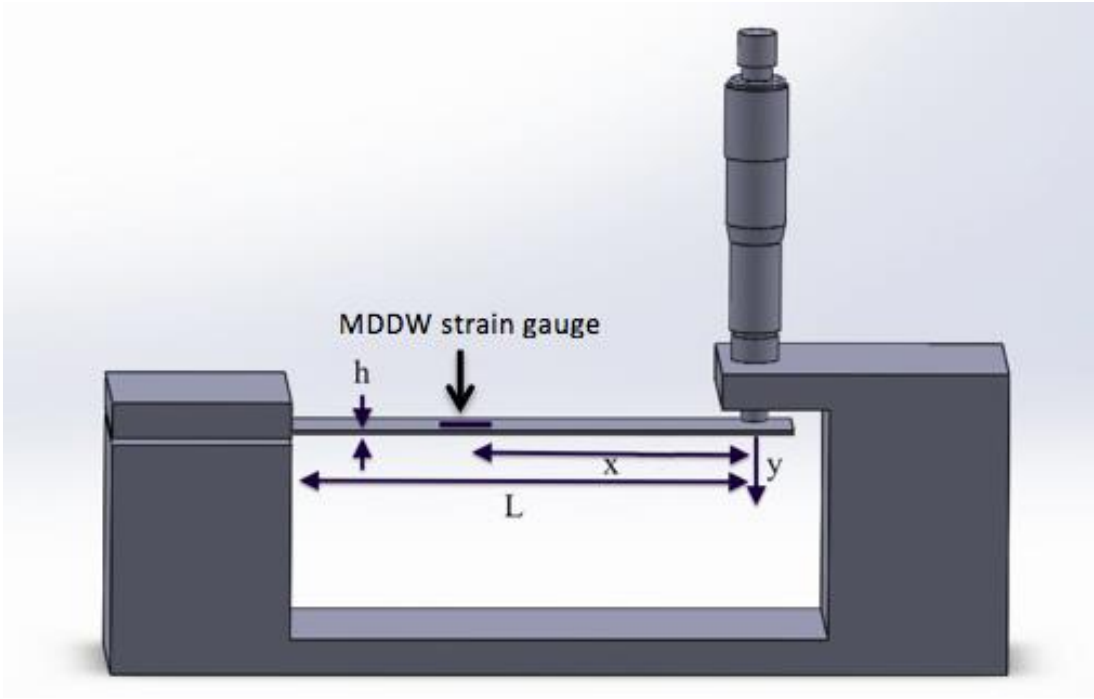

Figure 6.8 Designed cantilever beam rig

Track profile measurement

The consistency of the MDDW conductive track geometry and cross-sectional profile was investigated; using a surface profilometer from Mitutoyo (Surftest SJ-400, Kanagawa, Japan), see Figure 6.9. A surface profilometer is a contact method utilising a stylus and was used for measuring the MDDW cured conductive tracks profiles. Two types of methods can be used to measure the surface profile: skidded and skidless measurements (Figure 6.10).

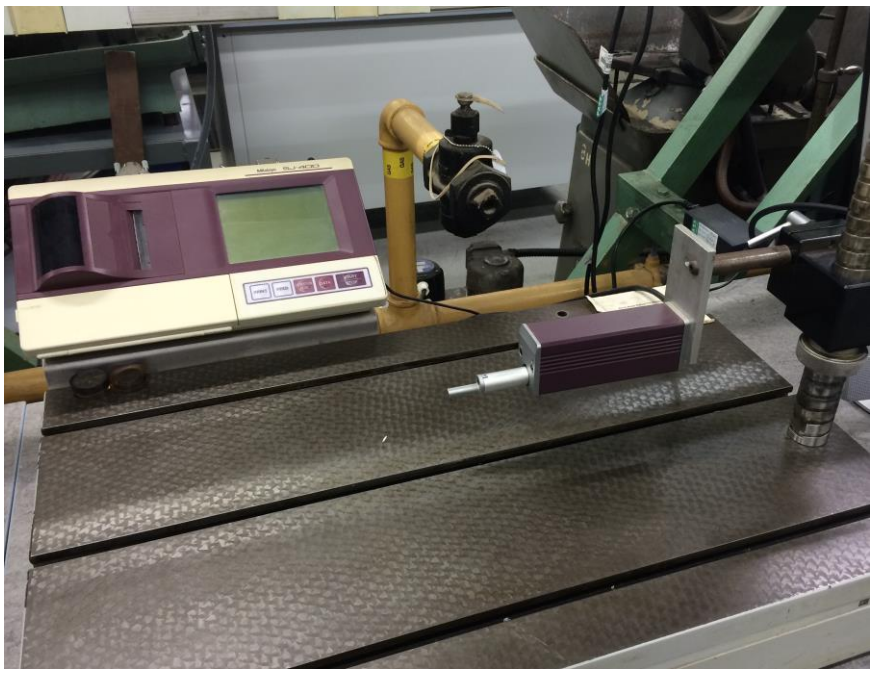

Figure 6.9 Mituyoto Surftest SJ-400 profilometer

In skidded measurements (Figure 6.10A), a skid is placed close to the stylus that results in a greater measuring range. In skidless measurement (Figure 6.10B), the surface features are measured directly by allowing the stylus to travel across the track and the profile of the track is relative to the surface which it has been deposited on. The measuring range is limited to the stylus vertical travel distance. The skidless measurement will allow measurements of waviness and finely stepped features more accurately. Thus the skidless measurement was selected to measure the cross-sectional profile of the dispensed conductive track [114].

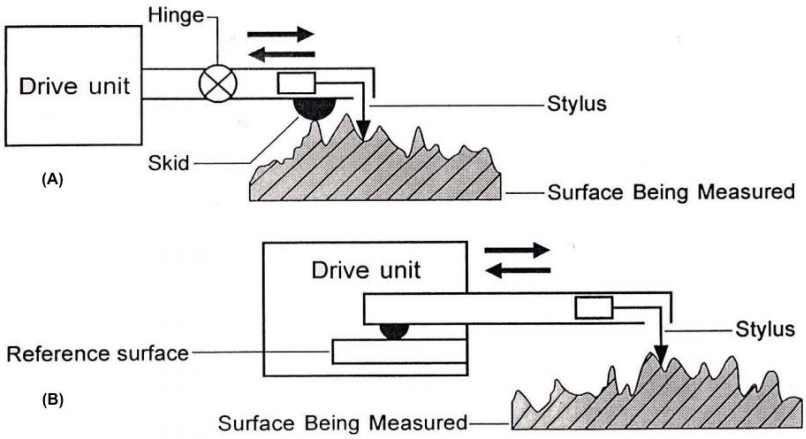

Figure 6.10 (A) Skidded and (B) skidless profilometer measurement [114]

Wire bond strength test (WBST)

Wire bond strength test (WBST) was used to test the quality of wire bonding between the connecting wires to the strain gauge electrodes. The bond pull test was carried out at Linwave Technology Ltd, using calibrated WBST test equipment as shown in Figure 6.11. The test bond wire samples were pulled to a maximum target weight of 100gm (industrial standard). If the bond wires became detached then the sample was destroyed.

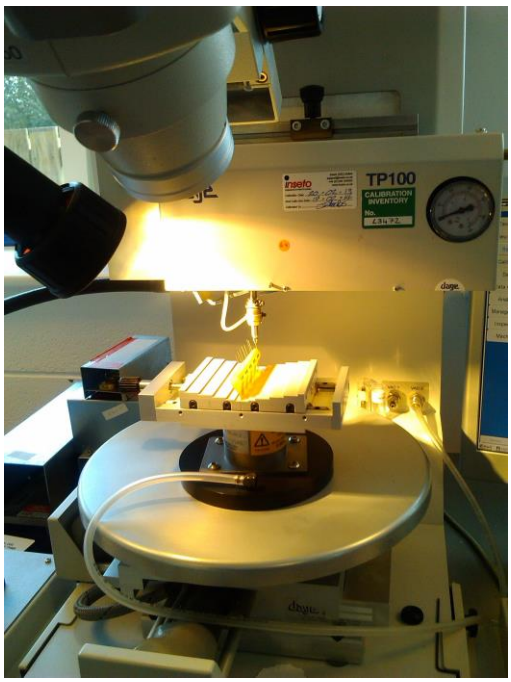

Figure 6.11 Wire bond strength tester

Atomic Force Microscopy (AFM)

Atomic force microscopy (Park XE 100) was used to obtain the surface morphology of the strain gauge samples. Atomic force microscopy employs a nanometre resolution probe scanning across the sample surface. The mechanism consists of a cantilever with a sharp probe physically in contact with the surface. The deflection was measured with a laser spot reflected from the top surface of the cantilever into an array of photodiodes.

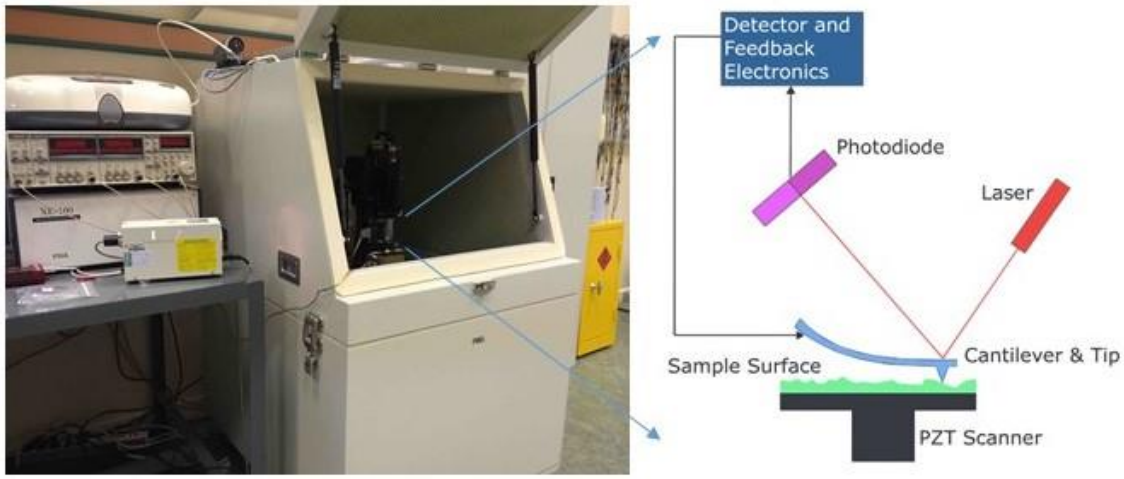

Figure 6.12 Schematic diagram of the AFM operation Park XE 100 Atomic Force Microscope

Scanning electron microscope and Energy Dispersive X-Ray Analysis

A scanning electron microscope (SEM) (EVO HD 15, Carl Zeiss, Germany) was used to analyse the cross sectional area of the strain gauge conductive tracks. The SEM emits a focused electron beam on the sample surface, which interacts with atoms in the sample. A surface topography image of the sample is produced by detecting the signals produced through the interaction. The SEM is integrated with an energy dispersive X-ray (EDX) detector from Oxford Instruments (X-Max, Oxford Instrument, UK). The EDX analysis was undertaken to identify the elemental composition of the track samples. The elements were identified from the energy detection of the emitted x-rays induced by the collision of the electron with the sample.

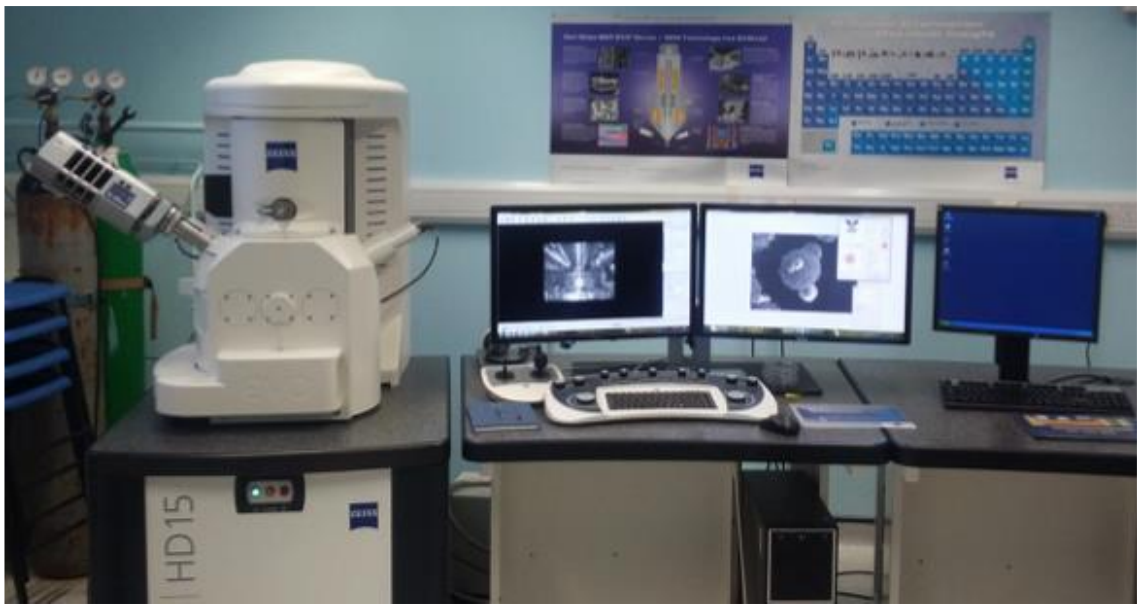

Figure 6.13 Scanning electron microscope with an integrated EDX system

Chapter 7. Direct write silver resistive strain gauges

7.1 Introduction

This chapter describes the experimental work on fabrication of silver strain gauges by micro dispensing direct write (MDDW) technology. The silver paste processing parameters were optimised in relationship to the size of the dispensing nozzle. Possible influences on print quality were investigated. The nScrypt dispensing parameters were then optimised for the dispensing of sufficient silver paste to produce continuous and reliable tracks. The MDDW silver strain gauge sensors were then fabricated and the sensitivity of the sensors characterised using three point bending measurements. The author believes this is the first time the nScrypt machine has been used to produce resistive silver strain gauges using off the shelf commercial silver conductive paste.

7.2 Temperature impact on print quality

During the pilot run, a phenomenon was observed where air was sucked back through the nozzle and an air bubble was formed resulting in a splash start (Figure 7.1) when dispensing silver conducting paste. As printing continued using the same dispensing parameters, the splash start was thought to be due to increasing temperature caused by change in paste viscosity as the viscosity of the conductive paste is highly temperature dependent [115]. Although minor changes on process parameters could be made to minimise the effect, it was not a long-term solution for consistent batch fabrication.

The viscosity of conductive paste highly depends on the particle content, size and shape. The viscosity is also temperature dependent and decreases significantly at temperatures above 30˚C [115]. Hypothesis was made that the increasing temperature was due to either/both friction from the motion controller of the machine and/or the extrusion of the metal particles through the nozzle. The following two trials were carried out for monitoring the temperature impact on print quality.

The process build chamber of the nScrypt machine was not environmentally controlled and therefore the ambient temperature may influence the extrusion performance. Therefore, two separate monitoring trials, each dependent on temperature were performed. The build chamber temperature was monitored as was the extruded paste exiting the nozzle tip.

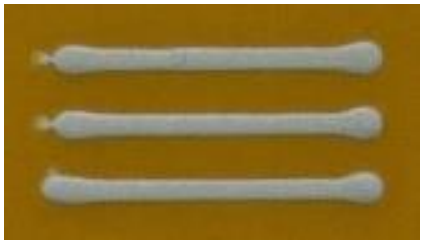

Figure 7.1 Splash start point of a set of silver track

7.2.1 Build chamber for temperature monitoring

As described the changing of temperature in the build chamber may affect the printing result when comparing the start to the end of the printing operation as the viscosity of the conductive paste is highly temperature dependent. During the printing of the trial track geometries, it was found that the motion controller movement might contribute to raising the temperature in the build chamber particularly if the printing time is over 30 minutes. In this process control experiment, an infrared (IR) camera (FLIR A40) Figure 7.2 was used to monitor the chamber temperature change over a pre-determined period of time. The FLIR A40 allows temperature measurement accuracy inside 2˚C when operating in the range from -40˚C to 120˚C, when the surface emission is known.

Figure 7.2 FLIR A40 thermal camera [116]

The IR camera lens was pre-focused on the SmartPump™ valve body and thermal images were taken when the machine started the printing run and 20mins later when the machine was still operating during the print run. The experimental setup for the chamber temperature monitoring is shown in Figure 7.3. To obtain continuous measurement, two K-type thermocouples were used. One thermocouple was placed at the valve body and the other thermocouple was placed on the top of print plate form. Both thermocouples were connected to TC-08 data logger (Pico Technology, UK) to record the temperature every 0.5sec. The TC-08 data logger measurement provided temperature resolution of ±0.5˚C.

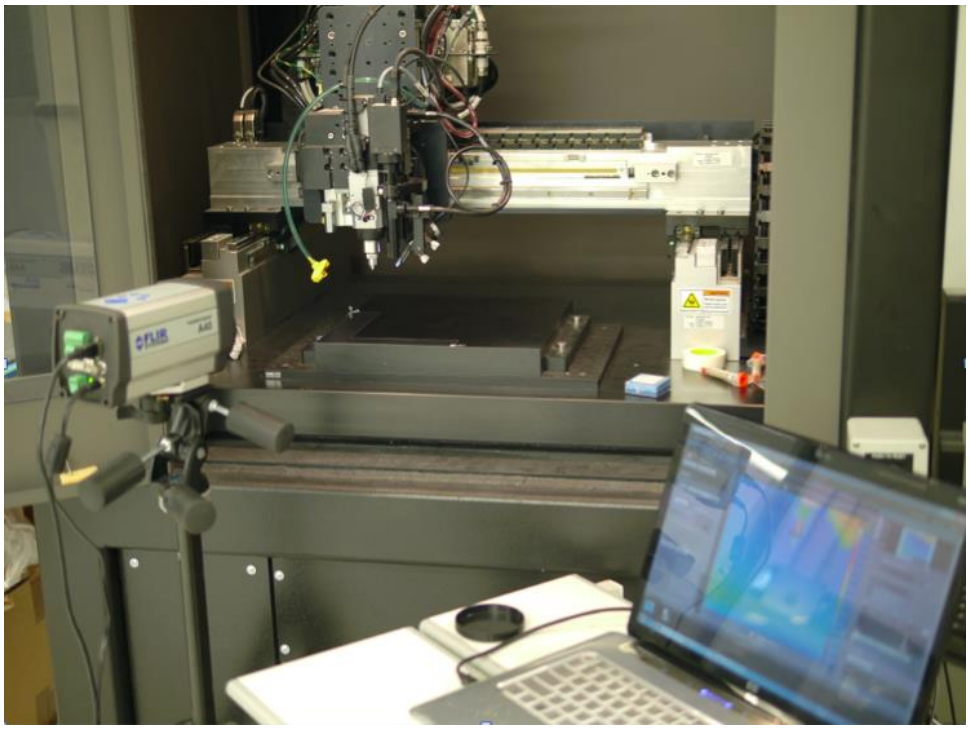

Figure 7.3 Chamber temperature monitoring setup

Results

Temperature increase was observed globally throughout the IR mapping image in the nScrypt build chamber after 20minutes of operation as shown in Figure 7.4. A temperature rise of approximately 1 degree Celsius was observed at the syringe and dispensing tip. The thermocouple temperature measurements on the build platform showed a proportional temperature rise from 26.5˚C reaching 27.5 degree after

operating the machine for 25mins. Similar result was found at the dispensing valve body as shown in Figure 7.5.

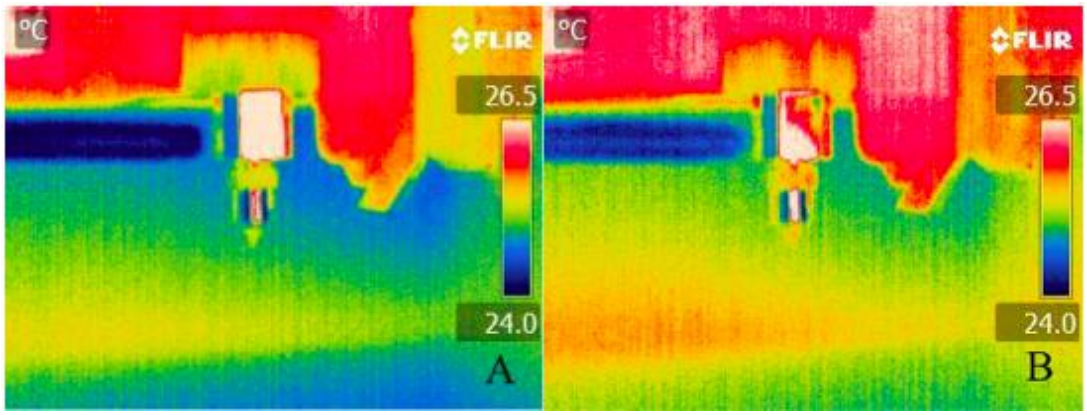

Figure 7.4 IR image of build chamber (A) before (B) after 20min operating

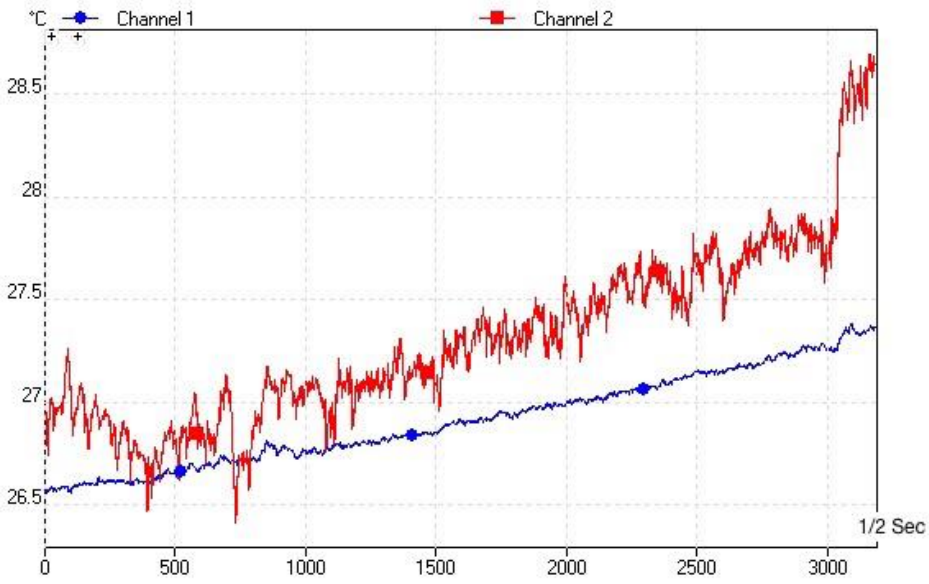

Figure 7.5 Thermocouple measurement of build chamber for 25min. Channel 1 – Build platform. Channel 2 – SmartPump valve body

In order to obtain the required dispensing quality, taken into account the temperature rise of the build chamber, the nScrypt machine was turned on for at least 20 minutes prior to any print job being conducted. This action was aimed to minimise the change in viscosity of the paste by stabilising the chamber temperature.

7.2.2 Extrusion Temperature Monitoring

Silver conductive paste consists of solid silver particles in a solvent. Screen printable silver paste has thixotropic and pseudoplastic properties, meaning the viscosity decreases as a function of increase in the shear force. Since viscosity is highly temperature dependent (viscosity decreases with temperature), the increased temperature might influence printing results during large batch fabrication. A previous study by Evans et al [117] on solder paste, found the paste viscosity increased with increasing the metal content (number of particles). Paste viscosity is also a function of particle size and particle distribution in the solvent. Thus, it is important to investigate how the temperature of the material changes during micro extrusion.

The silver conductive paste was preloaded into a 25ml syringe and connected to the SmartPump™ dispensing valve. A 125micron internal diameter (ID) nozzle was fitted to the valve body. To monitor the material temperature, a thermocouple was placed at the tip of the nozzle as shown in Figure 7.6. A TC-08 (Pico Technology, UK) data logger was used to record the temperature over 15 seconds. The logger was set to collect the readings every 0.5 seconds. Due to the technical difficulty of measuring the temperature during operation, real-time extrusion temperature monitoring while printing a pattern was not applicable.

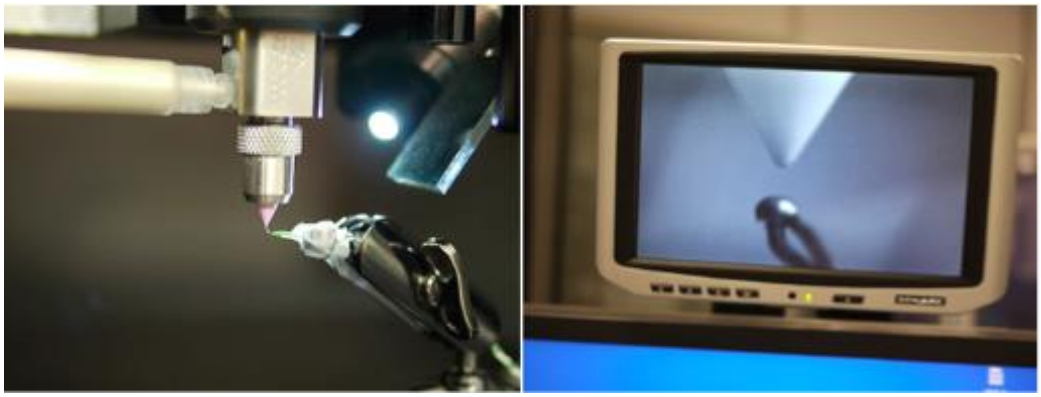

Figure 7.6 Material extrusion temperature setup

The ambient temperature was recorded at 23˚C when the experiment was undertaken. Figure 7.7 shows the plotted silver paste measured temperature as a function of the extrusion time for 30 seconds. At the beginning of extrusion cycle, the temperature of silver paste dropped to slightly less than the ambient temperature at approximately 22.7˚C. After 5 to 9 seconds of extrusion, the extruded paste temperature increased in direct proportion to extrusion time. After 15 seconds of extrusion, the paste temperature rose and stabilised at approximately 24.4˚C.

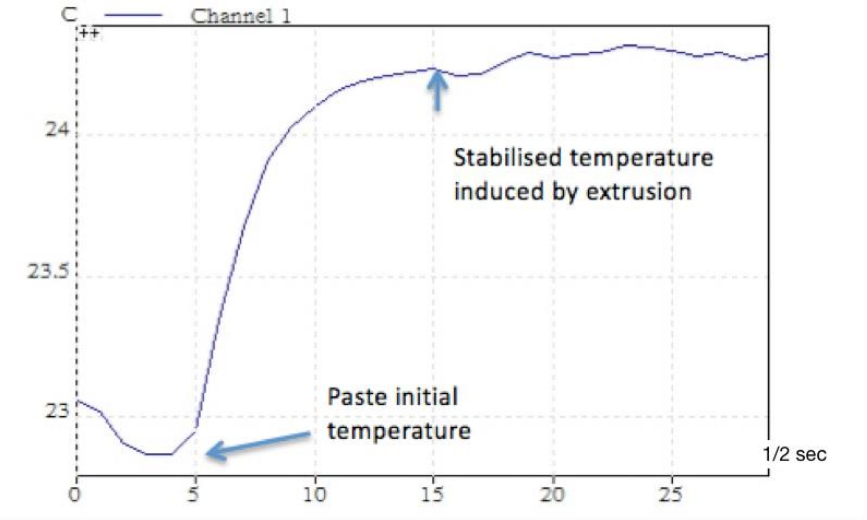

Figure 7.7 Silver paste extruded temperature vs. extrusion time

The experimental results showed extrusion causes the silver paste temperature to rise due to the nature of micro-dispensing mechanism. To conclude, a pre-extrusion cycle was needed to allow for the initial increase in the extrusion temperature before it stabilises, thus enabling a consistent printing process to follow. To allow for the above the first few tracks were excluded during the process parameter optimisation, which is described in section 7.3.3.

7.3 Parameter optimisation (silver paste with 125µm ID nozzle)

7.3.1 Preliminary silver printing trial for parameter optimisation

This trial was to investigate the feasibility of dispensing silver paste using nScrypt MDDW machine, utilising an nScrypt nTip ceramic nozzle of internal diameter (ID) of 125µm, and an outer diameter (OD) of 175µm. To optimise the dispensing parameters a set of parallel tracks of length 10mm was used as the test pattern. The valve open and close positions were found to be at 1.74mm and 1.34mm respectively using the method described in section 6.7.1. The initially chosen printing parameters are shown in Table 7.1.

Table 7.1 Initial setting of parameters

Parameters	Value
Dispensing Height (µm)	100
Valve Open (mm)	1.74
Valve Close (mm)	1.34
Material Feed Pressure (psi)	9
Dispensing Speed (mm/s)	50
Trigwait (s)	0.001
Trigvalverel (mm)	0.25

First the dispensing speed was changed to investigate the effect on the printed pattern. Track breakages were observed (Table 8-2) and this was thought to be due to the flowrate being too low to match the 50mm/s deposition speed. The dispensing speed was reduced to 40mm/s and then to 30mm/s and the tracks reprinted respectively. The track breakages were still observed as shown in Table 7.2. To increase the material flow during deposition, the valve-opening position (trigvalverel) was increased from 0.25mm to 0.55mm.

Table 7.2 Silver paste dispensing for different speed

50 mm/s	40mm/s	30mm/s
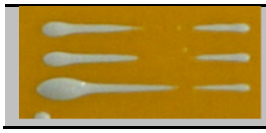	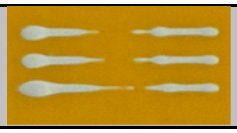	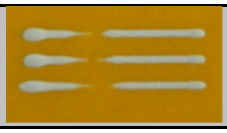

Continuous silver tracks were produced as the trigvalverel setting was moved from 0.25mm to 0.55mm as shown in Table 7.3, indicating the valve rod position was not opened wide enough to produce sufficient flowrate throughout track printing.

Table 7.3 Silver paste dispensing for valve-opening position (Trigvalvrel)

0.25mm	0.55mm
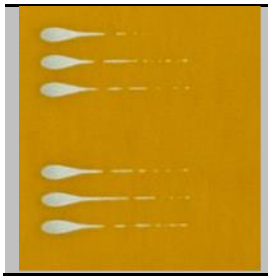	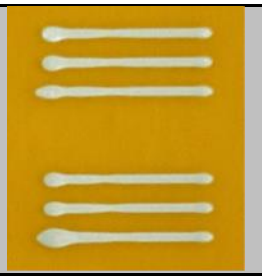

Tracks were then printed with increased dispense pressures from 6psi to 10psi in increments of 1psi. It was observed when increasing the pressure the printed tracks became thicker. When the nozzle pressure feed was between 9psi and 10psi, a splashed start was produced as shown in Table 7.4.

Table 7.4 Silver paste dispensing for different pressure

6 psi	7 psi	8 psi	9 psi	10 psi
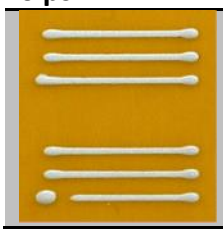	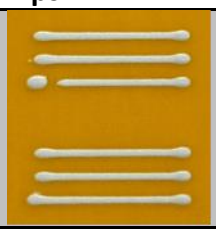	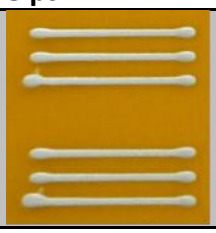	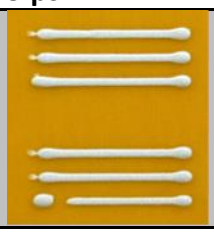	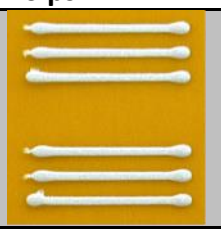

Fourthly, tracks were then printed using different dispensing heights (the stand-off distance between the tip of the nozzle and the substrate). It was experimentally found by reducing the nozzle dispensing height resulted in a clean track line with sharper corners. But if the dispensing height was too low, the material was not optimally extruded due to pressure build-up against the substrate. Furthermore, if the nozzle was too close to the substrate and the substrate thickness varied then the nozzle may touch the substrate causing a defective track and possibly damaging the nozzle. Increasing the dispensing height of the nozzle produced thicker lines, but if the

dispensing height was too great a tailing action was observed and inconsistent tracks may occur as shown in Table 7.5. Moreover, it was found problematic to produce sharp corners.

Table 7.5 Silver paste dispensing for different dispensing heights

0.08mm	0.18mm	0.2mm	0.22mm
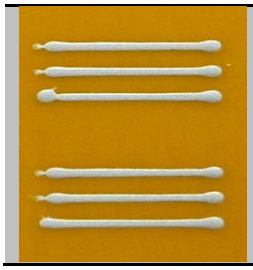	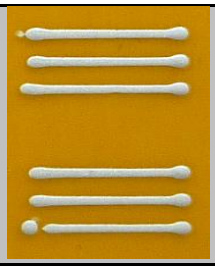	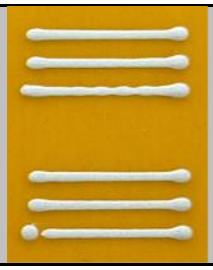	

To conclude, the nScrypt micro dispensing direct write machine with 125µm (ID) nTip nozzle can be used to deposit DuPont 5025 conductive silver paste tracks in a controlled manner. The described empirical approach enabled the initial printing parameters to be found allowing silver tracks to be deposited on a flexible polyimide substrate. However, further optimisation was required to obtain consistent results. Finally the parameters, which control the flowrate for example the trigvalverel (valve opening position) and Trigwait (to delay the deposition) had not been fully optimised at this stage and were used to fine-tune the final print results. In conclusion the above results have led to the operating range of the three critical process parameters, which included the dispensing height, dispensing speed, and material feed pressure. Using the experimental results the above process parameters were assigned with a range of operating values, which were designated as upper, medium and lower values as shown in Table 7.6.

Table 7.6 Upper and lower limit of the optimized MDDW process parameters

Parameters	Upper Level	Medium	Low Level
Dispensing Height (mm)	0.1	0.15	0.2
Dispensing Speed (mm/s)	40	50	60
Material Feed Pressure (psi)	5	6	7

7.3.2 Optimise processing parameters

This part of the experimental optimisation process was carried out using the above operating range of parameters from the previous experimental results in section 7.3.1 (Table 7.6). The aim was to optimise the process inside the determined limits (low to upper) of the most sensitive micro dispensing parameters, which included the dispensing height, dispensing speed, and material feed pressure when utilising a 125µm ID nozzle. These parameters were finally optimised to obtain a consistent track width.

As shown in Table 7.7, a full experimental optimisation design was carried out with a total number of 27 runs, which included the range of values defined as low, medium and upper limit for each process parameter, i.e. dispensing height (0.1mm, 0.15mm, 0.2mm), dispensing speed (40mm/s, 50mm/s, 60mm/s) and material feed pressure (5psi, 6psi, 7psi). The test sample track length was 10mm and was repeated 8 times for each parameter change. As already discussed in detail in section 7.2.4, the extrusion temperature takes a finite time to stabilise and therefore the first two tracks from each parameter run were excluded to ensure the results were produced under the same nozzle temperature condition.

The following MDDW parameters were kept constant throughout the optimisation design experiment:

- Valve open position: 1.74mm
- Valve close position: 1.34mm
- Trigwait: 0.001 second
- Trigvalverel: 0.55mm

Table 7.7 Experimental matrix for parameter optimisation (nozzle ID 125µm)

Dispensing Height (mm)	Dispensing Speed (mm/s)	Material Feed Pressure (Psi)		
		5 (3)	6 (1)	7 (2)
0.15 (1)	40 (3)	133	131	132
0.15 (1)	50 (1)	113	111	112
0.15 (1)	60 (2)	123	121	122
0.10 (3)	40 (3)	333	331	332
0.10 (3)	50 (1)	313	311	312
0.10 (3)	60 (2)	323	321	322
0.20 (2)	40 (3)	233	231	232
0.20 (2)	50 (1)	213	211	212
0.20 (2)	60 (2)	223	221	222

The dispensing sample track layout is shown in Figure 7.8. The track line widths were measured using an optical microscope (Veho® VMS-004, Southampton, UK) and were optically analysed by measuring the track width as the output information to determine the optimisation of the print parameters. The purpose of printing serpentine structures next to the test sample was to observe the sharpness of corners (a necessary requirement in the fabrication of a strain sensor).

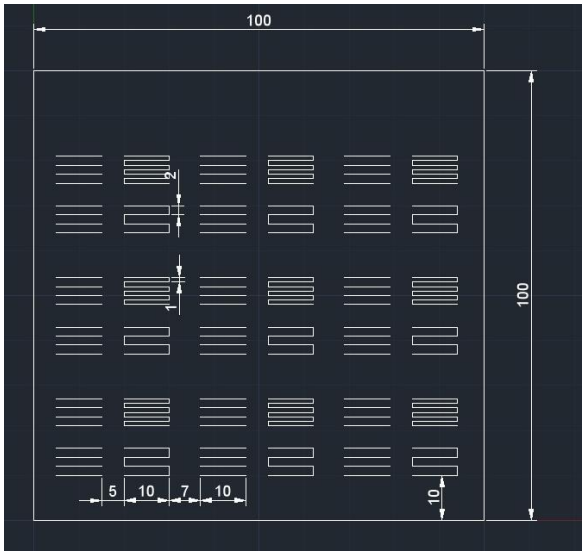

Figure 7.8 Parameter optimisation dispensing pattern

The JMP® statistical software was used to analyse the experimental results. A total number of 162 tracks were produced and the track width measured. The mean track width value was at 525.4µm with standard mean deviation error of 4.9µm. The full track width results are shown in the Appendix-1. Figure 7.9 shows a sample being printed during the process.

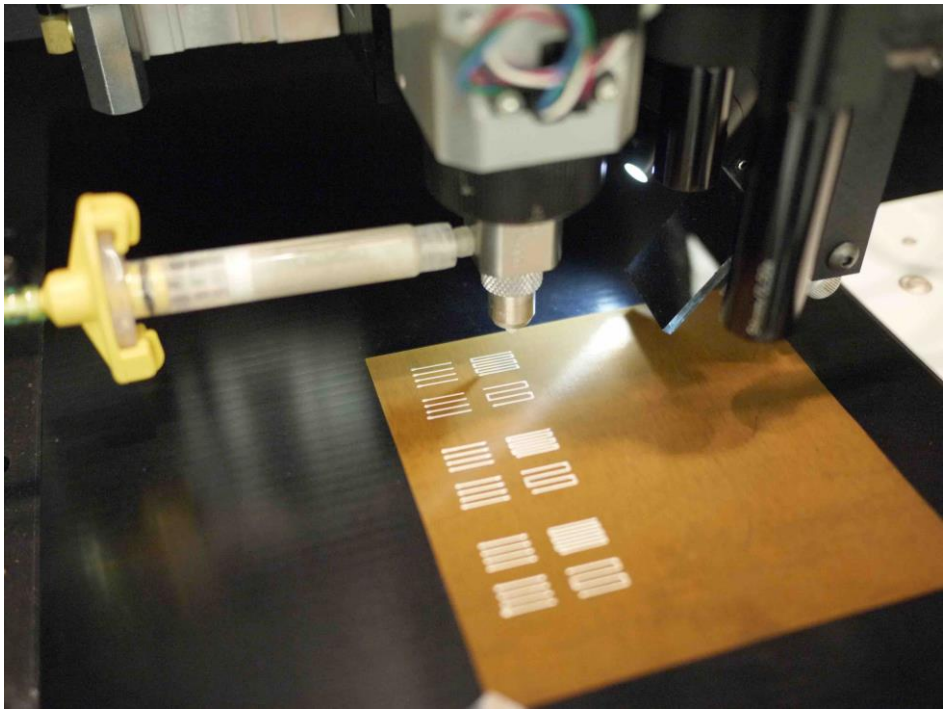

Figure 7.9 Silver paste parameter optimisation printing process

7.3.2.1 *Mean track width versus dispensing height*

Figure 7.10 shows the results of track width versus dispensing height as a function of material feed pressure. The presented error bars give the standard error of track widths measured from the set of processed tracks. At 0.1mm dispensing height, the measured track widths showed a tighter distribution indicating at a dispensing height of 0.1mm the printed silver track width was more consistent. When the applied material feed pressure was increased at a constant dispensing height, wider track widths were measured. For example, the measured track widths ranged between

400µm to 550µm for under 5psi pressure and between 500µm to 600µm for under 7psi pressure. The spread in track width increased with increasing dispensing height.

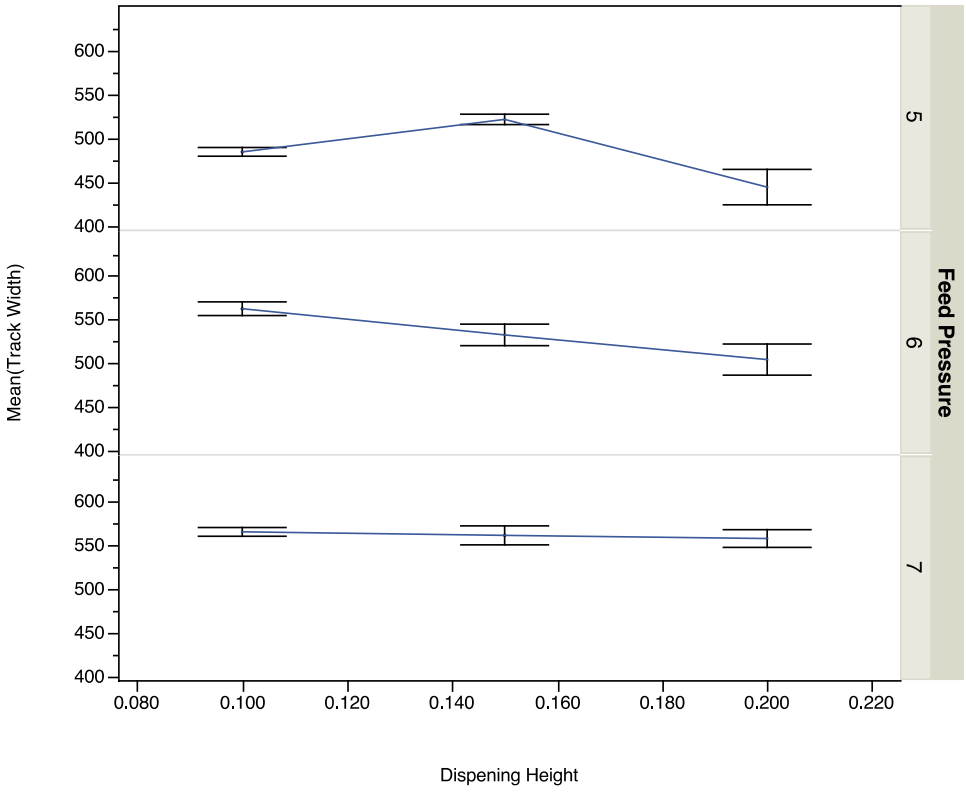

Figure 7.10 Track width vs. dispensing height as a function of feed pressure (nozzle ID 125µm)

7.3.2.2 *Mean track width versus dispensing speed*

Figure 7.11 shows the track width versus dispensing speed as a function of feed pressure. The plotted error bars give the mean standard deviation of the measurement. The figure shows, at a dispensing speed of 50mm/s, the track width distribution becomes tighter for the range of applied material feed pressures from 5psi to 7psi. The higher dispensing speed produces on average thinner tracks and vice versa. However, when the dispensing speed was too high, the repeatability became very poor resulting in thin tracks. Therefore, larger deviation of track widths was measured when dispensing speed was highest, in this case 60mm/s.

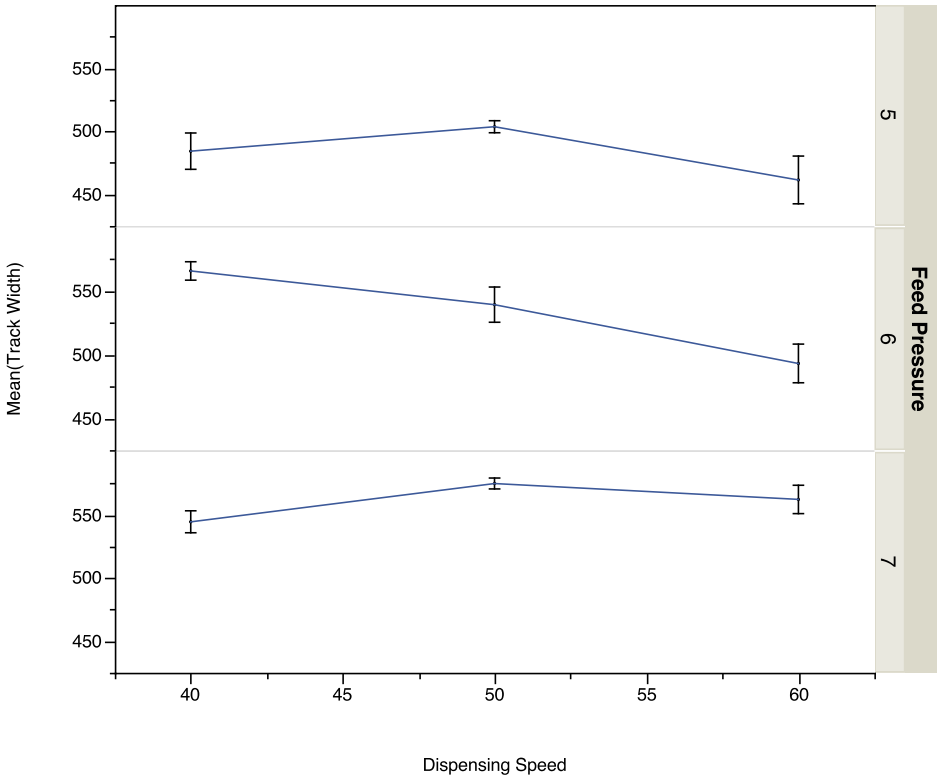

Figure 7.11 Track width vs. dispensing speed as a function of feed pressure (nozzle ID 125µm)

Figure 7.12 and Figure 7.13 are charts showing the variability of the track width from the 27 sets of experimental results. A total of 162 track widths were recorded with 6 repetitions of each set of parameters. It can be observed as material feed pressure, dispensing speed and dispensing height are at their higher limits, the standard deviation of the track widths in general increased.

Six sets of parameters were found from the variability chart resulting in tight standard deviation of the printed track width. The following sets of parameters (Table 7.8) show how the line width varies for each set of process parameters. The standard deviation of the line width was less than 10µm for each process parameter set:

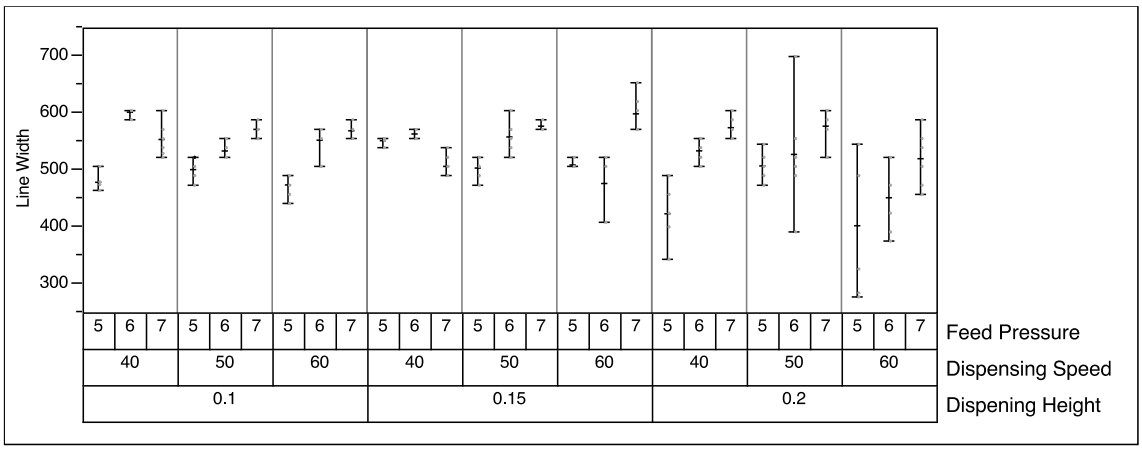

Figure 7.12 Variability chart for silver line width (125µm nozzle)

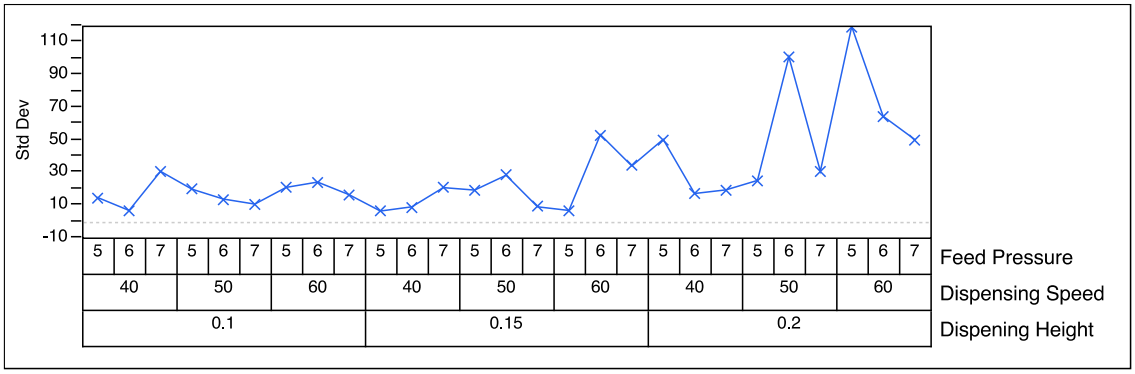

Figure 7.13 Variability chart for silver track line width- displayed as standard deviation, as a function of the three main process parameters

Table 7.8 Optimised parameter sets

	Set #1	Set #2	Set #3	Set #4	Set #5	Set #6
Dispensing height (mm)	0.1	0.1	0.15	0.15	0.15	0.15
Dispensing Speed (mm/s)	40	50	40	40	50	60
Material Feed Pressure (psi)	6	7	5	6	7	5
Mean Line Width (µm)	601.3	571.2	551.3	563	576.7	508.7
Standard Deviation (µm)	6.5	10.4	6.2	8.7	8.8	6.5

To obtain reproducible micro-extrusion using the nScrypt, it is important to choose the correct set of process parameters. Among the three main process parameters, dispensing height was found to be the most critical parameter. Dispensing speed and material feed pressure appeared to be dependent on each other. Hence, both parameters were able be to control the flowrate, e.g., increasing dispensing speed will invariably increase the material feed pressure and vice versa. However, if dispensing height was greater than 0.2mm, no combination of pressure and dispensing speed will give reproducible and reliable results.

The chosen parameters were then set for fabrication trials of the resistive strain gauge sensor on a polyimide substrate as shown below:

- Valve open position: 1.74mm
- Valve close position: 1.34mm
- Trigwait: 0.001 second
- Trigvalverel: 0.55mm
- Dispensing height: 0.10mm
- Dispensing speed: 40mm/s
- Material feed pressure: 6psi

It should be noted the nScrypt machine was placed in an open environment with no air filtration or ambient temperature control. Therefore dust and airborne particles may become trapped in the tip of the nozzle affecting printing and could result in non-uniform pattern deposition. Changes in the ambient temperature will result in the MDDW process parameters being modified, which again may alter the quality of the printed track. However, the work was carried out under similar room ambient temperatures, which ranged between 24 to 25˚C.

7.4 Silver paste curing condition trial

The silver paste curing conditions include curing temperature and the time required for the MDDW printed silver paste to obtain the required electrical and mechanical properties. The aim of this trial was to find the optimised conditions for curing the deposited tracks by measuring the electrical resistance using four-point probe technique (Figure 7.14), see section 6.3.3. The trial was conducted with the premise that a higher curing temperature will require less curing time and the measured resistance should be stable after curing.

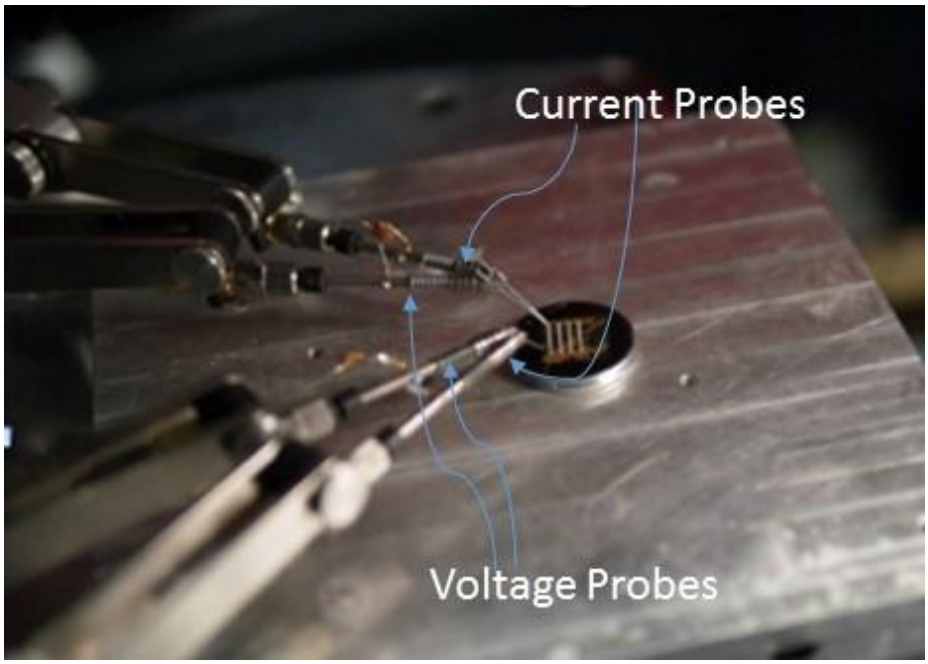

Figure 7.14 Four-point probe resistance measurement

Silver tracks of 10mm length were printed on polyimide substrates of 76µm thickness using the nScrypt micro dispensing system set to the optimised process parameters (Table 7.9). The printed patterned tracks on the substrates were then cured at a temperature of 100, 110, 120 and 130˚C in a box oven, and over different periods of time, 3, 5, 7 minutes respectively.

Table 7.9 Silver paste curing condition trails (100 - 130˚C)

Sample	Curing Temperature (˚C)	Curing Time (min)
1	100	3
2	100	5
3	100	7
4	110	3
5	110	5
6	110	7
7	120	3
8	120	5
9	120	7
10	130	3
11	130	5
12	130	7

For a curing temperature of approximately 110˚C (Figure 7.15), it was found that the measured electrical resistance decreased when the curing time was increased from 5min to 7min, indicating that the silver paste curing was incomplete. When the curing temperature was reduced to 100˚C (Figure 7.15), it was found that the resistance increased when the curing time was increased from 5min to 7min. This result may be due to the amorphous structure of uncured silver within the track, resulting in a higher resistance. For these reasons the curing temperature was increased to 120˚C (Figure 7.15) and it was found that the resistance linearly decreased with curing time. Further samples were also cured at 130˚C (Figure 7.15) and it was found that the tracks showed a wrinkled appearance, which was thought to be due to differences in linear expansion between the deposited paste and the polyimide substrate.

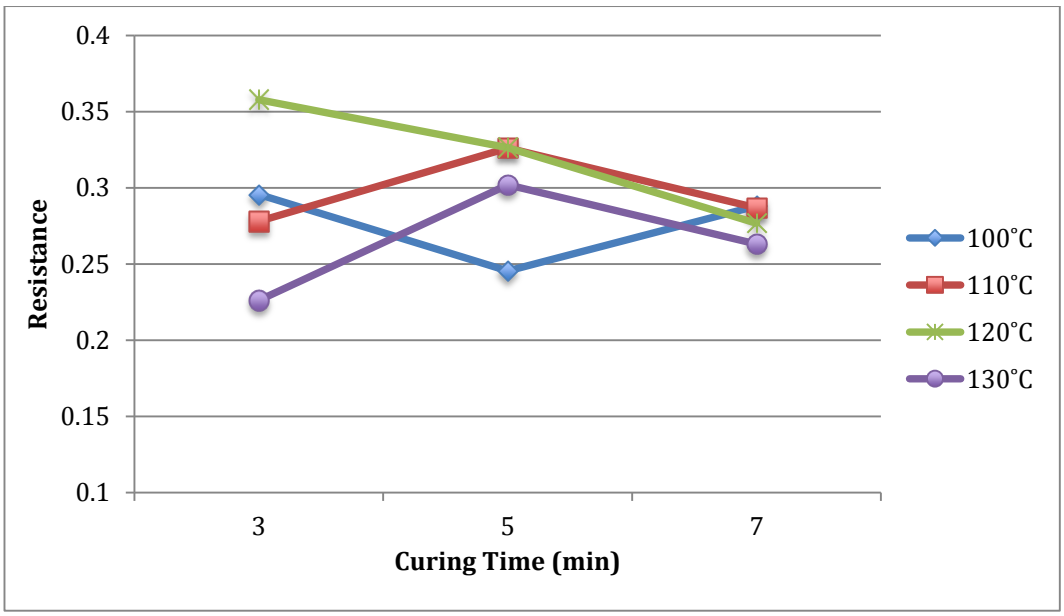

Figure 7.15 DW silver paste of 10mm length curing trial

The curing experiments were repeated using deposited silver tracks of 10mm length printed on 76µm thick polyimide substrates, which were cured at 120˚C in a box oven over time periods from 5min to 40min. The temperature of 120˚C was chosen as it gave the most consistent behaviour with increasing curing time from Trial 1.

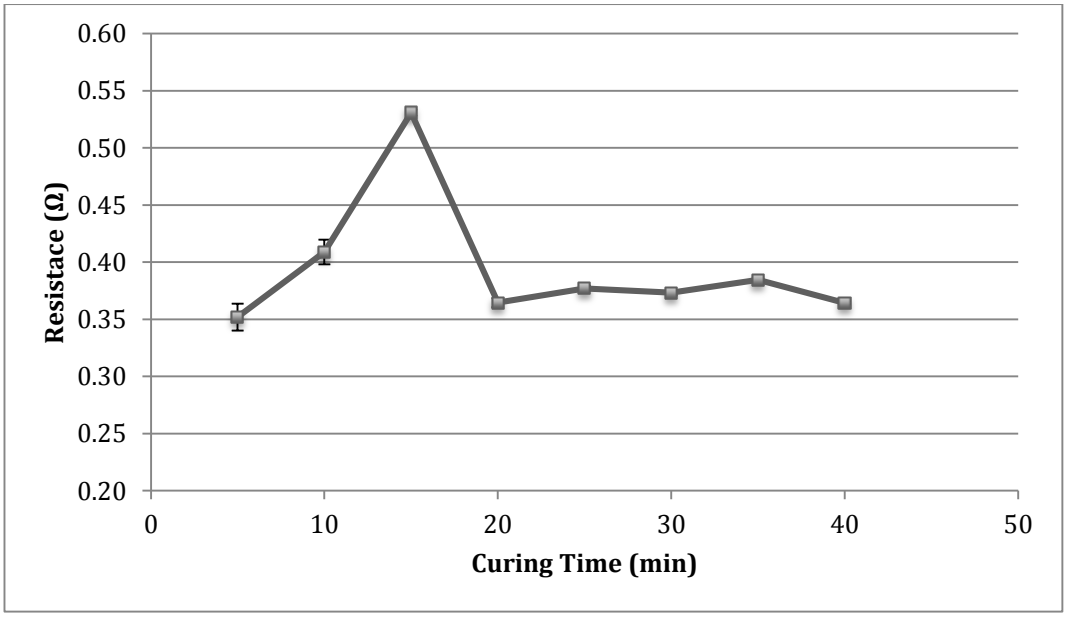

Figure 7.16 Silver track measured resistance vs. curing time at 120˚C

Figure 7.16 shows the results of measured track resistance versus curing time at a curing temperature of 120˚C. The error bar was the standard deviation from the measurement of 3 samples. Note an increase in resistance was observed for a curing time of 5min to 15min opposite to the results from the first curing experiment. The reason for the observed resistance change was thought to be due to silver particle movement in the uncured structure, which resulted in a larger increase in the track resistance when the curing time was less than 15min. It was observed for a curing time greater than 20 minutes, the standard deviation in the resistance was reduced and the measured resistance change was less than 10%, indicating sufficient curing was obtained, resulting in a stable resistance with time.

7.5 Silver resistive strain gauge fabrication

Following the optimisation of the MDDW process for printing silver conducting paste, the process was used to fabricate resistive strain gauges on a 76µm thick polyimide substrate. The strain gauge followed conventional strain gauge design with a serpentine pattern as shown in Figure 7.17. The gauge length was 8mm with 14 grid lines covering sensing area of 8mm x 8mm. The solder tabs (3mmx3mm) were considered as insensitive to strain due to their large cross-sectional area.

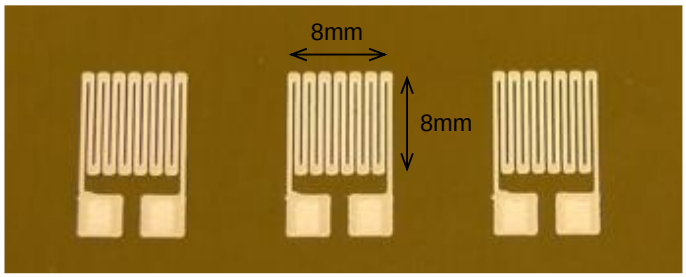

Figure 7.17 MDDW silver thin resistive resistance strain gauge samples

The consistency of the MDDW silver track geometry and cross-sectional profile was investigated using the profilometer (Surftest SJ-400, Mitutoyo, Kanagawa, Japan), which could travel to a maximum distance of 4mm covering 6 tracks of the strain gauge. The measurements indicated a good consistency of the tracks with approximate

track width of 250µm and height of 20µm. Figure 7.18 shows the resulting profile across 6 of the tracks inside the strain gauge.

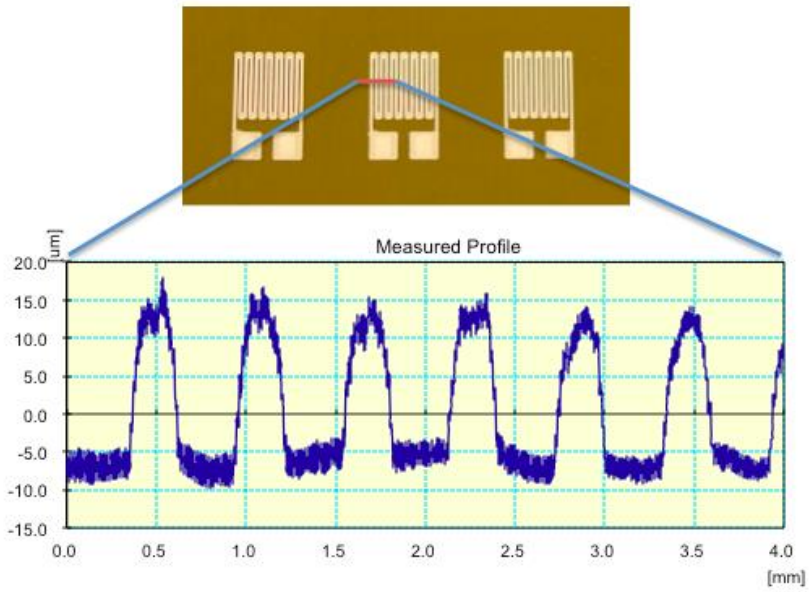

Figure 7.18 Silver tracks cross-sectional profiles

7.5.1 Silver strain gauge sensitivity measurement

7.5.1.1 *Strain gauge mounting procedure on test-plate*

The gauge factor, therefore the sensitivity of the resistive sensor gauge, was measured using mechanical bending. The resistive strain gauge was mounted on metal test-plate in order to apply the strain. The methods of mounting the strain gauge used a standard procedure summarised in the following steps [118]:

Surface preparation

1. Isopropanol alcohol was used to remove the grease from the test surface.
2. Emery cloth was used to abrase the site where the strain gauge was to be attached to remove dirt and dust particles.
3. A cotton-tip was used to apply metal conditioner in order to scrub the test-plate surface.

4. A new cotton-tip was used to apply neutraliser to scrub the surface. This was repeated several times to ensure the surface was neutralised.
5. The gauge position was marked on the surface of the test-plate using a ballpoint pen without damaging the surface.

Install strain gauge

1. The strain gauge was placed on the clean surface of the test-plate and aligning to desired orientation.
2. Using a piece of cello tape placed over the strain gauge and making sure the gauge was firmly attached to the cello tape.
3. Lift one end of the tape till the gauge was clear of the test-plate and apply one to two drops of adhesives (Loctite 496) on the test-plate at the boundary line of the strain gauge.
4. Apply thumb pressure across the strain gauge towards the free end to spread the adhesives over the test-plate under the gauge.
5. Allow 15 minutes for the adhesive to set securing the strain gauge to the surface of the test-plate and carefully remove the cello tape. The strain gauge is then ready for measurement of its gauge factor.

7.5.1.2 *Three-point bending measurement*

After the silver conducting paste had been cured the structures were electrically characterised using a 4-point probe current-voltage (I-V) electrical measurement technique. The three point bending rig was used to measure the change in resistance of the test strain gauge when a load was applied. The strain gauge sample with a sensing area of 8x8mm^2 was mounted on the centre of a carbon steel metal beam with dimension of 2.5cm x 0.4cm x 122cm. Mechanical bending was applied with interlock load weights of 1kg that were added to the 0.1kg hooked plate at the centre of the beam the strain gauge. A maximum load of 4kg was added in 1kg increments. The resistance was measured using 4-point probe measurement after each load was applied.

The strain on the strain gauge site was unknown with the experimental setup. Therefore, a calibrated commercial strain gauge was mounted next to test strain gauge, and enabled the gauge factor of the test strain gauge to be found. A total load of 4kg could be used to load the test-plate and is shown in Figure 7.19.

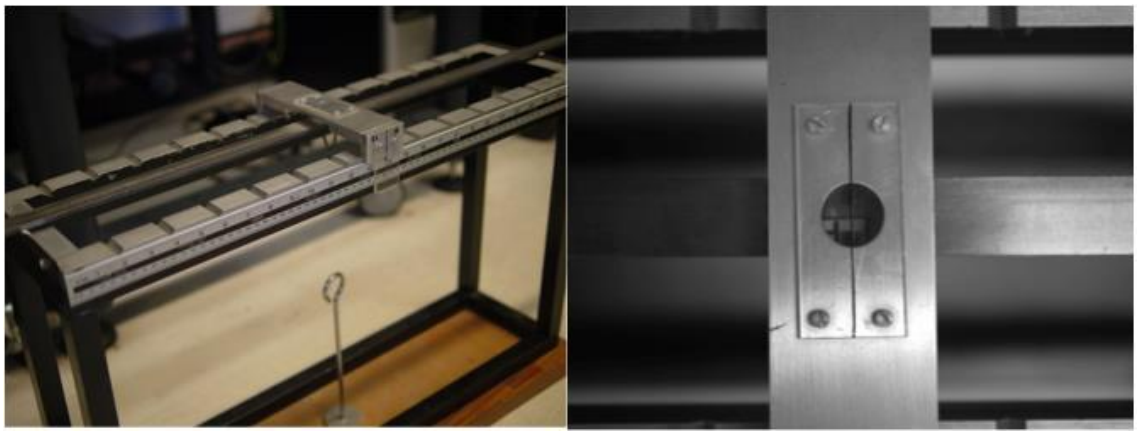

Figure 7.19 Mechanical test of silver strain gauge using three-point measurement

Figure 7.20 shows the measured change in resistance of the silver strain gauge with 8mm gauge length with an increasing applied load. A reduction in resistance was expected as the applied load produced a compressive strain applied to the strain gauge. When a linear trend line was fitted to the experimental results, the R^2 gave an indication of the fit to linear regression and was found to be only 68.6%, which was poor.

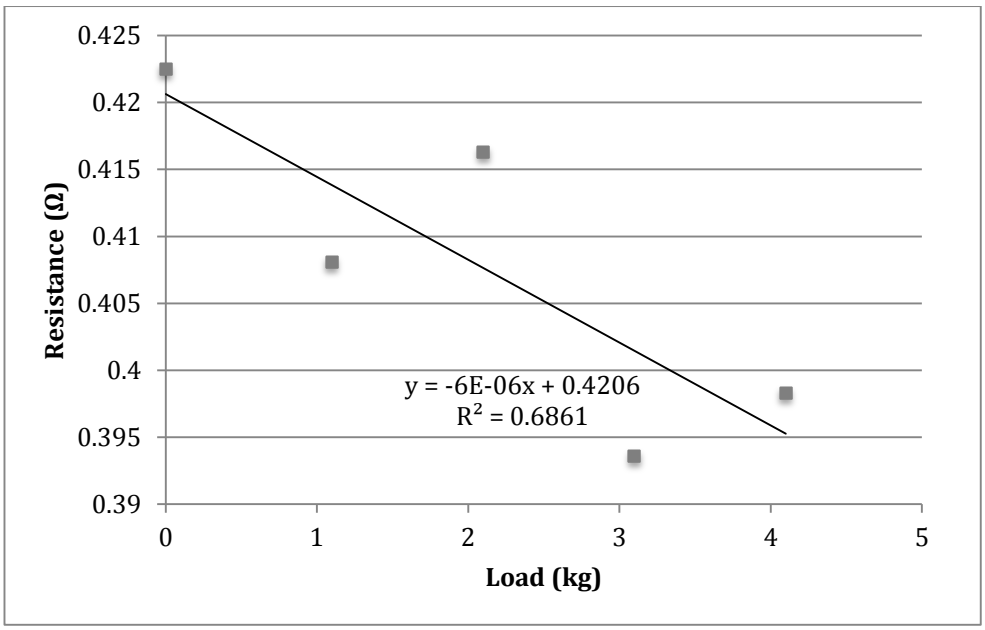

Figure 7.20 MDDW silver resistive strain gauge resistance vs load (8mm gauge length)

Further experimental investigation was made by doubling the gauge length (16mm) of the silver strain gauges to increase the sensing area. Figure 7.21 shows the experimental change in resistance of the strain gauge when a similar load as before was applied. The results were found to give even lower linearity with R^2 of 47.7%. Therefore, increasing sensing area did not improve the linearity of the gauge.

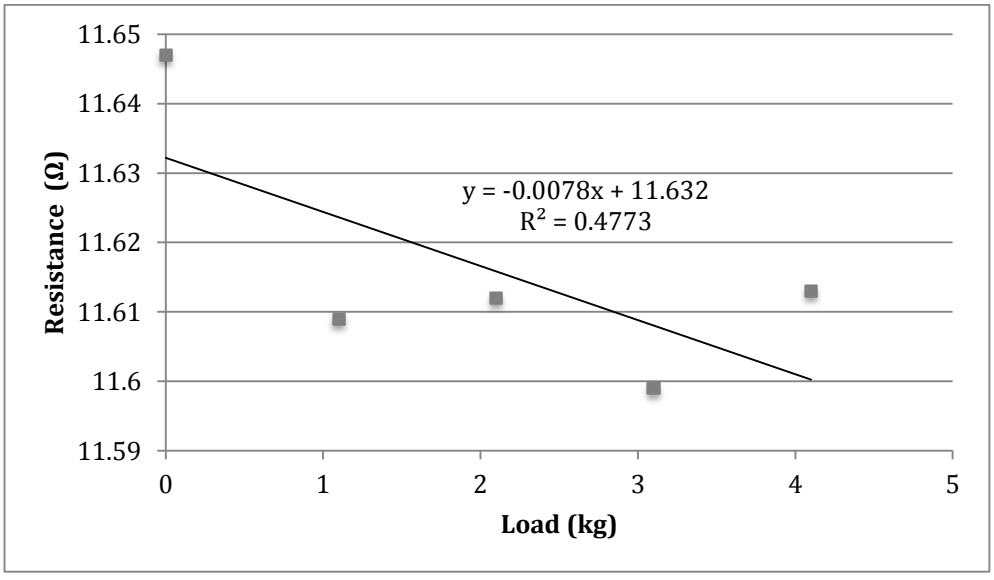

Figure 7.21 MDDW silver resistive strain gauge resistance vs load (16mm gauge length)

It was found when using the four-point probe to measure the strain resistance change; the measurement was highly sensitive to any mechanical movement. For example, applying the load weights to the metal beam, a slight movement would cause fluctuation in the resistance measurement.

To further investigate the cause of the poor linearity between the change in resistance and applied load, a number of experiments were carried out including measurement of the resistivity of the track material, consistency of the track geometry and chemical composition of the silver track using energy-dispersive spectroscopy (EDX) to analyse the elemental chemical composition of the silver strain gauge.

7.5.2 Resistivity of MDDW silver track

The trial was performed to determine the resistivity of MDDW silver tracks and compare with the resistivity of bulk silver. Tracks with lengths of 1cm to 5cm in 1cm incremental steps were printed on a 76µm thick polyimide substrate. After printing, the silver tracks were cured for 20min at 120˚C in a box oven. The resistance of each track was measured using 25µm tip four-point-probe resistance measurement system as described in section 6.8.6.

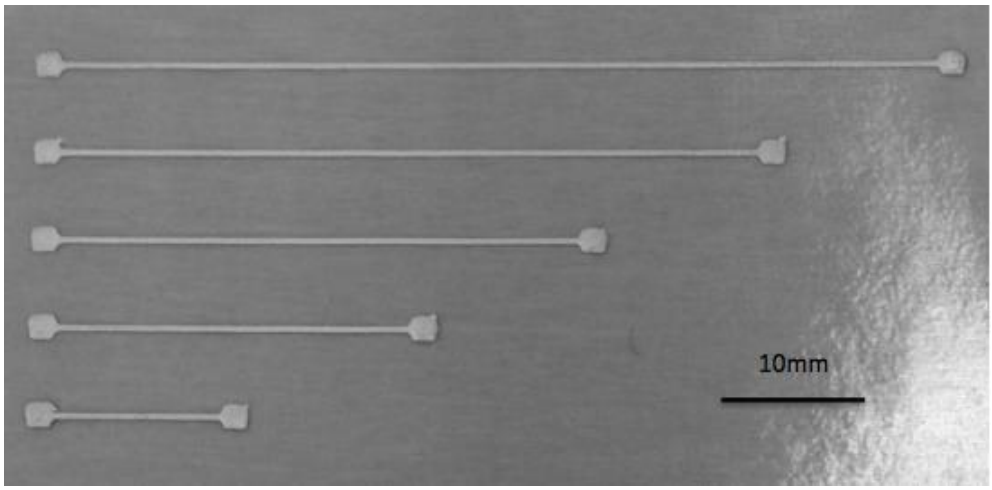

Figure 7.22 DWWM silver track lengths of 10mm to 50mm for resistivity measurements

Figure 7.22 shows one set MDDW silver track sample with track length from 10mm to 50mm for resistivity measurement. Total of 3 sets of samples were fabricated and measured. The cross-sectional profile of the metallised track was measured using a surface profilometer (Mitutoyo Surftest SJ-400, Kanagawa, Japan). The method was described in detail in section 6.3.3. A random track was chosen from the 3 sets of samples and the profile was measured at three locations along the track. The three measurements were overlaid as shown in Figure 7.23. The track width and height from the three locations had almost identical cross-sectional profile, track width and height. It was representative of the track profiles from the 3 sets of samples from this set of printing batch.

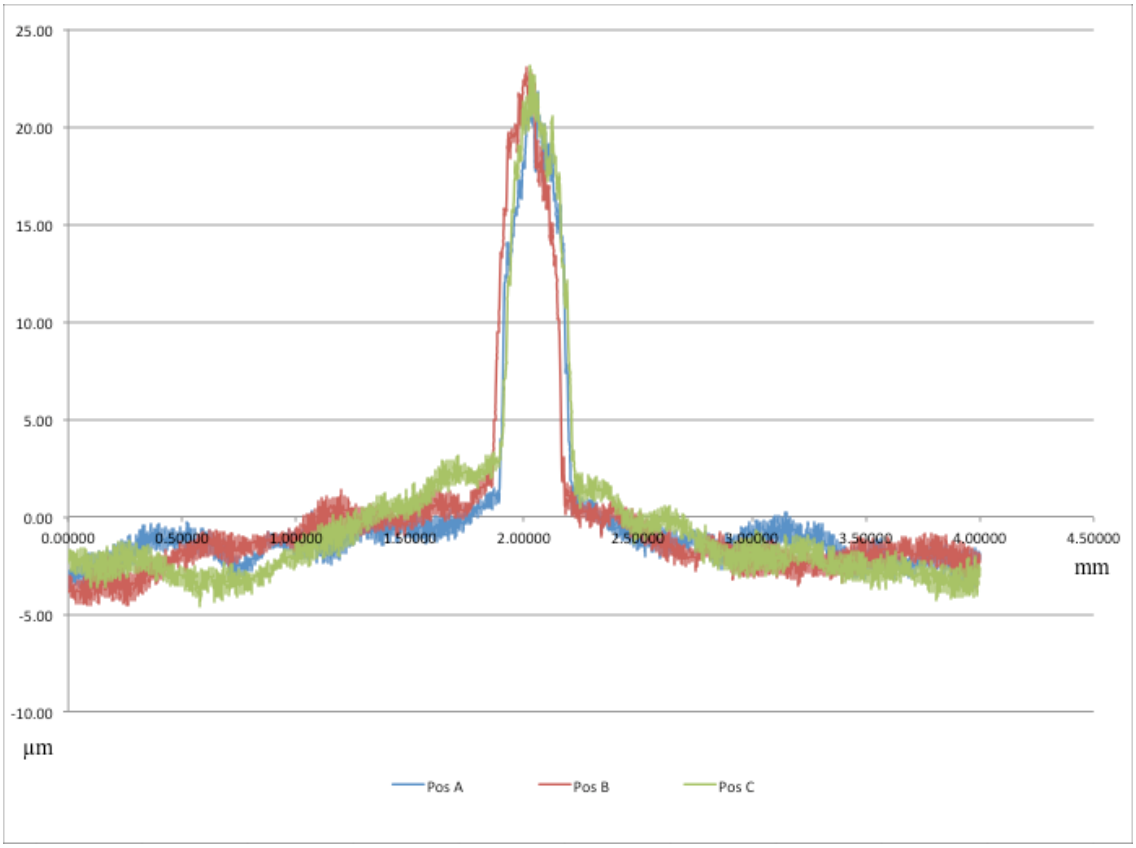

Figure 7.23 Cross-sectional profile of silver tracks

Figure 7.24 shows the measured plotted resistance versus MDDW silver track length. The resistance is proportional to the track length. The error bar indicated the mean standard deviation from three sets of samples. A slightly higher mean standard deviation was found for the longer track lengths, which may be a result of the substrate not being flat. However, the results on the whole indicated a good consistency of the track geometry across all samples.

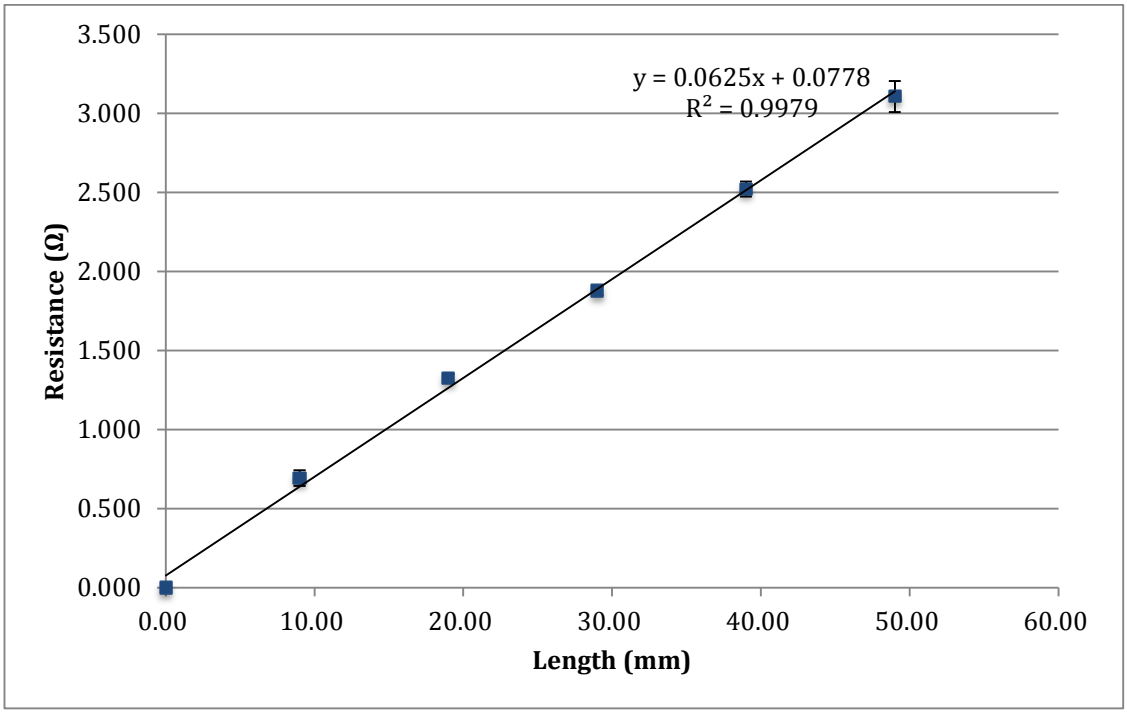

Figure 7.24 MDDW silver track resistance vs. track length

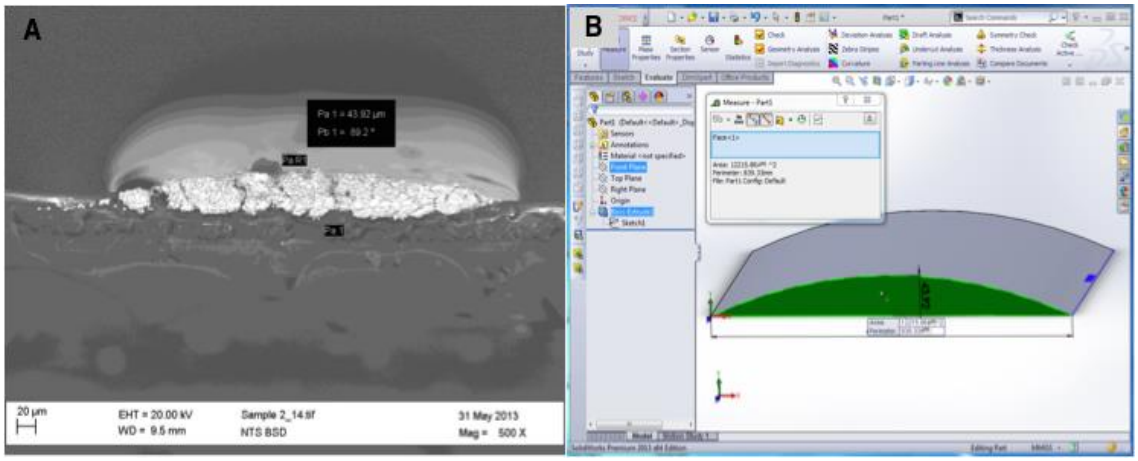

Figure 7.25 (a) SEM height measured the of cross-sectional area and voids observed (b) CAD software calculation

The silver track width and height was also measured using scan electron microscope (SEM). A computer aided design (CAD) software package, Solidworks®, was used to draw a cross-sectional area according to track width and height measured from the SEM images and the area was calculated using the measure function. An assumption was made, that the contact between the silver track and polyimide substrate was flat. The cross-sectional area was found to be 0.0122mm^2, see Figure 7.25. The resistivity (ρ) of MDDW silver tracks can be expressed using the following equation (section 4.2):

$$\rho = R\frac{A}{L} \quad (1)$$

Where ρ (Ω-m) is the electrical resistivity, R is the electrical resistance of the material measured in ohms. A is the cross-sectional area (m^2) of the track and L is the length (m) of the track. The resistivity of silver tracks was calculated to be **7.6x10^{-7}Ωm** using (2), which was approximately a factor of 2 greater when compared to the resistivity of bulk silver 1.6x10^{-8}Ωm [82]. The higher resistivity of the printed silver track is thought to be due to voids seen in microstructure of the cross-sectional area during SEM analysis and shown in Figure 7.25a.

As the silver strain gauges did not provide a linear relationship between the measured resistance and the applied load further analysis was carried out on the strain gauge to determine if there had been any chemical changes within the conducting paste. Energy-dispersive X-ray spectroscopy (EDX) was carried out to check the strain gauge chemical composition. 10 measurement points were taken from a random track of MDDW silver strain gauge sensor fabricated from the same batch of the sensors used in the resistance load measurements (section 7.5.1).

Table 7.10 shows the elemental composition of 10 measurements from a single track of a silver strain gauge used in the mechanical bending measurement (section 7.6.1). The EDX measurements gave an average of 70% silver in the strain gauges from 10 separate points along the track indicating significant impurity/granula structure of the material in the MDDW silver tracks. This was in-line with the measured higher resistivity, which was a factor of 2 greater when compared to bulk silver. The high percentage of carbon

and oxygen may be the residue from the organic solvent after curing the silver paste. A trace amount of magnesium was also found. In other studies, magnesium was added to silver-based conductor paste to prevent silver electromigration [119] [120] and can affect the overall resistance properties of the silver paste, since resistivity of magnesium (4.39 x10-8 Ω·m) is approximately 3 times greater than the silver material (1.59 x10-8 Ω·m). However, the percentage of magnesium was very small.

Table 7.10 EDX measurement results from silver strain gauge (weight%)

Spectrum	In stats.	C	O	Mg	Ag	Total
Line 2(1)	Yes	21.84	9.19	0.27	68.70	100.00
Line 2(2)	Yes	20.21	7.98	0.24	71.57	100.00
Line 2(3)	Yes	20.02	10.58	0.27	69.12	100.00
Line 2(4)	Yes	29.41	14.19	0	56.40	100.00
Line 2(5)	Yes	28.25	11.99	0.22	59.55	100.00
Line 2(6)	Yes	9.61	2.92	0.31	87.16	100.00
Line 2(7)	Yes	13.82	5.98	0.24	79.95	100.00
Line 2(8)	Yes	30.77	14.90	0	54.33	100.00
Line 2(9)	Yes	13.18	4.32	0.38	82.13	100.00
Line 2(10)	Yes	21.24	7.62	0	71.14	100.00

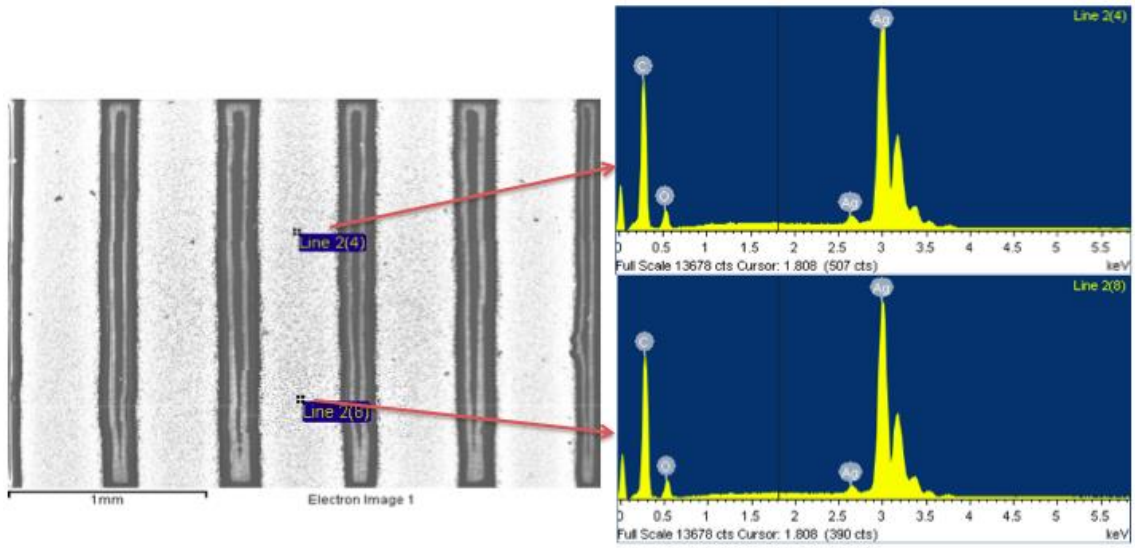

Figure 7.26 EDX measurement of the silver strain gauge sample taken location at one of the 10 locations

7.6 Discussion

The feasibility of fabrication of silver strain gauge using MDDW nScrypt system was investigated using 125µm ID nozzle. Two separate processes in the nScrypt system give rise to an increase in temperature of the process chamber. This rise in temperature will influence the printing process. These increases in temperature were investigated. Firstly, the process build chamber of the nScrypt machine is not temperature controlled and a temperature rise caused by the motion of the controller was measured. To minimise the effect of the temperature rise, the machine was turned on to stabilise the operating temperature before conducting the print job.

The second temperature increase was due to the high solid content of conductive paste. As the material was forced through the nozzle a material temperature rise was also observed because of friction between the extruded solid particles and the nozzle. The temperature rise will influence the print quality since the viscosity of the conductive paste is highly sensitive to temperature. To overcome this problem, a pre-extrusion process was included to minimise the impact particularly if the print job was stopped for any period of time.

After optimisation of the dispensing parameters, commercially available DuPont silver 5025 conductive paste was successfully extruded in a reproducible manner using a 125µm ID nTip ceramic nozzle. The author believes that this is the first time an nScrypt machine has been used to print silver strain gauges using commercially available paste. Silver strain gauges with gauge length of 8mm and 16mm were fabricated and a mechanical strain tests were performed using a three-point bending method for investigation of the gauge sensitivity. However, the results indicated the sensitivity of MDDW silver strain gauges was low and a non-linear relationship was observed between the resistance and the load applied. The measured resistivity of the MDDW silver tracks printed on the flexible polyimide substrate was found to be at $7.6 \times 10^{-7} \Omega m$, which was greater than bulk silver by factor of 2. Measurements carried out using EDX showed that the content of the dispensed track was only by average 70% of the total

weight. This is thought to be the reason for the measured higher resistivity when compared to bulk silver.

In order to increase the sensitivity of MDDW silver strain gauges, a higher nominal resistance is required which will lead to a larger change in strain gauge resistance (ΔR) with an applied load, thereby increasing its sensitivity [111]. The Initial idea of increasing the gauge length and therefore the gauge sensing area was not pursued, as this did not improve in the gauge sensitivity. Also, it would have led to substantially increase in the footprint of the strain gauge going against one of research objectives.

From the literature review section 5.5.1, work described by Gutierrez et al [97][98] and Huang et al [103] indicated that the sensitivity of the strain gauge could be increased by reducing the track width. This could be achieved by depositing thinner tracks using a smaller nozzle (e.g. 50µm ID nozzle). However, the silver paste could not be extruded reproducibly due the size of silver particles as tried in practice. Therefore, further work on the DuPont silver paste was curtailed and work moved on to carbon-based material, which has a much higher resistivity. Also, work described in the literature review indicated that using carbon nanotubes, high gauge sensitivity could be obtained (high gauge factor) but the described process was complicated. The approach here will be to use the simpler nScrypt direct write system with a low electrical conductivity commercial carbon paste, to find if small foot print resistive strain gauge can be fabricated and with a high gauge factor.

Chapter 8. Direct Write Carbon Resistive Strain Gauges

8.1 Introduction

This chapter describes the micro dispensing direct write (MDDW) fabrication of carbon resistive strain gauges using the nScrypt machine. An alternative higher resistance carbon paste was investigated to increase the resistance and sensitivity of the sensing layer of the MDDW deposited resistive strain gauge.

DuPont 7082 carbon paste was selected to be in-line with the very recent work of using carbon nanotubes in the fabrication of resistive strain gauges [64][98]. The processing parameters were optimised for the nScrypt machine using 125µm ID nozzle to deposit carbon paste as well as the paste curing conditions.

The carbon resistive strain gauges with 10mm gauge length were fabricated and this work paved the way to the fabrication of miniaturised carbon resistive strain gauges using 50µm ID nozzle in the nScrypt machine. Cantilever-bending measurements were carried out to investigate the sensitivity of the fabricated gauges.

8.2 Carbon resistive strain gauge fabrication - 125µm ID nozzle

8.2.1 Optimise Processing parameters

The carbon conductive paste (DuPont 7082) has the viscosity range from 210 to 260Pa.s and so is more viscous than silver paste (DuPont 5025) used in chapter 7. From the findings of the optimisation of the processing parameters carried out for the silver paste (section 7.3), the dispensing height was found to be 0.1mm for consistency of track width when using the 125µm ID nozzle. This height was adopted as the starting point for the carbon paste. It was also found earlier using the silver paste that the dispensing speed and material feed pressure can be used to compensate each other.

For the above reasons, a dispensing height (0.1mm) and dispensing speed (40mm/s) were adopted as a starting point to find the optimised feed pressure. The test pattern used was a 7-turn strain gauge of length 10mm, the gap between each grid line was 0.5mm. The material feed pressure was changed from 8psi to 15psi in 1psi incremental steps.

Figure 8.1 shows the micrograph of carbon paste patterns with material feed pressure of 8psi, 10psi, 12psi and 14psi. The test samples where the feed pressure was below 12psi, the tracks of the samples were inconsistent as discontinuous deposition can be observed. Increasing the feed pressure to 12psi a consistent track width was observed. When increasing the feed pressure to 14psi, the track width increased but remained continuous and the end loops (see Figure 8.1) of the strain gauge were less well defined. Therefore, the processing parameters for fabricating micro-dispensing carbon paste strain gauges were selected as follows:

- Dispensing height: **0.10mm**
- Dispensing speed: **40mm/s**
- Material feed pressure: **12psi**

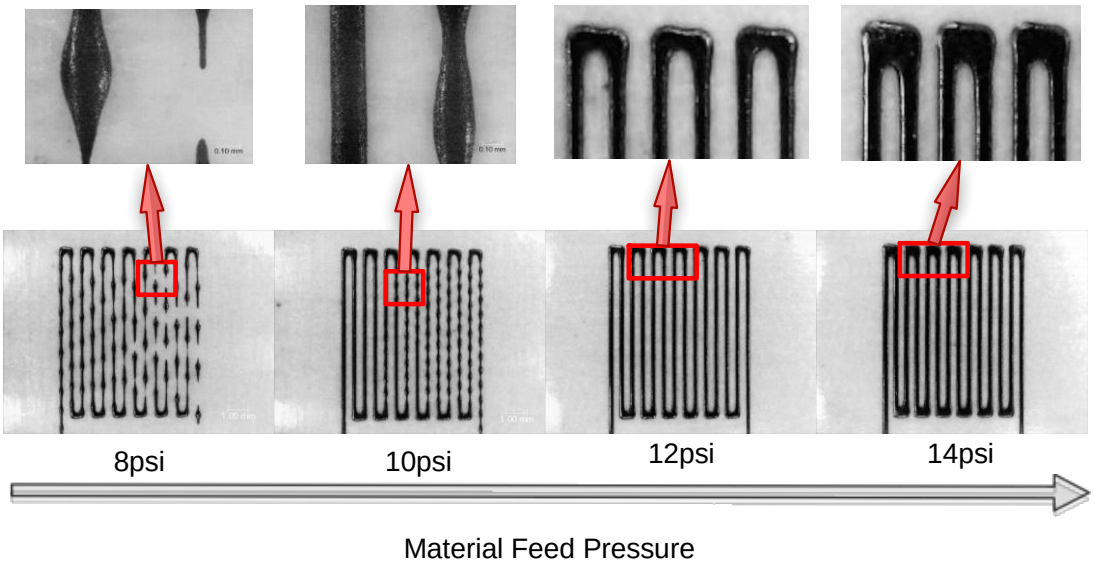

Figure 8.1 Carbon Pressure parameter optimisation

8.2.2 Curing condition trial for MDDW carbon paste

The curing condition for the carbon paste when using it in the screen-printing process, was 120˚C in a box oven for 10 minutes according to manufacturer's data sheet. From the previous experiments on curing silver paste (section 7.4), the curing condition was found to vary due to the adopted fabrication method. The following trial was aimed to find the curing condition for carbon track produced using nScrypt MDDW fabrication process.

Three-turn carbon resistive strain gauges with a gauge length of 10mm were deposited on a 76µm thick polyimide substrate. The optimised process parameters were used as described in section 8.2.1. The experiments to optimise the curing conditions were carried out with curing times ranging from 5min to 40min. Table 8.1 shows the experimental matrix; five samples were cured under each set of curing conditions.

Table 8.1 Carbon curing condition trial

Curing time (min)	Temperature (˚C)	Number of samples
5	120	5
10	120	5
15	120	5
20	120	5
25	120	5
30	120	5
35	120	5
40	120	5

As described in Chapter 6, when the paste is cured sufficiently, there is less than 10% expected change in resistance of the track [112]. Figure 8.2 shows the average resistance measured at curing times from 5min to 40min in 5min increments at a temperature of 120˚C. The resistance reduced and remained essentially constant after 15min of curing. The resistance change between curing time of 15min and 40min was

calculated to be approximately 8.9%. Therefore, the micro-dispensed carbon strain gauge patterns were considered to be fully cured using the following process conditions of 120˚C for 15min. Although there was a further small decrease in resistance observed after 30 minutes curing, the cured structures were considered sufficiently stable. It should be noted that less than 10% change in nominal resistance is negligible for strain gauge applications since the change in resistance under strain is far more important than nominal resistance of the gauge.

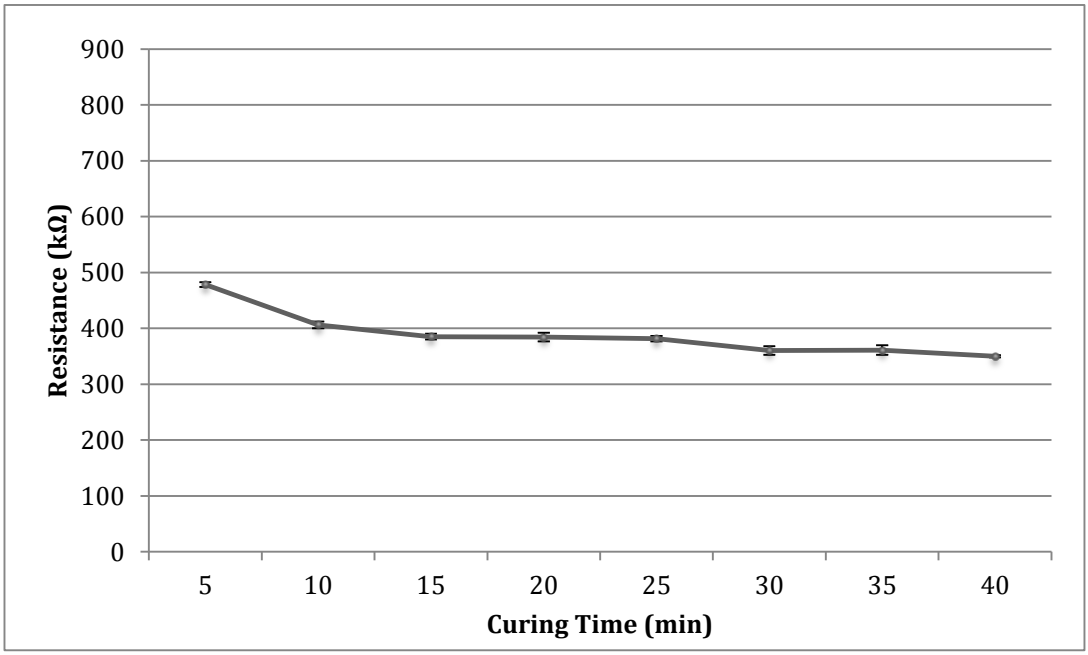

Figure 8.2 Carbon paste curing condition trail at 120˚C for 5min to 40min

8.2.3 Carbon resistive strain gauge sample fabrication

The carbon strain gauge was fabricated using carbon paste extruded from a 125µm ID nozzle with nScrypt micro dispensing system on to a 76µm thick polyimide substrate. Before deposition of the carbon paste the polyimide substrate was wiped with isopropanol to remove grease from the surface. The dispensed gauge patterns were cured at 120˚C for 15min. The carbon strain gauge dimensions were designed to match the gauge length of 10mm of the reference commercial metal gauge used for the calibration of the mechanical test to obtain the gauge factor. Further, carbon based

strain gauges with 2 to 5 number of turns were also fabricated for investigation. Carbon strain gauges were fabricated using the optimised process parameters as given in section 8.2.1. The average track width of the fabricated carbon based strain gauge was measured as 224.5±8.4µm.

Figure 8.3 (A) shows the carbon strain gauge samples using MDDW dispensed with the 125µm ID nozzle. The carbon strain gauge patterns had 2 to 5 turns in increment of one turn and a gauge length of 10mm and were all fabricated on a single polyimide substrate. The gap between the sensing grids was 0.5mm. The polyimide backing was then cut to form individual strain gauge samples all of size approximately 8mmx18mm. A comparison between the fabricated carbon strain gauge with a commercial metal foil gauge of the same gauge length (10mm) is shown in Figure 8.3 (B).

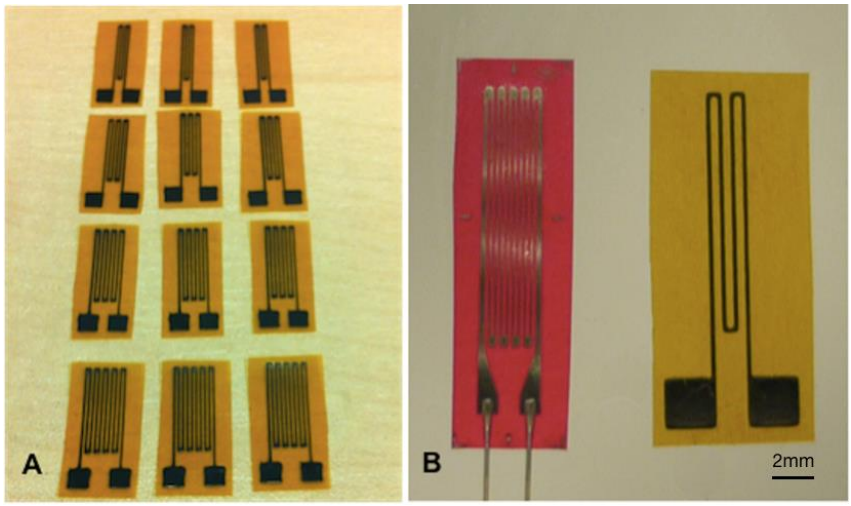

Figure 8.3 (A) MDDW carbon strain gauge samples (B) Comparison with commercial metal foil strain gauge (TML FLA-10-11)

The electrical resistance of all the fabricated carbon strain gauges was measured using Fluke 289 multimeter and the average resistance is shown in Table 8.2. The standard deviation was calculated from the measurement of 5 samples of each type of strain gauge. It was interesting to note that higher values of standard deviation were obtained for strain gauges with larger number of turns and was put down to the larger

footprint of the dispensed strain gauge pattern. The gauge factor measurement of the MDDW carbon strain gauge samples will be described in detail in section 8.2.5.

Table 8.2 The total electrical resistance of fabricated MDDW carbon strain gauges

No of Turns	Average electrical resistance (kΩ)	% Error (kΩ)
2	229.9±2.2	0.9
3	343.3±5.3	1.5
4	471.5±6.0	1.2
5	634.6±10.3	1.6

8.2.4 Wire bonding strength test

To make electrical connection between strain gauge electrodes and the connecting wire, silver based solder material was normally used. However, the bonding strength of silver based solder to carbon-based electrodes was found to be insufficient as delamination between the solder joint and the strain gauge electrode occurred when handling. Therefore, two-part silver epoxy (EPO-TEK® H20E) was used to ensure good electrical contact and sufficient mechanical bonding strength for handling during mechanical and electrical testing.

An alternative to bonding the connecting wires to the strain gauge electrode was also investigated and required merging the connecting wire into the deposited conducting carbon paste, which forms the strain gauge electrodes before curing the carbon paste. To investigate the strength of the above wire connection, wire bond strength test (WBST) experiments were carried out. As a comparison WBST experiments were also carried out using connecting wires, which were two-part silver epoxy bonded to the electrodes of a similar set of strain gauges. Note in this case the carbon based electrodes had been temperature cured before attaching the connecting wires using the two-part epoxy. These gauges were also all fabricated on polyimide substrates.

The WBST experiments were carried out as follows: the strain gauge patterns were dispensed and pre-cut copper wires were placed and merged into carbon paste electrodes before temperature curing as shown in Figure 8.4. Then the carbon strain gauges with the copper contact wires were cured at 120˚C for 15minutes.

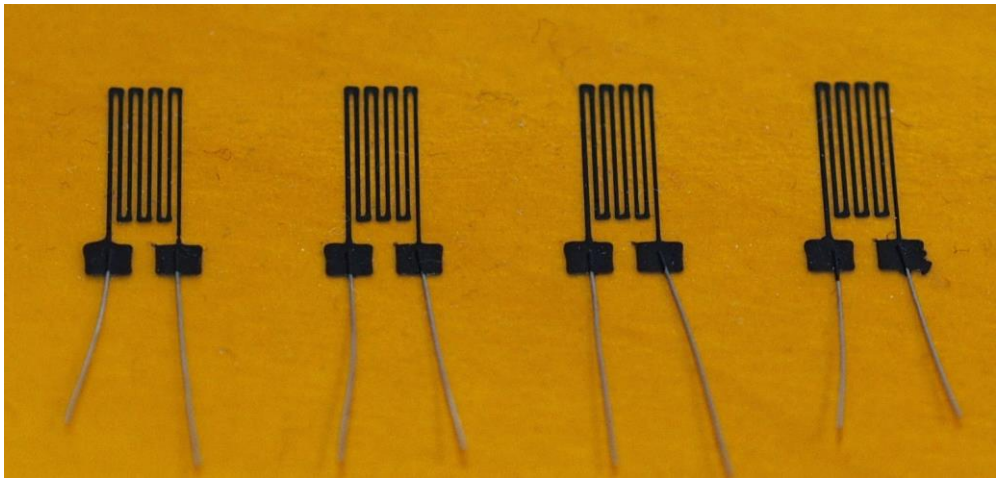

Figure 8.4 Connecting wires bonded in carbon curing process

In order to obtain quantitative results from the WBST experiment, the bond pull test was carried out at Linwave Technology Ltd, using calibrated WBST test equipment. In order to mount the sample into the wbst machine, the flexible polyimide substrate was bent to expose the connecting wires as shown in Figure 8.5. A pneumatic tweezer (Figure 8.5) was used to pull the bonded connecting wire to a calibrated maximum strength of 100gm. A total of 10 samples were made using the described process and as already described a further 10 sample were fabricated where the connecting wires were bonded to the strain gauge electrodes using the two part silver epoxy.

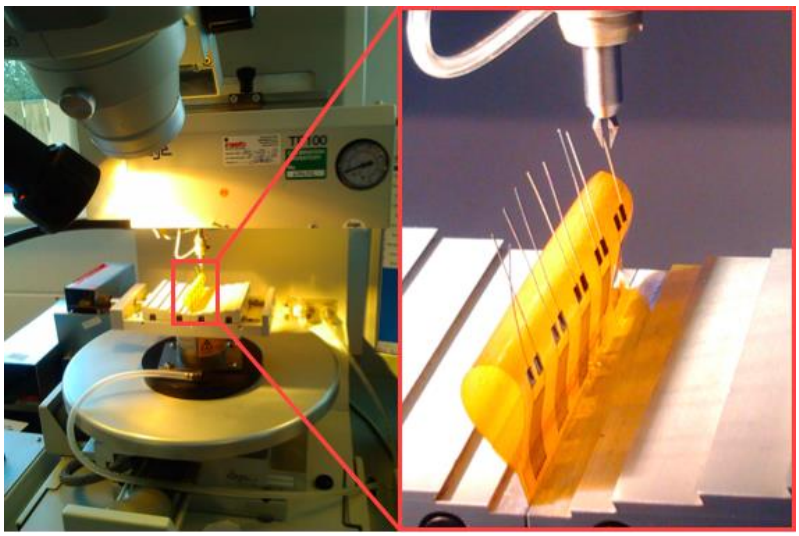

Figure 8.5 Wire bonding strength test (WBST)

Table 8.3 shows the results from the wire bonding strength tests. For the samples where the connecting wires were part of the carbon paste curing process, two of the leads from the samples became detached when subjected to the WBST test. It was also noted that only a small sideway force was needed to detach the wires; the side way force was thought to be small as there was no bending of the connecting wires.

Table 8.3 Wire bonding strength test results

Sample no.	In process bonding using carbon paste	Silver epoxy bonding (EPO-TEK® H20E)
1	100gm	100gm
2	**53gm**	100gm
3	100gm	100gm
4	100gm	100gm
5	100gm	100gm
6	100gm	100gm
7	100gm	100gm
8	100gm	100gm
9	**75gm**	100gm
10	100gm	100gm

The wire bond pull tests performed on the samples using silver two-part epoxy bonding (EPO-TEK®H20E) all reached the maximum force of 100gm presented by the tester. The contact resistances of both wire bonding connection processes were also measured using a digital multimeter (Fluke 289) and were found to be at 0.5kΩ for silver epoxy and 1.5kΩ for the carbon paste curing processes respectively. The wire bonding using silver epoxy resulted in less contact resistance and stronger bonding strength when compared to wire bonding using the carbon paste curing process. Therefore, the silver two-part epoxy was the preferred method for gauge factor measurements.

8.2.5 MDDW carbon strain gauge sensitivity measurement

The MDDW carbon strain gauge samples were mounted with cyanoacrylate (Loctite 496) on carbon steel test-plates using conventional mounting method described in detail in section 7.5.1.1.

The steel test-plates with dimension of 2cm x 18cm x 0.9cm were prepared for cantilever beam bending rig. Two-part silver epoxy (EPO-TEK® H20E) was used to bond the connecting wires to the strain gauge electrodes. The silver two-part epoxy was cured at 120˚C for 15min to ensure a strong bonding according to manufacturer recommendation, which was the same curing condition for the carbon paste. The lead wires were then connected to a multimeter (Fluke 289) via copper foil connecting terminals (TML TPF-2S).

The prepared samples are shown in Figure 8.6. A reference commercial metal foil strain gauge (TML FLA-10-11) with the same 10mm gauge length was also mounted on each of the test-plates next to the test carbon strain gauge to ensure that both strain gauges were under very similar loads during bending of the test-plates.

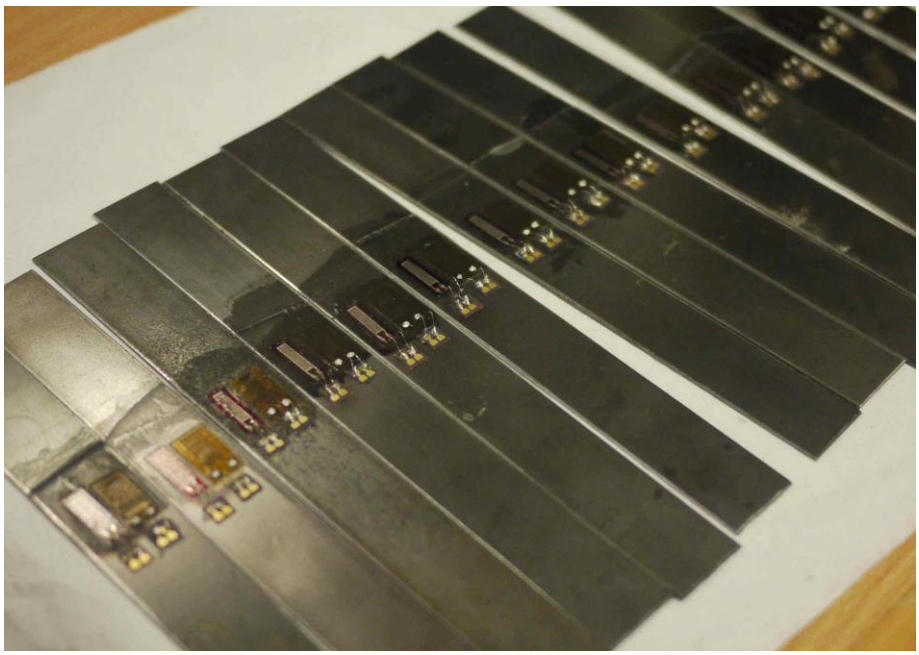

Figure 8.6 MDDW carbon strain gauge samples each with reference commercial gauge mounted on steel test-plates for the mechanical tests

The custom-made cantilever rig is shown in Figure 8.6 and was used to apply a known strain on the commercial and test strain gauges, which were mounted next to each other at the centre of the test-plate. A deflection was applied to the free end of the test-plate using a micrometre; the deflection was applied in 0.5mm increments to a maximum of 10 increments. A maximum of 277 microstrain was applied on the centre of each gauge.

The commercial reference gauge was connected to a Tinsley strain measurement bridge to record the strain being applied to the carbon based strain gauges and also to verify strain calculation method described in section 6.3.3. A K-type thermocouple was connected to TC-08 data logger and placed on the test-plate to record the ambient temperature during testing.

The measured ambient temperature during the strain measurement was between 24 to 25˚C. The applied strain was calculated using (2) [102][113]. The difference between the calculated strain (27.7με) and the measured strain (27με) was small as to be

considered negligible; the calculated strain was used in all the gauge factor measurement on the test carbon strain gauges.

$$\varepsilon(x) = \frac{3hy}{2L^3}x \tag{6}$$

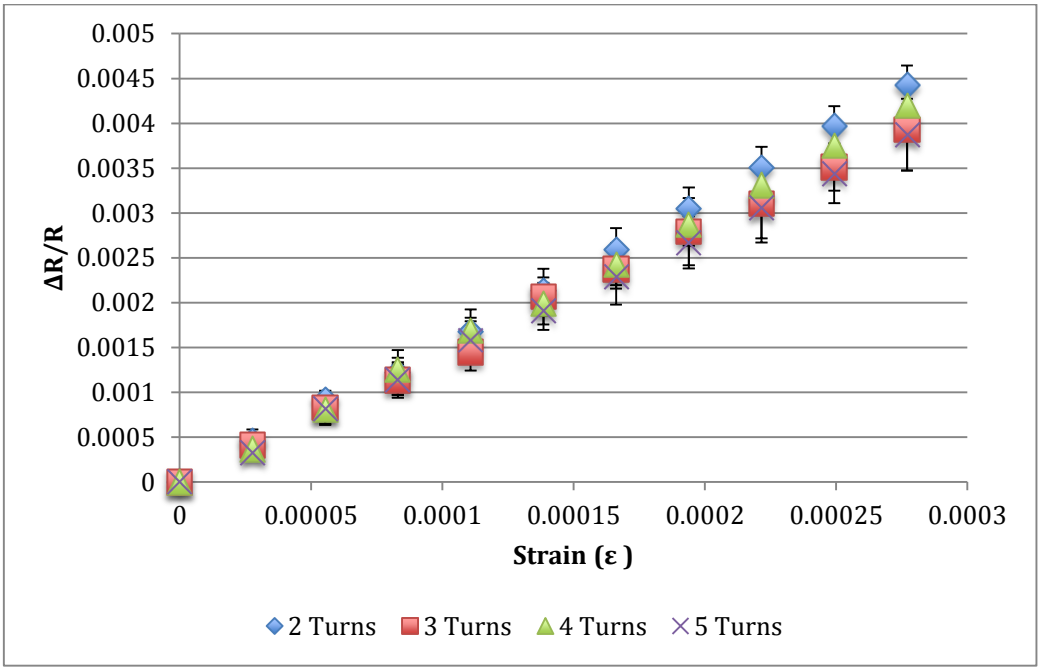

Figure 8.7 MDDW carbon strain gauge sensitivity measurement (125µm ID nozzle)

As described previously in section 4.2, the sensitivity of the gauge, can be expressed as the gauge factor (GF), which is the relative resistance change ($\Delta R/R_0$) in relation to the applied strain. The gauge factor was calculated using the equation below:

$$GF = \frac{\Delta R/Ro}{\varepsilon} \tag{2}$$

The carbon resistive strain gauges with 2, 3, 4 and 5 turns were tested. The gauge factor value of the MDDW carbon strain gauges was found to range from **13.9** to **15.7**, see Table 8.4. This was 6 to 8 times greater than the commercial metal foil strain gauge

(with the same gauge length of 10mm), which had a gauge factor of approximately 2. Therefore, the MDDW strain gauges are 6 to 8 times more sensitive than a comparable size commercial foil strain gauge. A strain gauge measures the strain over the covered sensing area of the strain gauge, which is the area of serpent geometry and does not include the rectangular electrodes to make contact with the connecting wires. Although strain gauges with a high number of turns measure over larger area than strain gauges with a low number of turns, it is worth noting that all strain gauges had the same total gauge length and were fixed to the test-plate with the same orientation with respect to the applied strain. Thus the measured ΔR/R value should be the same for each of the samples.

From the measured results (Table 8.4), there was no significant relationship between the sensitivity of the strain gauge and the number of turns. To miniaturise the strain gauge, the fabrication of a carbon sensor with 2 turns was carried out using a smaller nScrypt nozzle size to reduce strain gauge surface area footprint.

Table 8.4 MDDW carbon strain gauge sensitivity, average gauge factor as a function of the number of turns making up the strain gauge

No of turns	Nominal Resistance	R^2	Avg. Gauge Factor
2	218.3±2.4	0.999	15.7±1.2
3	323.1±7.7	0.998	14.2±1.8
4	452.9±2.8	0.999	14.7±1.7
5	611.6±10.9	0.999	13.9±1.6

8.3 Fabrication of miniaturised carbon resistive strain gauge

From the results in section 8.2, the carbon resistive strain gauges were fabricated using micro-dispensing direct write technology utilising a nozzle with an inner diameter of 125µm. These strain gauges had a much higher gauge factor than comparable commercial strain gauges. To improve the strain sensor resolution, a smaller surface

area strain gauge was required in order to measure the peak strain at specific points, for example on a bone implant. Previous fabrication described in section 8.2 utilised an nTip nozzle with inner diameter of 125µm and outer diameter of 175µm. In the following experiment, a smaller nozzle with inner diameter of 50µm and outer diameter of 75µm was used to reduce the carbon track width to minimise the strain gauge footprint. Moreover, employing smaller inner diameter nozzle will produce finer track width; therefore, increase the gauge sensitivity.

8.3.1 Optimise processing parameters

Since the nozzle diameter was reduced from 125µm down to 50µm, optimising the dispensing parameters was again required to ensure consistency and quality of the dispensing result. An empirical approach was carried out (similar to section 7.3.1) to find the range of process parameters, which will allow sufficient carbon paste flowrate to be extruded through the fine nozzle. The parameter ranges are shown in Table 8.5.

Table 8.5 Parameter optimisation (50µm ID nozzle)

Parameters	Upper level	Medium	Lower level
Dispensing height (µm)	15	20	25
Dispensing speed (mm/s)	6	7	8
Material feed pressure (psi)	14	15	16

As described previously in section 7.3.2, a parameter optimisation experimental matrix was undertaken to cover all combination of the three dispensing parameters. In this trial, the two limits and median (upper, medium and lower) for each parameter are shown in Table 8.6. There were 27 sets of parameters for 8 samples giving a total number of 216 measurements.

Table 8.6 Experimental matrix for parameter optimisation (50µm ID nozzle)

Dispensing Height (mm)	Material Feed Pressure (psi)	Dispensing Speed (mm/s)		
		8 (3)	6 (1)	7 (2)
15 (1)	16 (3)	133	131	132
15 (1)	14 (1)	113	111	112
15 (1)	15 (2)	123	121	122
25 (3)	16 (3)	333	331	332
25 (3)	14 (1)	313	311	312
25 (3)	15 (2)	323	321	322
20 (2)	16 (3)	233	231	232
20 (2)	14 (1)	213	211	212
20 (2)	15 (2)	223	221	222

The strain gauge dimensions for the 8 samples is shown in Figure 8.8 where n is the number of turns (n=2), L is the gauge length (5mm), p is the pitch of the grid lines (0.5mm), and w is the track width, which depended on the dispensing parameters used. The overall footprint of the strain gauge was substantially reduced by factor of 2.

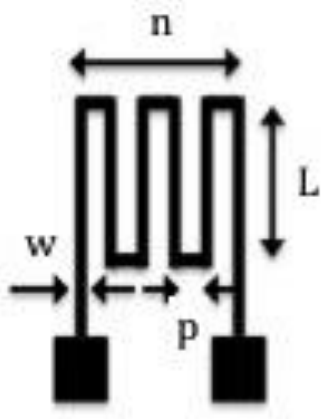

Figure 8.8 Carbon strain gauge dimension (50µm nozzle)

Figure 8.9 shows the process run of cured carbon strain gauge samples on a polyimide substrate. Since the dispensing height (distance between the nozzle and the substrate) was required to be as small as 15µm to 25µm, the substrate flatness was critical to the dispensing track quality. It was observed in some regions, the paste was not able to

extrude due to the uneven surface flatness (on a micron scale) of the polyimide substrate. The phenomenon was not observed or was much less apparent on earlier trials utilising the 125µm ID nozzle, since the optimised height was much greater (of the order of 100microns). Although the commercial control of the flatness of the substrate was excellent, it was hard to maintain the flatness once placed on the nScrypt build platform.

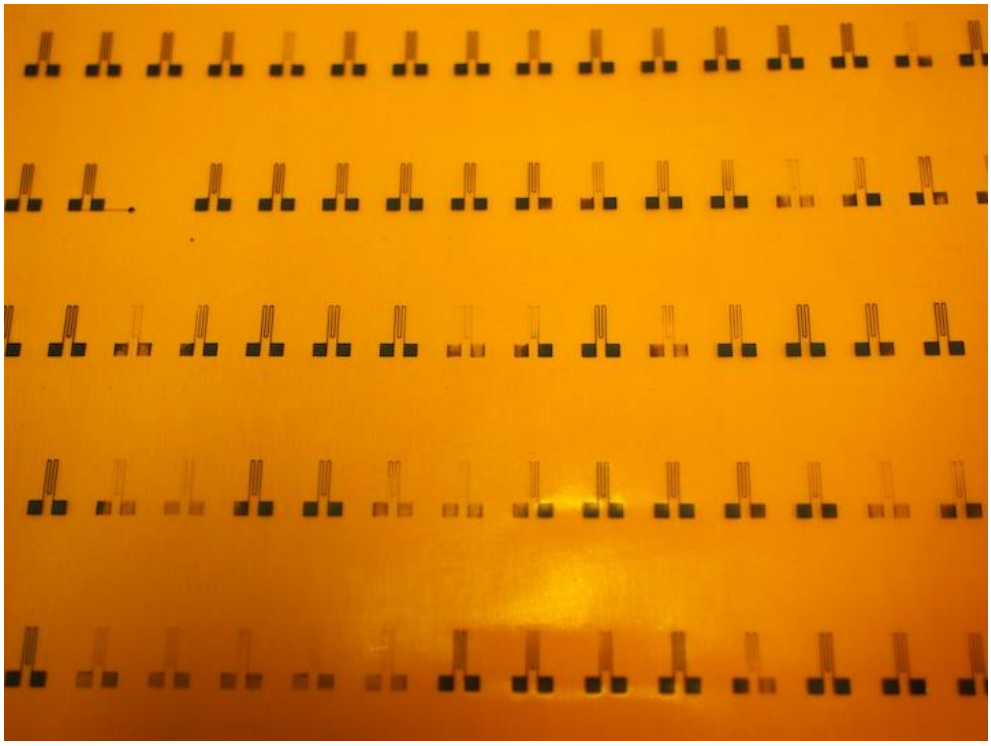

Figure 8.9 A sample of fabricated strain gauges using the 50µm ID nozzle

According to Li et al [121], the dispensing height above the substrate is critical to material flowrate especially when dispensing small features. The pressure inside the nozzle changes with different dispensing heights. When the dispensing height is low (5µm), the pressure increases and is dominated by the substrate. When dispensing height is large (30µm); the pressure drops and is dominated by the nozzle orifice. At the transition region (5µm to 30µm), the pressure drop can be affected by both dispensing height and nozzle orifice (see Figure 8.10) [121].

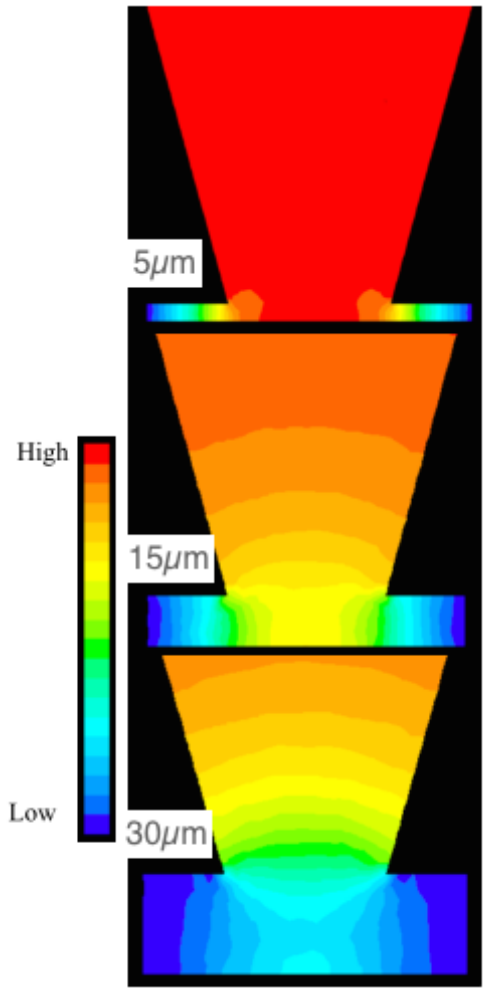

Figure 8.10 Pressure drop as a function of dispensing height

Figure 8.11 shows the plotted flowrate versus dispensing height with the 50µm ID nozzle [121]. When a constant pressure is applied, the flowrate is dependent on the dispensing height. When the dispensing height is greater than 50µm, the flowrate reaches a constant value. Material feed pressure is dominated in controlling the flowrate. When dispensing height is less than 20µm, the flowrate drops significantly due to pressure build-up caused by the close proximity of the substrate.

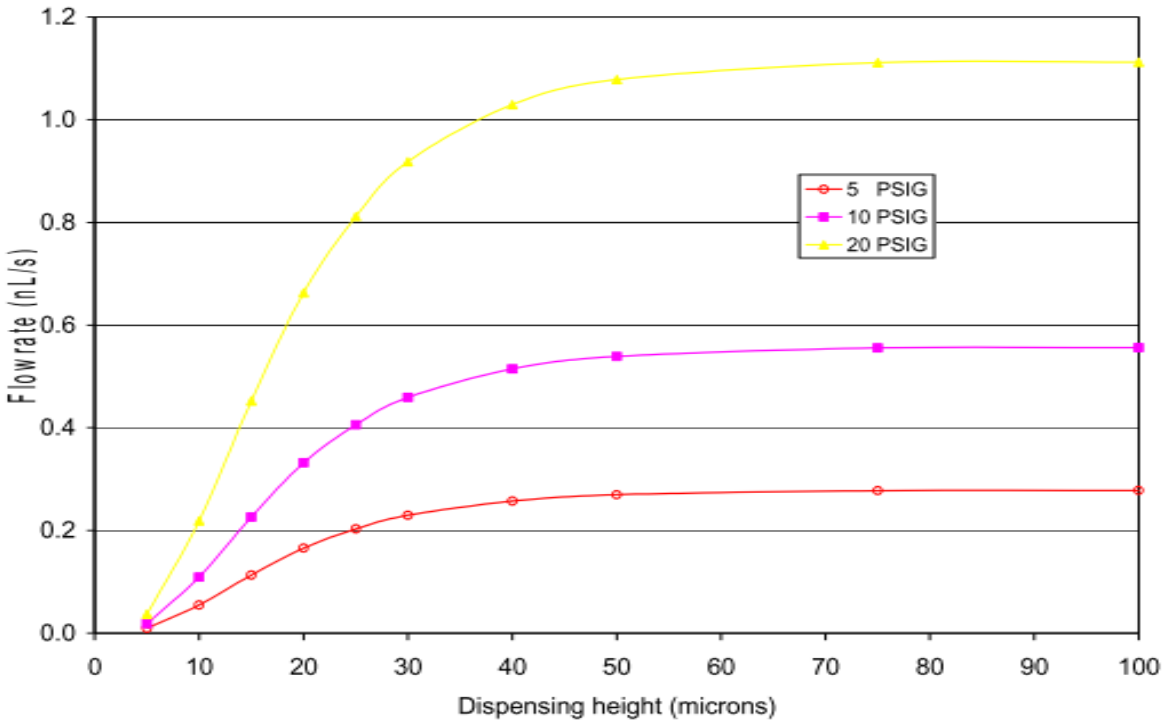

Figure 8.11 Flowrate vs. dispensing height using a 50µm I.D. nozzle [121]

Due to the limitation to control the flatness to a micron-scale of the polyimide substrate, in some of the fabricated strain gauge samples the track was not formed or non-uniform thickness. This was due to the flowrate varying as a function of the thickness of the substrate as shown in Figure 8.9. Nevertheless, a total of 109 strain gauge samples out of 216 samples were of sufficient quality to be selected for further characterisation. The track width and electrical resistance of each sample were measured.

8.3.1.1 *Mean track width versus dispensing height*

Figure 8.12 shows a plot of the measured average track width versus the dispensing height. The average track width was taken from measurements of the fabricated 109 samples. The error bars indicate the standard mean error of the measurement. With constant pressure applied, the track width increased with increasing dispensing height, until the feed pressure approached 15psi. This may have been because of the changes in the dispensing height due to the uneven flatness of the polyimide substrate. When

reducing the dispensing height, a wider track width was obtained. On reducing the dispensing height further, the increase in pressure caused by the substrate significantly reduced flowrate until nothing was dispensed.

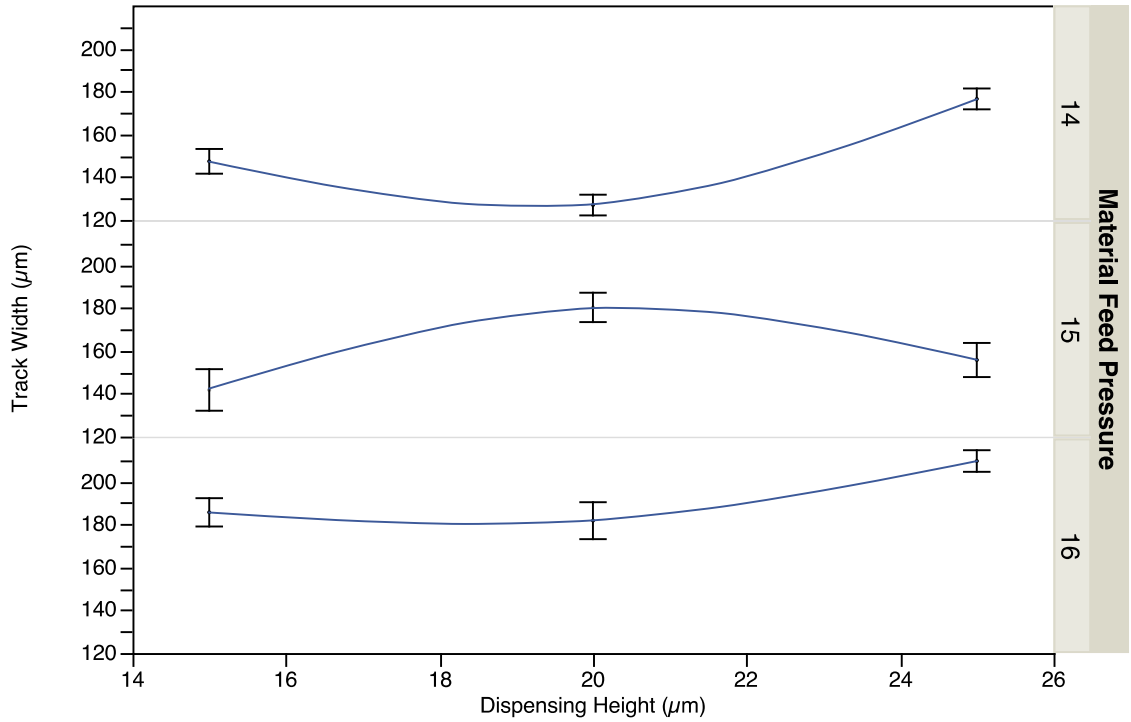

Figure 8.12 Average track width vs. dispensing height as a function of material feed pressure (50μm ID nozzle)

8.3.1.2 *Mean track width versus dispensing speed*

Figure 8.13 shows the plotted track width versus dispensing speed as a function of material feed pressure. It can be seen that when material feed pressure was between 15psi and 16pis, the track width is dominated by the dispensing speed. The average track width reduces with increasing dispensing speed. When the material feed pressure applied was at 14psi, the trend was less evident and therefore, the track width was dominated by other process parameter e.g. dispensing height.

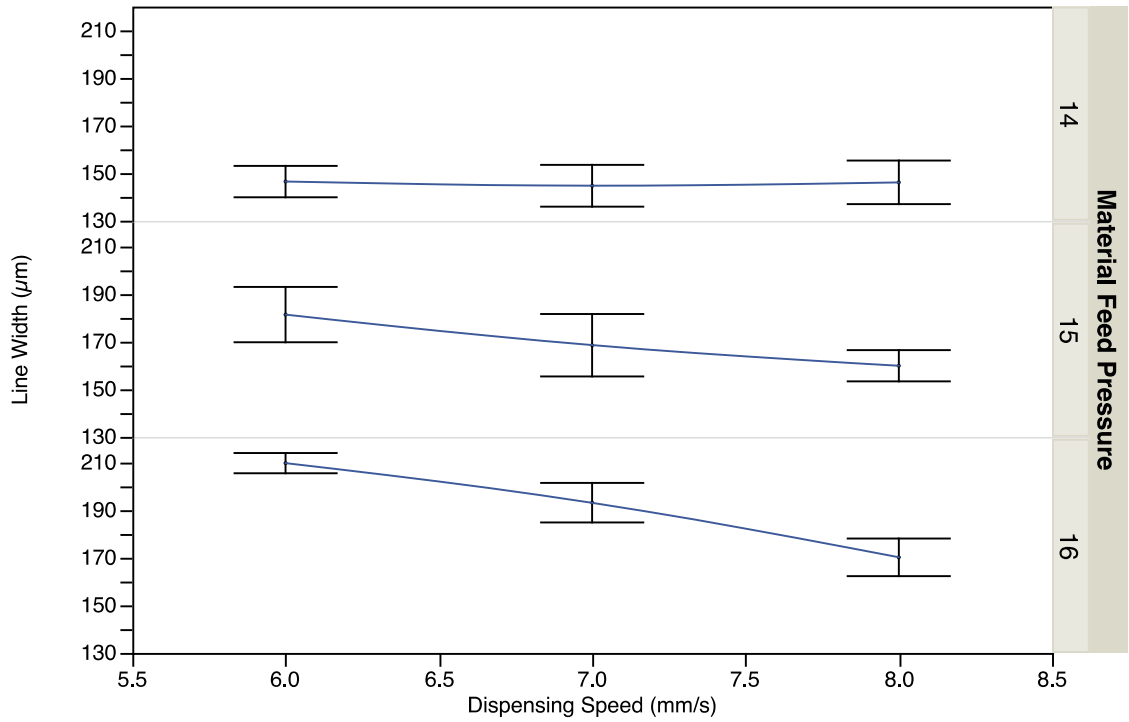

Figure 8.13 Track width (mean) vs. dispensing speed as a function of material feed pressure (50µm nozzle)

8.3.1.3 *Variability chart*

Figure 8.14 and Figure 8.15 show plotted variability charts for each set of the process parameters. The charts show there were less working samples made at dispensing height of 15µm. The 15µm dispensing height was too small and the flowrate was dominated by the substrate. As the substrate flatness was unable to be controlled to the micron level, insufficient flowrate caused discontinuity in width of the fabricated strain gauge tracks.

From the results given in the variability chart (Figure 8.14), the set of process parameters giving the lowest standard deviation (Figure 8.15) was chosen and these

had the following process parameters **dispensing height of 25µm**, **material feed pressure of 14psi**, and **dispensing speed of 7mm/s**. With these process parameters, the average track width was measured as **183.7±0.5µm**. Therefore; these process parameters were selected for the fabrication of the miniature strain gauges.

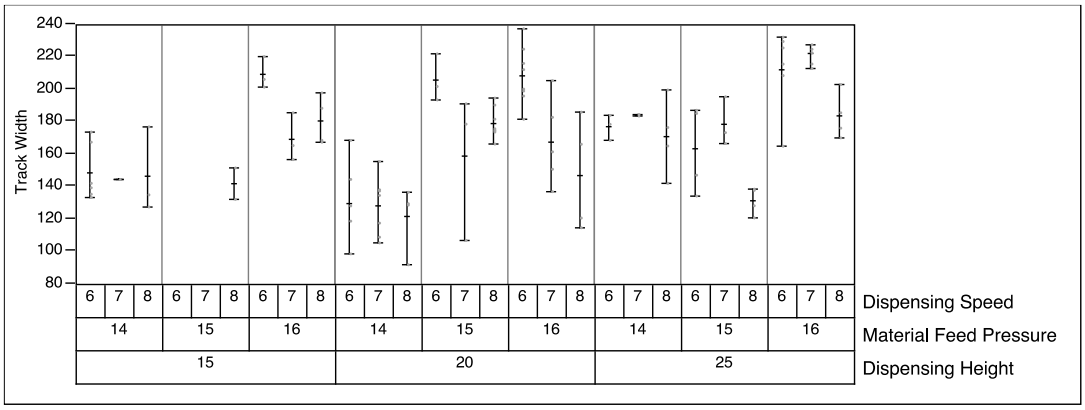

Figure 8.14 Variability chart for the carbon strain gauge line width (50µm nozzle)

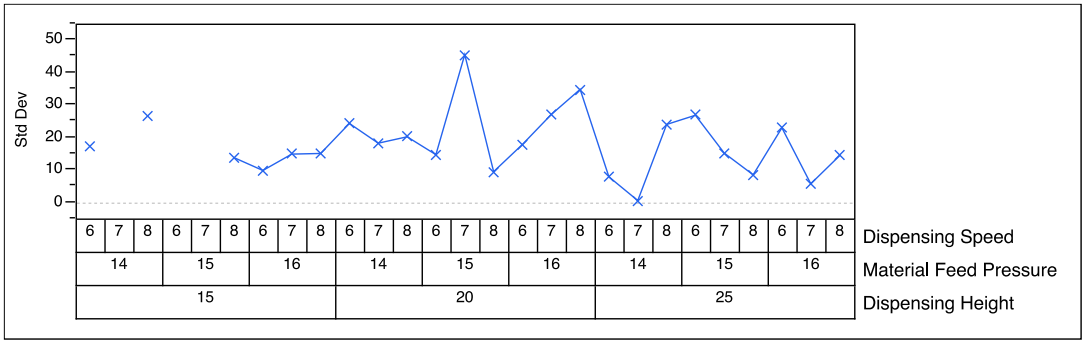

Figure 8.15 Variability chart for the carbon strain gauge line width as a standard deviation (50µm nozzle)

8.3.2 Carbon resistive strain gauge with 50µm ID Nozzle

In section 8.2, carbon resistive strain gauges were fabricated using 125µm ID nozzle. In order to provide direct comparison of gauge performance using the smaller ID nozzle, strain gauges with 2 Turns and 10mm gauge length were fabricated with the 50µm ID nozzle. A total of three carbon resistive strain gauge samples were fabricated using the optimised process parameters found for the 50µm ID nozzle.

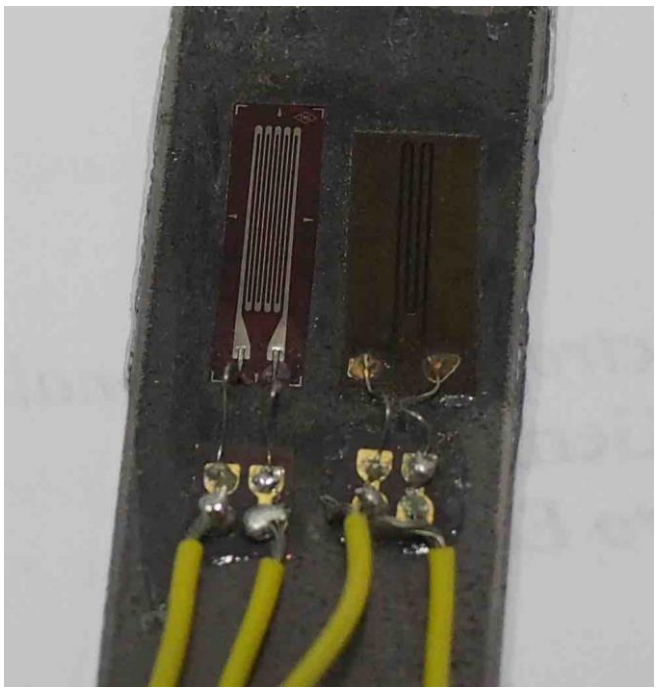

Figure 8.16 MDDW carbon resistive strain gauge factor measurement (50µm nozzle, 2 Turn, 10mm gauge length)

The strain gauge mounting procedure was followed using method described in section 7.5.1.1 to attach the strain gauges to steel test-plates. These were used to measure the gauge factor using the cantilever beam bending technique (section 8.2.5). Figure 8.17 shows the plot of change in resistance versus strain from the cantilever measurements. Good linearity was found between the change in resistance and the applied strain with correlation coefficient R^2 greater than 0.996.

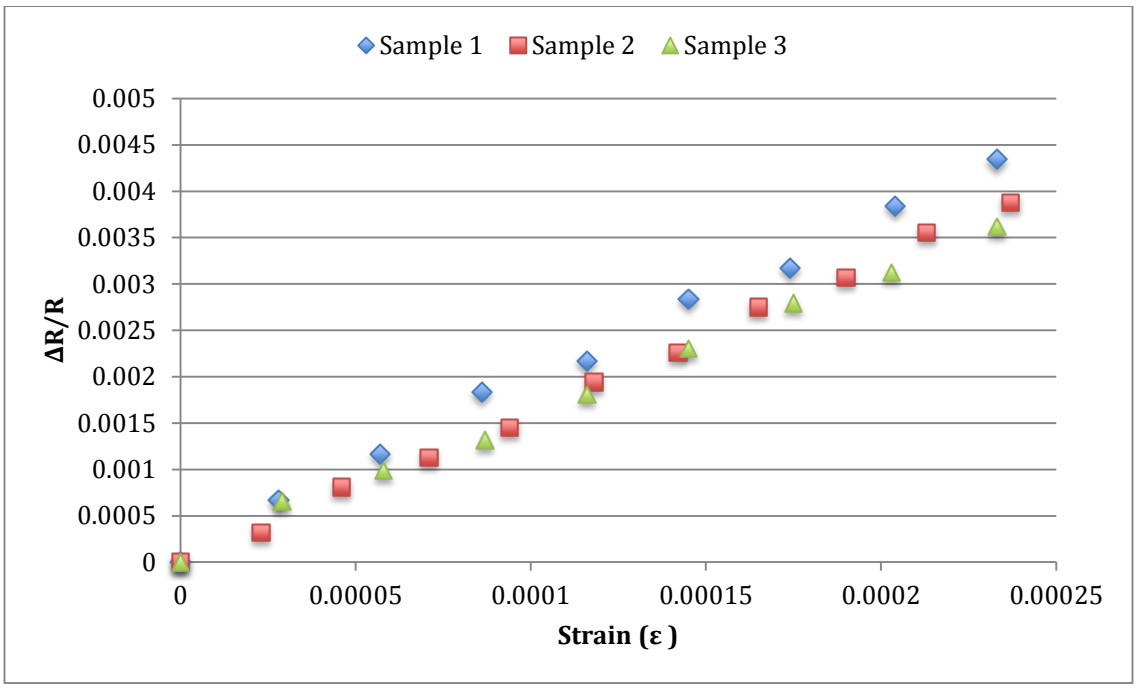

Figure 8.17 Change in resistance vs. strain for MDDW carbon resistive strain gauge (50µm ID nozzle, 2 Turn, 10mm gauge length) factor measurement

The measured gauge resistance values from the 3 samples were between 598.7kΩ to 618.6kΩ as shown in Table 8.7. With the same gauge footprint, using the 50µm ID nozzle the track widths were reduced from an average width of 224 to 183µm, which improved the average gauge factor from 15.9 to 16.6 with the measured highest of 18.2.

Table 8.7 Gauge factor of carbon resistive strain gauge (10mm gauge length) fabricated using 50µm ID nozzle

Sample No.	Nominal Resistance (kΩ)	R^2	Gauge Factor
1	598.7	0.996	18.2
2	618.6	0.999	16.5
3	607.7	0.997	15.2

8.3.3 Fabrication of miniaturised carbon resistive strain gauges

The carbon resistive strain gauge samples were fabricated using the optimised parameters where Dispensing height: 25µm, Material feed pressure: 14psi, Dispensing speed: 7mm/sec (Section 8.3.2). The miniaturised carbon resistive strain gauge samples were designed to an overall individual gauge size 8x12mm and the covered sensing area was comparable to the commercial metal foil strain gauge with 5mm gauge length (see Figure 8.18). The technology could be used to reduce the gauge size further if required.

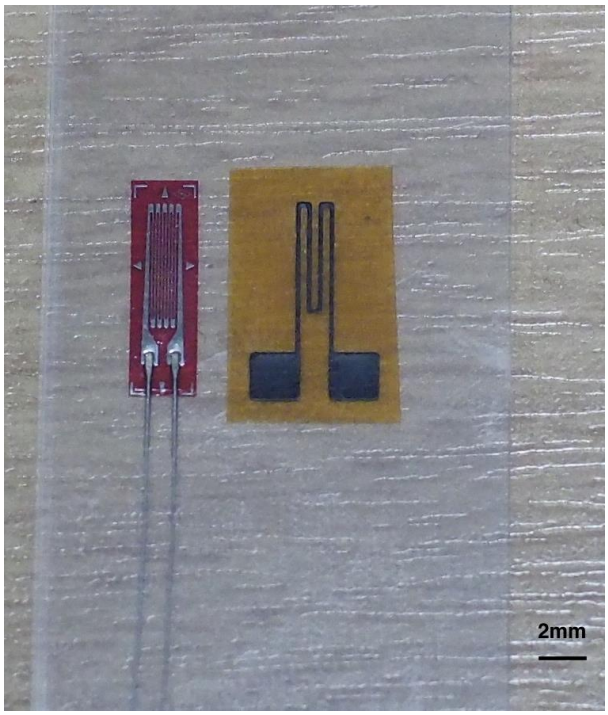

Figure 8.18 Miniaturised carbon resistive strain gauge (5mm gauge length) compared to commercial strain gauge

8.3.3.1 *Gauge Factor Measurement*

To measure the gauge sensitivity, the cantilever bending technique was used, which was the same method employed in section 8.2.5 and described in section 6.3.3. However, this time a titanium test-plate (Grade I) was used, as it was more comparable with the material used for medical implants. The samples were mounted on titanium test-plates using the method described in section 7.5.1.1. Figure 8.19 shows a

miniaturized carbon strain gauge sample mounted on a titanium test-plate. The titanium test-plates were 110x10mm and 1mm thick and were cut using a diamond wheel cooled by water jet. To provide the strain to the sample a deflection was applied to the test-plate in 0.25mm increments to a maximum deflection of 2mm. The strain applied at the test gauge location was calculated using equation 1. The maximum of 200 microstrain was applied. Three samples were tested and each sample was measured five times.

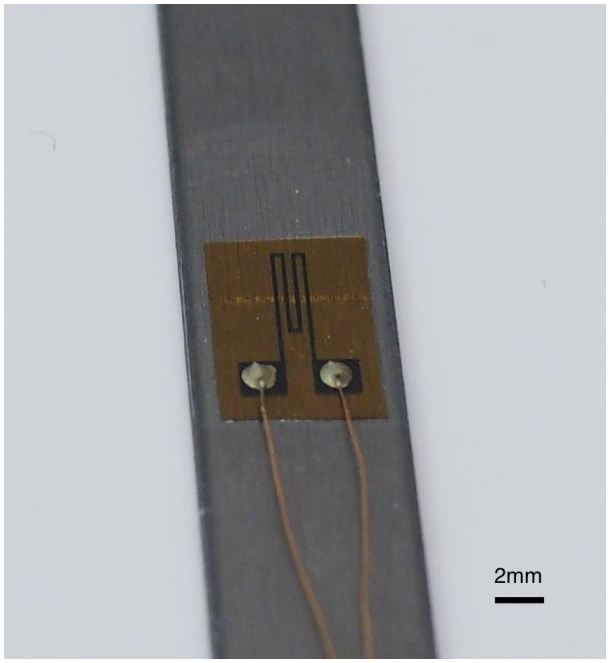

Figure 8.19 Miniatursied carbon resistive strain gauge on a titanium test-plate

Figure 8.20 shows the measured plotted resistance change versus strain of the miniaturised carbon strain gauges. The error bars indicate the standard mean error of the measurements. The measured gauge factor of the miniaturised resistive gauges with 5mm gauge length was between 8.8 and 9.6. The sensitivity was approximately half when compared to strain gauge with double the gauge length (Table 8.7).

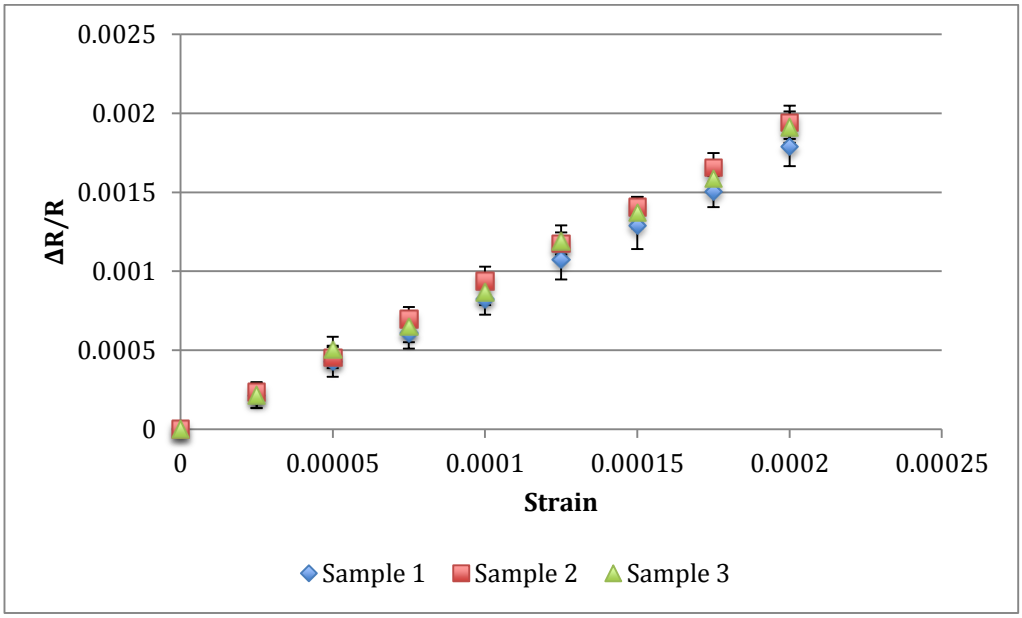

Figure 8.20 Resistance vs. strain for the 5mm gauge length MDDW carbon resistive strain gauge factor measurement

Table 8.8 Nominal resistance, linearity and gauge factor of carbon strain gauges

	Nominal resistance (kΩ)	R^2	Gauge factor
Sample 1	558.4	0.998	8.8
Sample 2	440.8	0.999	9.6
Sample 3	554.1	0.996	9.4

8.4 Discussion

The optimised process parameters for DuPont 7082 carbon conductive paste were found using 125µm ID nTip nozzle. The average track width was 224.5±8.4µm. The carbon strain gauge samples with gauge length of 10mm were fabricated. The gauge factor measurements were carried out using a custom made cantilever-bending rig. The linear correlation coefficient R^2 between the measured change in resistance and the applied strain was found to be 0.999, which was far more linear than obtained for the silver strain gauge samples (R^2=0.686). Carbon strain gauge samples with 2 to 5 turns were fabricated and the measured gauge factor values were found to be between 13.9 and 15.9. As the same amount of strain was applied along the sensing grids to each sample, the number of turns did not affect the overall sensitivity. Therefore a uniform strain sensitivity of each gauge sample was as expected. The variation in gauge sensitivity was thought to be due to the track width variation of each gauge sample; as the obtained track width standard deviation of the track width was 8.4µm.

In order to increase the gauge sensitivity, a 50µm ID nTip nozzle was used to reduce strain gauge track width. The process parameters were optimised using full factorial design of experiment methods. It was found that since the nozzle diameter was reduced by factor of 2.5, the optimised dispensing height was also reduced from 100µm to 25µm. Furthermore, since the dispensing height played an important factor to flowrate, it was harder to control the flowrate in a batch production since the flatness of the polyimide substrate became more critical. The polyimide substrates used for this experiment were not flat to a micron-scale when placed on the nScrypt build platform. After parameter optimisation, it was found that using the 50µm ID nozzle and comparing to the 125µm ID nozzle, the measured average track width was reduced from 224.5 to 183.7µm; the standard deviation of measured track width was also reduced from 8.4 to 0.5µm. As a comparison, strain gauge samples with same gauge footprint (2 turns and gauge length of 10mm) were fabricated using 50µm ID nozzle. The measured average gauge factor values improved from 15.7 to 16.6 with highest measured gauge factor of 18.2.

The designed miniaturised strain gauge samples had a reduced gauge length from 10mm to 5mm. Hence, the sensing area reduced by factor of 2. The strain gauges were fabricated using the 50µm ID nozzle and deposited on polyimide substrate. The measured average gauge factor values were found to be 9.3; the sensitivity of the gauge was found to be reduced by a factor of 2, as expected. Nevertheless, the gauge sensitivity of the gauge samples was still approximately 10 times greater when compared to a commercial metal foil strain gauge with a similar footprint.

Chapter 9. Integrated carbon strain gauge sensor

9.1 Introduction

In chapter 8, the fabrication and characterization of high sensitivity miniaturised carbon resistive strain gauges using nScrypt direct write technology was described. This chapter describes the experimental work to investigate the feasibility of fabricating integrated sensors on equivalent biocompatible test-plates using MDDW technology. Ceramic and titanium test-plates were selected for MDDW integrated carbon sensor fabrication. Both materials are well-accepted inert biomaterials for bone fixation plates (Table 2.2) and load bearing implant scaffold applications (Figure 2.7) due to their mechanical properties.

9.2 Parylene C coating

Parylene C coating is absolutely conformal and can be laid down in thicknesses from a few angstroms (Å) to 50μm or more depending on the requirements of the application [122]. Figure 9.1 shows the steps of chemical vapour deposition (CVD) polymerization that was used for parylene C coating:

1. The process requires the vaporisation of high purity crystalline dimer di-p-xylylene at 150°C.
2. The vapourised dimer is then pyrolised (decomposed) at about 650°C to form the gaseous monomer
3. The gaseous monomer condenses on the sample in the coating chamber at room temperature to form the polymer, thus no residual stress remains on the surface

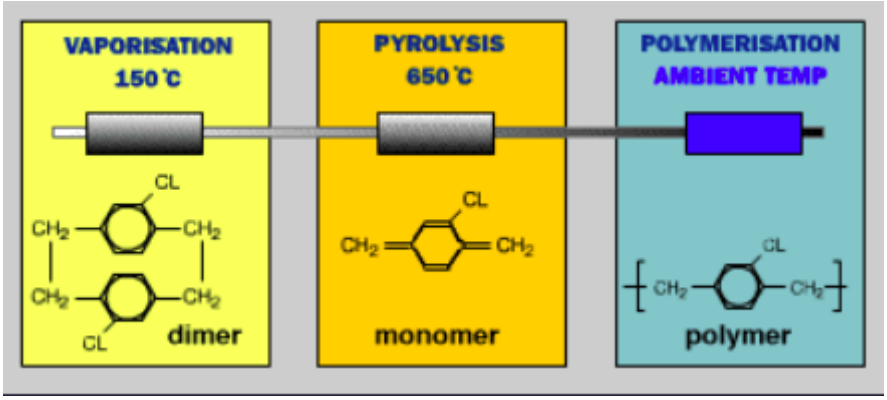

Figure 9.1 Parylene C coating process [122]

In this work, parylene C was deposited using CVD technique provided by ParaTech Coating Ltd (Northampton, UK). The company provided a certificate of conformity of parylene C layer, which is attached in Appendix – 1.

To realise the integrated sensors, a biocompatible parylene (poly-para-xylylenes) C layer was utilised in two ways (a) as a dielectric layer to isolate the gauge from the conductive test-plate surface, and (b) as an encapsulation layer to protect the sensor and ensure biocompatibility. The first approach (a) the author believes is novel to this research work. Due to the bio-inert property of parylene C, it is a commonly used polymeric material for encapsulation of medical implant devices. The fabrication of parylene-based strain gauges for bone strain sensors has been reported by Yang et al [73]; however, the approach required adhesive to bond the strain gauges on to the test-plate surface (implant). The reported integrated carbon strain gauges in this research were fabricated using a novel fabrication process directly to the test surface without the use of adhesives. Thus this approach eliminates the use of adhesives for the attachment of the strain gauge to the test surface and therefore the unknown layer properties between the strain gauge and the test surface. More importantly the same process can be used to fix the strain gauge to materials used in implants and bone fixation plates.

Utilising the process information from the resistive strain gauge fabrication, an integrated strain gauge sensor was fabricated using MDDW directly on to ceramic and titanium test-plates to demonstrate the feasibility of using the process on bio-inert implantable materials. Note biocompatible materials have a very high purity and therefore a high cost, and to minimise the cost of materials used in this project comparable and equivalent non-biocompatible materials were used; it is believed that the equivalent lower purity materials used will have little effect on the fabrication process. Since titanium is electrical conducting, the feasibility of using biocompatible parylene C polymer layer as the dielectric insulation layer was investigated, which the author believes was novel. The work also included investigating the use of parylene C as an encapsulation layer on strain gauges printed directly on ceramic substrates. The experimental workflow of MDDW integrated strain gauge sensor fabrication process is shown in Figure 9.2.

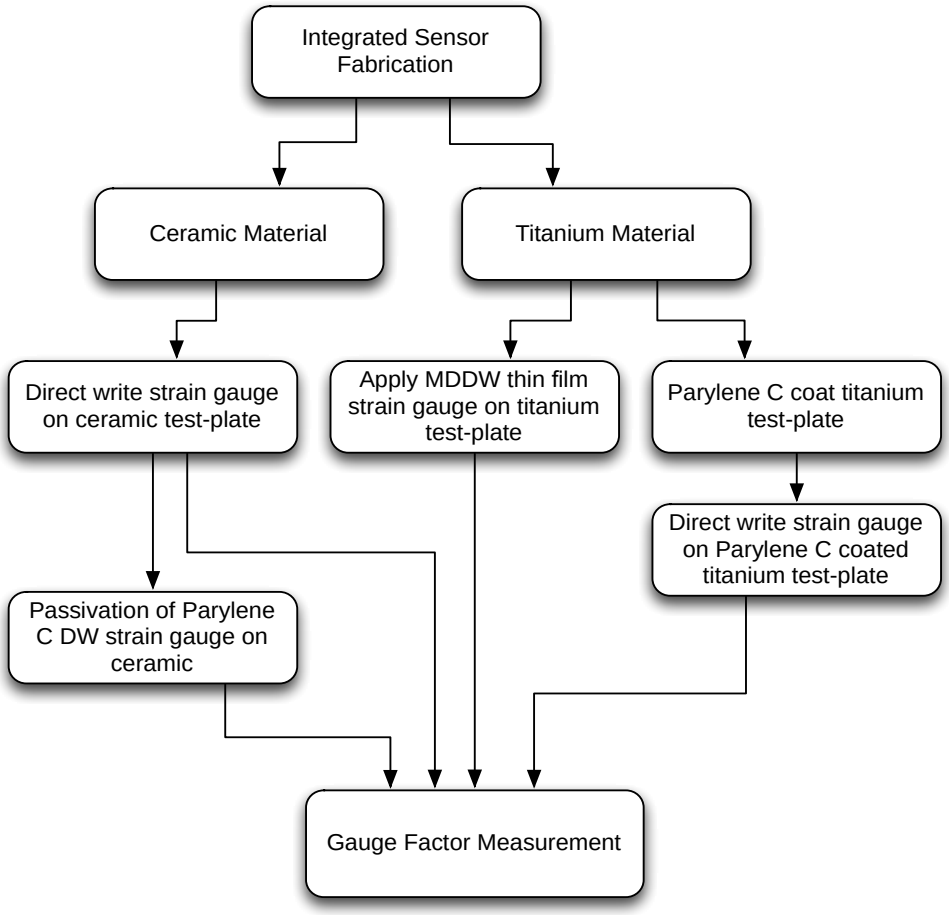

Figure 9.2 Integrated sensor fabrication experimental workflow

9.3 Fabrication of integrated sensor

Grade I titanium (Advanced Titanium Materials Ltd. Sheffield, UK) and 96% alumina ceramic (Coors Tech, Glenrothes, UK) substrates were used as materials to represent the implants.

The ceramic and titanium test-plates with dimension of 110x10x1mm were prepared; these dimensions were chosen to be the same as used for the titanium plates for the measurement of the miniaturised (5mm gauge length) carbon strain gauge sensitivity, in section 8.3.3.1. The gauge factor measurement methods were fully described as in section 8.3.3.1. The nScrypt 3Dn-300 MDDW machine was used to deposit the carbon strain gauge patterns. The processing parameters, nozzle size and the gauge dimension used for the integrated sensors were the same as specified in section 8.3.3 for fabricating miniaturised carbon resistive strain gauges.

9.3.1 Fabrication integrated carbon strain gauge on ceramic test-plate

Since ceramic is a dielectric insulator material, carbon conductive strain gauge patterns were directly deposited and cured on the test-plates surface using the nScrypt machine. A total of 8 integrated carbon strain gauge samples were fabricated on ceramic test-plates. The fabrication steps of integrated carbon resistive strain gauge sensors on ceramic test-plates are shown in Figure 9.3 and details described as follows:

1. Using nScrypt machine MDDW carbon strain gauge patterns were fabricated on ceramic test-plates
2. The ceramic test-plates with strain gauge sensor patterns were placed in a box oven to cure of the carbon paste at 120˚C for 15min
3. The connecting wires were attached to the strain gauge electrodes using two-part silver epoxy and the silver epoxy was cured at 120˚C for 15mins. For each sensor the gauge factor was measured 5 times to obtain an average value.
4. A 3.5µm thick Parylene C layer was then conformally deposited using CVD (ParaTech Coating Ltd) over the carbon strain gauge to act as an encapsulation

layer. For each coated sensor the gauge factor was again measured 5 times to obtain an average value.

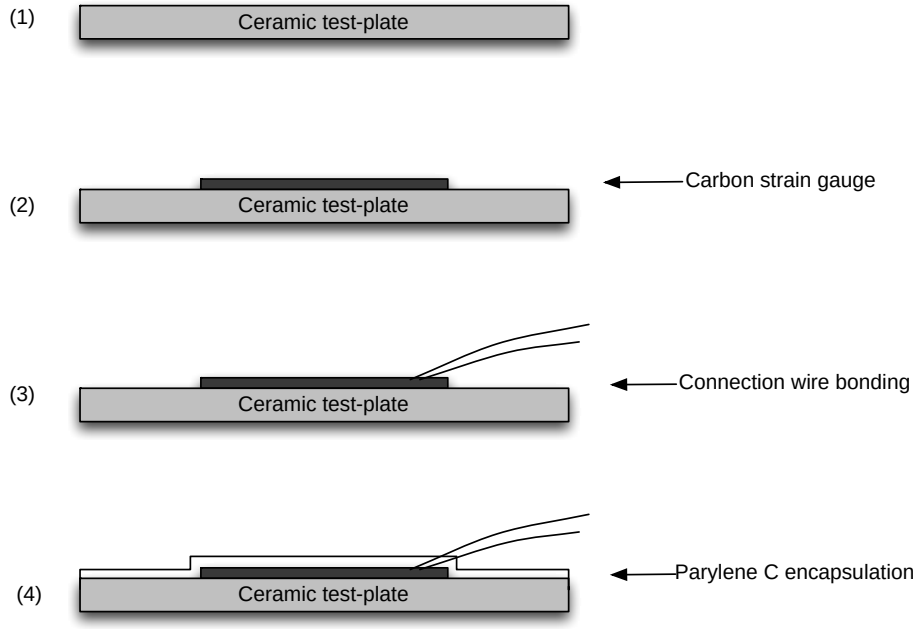

Figure 9.3 Fabrication steps of integrated carbon strain gauge on ceramic test-plate

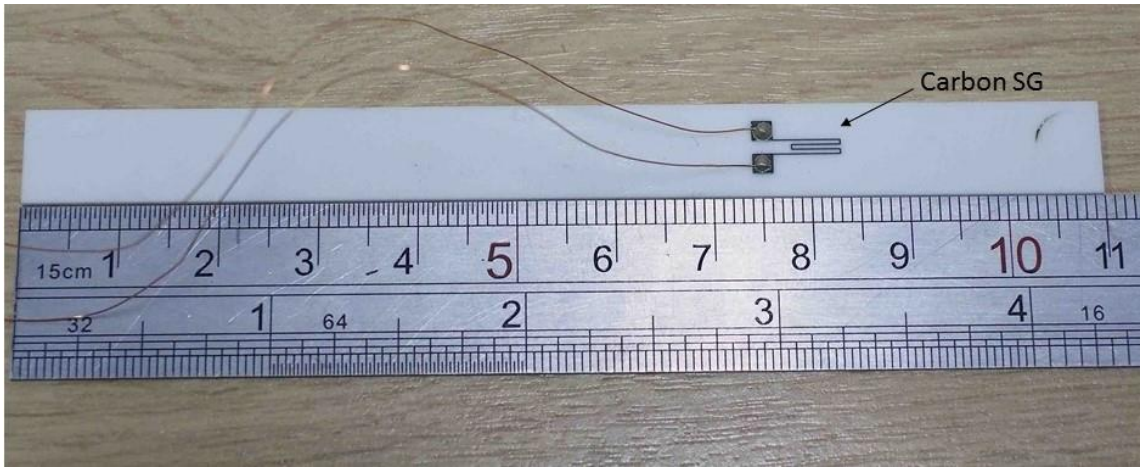

Figure 9.4 Image of a sample of MDDW carbon strain gauge on ceramic test-plate

9.3.1.1 *Gauge factor measurement*

The measurement was made using the cantilever bending technique as previously described in 8.3.3.1. During mechanical bending of the test-plates to obtain the gauge factor, fluctuation of gauge resistance was observed and found to be smaller for the samples after parylene C encapsulation.

Figure 9.5 and Figure 9.6 show the plotted change in resistance versus applied strain before and after parylene C coating of the 8 samples. The error bars present the variance from the five measurements for each of the 8 samples. The error between each measurement decreased after the same samples were encapsulated with parylene C. The reason for the fluctuation in resistance was thought to be due to encapsulation making the device less sensitive to changes in humidity, as the humidity can cause drift change in resistance [108]. The measured linearity was also found to have improved correlation coefficient, R^2 increased from 0.997 to 0.999.

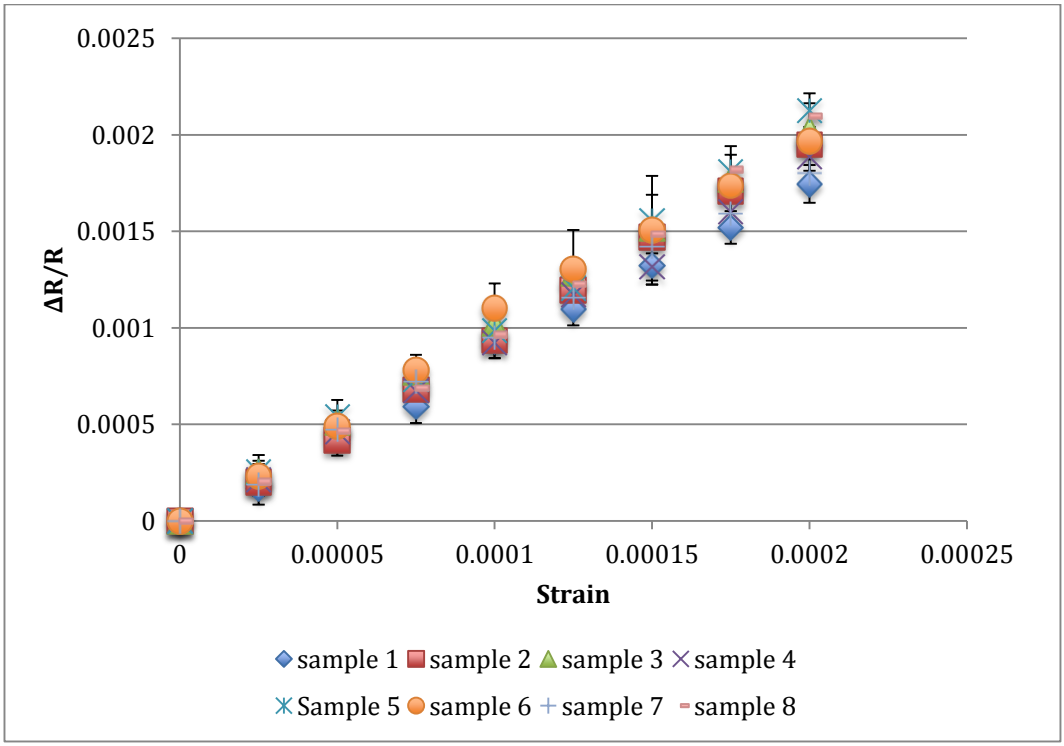

Figure 9.5 Change in resistance versus strain plot of integrated ceramic test-plates before parylene C coating

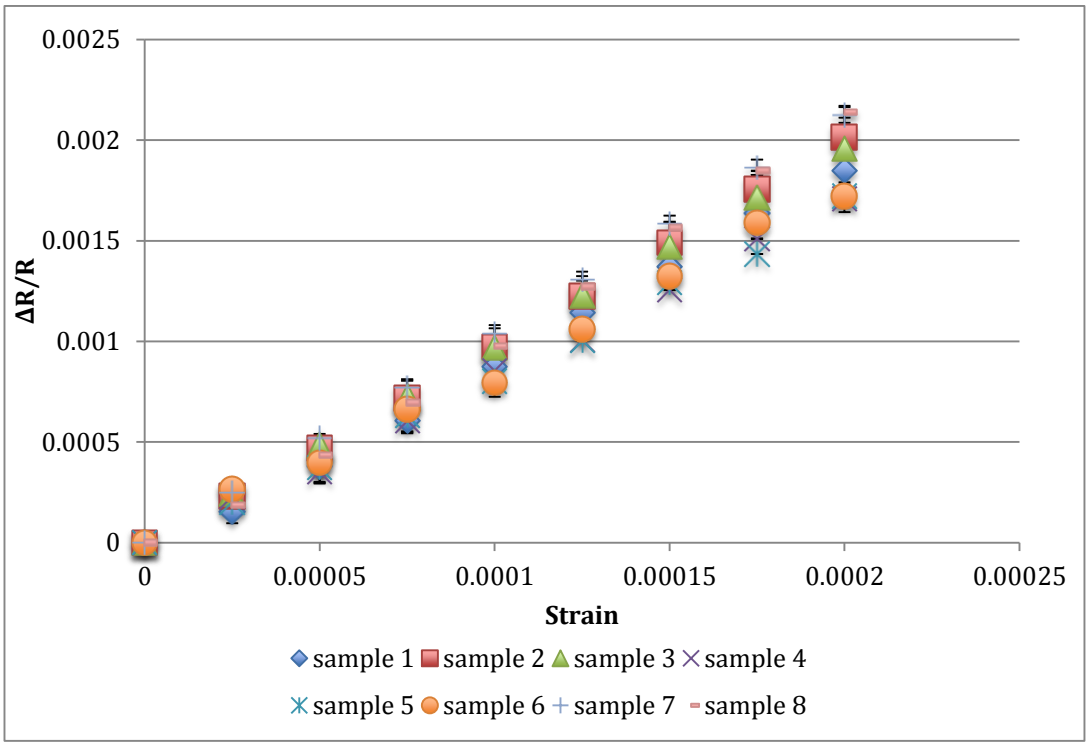

Figure 9.6 Change in resistance versus strain plot of integrated ceramic test-plate samples after parylene C coating

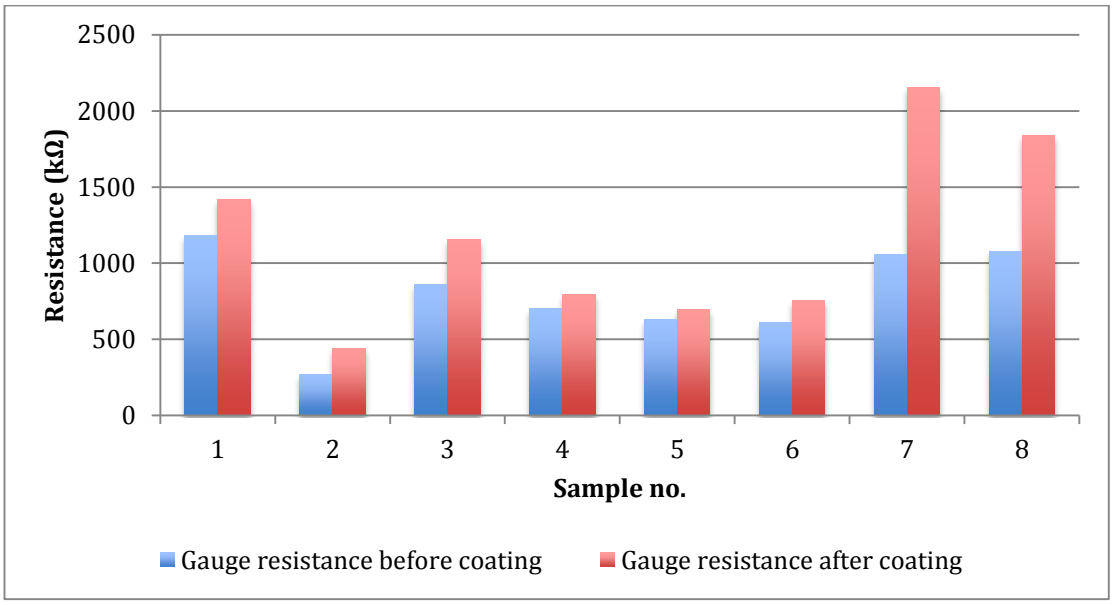

Figure 9.7 A comparison of gauge resistance measured before and after parylene C coating (ceramic test-plate)

Figure 9.7 shows the nominal resistance measured of the 8 integrated carbon strain gauge samples before and after parylene C coating was performed. It can be seen the resistance of the samples was increased after coating. Since the deposition of parylene C is under vacuum and the dielectric polymers can fill the pores in the granula carbon structure where the pore size was greater than 10 microns [122]. Therefore, it was postulated that the polymeric particles filling the open pores of the carbon track surfaces will prevent ingression of water in the granula structure thereby increasing the overall total resistance. Further work will be required to look at changes in stability of granula strain gauges before and after encapsulation.

Table 9.1 Gauge factor values and linearity of integrated carbon strain gauges on ceramic test-plates before and after parylene C coating

Sample no.	*Before parylene C coating*		*After parylene C coating*	
	Gauge factor	R^2	Gauge factor	R^2
1	8.9	0.997	8.9	0.997
2	9.6	0.999	9.6	0.999
3	10.1	0.999	10.1	0.999
4	9.3	0.998	9.3	0.998
5	10.5	0.997	10.5	0.997
6	10.0	0.996	10.0	0.997
7	9.2	0.998	9.2	0.998
8	10.5	0.997	10.5	0.997

Table 9.1 shows measured gauge factor values and correlation coefficient R^2 values of the 8 samples. The measured gauge factor values ranged between 8.9 and 10.5, giving an average gauge factor of 9.8 with a standard deviation of 0.6. It was found that the gauge factor was identical before and after parylene C encapsulation. The filling of the voids in the carbon track appeared to increase the total resistance of the resistive strain gauges and had little effect on the change in the resistance due to an applied

strain. Moreover, the measured linearity was very similar for both sets of strain gauges and both sets had very similar R^2 with correlation coefficients. Therefore, it was concluded that the parylene C coating as an encapsulation layer would not change the gauge sensitivity.

Figure 9.8 shows the plotted average gauge factor versus the average total strain gauge resistance for each of the 8 samples each measured 5 times. The average resistance values of the 8 integrated ceramic samples vary due to variation of measured track widths. Strain gauges with lower resistance exhibit larger track width and vice versa. Although there were differences in track width of each sample, which resulted in different average total resistance values, there was no evidence of a defined relation between the measured gauge factors and the total average gauge resistance value. Hence, carbon strain gauge track width variation due to MDDW process played little effect on the gauge factor, since the process produced high aspect ratio cross sectional area tracks [78]. According to Huang et al [103], the higher aspect ratio of the track, the less effect on the gauge factor by the track width.

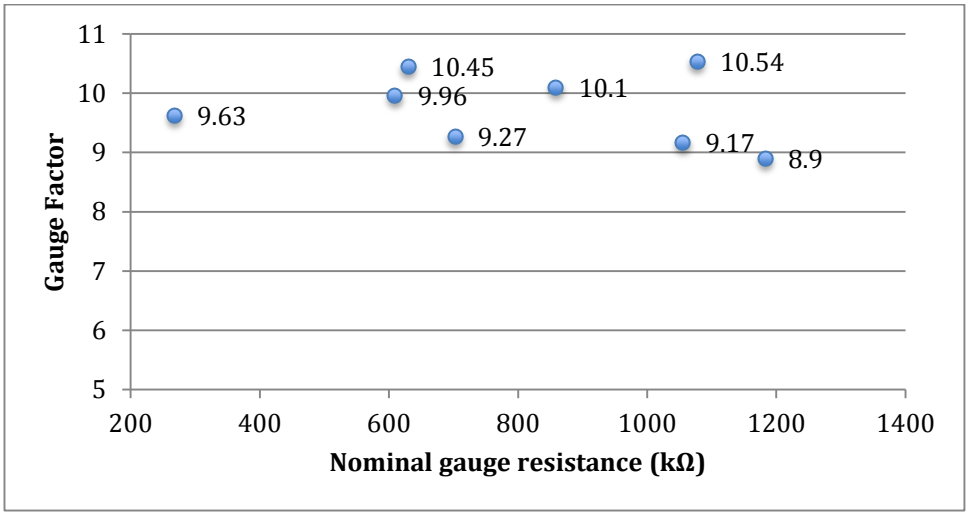

Figure 9.8 Measured gauge factor value versus nominal gauge resistance

9.3.2 Fabrication of integrated carbon strain gauge on titanium test-plate

Titanium is metallic material commonly used in medical implants. As titanium is metal and it has a relatively high electrical conductive when compared with a dielectric for example ceramic. Therefore, an electrical insulating layer was needed to provide electrical insulation between the deposited carbon strain gauge and the titanium test-plate surface. Two experimental approaches were undertaken. The first approach was a more standard: resistive carbon strain gauges were fabricated on polyimide carriers, which were then glued to the titanium test-plates. The second approach was novel and required to first coat the titanium test-plate with a parylene C layer, which acted as a dielectric layer. The carbon strain gauge was then directly deposited on the parylene C layer. A total of 3 samples were fabricated using each approach. Note the number of samples was restricted as the CVD deposition of parylene C coating was contracted out to an industrial company (ParaTech).

9.3.2.1 *Polyimide based resistive strain gauge on the titanium test-plate*

The fabrication of the polyimide based resistive carbon strain gauge on a titanium test-plate is schematically shown in Figure 9.9 and describes in the steps below:

1. Fabricate carbon resistive strain gauges on flexible polyimide carrier using MDDW process. The method was described in detail in section 8.3.3.
2. Mount the MDDW carbon resistive strain gauge on titanium substrate using cyanoacrylate adhesive, this was described in detail in section 7.5.1.1
3. Connect the electrical wires to the electrodes of the strain gauge using two-part silver epoxy and cure the silver epoxy at 120˚C for 15mins. For each strain gauge the gauge factor was measured 5 times and an average taken.
4. The structures were then coated using parylene C CVD process (ParaTech) to a thickness of 3.5µm at room temperature. This provided a conformal coating. The gauge factor measurements were repeated 5 times for each strain gauge, and the average taken.

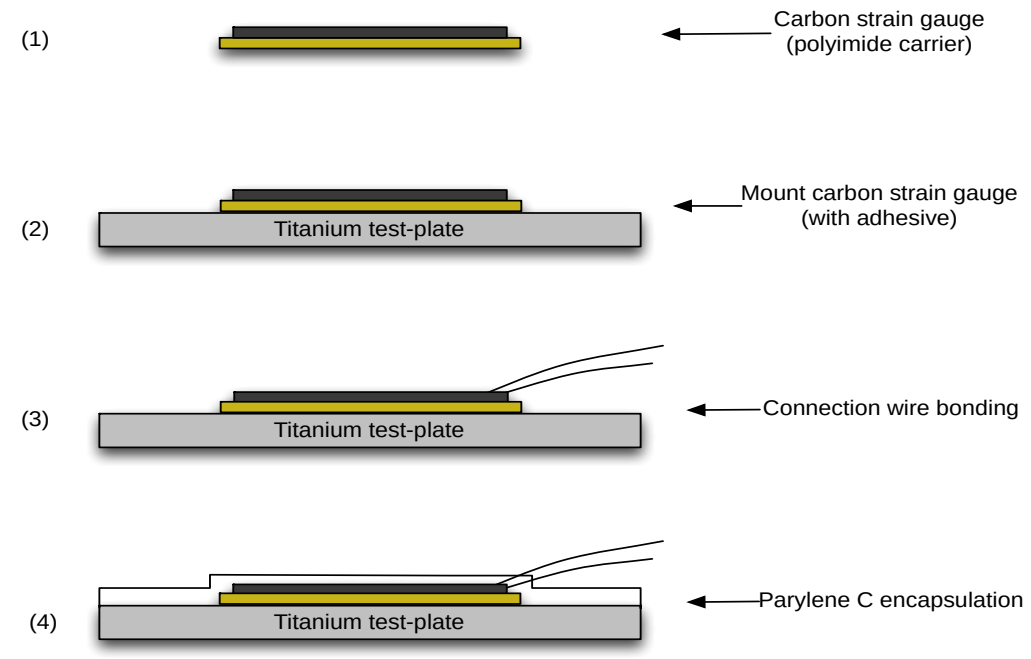

Figure 9.9 The strain sensor fabricated on polyimide flexible substrate, glued to the titanium test-plate and conformally coated with parylene C

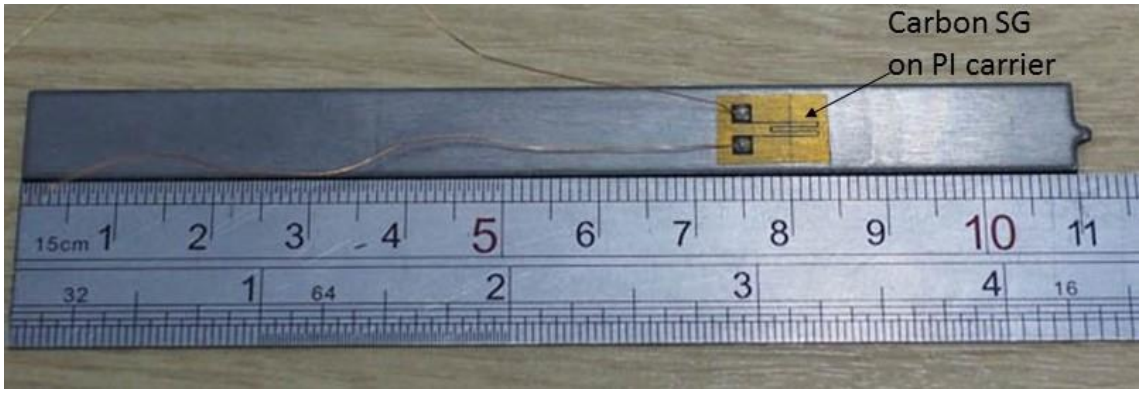

Figure 9.10 Image of a carbon resistive strain gauge sample on titanium test-plate

9.3.2.1.1 Gauge factor measurement

The gauge factor measurements were made using the cantilever bending technique as previously described in 8.3.3.1. Figure 9.11 shows the plot of measured change in resistance against applied strain for carbon resistive strain gauge before the parylene C coating. The error bars indicate the variance of the five measurements on each of the samples. The linearity of the gauge factor value as a function of applied strain, as a

correlation coefficient R^2 for each sample is shown in Table 9.2. From the measurements, the average gauge factor was 9.23 with standard deviation of 0.4. The results were as expected and very similar in the behaviour and magnitude to the results for miniaturised carbon strain gauges as described in section 8.3.3.1. However, after coating with parylene C the gauge factor could not be measured (see Table 9.2).

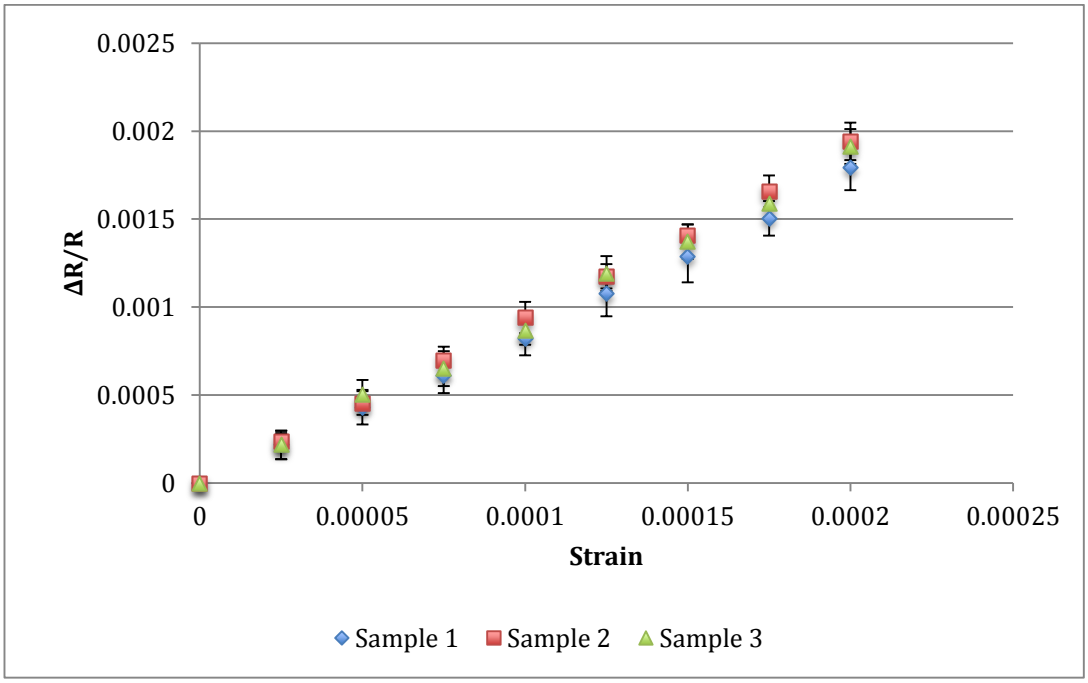

Figure 9.11 Change in resistance versus strain plot of carbon resistive strain gauge samples glued to the titanium test-plates without parylene coating

Table 9.2 The linearity of the gauge factor values of the carbon strain gauge samples glued to the titanium test-plates before and after parylene C coating

Sample no.	*Before parylene C coating*		*After parylene C coating*	
	Gauge factor	R^2	Gauge factor	R^2
1	8.8	0.998	n/a	n/a
2	9.6	0.999	n/a	n/a
3	9.3	0.996	n/a	n/a

After parylene C coating the gauge resistance of the samples was found to be very high in magnitude (see Table 9.3) and on one sample the electrode connections appeared to

be open circuited. This observation was not expected and the reason not understood. It could be as a result of chemical interaction between the polyimide carrier/glue and parylene C during CVD process in the vacuumed chamber. However, no evidence in the literature was found to support the hypothesis. The experimental result requires further work to ascertain the reason for the observed change in resistance to very high values (Table 9.3).

Table 9.3 Gauge resistance before and after parylene C coating

Sample no.	*Before parylene C coating*	*After parylene C coating*
1	558.4kΩ	41.8MΩ
2	440.8kΩ	185MΩ
3	554.1kΩ	Open circuit

9.3.2.2 *Integrated sensor using parylene C coated titanium test-plate (novel approach)*

The second fabrication approach the carbon strain gauge was deposited onto the titanium substrate forming a fully integrated structure. Parylene C was first coated to a thickness of 3.5µm directly to the surface of the titanium substrate to provide an insulating dielectric layer over the titanium substrate. The carbon strain gauge pattern was then deposited on to the parylene C layer. In order to keep the physical property of the parylene C layer intact while curing the carbon paste, the curing temperature was reduced from 120˚C to 80˚C [122].

The fabrication steps for the above process are described as follows:

1. The titanium substrate was coated with parylee C to a thickness of 3.5µm
2. The carbon based strain gauge was then direct write deposited on to the parylene C using the developed MDDW fabrication methods (section 8.7)
3. The samples were then placed in a box oven to cure the carbon paste at 80˚C for 3 hours*

4. The electrical connecting wires were connected to the electrodes of the strain gauge using two-part silver epoxy and the silver epoxy cured at 80˚C for 3 hours.
5. The gauge factor of each strain gauge was measured 5 times, and the average taken.

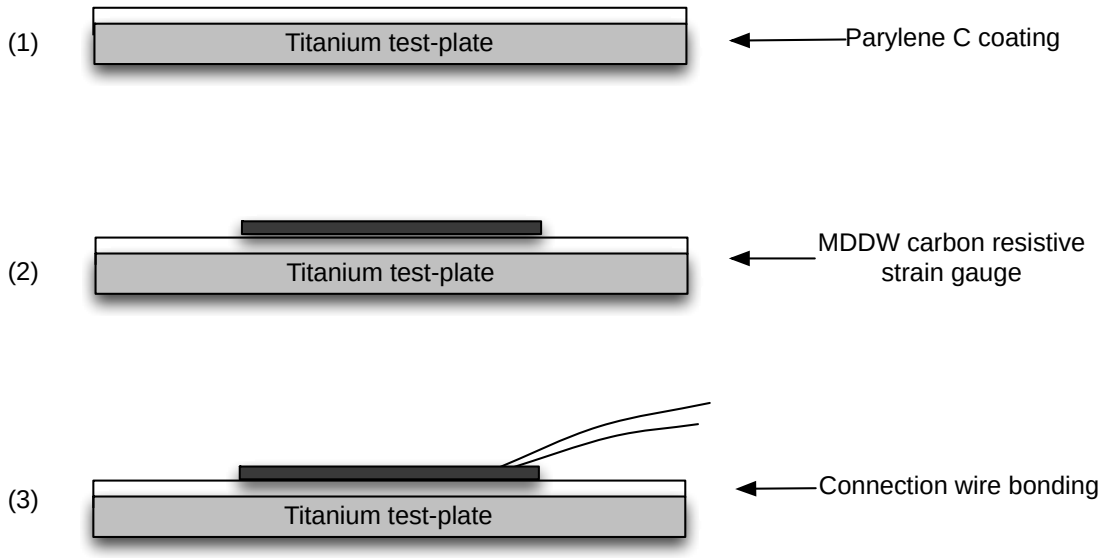

Figure 9.12 Titanium substrate

An image of a carbon resistive strain gauge sample on titanium test-plate is shown in Figure 9.13.

Figure 9.13 MDDW carbon strain gauge on parylene C coated titanium test-plate

The data on parylene C from ParaTech Company indicates that parylene C will retain its specified physical and mechanical properties at 80˚C for ten years. For this reason all subsequent processing steps after the parylene C coating were restricted to curing temperature of below or equal to 80˚C. It was assumed that the curing trend for the silver epoxy was similar to the curing trend for carbon past. At curing temperature 120˚C, silver epoxy requires 15 minutes curing time and according to the data sheet for a curing temperature of 80˚C, a longer curing time of 3 hours was required. Therefore it was assumed, a 3 hours curing time could be applied when curing carbon paste with parylene C as the insulation layer. This was justified by atomic force microscope (AFM) measurements made on carbon paste samples cured at both 120˚C for 15 minutes and 80˚C for 3 hours. Figure 9.14 shows the measured surface topology of the MDDW deposited carbon track cured at 80˚C for 3 hours, and 120˚C for 15 minutes respectively. The resulting images show very similar surface topology with perhaps a little more structure on the sample cured at 80˚C. Suggesting there is little difference in the material topology for the different curing conditions.

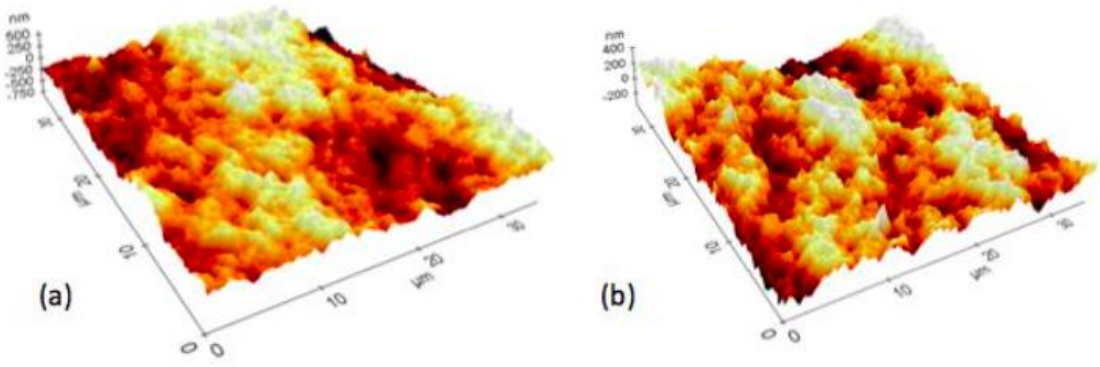

Figure 9.14 AFM image of surface topology of MDDW carbon strain gauge (a) cured at 80˚C for 3 hours (b) cured at 120˚C for 15 minutes

Further the measured track width of the 5mm strain sensors was 237.2±6.6µm and the total resistance was 203.2±11.4kΩ which were very similar values to the 5mm strain gauges where the carbon paste was cured at 120˚C for 15minutes as shown in Figure 9.15. The comparison also provides further strong experimental evidence that the resistive properties of the carbon paste are not compromised curing at a low temperature 80˚C over a longer period of time 3 hours. The track width (W) values are proportional to 1/R, see Figure 9.16, is expected as W = k ($\frac{1}{R}$), where k is a constant dependent on the material resistivity, length and thickness of the track. The experimental error will become large when the track width is comparable or less than the thickness of the track. The scatter of experimental point is thought to be due to the measurement from different 5mm strain gauge process batches in which thickness of the track varies.

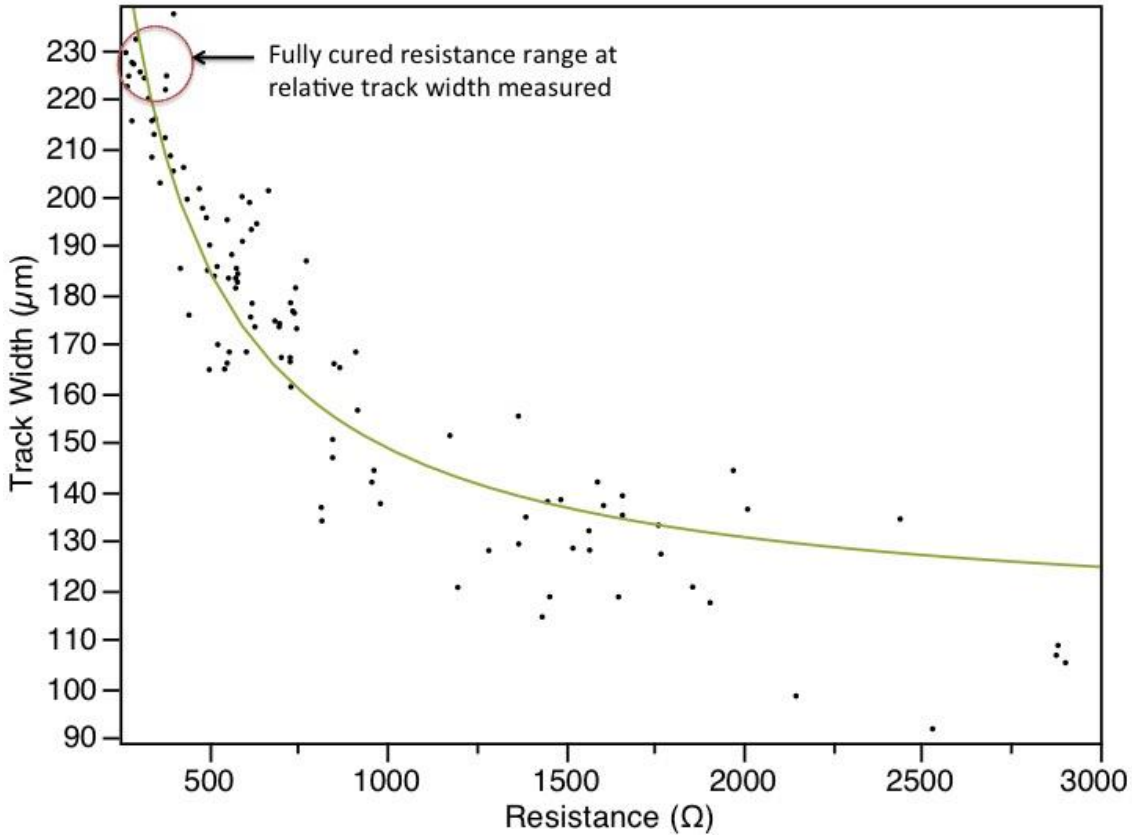

Figure 9.15 Measured track width versus resistance 5mm gauge length using 50µm ID nozzle

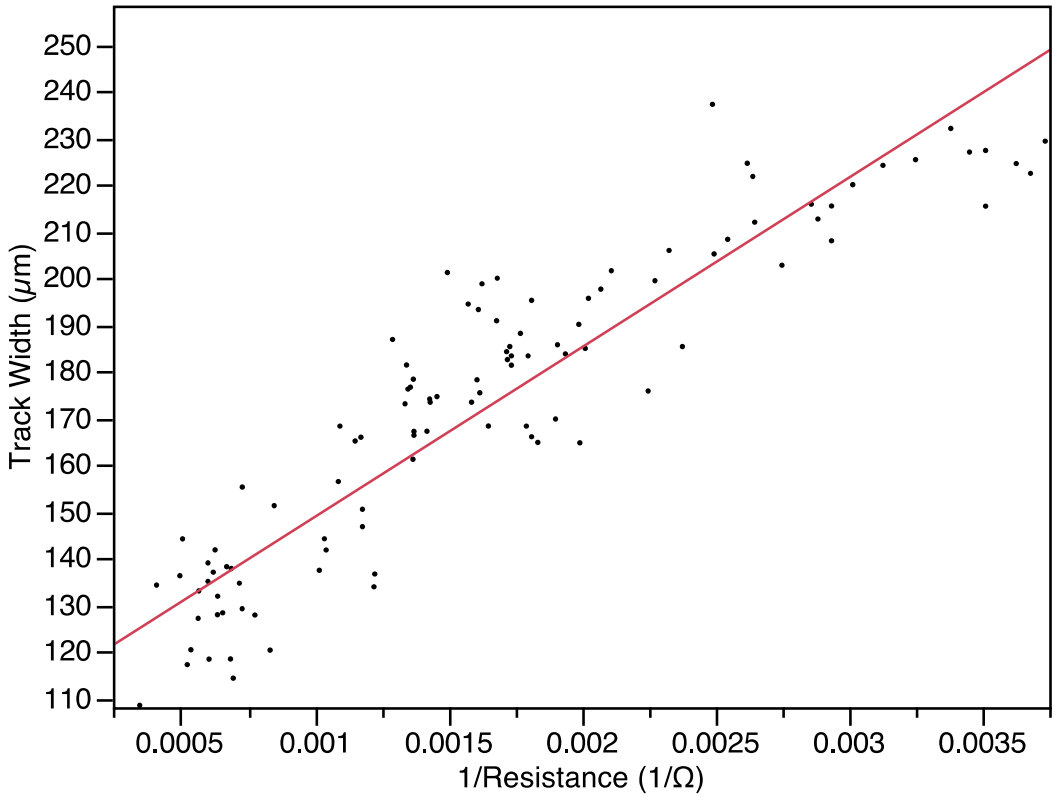

Figure 9.16 Measured track width versus 1/R for 5mm gauge length using 50μm ID nozzle

9.3.2.2.1 Gauge factor measurement

The gauge factor measurement was made using cantilever bending technique as previously described in section 8.3.3.1. Figure 9.17 shows the plot of change in resistance versus strain of integrated carbon strain gauges on parylene C coated titanium test-plate samples. The error bars indicate the standard error from five measurements carried out on each sample. The average gauge factor values were measured to be 9.97 with a standard deviation of 0.7 as shown in Table 9.4. The linearity with correlation coefficient R^2 = 0.999 which was improved and could be as a result of the absence of adhesive layer between the carbon strain gauge and the test-plate surface.

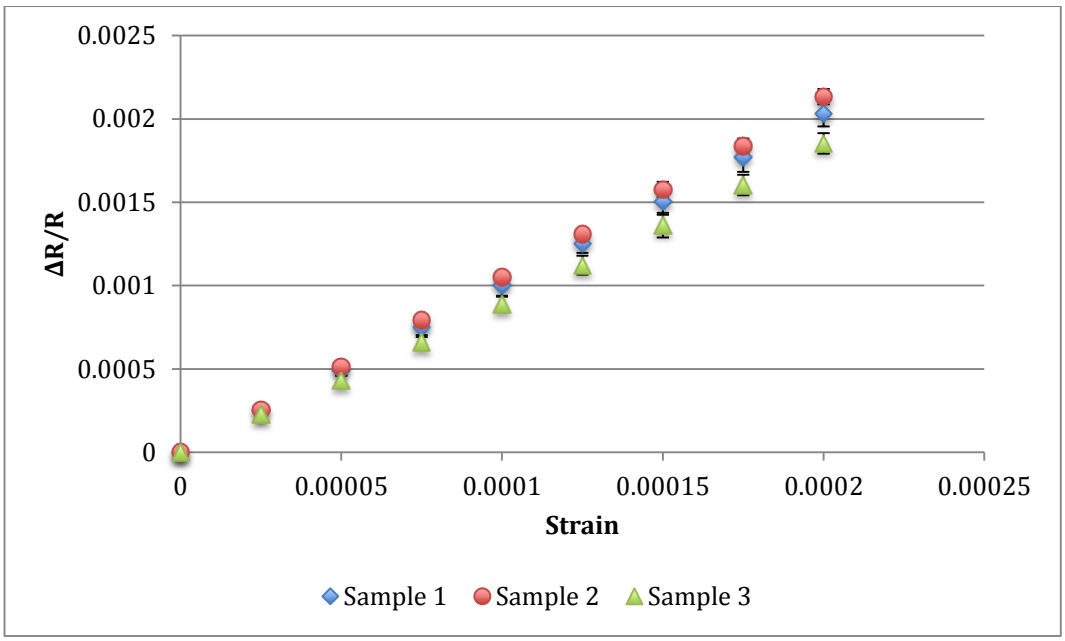

Figure 9.17 Change in resistance versus strain plot of integrated carbon strain gauges on parylene C coated titanium test-plates

Table 9.4 Gauge factor values and linearity of integrated carbon strain gauge samples on parylene C coated titanium test-plates

Sample no.	*Gauge factor*	R^2
1	10.1	0.999
2	10.6	0.999
3	9.2	0.999

9.4 Discussion

The integrated MDDW carbon strain gauge samples were fabricated on alumina ceramic and titanium test-plates to mimic materials used in medical implants. Chemical vapour deposition parylene C layer was used to ensure the biocompatibility of the integrated sensor.

To fabricate the integrated carbon sensor on the ceramic test-plate, parylene C was used purely as an encapsulation layer. The average total resistance of the strain gauges were found to increase after the application of the parylene C passivation layer. However, it was found that the measured gauge sensitivity was identical before and after parylene C coating; the measured average gauge factor was 9.8±0.6. Moreover, after parylene C coating an improvement was found in linearity between the change in resistance to applied strain where the correlation coefficient R^2 changes from 0.997 to 0.999 before and after parylene C coating. The gauge sensitivity was slightly improved when directly compared to the polyimide-based strain gauge samples with the same geometry, shown in section 8.3.3.1. The measured gauge factor of the polyimide-based strain gauges was between 8.5 and 9.5. The improved gauge sensitivity was thought due to the absence of the adhesive layer.

For standard fabrication approach of gluing the carbon strain gauges on the titanium test-plates, a polyimide based carbon strain gauge samples were attached on the titanium test-plate surface using cyanoacrylate adhesives; the measured gauge factor values ranged from 8.8 to 9.6. However, after parylene C coating to encapsulate the strain gauge on the titanium test-plate, the total measured resistance of the strain gauge was very high and on one sample was an open circuit. The reason for this effect is unknown, but may be due to the parylene CVD process interacting with adhesive. This hypothesis is strong when considering that identical processed strain gauges were fabricated directly on to ceramic and encapsulated in parylene C and also directly onto parylene C coated titanium substrate. In both cases an adhesive was not used and the very large increase in the total resistance was not observed.

A novel approach of direct writing the carbon conductive strain gauge on to the parylene C coated titanium test-plates was investigated. The parylene C acts as a dielectric layer between the sensor and the electrical conducting titanium test-plate. The curing temperature was reduced from 120˚C to 80˚C to suit the minimal temperature requirement of the parylene C layer, in order to stay in the temperature range in which the parylene C physical properties are not changed. The measured average gauge factor value using this approach was 9.97±0.7 and the samples gave very good linearity with the correlation coefficient R^2 was 0.999.

Chapter 10. Conclusion and further work

The use of commercial screen printable silver and carbon paste for fabrication of resistive and integrated resistive strain gauges utilising micro dispensing direct write (MDDW) using the nScrypt 3Dn-300 machine, was to the author's knowledge, the first time this has been carried out. The work led to the development of a method for depositing a miniature resistive strain gauge directly to a titanium metal surface without the use of an adhesive to attach the resistive strain gauge to the titanium surface. The technology will be directly applicable to medical applications, for example the deposition of resistive strain gauges to an implant. The main findings and conclusions are summarised in this chapter.

10.1 Conclusion

The nScrypt process parameters for fabricating MDDW silver based strain gauges, using a 125µm nozzle were found using a 3-level full-factorial design of experiment method. The fabricated silver strain gauges showed poor sensitivity when compared with similar geometrical size available commercial strain gauges.

The dispensing quality and control of the silver paste was improved through temperature monitoring trials of both the build chamber and the dispensing nozzle of the nScrypt 3Dn-300 machine: using these measurements the deposition process parameters were futher optimised. The measured average silver track width using the optimised parameters was 601.3±6.5µm. Further, the resistivity of MDDW silver tracks was measured to be 7.6×10^{-7} Ω-m, which was greater than the bulk silver by a factor of 2. SEM and EDX analysis showed the increased resistivity was probably due to voids and impurities (residual of organic solvent and trace magnesium element) in the silver paste material. The silver strain gauges had a low sensitivity and therefore were not suitable for medical applications.

To improve the sensitivity of the resistive strain gauge, high resistivity carbon paste MDDW strain gauges were fabricated using the nScrypt 3Dn-300 machine fitted with a

125µm ID nozzle. The fabricated strain gauges had 2 to 5 number of turns and the gauge length of 10mm. The measured average gauge factor was 14.6±1.7. To further increase the resistance of the MDDW carbon resistive strain gauge a 50µm ID nozzle was used to reduce the gauge track width. These strain gauges had 2 turns, a gauge length of 10mm and the average measured gauge factor was 16.6±1.5. The gauge sensitivity was significantly improved when compared to the strain gauge samples fabricated using 125µm ID nozzle, primarily due to the gauge track width being reduced.

To further miniaturise the strain gauge, MDDW carbon resistive strain gauges with gauge length of 5mm were fabricated using 50µm ID nozzle. The average measured gauge factor was 9.3±0.4. It was found by reducing the gauge length by a factor of 2, the gauge sensitivity was also reduced approximately by a factor of 2. However, the standard deviation from batch to batch fabrication runs the gauge factor for the miniature 5mm gauge length strain gauge was found to be smaller, therefore giving a more consistent gauge sensitivity when compared with the 10mm strain gauge.

The measured resistance of the carbon strain gauge deposited directly on to ceramic substrates was found to increase, after coating the strain gauge structures with CVD parylene C. However, the measured gauge sensitivity of the ceramic samples remained the same before and after parylene C coating. The measured gauge factor values were between 8.9 and 10.5 and the average gauge factor was 9.8±0.6. It was also observed that with parylene C passivation layer coating the strain gauge, the measured linearity between the change in resistance to applied strain, the correlation coefficient R2 was found to improve from 0.997 to 0.999.

A similar set of measurements as above was carried out, but this time the MDDW carbon strain gauges fabricated on a polyimide substrate, which was subsequently glued to a titanium base plate. The whole structure was then coated with CVD parylene C. It was found this time the gauge resistance increased significantly (even one sample

going to an infinite resistance – open circuit), this was thought to be due to the interaction between the parylene CVD process and the adhesive/polyimide layer. Further experimental work will be required to confirm the effect. Therefore, the gauge factor values were not measurable for these strain gauge samples.

To the author's knowledge the fabrication of MDDW carbon strain gauges directly to a parylene C layer coated a titanium plate was the first time this has been carried out. The process has a number of advantages over more conventional processes as it removes the layer of adhesive between the strain gauge and titanium plate.

The curing temperature of the carbon paste was reduced from 120˚C to 80˚C to be compliant with maximum process temperature of 80˚C for the deposition of the parylene C layer. The surface morphology differences of the carbon track between two curing conditions (120˚C for 15mintes, 80˚C for 3 hours) was measured and found to be very similar; therefore the assumption was made that the carbon paste could be cured at 80˚C for 15 minutes. The 80˚C temperature was also in-line with the published curing schedule for the two-part silver epoxy, which was used to connect the electrical connecting wires to the strain gauge. The measured gauge factor was 9.97±0.7, which was very similar to the same geometry strain gauges fabricated on polyimide. It was experimentally found that the linearity of the integrated strain gauge deposited on a layer of parylene C, which coated the titanium substrate was excellent, with a measured $R^2 = 0.999$. This was possibly due to the removal of the adhesive layer.

10.2 Summary of the novelty

This PhD research has provided a robust method for strain gauge sensor fabrication using the micro dispensing direct write (MDDW) nScrypt machine. The research contributes a fabrication method, which utilise a parylene C layer as the dielectric layer between the high sensitivity carbon MDDW strain gauge and titanium metal surface. This negates the need for an adhesive layer between the strain gauge and the metal surface, in this research titanium, which is used for implants. The complete structure

could then be encapsulated in parylene C producing a fully biocompatible sensor. This aspect in the project was explored using strain gauge sensor deposited on ceramic substrates. Other areas of novelty include using nScrypt direct write to deposit silver and carbon strain gauges using commercial grade screen printing paste. The technology could be easily adapted to fabricate bespoke strain gauges directly to a metal surface without using an adhesive for a variety of applications, including medical implants.

10.3 Future work

- To further reduce the strain gauge footprint and increase sensitivity a bespoke conducting paste needs to be developed with reduced electrical conductivity compared with available commercial carbon paste, and which is suitable for small diameter nozzle nScrypt dispensing.

- The presented research work has demonstrated the fabrication of uniaxial integrated strain gauge sensor using micro dispensing direct write approach on a flat substrate surface. In practical situation, the strain direction is not predictable. In future work, the fabrication of multi-axial integrated strain sensor (in rosette) on a curved surface of an implant should be explored, for detecting the strain direction, distribution and magnitude. The conformal deposition on curvature surfaces will require updating the nScrypt system with z tracking equipment.

- The author suggests that the developed bespoke sensor could be used in mandibular reconstruction. For example, Additive Manufacturing (AM) technology can be used to create a real case situation by making a skull model using stereolithography apparatus (SLA) from a patient's computer tomography (CT) scans. The medical grade titanium scaffold can be fabricated using the selective laser sintering (SLM) or electron beam melting (EBM) to fit the SLA skull model. The integrated carbon strain gauge then fabricated on the titanium

scaffold using MDDW as presented in this research thesis. The connecting wires to the strain gauge can be replaced by MDDW silver tracks. A microchip and micro battery embedded inside the denture will allow wireless transmission of electrical information for continuous strain monitoring. An articulate can be fitted in the skull model to simulate the biting force to evaluate the sensor *in situ*.

- Develop other miniature passive circuit components for example high Q inductors and capacitors using nScrypt direct write technology on parylene C and integrate with the strain gauge. The approach could be used to form a passive circuit, which can be remotely interrogated to obtain strain information.

- The fabricated strain gauge sensor on titanium test-plates has shown good gauge performance for example gauge sensitivity and linearity. In this work the carbon conductive strain gauge sensing pattern was directly deposited on parylene C coated titanium surface, the carbon paste was cured at 80˚C for 3 hours along with the parylene C layer. Parylene C is known to maintain its physical and mechanical properties for ten years provided the maximum temperature seen by paraylene C is less or equal to 80˚C. To improve the versatility of process using paraylene C layers, its biocompatibility over a much wider temperature range needs to be investigated.

- The presented work on performance of strain gauge was carried out under room temperatures (20 to 25C). For medical implant application, the sensor performance tests need to be carried out at near body temperature of 37˚C and to include the temperature fluctuations of the order of ±1˚C from the core body temperature (37˚C). Preliminary work was carried out over this research period, but difficulties were encountered in maintaining the temperature of 37˚C during the strain gauge electrical and mechanical characterisation.

- It was found this time the gauge resistance increased significantly (even one sample going to an infinite resistance – open circuit), when strain gauges were fabricated on polyimide and subsequently glued to the implant, and then coasted with prylene C at 80˚C using the CVD process. This was thought to be due to the interaction between the parylene CVD process and the adhesive/polyimide layer. Further experimental work will be required to confirm this effect.

Reference

[1] Wohlers T. *Wohlers report 2012.* Fort Collins, Col.: Wohlers Associates; 2012.

[2] M. Bak, A. S. Jacobson, D. Buchbinder, and M. L. Urken, “Contemporary reconstruction of the mandible.,” *Oral Oncol.*, vol. 46, no. 2, pp. 71–6, Feb. 2010.

[3] D. D. D’Lima, B. J. Fregly, and C. W. Colwell, “Implantable sensor technology: measuring bone and joint biomechanics of daily life in vivo.,” *Arthritis Res. Ther.*, vol. 15, no. 1, p. 203, Jan. 2013.

[4] R. Al Nazer, J. Lanovaz, C. Kawalilak, J. D. Johnston, and S. Kontulainen, “Direct in vivo strain measurements in human bone-a systematic literature review.,” *J. Biomech.*, vol. 45, no. 1, pp. 27–40, Jan. 2012.

[5] L. E. Claes and J. L. Cunningham, “Monitoring the mechanical properties of healing bone.,” *Clin. Orthop. Relat. Res.*, vol. 467, no. 8, pp. 1964–71, Aug. 2009.

[6] J. B. Jones, A. Tallis, V. Tillotta, A. Moroz, and D. I. (David I. . Wimpenny, “Rheological Properties of HA Slurry for the Production of Bone Scaffolds by Layer Manufacturing ,” in *8th National Conference on Rapid Design, Prototyping and Manufacture*, 2007.

[7] A. Tallis, J. B. Jones, and D. I. (David I. . Wimpenny, “Rapid manufacturing of bioceramic implants by direct writing,” in *The 2nd International Conference on Additive Technologies*, 2008.

[8] S. Wüst, R. Müller, and S. Hofmann, *Controlled Positioning of Cells in Biomaterials—Approaches Towards 3D Tissue Printing*, vol. 2, no. 4. 2011.

[9] M. Ueda, Y. Sumi, H. Mizuno, M. Honda, T. Oda, K. Wada, J. S. Boo, and K.-I. Hata, “Tissue engineering: applications for maxillofacial surgery,” *Mater. Sci. Eng. C*, vol. 13, no. 1–2, pp. 7–14, Sep. 2000.

[10] J. Franco, P. Hunger, M. E. Launey, a P. Tomsia, and E. Saiz, “Direct write assembly of calcium phosphate scaffolds using a water-based hydrogel.,” *Acta Biomater.*, vol. 6, no. 1, pp. 218–28, Jan. 2010.

[11] T. M. Keaveny, E. F. Morgan, O. C. Yeh, C. Material, C. Bone, and T. Bone, “BONE MECHANICS,” in *STANDARD HANDBOOK OF BIOMEDICAL ENGINEERING AND DESIGN*, 2004, pp. 1–24.

[12] S. Ramakrishna, J. Mayer, E. Wintermantel, and K. W. Leong, “Biomedical applications of polymer-composite materials: a review,” *Compos. Sci. Technol.*, vol. 61, no. 9, pp. 1189–1224, Jul. 2001.

[13] L. L. Hench, “The skeletal system,” in *Biomaterials, artificial organs and tissue engineering*, L. L. Hench and J. R. Jones, Eds. 2004, pp. 79–96.

[14] I. G. Turner, “Ceramics and Glasses,” in *Biomedical Materials*, R. Narayan, Ed. Boston, MA: Springer US, 2009, pp. 3–39.

[15] D. Lacroix and J. A. Planell, “Biomaterials: Processing, Characterization, and Applications,” in *Biomedical Materials*, R. Narayan, Ed. Boston, MA: Springer US, 2009, pp. 123–154.

[16] L. L. Hench, “Repair of skeletal tissues,” in *Biomaterials, artificial organs and tissue engineering*, L. L. Hench and J. R. Jones, Eds. 2004, pp. 119–128.

[17] H. Mehboob and S.-H. Chang, “Application of composites to orthopedic prostheses for effective bone healing: A review,” *Compos. Struct.*, vol. 118, pp. 328–341, Dec. 2014.

[18] J. Q. Swift, “Treatment Planning for Implant Surgery,” in *Clinician’s Manual of Oral and Maxillofacial Surgery*, 2001, pp. 327–337.

[19] M. Bohner, L. Galea, and N. Doebelin, “Calcium phosphate bone graft substitutes: Failures and hopes,” *J. Eur. Ceram. Soc.*, vol. 32, no. 11, pp. 2663–2671, Aug. 2012.

[20] D. W. Hutmacher, “Scaffolds in tissue engineering bone and cartilage.,” *Biomaterials*, vol. 21, no. 24, pp. 2529–43, Dec. 2000.

[21] T. Yamamuro, “Bioceramics,” in *Biomechanics and Biomaterials in Orthopedics*, 2004, pp. 22–33.

[22] J. R. Jones, “Scaffolds for tissue engineering,” in *Biomaterials, artificial organs and tissue engineering*, L. L. Hench and J. R. Jones, Eds. 2004, pp. 201–214.

[23] M. Zhao, M. An, Q. Wang, X. Liu, W. Lai, X. Zhao, S. Wei, and J. Ji, “Quantitative proteomic analysis of human osteoblast-like MG-63 cells in response to bioinert implant material titanium and polyetheretherketone.,” *J. Proteomics*, vol. 75, no. 12, pp. 3560–73, Jun. 2012.

[24] J. T. W. Kuo, L.-Y. Chang, P.-Y. Li, T. Hoang, and E. Meng, “A microfluidic platform with integrated flow sensing for focal chemical stimulation of cells and tissue,” *Sensors Actuators B Chem.*, vol. 152, no. 2, pp. 267–276, Mar. 2011.

[25] J. F. Mano, R. a Sousa, L. F. Boesel, N. M. Neves, and R. L. Reis, “Bioinert, biodegradable and injectable polymeric matrix composites for hard tissue replacement: state of the art and recent developments,” *Compos. Sci. Technol.*, vol. 64, no. 6, pp. 789–817, May 2004.

[26] J. M. Williams, A. Adewunmi, R. M. Schek, C. L. Flanagan, P. H. Krebsbach, S. E. Feinberg, S. J. Hollister, and S. Das, “Bone tissue engineering using polycaprolactone scaffolds fabricated via selective laser sintering.,” *Biomaterials*, vol. 26, no. 23, pp. 4817–27, Aug. 2005.

[27] R. a. Barry, R. F. Shepherd, J. N. Hanson, R. G. Nuzzo, P. Wiltzius, and J. a. Lewis, “Direct-Write Assembly of 3D Hydrogel Scaffolds for Guided Cell Growth,” *Adv. Mater.*, vol. 21, no. 23, pp. 2407–2410, Jun. 2009.

[28] J. A. Szivek, D. S. Margolis, B. K. Garrison, E. Nelson, R. K. Vaidyanathan, and D. W. DeYoung, “TGF-β1-Enhanced TCP-Coated Sensate Scaffolds Can Detect Bone Bonding,” *J Biomed Mater Res B Appl Biomater*, vol. 73, no. 1, pp. 43–53, 2005.

[29] T. Srichana and D. Abraham J, “Polymeric Biomaterials,” in *Biomedical Materials*, 2009, pp. 83–118.

[30] V. Cannillo, F. Chiellini, P. Fabbri, and a. Sola, “Production of Bioglass?? 45S5 - Polycaprolactone composite scaffolds via salt-leaching,” *Compos. Struct.*, vol. 92, no. 8, pp. 1823–1832, 2010.

[31] C. M. Smith, T. D. Roy, A. Bhalkikar, B. Li, J. J. Hickman, and K. H. Church, “Engineering a titanium and polycaprolactone construct for a biocompatible interface between the body and artificial limb.,” *Tissue Eng. Part A*, vol. 16, no. 2, pp. 717–724, 2010.

[32] Y. Wang, Y. Shen, Z. Wang, J. Yang, N. Liu, and W. Huang, “Development of highly porous titanium scaffolds by selective laser melting,” *Mater. Lett.*, vol. 64, no. 6, pp. 674–676, Mar. 2010.

[33] J. Van Der Stok, O. P. Van Der Jagt, S. Amin Yavari, M. F. P. De Haas, J. H. Waarsing, H. Jahr, E. M. M. Van Lieshout, P. Patka, J. a N. Verhaar, A. a. Zadpoor, and H. Weinans, “Selective laser melting-produced porous titanium scaffolds regenerate bone in critical size cortical bone defects,” *J. Orthop. Res.*, vol. 31, no. 5, pp. 792–799, 2013.

[34] R. Tejero, E. Anitua, and G. Orive, “Toward the biomimetic implant surface: Biopolymers on titanium-based implants for bone regeneration,” *Prog. Polym. Sci.*, Jan. 2014.

[35] L. L. Hench, “Joint Replacement,” in *Biomaterials, artificial organs and tissue engineering*, L. L. Hench and J. R. Jones, Eds. 2004, p. 140.

[36] Y.-K. Jun, W. H. Kim, O.-K. Kweon, and S.-H. Hong, “The fabrication and biochemical evaluation of alumina reinforced calcium phosphate porous implants,” *Biomaterials*, vol. 24, no. 21, pp. 3731–3739, Sep. 2003.

[37] H. Kokemueller, S. Spalthoff, M. Nolff, F. Tavassol, H. Essig, C. Stuehmer, K.-H. Bormann, M. Rücker, and N.-C. Gellrich, “Prefabrication of vascularized bioartificial bone grafts in vivo for segmental mandibular reconstruction: experimental pilot study in sheep and first clinical application.,” *Int. J. Oral Maxillofac. Surg.*, vol. 39, no. 4, pp. 379–87, Apr. 2010.

[38] J.-P. Kruth, G. Levy, F. Klocke, and T. H. C. Childs, “Consolidation phenomena in laser and powder-bed based layered manufacturing,” *CIRP Ann. - Manuf. Technol.*, vol. 56, no. 2, pp. 730–759, Jan. 2007.

[39] W.-Y. Yeong, C.-K. Chua, K.-F. Leong, and M. Chandrasekaran, “Rapid prototyping in tissue engineering: challenges and potential.,” *Trends Biotechnol.*, vol. 22, no. 12, pp. 643–52, Dec. 2004.

[40] G. N. Levy, R. Schindel, and J. P. Kruth, “RAPID MANUFACTURING AND RAPID TOOLING WITH LAYER MANUFACTURING (LM) TECHNOLOGIES, STATE OF THE ART AND FUTURE PERSPECTIVES,” *CIRP Ann. - Manuf. Technol.*, vol. 52, no. 2, pp. 589–609, Jan. 2003.

[41] D. Kalisz, “Stereolithography: speeding time to market,” in *Proceedings of WESCON ’94*, 1993, no. Figure 3, pp. 286–290.

[42] A. Woesz, “Virtual Prototyping & Bio Manufacturing in Medical Applications,” in *Virtual Prototying & Bio Manufacturing in Medical Applications*, B. Bidanda and P. Bártolo, Eds. Boston, MA: Springer US, 2008, pp. 171–206.

[43] F. Scalera, C. Esposito Corcione, F. Montagna, A. Sannino, and A. Maffezzoli, “Development and characterization of UV curable epoxy/hydroxyapatite suspensions for stereolithography applied to bone tissue engineering,” *Ceram. Int.*, Jul. 2014.

[44] N. Peckitt, “PROTHETIC IMPLANTS U.S. PATENT NO. 6254639,” 6254639 B1, 2001.

[45] H. Yamada, K. Ishihama, K. Yasuda, Y. Hasumi-Nakayama, M. Okayama, T. Yamada, and K. Furusawa, “Precontoured mandibular plate with three-dimensional model significantly shortened the mandibular reconstruction time,” *Asian J. Oral Maxillofac. Surg.*, vol. 22, no. 4, pp. 198–201, Oct. 2010.

[46] P. Chennakesava and Y. S. Narayan, “Fused Deposition Modeling,” *Castle Island’s Worldw. Guid. to Rapid Prototyp.*, pp. 2–4, 2012.

[47] C. K. Chua, K. F. Leong, and K. H. Tan, “Specialized Fabrication Processes: Rapid Prototyping,” in *Biomedical Materials*, 2009, pp. 493–523.

[48] H. Chim, D. W. Hutmacher, a M. Chou, a L. Oliveira, R. L. Reis, T. C. Lim, and J.-T. Schantz, “A comparative analysis of scaffold material modifications for load-bearing applications in bone tissue engineering.,” *Int. J. Oral Maxillofac. Surg.*, vol. 35, no. 10, pp. 928–34, Oct. 2006.

[49] R. Ganeriwala and T. I. Zohdi, “Multiphysics Modeling and Simulation of Selective Laser Sintering Manufacturing Processes,” *Procedia CIRP*, vol. 14, pp. 299–304, 2014.

[50] S. Lohfeld, “A method to fabricate small features on scaffolds for tissue engineering via selective laser sintering,” *J. Biomed. Sci. Eng.*, vol. 03, no. 02, pp. 138–147, 2010.

[51] D. Wang, Y. Yang, R. Liu, D. Xiao, and J. Sun, “Study on the designing rules and processability of porous structure based on selective laser melting (SLM),” *J. Mater. Process. Technol.*, vol. 213, no. 10, pp. 1734–1742, Oct. 2013.

[52] L. Löber, F. P. Schimansky, U. Kühn, F. Pyczak, and J. Eckert, “Selective laser melting of a beta-solidifying TNM-B1 titanium aluminide alloy,” *J. Mater. Process. Technol.*, vol. 214, no. 9, pp. 1852–1860, Sep. 2014.

[53] E. Brandl, U. Heckenberger, V. Holzinger, and D. Buchbinder, “Additive manufactured AlSi10Mg samples using Selective Laser Melting (SLM): Microstructure, high cycle fatigue, and fracture behavior,” *Mater. Des.*, vol. 34, pp. 159–169, Feb. 2012.

[54] L. Mullen, R. C. Stamp, W. K. Brooks, E. Jones, and C. J. Sutcliffe, “Selective Laser Melting: a regular unit cell approach for the manufacture of porous, titanium, bone in-growth constructs, suitable for orthopedic applications.,” *J. Biomed. Mater. Res. B. Appl. Biomater.*, vol. 89, no. 2, pp. 325–34, May 2009.

[55] M. Kawase, T. Hayashi, M. Asakura, A. Mieki, H. Fuyamada, M. Sassa, S. Nakano, M. Hagiwara, T. Shimizu, and T. Kawai, “Cell Proliferation Ability of Mouse Fibroblast-Like Cells and Osteoblast-Like Cells on a Ti-6Al-4V Alloy Film Produced by Selective Laser Melting,” *Mater. Sci. Appl.*, vol. 05, no. 07, pp. 475–483, 2014.

[56] K. Puebla, L. E. Murr, S. M. Gaytan, E. Martinez, F. Medina, and R. B. Wicker, “Effect of Melt Scan Rate on Microstructure and Macrostructure for Electron Beam Melting of Ti-6Al-4V,” vol. 2012, no. May, pp. 259–264, 2012.

[57] D. Drs, J. Poukens, I. P. Laeven, and I. M. Beerens, “Custom surgical implants using additive manufacturing,” pp. 30–33, 2010.

[58] J. Parthasarathy, B. Starly, S. Raman, and A. Christensen, “Mechanical evaluation of porous titanium (Ti6Al4V) structures with electron beam melting (EBM).,” *J. Mech. Behav. Biomed. Mater.*, vol. 3, no. 3, pp. 249–59, Apr. 2010.

[59] J. Winder, “Computer Assisted Cranioplasty,” in *Virtual Prototying & Bio Manufacturing in Medical Applications*, B. Bidanda and P. Bártolo, Eds. 2008, pp. 1–19.

[60] S. Singare, L. Dichen, L. Bingheng, L. Yanpu, G. Zhenyu, and L. Yaxiong, “Design and fabrication of custom mandible titanium tray based on rapid prototyping.,” *Med. Eng. Phys.*, vol. 26, no. 8, pp. 671–6, Oct. 2004.

[61] M. W. Naing, C. K. Chua, K. F. Leong, and Y. Wang, “Fabrication of customised scaffolds using computer-aided design and rapid prototyping techniques,” *Rapid Prototyp. J.*, vol. 11, no. 4, pp. 249–259, 2005.

[62] M. A. Jayaram, *Mechanics of Materials with Programs in C*. 2007.

[63] “Standard Test Methods for Performance Characteristics of Metallic Bonded Resistance Strain Gauges. E251-92. ASTM Standard,” vol. 92, no. Reapproved 2009, pp. 1–20, 2009.

[64] D. Lee, H. P. Hong, M. J. Lee, C. W. Park, and N. K. Min, “A prototype high sensitivity load cell using single walled carbon nanotube strain gauges,” *Sensors Actuators A Phys.*, vol. 180, pp. 120–126, Jun. 2012.

[65] W. M. Murray and W. R. Miller, “Fundamental Concepts for Strain Gages,” in *The Bonded Electrical Resistance Strain Gage*, New York: Oxford University Press, 1992, pp. 3–41.

[66] J. Abduo and K. Lyons, “Effect of vertical misfit on strain within screw-retained implant titanium and zirconia frameworks.,” *J. Prosthodont. Res.*, vol. 56, no. 2, pp. 102–9, Apr. 2012.

[67] G. Y. Yang, V. J. Bailey, W. C. Tang, and J. H. Keyak, “Fabrication and characterization of microscale sensors for bone surface strain measurement,” *Proc. IEEE Sensors, 2004.*, pp. 1355–1358, 2004.

[68] P. F. Yang, G.-P. Brüggemann, and J. Rittweger, “What do we currently know from in vivo bone strain measurements in humans?,” *J. Musculoskelet. Neuronal Interact.*, vol. 11, no. 1, pp. 8–20, Mar. 2011.

[69] K. Hoffmann, *An Introduction to Measurements using Strain Gages*. Hottinger Baldwin Messtechnik Gmbh, Darmstadt, 1989.

[70] I. C. Morgan, W. Grove, P. A. Us, H. T.- Hall, C. Spnngs, J. M. Green, G. Flexner, S. P. A. Us, C. E.- Geltzi, X. H. Dre, and A. Ag, “ORTHOPAEDIC IMPLANT WITH SENSORS U.S. PATENT NO. 8083741,” 2011.

[71] F. Bush, P. E. C. Barrett, and A. E. E. Waggle, “METHOD FOR MEASURING THE STRENGTH OF HEALING BONE AND RELATED TISSUES U.S. PATENT NO. 7878988,” 2011.

[72] W. C. de Jong, J. H. Koolstra, L. J. van Ruijven, J. a M. Korfage, and G. E. J. Langenbach, “A fully implantable telemetry system for the long-term measurement of habitual bone strain.,” *J. Biomech.*, vol. 43, no. 3, pp. 587–91, Feb. 2010.

[73] G. Y. Yang, S. Member, G. Johnson, W. C. Tang, S. Member, J. H. Keyak, and A. Design, “Parylene-Based Strain Sensors for Bone,” vol. 7, no. 12, pp. 1693–1697, 2007.

[74] J. A. Lewis, “Direct-write assembly of ceramics from colloidal inks,” vol. 6, pp. 245–250, 2002.

[75] Q. Fu, E. Saiz, and A. P. Tomsia, “Direct ink writing of highly porous and strong glass scaffolds for load-bearing bone defects repair and regeneration.,” *Acta Biomater.*, vol. 7, no. 10, pp. 3547–54, Oct. 2011.

[76] S. Yang, H. Yang, X. Chi, J. R. G. Evans, I. Thompson, R. J. Cook, and P. Robinson, “Rapid prototyping of ceramic lattices for hard tissue scaffolds,” *Mater. Des.*, vol. 29, no. 9, pp. 1802–1809, Oct. 2008.

[77] J. M. Fitz-Gerald, D. B. Chrisey, A. Piqu, R. C. Y. Auyeung, R. Mohdi, H. D. Young, H. D. Wu, S. Lakeou, and R. Chung, “Matrix assisted pulsed laser evaporation direct write (MAPLE DW): A new method to rapidly prototype active and passive electronic circuit elements,” *Solid Free. Addit. Fabr.*, vol. 625, pp. 99–110 220, 2000.

[78] X. C. X. Chen, K. Church, and H. Y. H. Yang, “High speed non-contact printing for solar cell front side metallization,” *Photovolt. Spec. Conf. PVSC 2010 35th IEEE*, pp. 1343–1347, 2010.

[79] A. A. Gheethan, D. E. Anagnostou, A. Amert, and K. W. Whites, “A Printed Paper-Based inverted F-Antenna (PIFA) for WLAN Application.”

[80] I. T. Nassar, S. Member, T. M. Weller, and S. Member, “Development of Novel 3-D Cube Antennas for Compact Wireless Sensor Nodes,” vol. 60, no. 2, pp. 1059–1065, 2012.

[81] A. Piqué, D. W. Weir, P. K. Wu, B. Pratap, C. B. Arnold, and B. R. Ringeisen, “Direct-Write of Sensor Devices by a Laser Forward Transfer Technique,” vol. 4637, pp. 361–368, 2002.

[82] R. Faddoul, N. Reverdy-Bruas, and A. Blayo, “Formulation and screen printing of water based conductive flake silver pastes onto green ceramic tapes for electronic applications,” *Mater. Sci. Eng. B*, vol. 177, no. 13, pp. 1053–1066, Aug. 2012.

[83] D. a. Roberson, R. B. Wicker, L. E. Murr, K. Church, and E. MacDonald, “Microstructural and Process Characterization of Conductive Traces Printed from Ag Particulate Inks,” *Materials (Basel).*, vol. 4, no. 12, pp. 963–979, May 2011.

[84] D. B. Chrisey and A. Piqué, “Introduction to Direct-Write Technologies for Rapid Prototyping,” in *Direct-Write Technologies for Rapid Prototyping Applications*, San Diego: Academic Press, 2002, pp. 1–13.

[85] K. Hon, L. Li, and I. Hutchings, “Direct writing technology—Advances and developments,” *CIRP Ann. Manuf. Technol.*, vol. 57, no. 2, pp. 601–620, Jan. 2008.

[86] G. M. Gratson, “Direct writing in three dimensions,” no. August, pp. 32–39, 2004.

[87] a. Piqué, S. a. Mathews, B. Pratap, R. C. Y. Auyeung, B. J. Karns, and S. Lakeou, “Embedding electronic circuits by laser direct-write,” *Microelectron. Eng.*, vol. 83, no. 11–12, pp. 2527–2533, Nov. 2006.

[88] J. a. Lewis, “Direct Ink Writing of 3D Functional Materials,” *Adv. Funct. Mater.*, vol. 16, no. 17, pp. 2193–2204, Nov. 2006.

[89] D. B. Wallace, W. R. Cox, and D. J. Hayes, “Direct Write Using Ink-Jet Techniques,” in *Direct-Write Technologies for Rapid Prototyping Applications*, 2002, pp. 177–227.

[90] P. G. Clem, N. S. Bell, G. L. Brennecka, and D. B. Dimos, “Micropen Printing of Electronic Components,” in *Direct-Write Technologies for Rapid Prototyping Applications*, A. Pique and D. B. Chrisey, Eds. 2002, pp. 229–259.

[91] “MicroPen Technologies | Precisely write patterns with any flowable material on any surface imaginable.” [Online]. Available: http://www.micropen.com/mm/Micropenning/how_it_works.php.

[92] NScrypt, “nScrypt User’s Guide,” vol. 3. 2012.

[93] B. Ando, S. Baglio, S. La Malfa, and G. L’Episcopo, “All inkjet printed system for strain measurement,” in *2011 IEEE SENSORS Proceedings*, 2011, pp. 215–217.

[94] R. Edson, R. Bonadiman, S. Neto, I. Nokia, and D. T. Indt, “Finite Element Simulation of Inkjet Printed Strain Gage on Polyimide Substrates Applied to Flexible Boards,” pp. 1–5, 2009.

[95] M. Maiwald, C. Werner, V. Zoellmer, and M. Busse, “INKtelligent printed strain gauges,” *Procedia Chem.*, vol. 1, no. 1, pp. 907–910, Sep. 2009.

[96] M. Maiwald, C. Werner, V. Zoellmer, and M. Busse, “INKtelligent printed strain gauges,” *Sensors Actuators A Phys.*, vol. 162, no. 2, pp. 198–201, Aug. 2010.

[97] C. a Gutierrez and E. Meng, “Low-cost carbon thick-film strain sensors for implantable applications,” *J. Micromechanics Microengineering*, vol. 20, no. 9, p. 095028, Sep. 2010.

[98] C. A. Gutierrez and E. Meng, “An implantable low-cost carbon thick-film strain sensors for implantable applications,” in *Journal of Micromechanics and Microengineering*, 2010, vol. 20, no. 9, p. 095028.

[99] A. Bessonov, M. Kirikova, S. Haque, I. Gartseev, and M. J. a. Bailey, “Highly reproducible printable graphite strain gauges for flexible devices,” *Sensors Actuators A Phys.*, vol. 206, pp. 75–801. Bessonov, A., Kirikova, M., Haque, S., Gar, Feb. 2014.

[100] G. Di Girolamo, “Strain gauges fabricated by C+ ion implantation in bulk polymers,” *Sensors Actuators A Phys.*, vol. 178, pp. 136–140, May 2012.

[101] J. Longtin, S. Sampath, R. J. Gambino, S. Tankiewicz, and R. Greenlaw, “Sensors for harsh environments by direct write thermal spray,” in *Proceedings of IEEE Sensors*, 2002, vol. 1, no. M, pp. 598–601.

[102] J. Li, J. P. Longtin, S. Tankiewicz, A. Gouldstone, and S. Sampath, “Interdigital capacitive strain gauges fabricated by direct-write thermal spray and ultrafast laser micromachining,” *Sensors Actuators A Phys.*, vol. 133, no. 1, pp. 1–8, Jan. 2007.

[103] Y.-T. Huang, S.-C. Huang, C.-C. Hsu, R.-M. Chao, and T. K. Vu, “Design and fabrication of single-walled carbon nanonet flexible strain sensors.,” *Sensors (Basel).*, vol. 12, no. 3, pp. 3269–80, Jan. 2012.

[104] P. Alpuim, S. a. Filonovich, C. M. Costa, P. F. Rocha, M. I. Vasilevskiy, S. Lanceros-Mendez, C. Frias, a. T. Marques, R. Soares, and C. Costa, “Fabrication of a strain sensor for bone implant failure detection based on piezoresistive doped nanocrystalline silicon,” *J. Non. Cryst. Solids*, vol. 354, no. 19–25, pp. 2585–2589, May 2008.

[105] J. Cordey and E. Gautier, “Strain gauges used in the mechanical testing of bones. Part II: ‘In vitro’ and ‘in vivo’ technique.,” *Injury*, vol. 30 Suppl 1, pp. A14–20, Jan. 1999.

[106] N.-S. Kim and K. N. Han, “Future direction of direct writing,” *J. Appl. Phys.*, vol. 108, no. 10, p. 102801, 2010.

[107] B. Li, P. A. Clark, and K. H. Church, “Robust Printing and Dispensing Solutions with Three Sigma Volumetric Control for 21st Century Manufacturing and Packaging,” *Mater. Res. Soc. Symp. N – Print. Methods Electron. Photonics Biomater.*, pp. 1–7, 2007.

[108] G. I. Hay, P. S. a. Evans, D. J. Harrison, D. Southee, G. Simpson, and P. M. Harrey, “Conductive lithographic film fabricated resistive strain gauges,” *Proc. IEEE Sensors 2003 (IEEE Cat. No.03CH37498)*, vol. 1, pp. 248–252.

[109] J. Sidhu and J. L. MacDonald, “Direct Write and Additive Manufacturing Process. US Patent 2010/0171792 A1,” US 2010/0171792 A1, 2010.

[110] T. H. J. van Osch, J. Perelaer, a. W. M. de Laat, and U. S. Schubert, “Inkjet Printing of Narrow Conductive Tracks on Untreated Polymeric Substrates,” *Adv. Mater.*, vol. 20, no. 2, pp. 343–345, Jan. 2008.

[111] G. Y. Yang, V. J. Bailey, G. Lin, W. C. Tang, and J. H. Keyak, “Design of microfabricated strain gauge array to monitor bone deformation in vitro and in vivo,” *Proceedings. Fourth IEEE Symp. Bioinforma. Bioeng.*, pp. 30–37, 2004.

[112] S. Martin, “Personal communication.” 2013.

[113] a. Arshak, K. Arshak, D. Morris, O. Korostynska, and E. Jafer, “Investigation of TiO2 thick film capacitors for use as strain gauge sensors,” *Sensors Actuators A Phys.*, vol. 122, no. 2, pp. 242–249, Aug. 2005.

[114] B. C. MacDonald, “Basic components and elements of surface topography,” 2006. [Online]. Available: http://www.bcmac.com/pdf_files/surface finish 101.pdf.

[115] M. Dušek, L. Zou, and C. Hunt, “Rheology Testing of Solder Pastes and Conductive Adhesives – A Guide,” 2002.

[116] I. FLIR Systems, “Thermal imaging cameras keeping viral infections under control.” [Online]. Available: http://www.flir.com/cs/emea/en/view/?id=42362.

[117] J. W. Evans and J. K. Beddow, “Characterization of Particle Morphology and Rheological Behavior in Solder Paste Influence of Particle Size,” no. 8714429, pp. 224–231, 1987.

[118] W. M. Murray and W. R. Miller, “Strain Gage Selection And Application,” in *The Bonded Electrical Resistance Strain Gage*, pp. 390–401.

[119] K. Gilleo, *Polymer Thick Film: Today’s Emerging Technology for a Clean Environment Tomorrow*. 1995.

[120] P. G. Slade, *Electrical Contacts: Principles and Applications, Second Edition*. 2013.

[121] B. Li and N. A. Trail, “Robust Direct-Write Dispensing Tool and Solutions For Micro/Meso-scale Manufacturing and Packaging,” in *Proceedings of the 2007 International Manufacturing Science And Engineering Conference*, 2007, pp. 1–7.

[122] “Parylene and Conformal Coatings from Para Tech Coating UK Limited.” [Online]. Available: http://www.paratechcoating.co.uk.

Appendix - 1 Certificate of conformity of parylene C coating

Certificate of Conformity

No. 9768

Para Tech Coating UK Ltd
Unit 3
Gladstone Road
Northampton NN5 7RX

tel 01604 757756
fax 01604 757756
e-mail info@paratechcoating.co.uk

Customer : **DE Montfort University**
Faculty Of Technology
Gate way House
Leciester
LE1 9BH

phone:
fax:

Customer Order no : P214512_1

PTCUK Job no : **9568**

Item	Qty	Description	Serial Numbers	Coating Type	Coating Thickness
1	12	Samples		Parylene C	3.5 microns

Special Conditions

The material used for this coating is listed in QPL-46058-84 as a product qualified under MIL-I-46058

Certified that the goods listed have been inspected and unless otherwise stated conform to the full requirements of the purchase order.

Signed:

Russell Thomas, Managing Director

Date: 25.07.14

Certificate No. FS 512544

Qform03
Revision 2 04 April 2011

Appendix-2 Two-part silver epoxy technical data sheet

EPO-TEK® H20E

Technical Data Sheet

For Reference Only

Electrically Conductive, Silver Epoxy

Number of Components:	Two	Frozen Syringe	Minimum Bond Line Cure Schedule*:	
Mix Ratio By Weight:	1:1		175°C	45 Seconds
Specific Gravity:		2.67	150°C	5 Minutes
Part A	2.03		120°C	15 Minutes
Part B	3.07		100ºC	2 Hours
Pot Life:	2.5 Days		80°C	3 Hours
Shelf Life:	One year at 23°C	One year at -40°C		

*Note: Container(s) should be kept closed when not in use. For filled systems, mix contents of each container (A & B) thoroughly before mixing the two together. *Please see Applications Note available on our website.*

Product Description:

EPO-TEK® H20E is a two component, 100% solids silver-filled epoxy system designed specifically for chip bonding in microelectronic and optoelectronic applications. It is also used extensively for thermal management applications due to its high thermal conductivity. It has proven itself to be extremely reliable over many years of service and is still the conductive adhesive of choice for new applications. Also available in a single component frozen syringe.

EPO-TEK® H20E Advantages & Application Notes:

- Processing info: It can be applied by many dispensing, stamping and screen printing techniques.
  - Dispensing: compatible with pressure/time delivery, auger screws, fluid jetting and G27 needles, in a single-component fashion.
  - Screen Printing: best using >200 metal mesh, with polymer squeegee blade with 80D hardness.
  - Stamping: small dots 6 mil in diameter can be realized.
- Misc / Other notes
  - Many technical papers written over 30-40 year lifetime. Contact techserv@epotek.com.
  - Over 1 trillion chips attached at a single company: no failures, Six Sigma and Certified Parts Supplier award winner.
  - Versatility in curing techniques including box oven, SMT style tunnel oven, heater gun, hot plate, IR, convection, or inductor coil.
  - Many custom modified products available, for the following improvements: viscosity and appearance, flexibility and thermal conductivity. Contact techserv@epotek.com for your best recommendation.
  -

Typical Properties: ***(To be used as a guide only, not as a specification. Data below is not guaranteed. Different batches, conditions and applications yield differing results; Cure condition: 150°C/1 hour; *denotes test on lot acceptance basis)***

Physical Properties:	
***Color:** **Part A:** Silver **Part B:** Silver	**Weight Loss:**
***Consistency:** Smooth, thixotropic paste	**@ 200°C:** 0.59%
***Viscosity (@ 100 RPM/23°C):** 2,200 – 3,200 cPs	**@ 250°C:** 1.09%
Thixotropic Index: 4.63	**@ 300°C:** 1.67%
***Glass Transition Temp.(Tg):** ≥ 80°C (Dynamic Cure 20—200°C /ISO 25 Min; Ramp -10—200°C @ 20°C/Min)	**Operating Temp:**
Coefficient of Thermal Expansion (CTE):	**Continuous:** -55°C to 200°C
Below Tg: 31 x 10^{-6} in/in/°C	**Intermittent:** -55°C to 300°C
Above Tg: 158 x 10^{-6} in/in/°C	**Storage Modulus @ 23°C:** 808,700 psi
Shore D Hardness: 75	**Ions:** Cl^- 73 ppm
Lap Shear Strength @ 23°C: 1,475 psi	Na^+ 2 ppm
Die Shear Strength @ 23°C: > 10 Kg / 3,400 psi	NH_4^+ 98 ppm
Degradation Temp. (TGA): 425°C	K^+ 3 ppm
	***Particle Size:** ≤ 45 Microns
Electrical Properties:	
***Volume Resistivity @ 23°C:** ≤ 0.0004 Ohm-cm	
Thermal Properties:	
Thermal Conductivity: 2.5 W/mK	**Thermal Resistance: (Junction to Case)**
Based on standard method: Laser Flash	TO-18 package with nickel-gold metallized 20 x 20 mil chips and bonded with EPO-TEK® H20E (2 mils thick)
Thermal Conductivity: 29 W/mK	**EPO-TEK® H20E:** 6.7 to 7.0°C/W
Based on Thermal Resistance Data: R = L x K^{-1} x A^{-1}	**Solder:** 4.0 to 5.0°C/W

EPOXY TECHNOLOGY, INC.
14 Fortune Drive, Billerica, MA 01821-3972 **Phone**: 978.667.3805 **Fax**: 978.663.9782
www.EPOTEK.com

Epoxies and Adhesives for Demanding Applications™

Rev. XII
Mar 2014